AD-A139 086 CORROSION CONTROL THROUGH A BETTER UNDERSTANDING OF THE METALLIC SUBSTRAT..(U) LEHIGH UNIV BETHLEHEM PA CENTER FOR SURFACE AND COATINGS RESE.. H LEIDHEISER ET AL. 1/3

UNCLASSIFIED 01 JAN 84 N00014-79-C-0731 F/G 11/6 NL

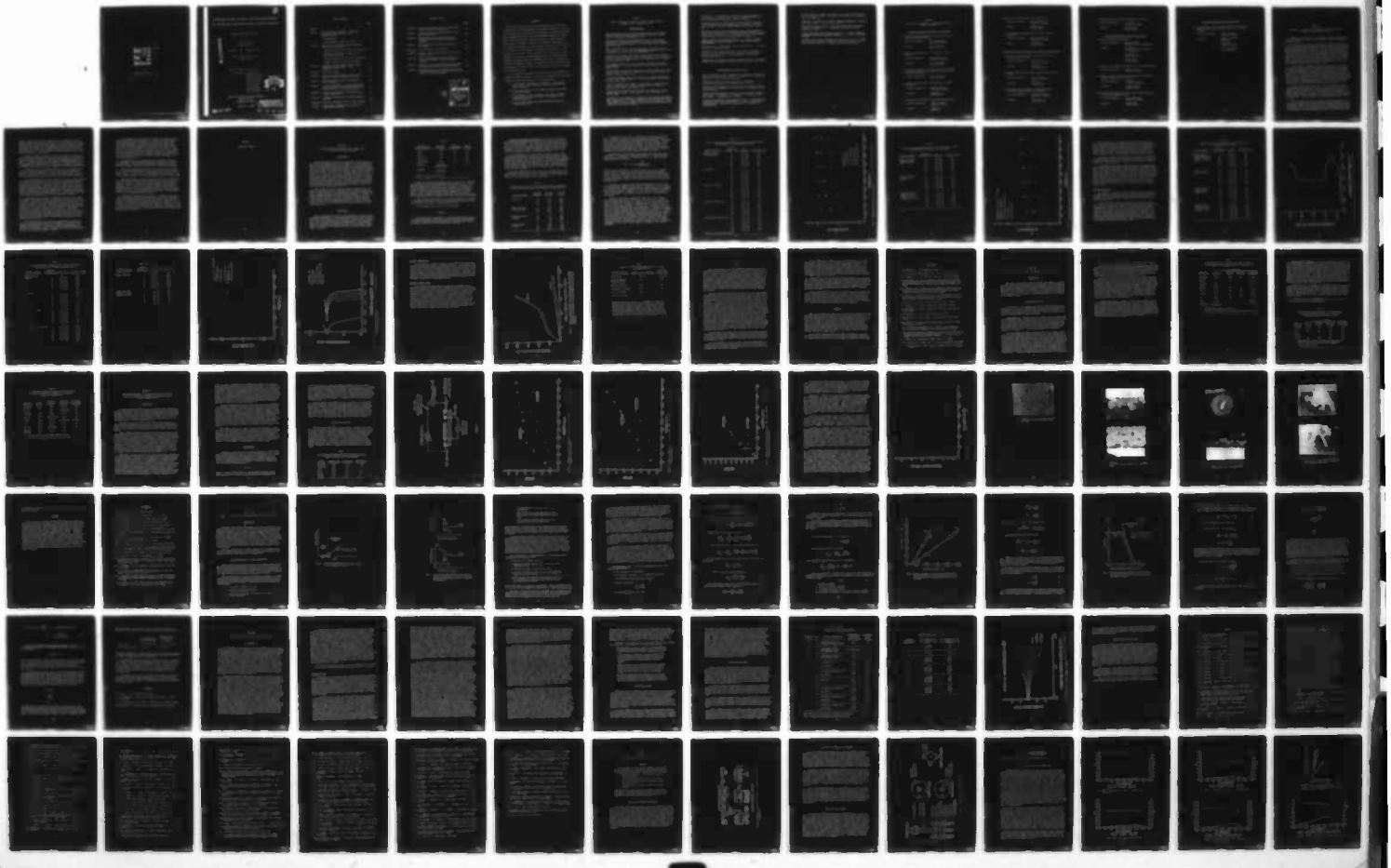

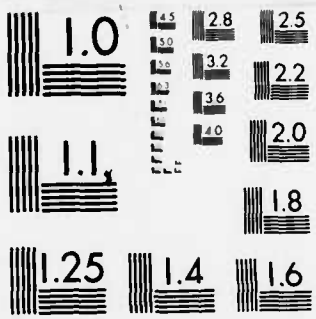

CORROSION CONTROL THROUGH A BETTER UNDERSTANDING OF THE METALLIC SUBSTRATE/ORGANIC COATING/INTERFACE

Agreement No. N00014-79-C-0731

Fourth Annual Report

Covering the Period,

September 1, 1982 - September 30, 1983

Sponsor: Office of Naval Research
Washington, D.C.

Principal Investigator: Henry Leidheiser, Jr.

Co-Investigators: Eugene M. Allen
Mohamed S. El-Aasser
Frederick M. Fowkes
Richard D. Granata
Roland W. Lovejoy
John A. Manson
Jack F. McIntyre
Fortunato J. Micale
Gary W. Simmons
John W. Vanderhoff

Center for Surface and Coatings Research
Lehigh University
Bethlehem, Pa. 18015

January 1, 1984

TABLE OF CONTENTS

CONTENTS (Cont'd.)

FOREWORD

This report represents the fourth annual summary of research carried out under Office of Naval Research Contract No. N00014-79-0731. The objective of this research is to obtain a better understanding of the metallic substrate/organic coating/interface system so that improvements may be made in corrosion control of metals by painting. The report this year includes a summary of progress made in 16 different components of the program. These activities are arranged for convenience into those primarily concerned with (a) corrosion at the interface, (b) the chemistry of the metal/coating interface, (c) the properties of the coating, (d) the properties of iron oxides with particular relevance to the painting of rusted steel. Each of the 16 sections has been authored by the program component director and there is thus a difference in the style of presentation in many of the sections. It should be noted that the program number in this year's report is not necessarily the same as the number in the third annual report.

It is recognized that readers of this report will be interested in the contents for different purposes. In an effort to accommodate to these diverse interests, the report is presented in the following format.

(1) A list of public disclosures of the research. The references may be useful to those who wish to explore the research results in greater detail.

(2) A list of the titles of the 16 component programs and the names of the participants.

(3) A condensation of the total program. This summary is aimed at those who wish to obtain an overview of the program and the approaches being used.

(4) A more detailed outline of the results generated during the present report period.

SECTION 1

A List of Public Disclosures of the Research during the Period, September 1, 1982 - September 30, 1983

Published Papers

"Drying and Curing of Epoxy Resin-Curing Agent Systems," Ata-Ur Rahman, A Research Report in partial fulfillment for the M.S. degree in Polymer Science & Engineering, Lehigh University, 1983.

"Structure Investigations of Electrodeposited Nickel," Attila Vértes, Zsolt Kajcsos, Ilona Czakó-Nagy, Magda Lakatos-Varsányi, Laszlo Csordás, Gerhard Brauer, and Henry Leidheiser, Jr., Nuclear Instruments and Methods 199, 353-57 (1982).

"Cobalt and Nickel Cations as Corrosion Inhibitors for Galvanized Steel," H. Leidheiser, Jr., and I. Suzuki, in Atmospheric Corrosion, William H. Ailor, Editor, John Wiley & Sons, New York, 615-29 (1982).

"Activities in Corrosion at the Center for Surface and Coatings Research, Lehigh University, Bethlehem, Pa., USA," Henry Leidheiser, Jr., in Newsletter, Division of Colloid and Surface Chemistry, The Chemical Society of Japan 7, No. 6 (Nov. 1982), pp. 9-10.

"The Atmospheric Corrosion of Iron As Studied by Mössbauer Spectroscopy," Henry Leidheiser, Jr., and Svetozar Musić, Corrosion Science 22, No. 12, 1089-96 (1982).

"The Mechanism for the Cathodic Delamination of Organic Coatings from a Metal Surface," Henry Leidheiser, Jr., Wendy Wang, and Lars Igetoft, Progress in Organic Coatings 11, 19-40 (1983).

"A Two-Step Anodization Process for Inhibition of the Oxygen Reduction Reaction on Iron," Henry Leidheiser, Jr., and Hidetaka Konno, J. Electrochem. Soc. 130, 747-53 (1983).

"Effect of Stresses on the Mössbauer Line Intensities in Nickel Electrodeposits of [100] Texture," L. Takacs, A. Vértes, and H. Leidheiser, Jr., physica status solidi (a) 74, K45-K48 (1982).

Whitney Award Lecture-1983, "Towards a Better Understanding of Corrosion Beneath Organic Coatings," Henry Leidheiser, Jr., Corrosion 39, No. 5, 189-201 (1983).

"New Studies of the De-Adhesion of Coatings from Metal Substrates in Aqueous Media—Interpretation of Cathodic Delamination in Terms of Plarization Curves," Henry Leidheiser, Jr., Lars Igetoft, Wendy Wang and Keith Weber, Proc. VIIth International Conference in Organic Coatings Science and Technology, Athens, Greece, July 13-17, 1983, pp. 327-58.

"Inhibition of the Oxygen Reduction Reaction Using 8-Hydroxyquinoline," H. Leidheiser, Jr., H. Konno, and A. Vertes, in Proceedings, NACE Intl. Conf. on Corrosion Inhibitors, Dallas, Texas, May 1983.

"Passivation of Steel in a Borate Buffer Containing Organic Compounds as a Means for Improving Corrosion Resistance," in Proceedings of the Fifth Intl. Symposium on Passivity, Bombannes-Bordeaux, France, May 30-June 3, 1983.

"The Effect of Surface Treatment and Substrate Metal on Electrochemical Behavior after Passivation in a Borate Buffer Containing 8-Hydroxyquinoline," H. Konno and H. Leidheiser, Jr., in Extended Abstracts Vol. 83-2, October 1983 Fall Meeting of The Electrochemical Society, Washington, D.C.

"Acid-Base Interactions in Polymer Adhesion," F. M. Fowkes, in Physico-chemical Aspects of Polymer Surfaces, ed. K. Mittal, Plenum Press, 2, 583-603 (1983).

"Characterization of Solid Surfaces by Wet Chemical Methods," F. M. Fowkes, ACS Symp. Ser. 199, 69-88 (1982).

"New Concepts of Interfacial Interaction in Particulate and Fibrous Composites," in Proceedings, Intl. Conf. on the Interface-Interphase in Composite Materials, Society of Plastics Engineers, Liege, Belgium, October 16-20, 1983, p.1.

"Pigment-Binder Interactions in Corrosion-Protecting Coatings," M.S. Report, Polymer Science and Engineering Program, Lehigh University, October 1983.

Papers Submitted, Accepted or In Press

"Direct Determination of Molar Enthalpies of Adsorption in Flow Microcalorimetry," S. T. Joslin and F. M. Fowkes, in preparation; to be submitted to the Journal of Colloid and Interface Science.

"Fundamental Aspects of Corrosion Protection," H. Leidheiser, Jr., P. A. Clarkin, and E. McCafferty, Naval Research Review, in press.

"Improved Corrosion Resistance of Steel in Water after Abrasive Blasting with Alumina," H. Leidheiser, Jr., S. Music, and J. F. McIntyre, Corrosion Science, in press.

"Metal/Flame-Sprayed-Aluminum Interface as Studied by Emission Mössbauer Spectroscopy," H. Leidheiser, Jr., H. Herman, R. A. Zatorski, S. Music, and A. Vértes, J. Electrochem. Soc., in press.

"Structure Investigations of Electrodeposited Nickel I. (X-Ray Diffraction and Mössbauer Spectroscopic Measurements)," A. Vértes, I. Czakó-Nagy, M. Lakatos-Varsányi, L. Csordas, and H. Leidheiser, Jr., submitted to J. Electrochem. Soc.

"Structure Studies of Nickel Electrodeposits II. Positron Lifetime Measurements," A. Vértes, C. Szeles, Zs. Kajcsos, and H. Leidheiser, Jr., submitted to J. Electrochem. Soc.

"Coatings," H. Leidheiser, Jr., Chapter in Corrosion Mechanisms, F. Mansfeld, Editor, Marcel Dekker, accepted for publication.

"Mössbauer Spectroscopic Study of Rust Formed during Simulated Atmospheric Corrosion," H. Leidheiser, Jr., I. Czakó-Nagy, submitted to Corrosion Science (Oct. 1983).

"Interface Acid-Base/Charge Transfer Properties," F. M. Fowkes, in Surface and Interfacial Aspects of Biomedical Polymers, ed. J. Andrade, Plenum Press, in press.

"Acid-Base Contributions to Adsorption on Polymers on Fillers," F. M. Fowkes, paper presented in Houston, TX, Rubber Division, American Chemical Society Meeting, October 25-28, 1983. Manuscript submitted for publication.

SECTION 2

The Titles of the Component Programs Summarized Herein and the Participants

Programs Concerned with Corrosion at the Interface

(1) Improved Corrosion Resistance of Steel in Mild Media after Abrasive Blasting with Alumina

Principal Investigator:	Henry Leidheiser, Jr. Professor of Chemistry
Associate:	Jack F. McIntyre Research Associate

(2) Towards an Understanding of the Phenomenon of Poor Wet Adhesion

Principal Investigator:	Henry Leidheiser, Jr. Professor of Chemistry
Associate:	H. E. George Rommal Graduate Student

(3) Interfacial Breakdown in a Coating/Metal System as Studied by Thin Film Conduction Techniques and Optical Microscopy from the Substrate Side

Principal Investigator:	Jack F. McIntyre Research Associate

(4) A Model for the Quantitative Interpretation of Cathodic Delamination

Principal Investigator:	Henry Leidheiser, Jr. Professor of Chemistry
Associate:	Wendy Wang Graduate Student

(5) Catalysis and Inhibition of the Oxygen Reduction Reaction

Principal Investigator:	Richard D. Granata Research Scientist
Associate:	Jane Heitz Technician

(6) Detection of Aggregated Water in Polymer Coatings

Principal Investigator:	Henry Leidheiser, Jr. Professor of Chemistry
Associate:	Douglas Eadline Graduate Student

(7) Investigation of Phosphated Steel Surfaces by Laser Raman Spectroscopy

Principal Investigator:	Henry Leidheiser, Jr. Professor of Chemistry
Associate:	André Sommer Graduate Student

Programs Concerned with the Chemistry of the Metal/Coating Interface

(8) Studies of the Coating/Substrate Interface Using Surface Enhanced Raman Spectroscopy

Principal Investigator:	Roland Lovejoy Professor of Chemistry
Associate:	David Koran Visiting Scientist

(9) Acid/Base Properties of Hydrated Oxides on Iron and Titanium Surfaces

Principal Investigator:	Gary W. Simmons Professor of Chemistry
Associate:	Bruce Beard Graduate Student

(10) Determination of the Acidity of Iron Oxide Surfaces. Acid Sites on Hematite Using Flow Calorimetry

Principal Investigator:	Frederick M. Fowkes Professor of Chemistry
Associate:	Sara Joslin Graduate Student

(11) Characterization of the Surface Properties of Iron Oxides

Principal Investigator: F. J. Micale
Professor of Chemistry

Associate: Dennis Kiernan
Graduate Student

Programs Concerned with Properties of the Coating

(12) Drying and Curing of Epoxy Films

Principal Investigator: Mohamed El-Aasser
Professor of Chemical Engineering

Associates: Cesar Silebi
Associate Professor of Chemical Engineering

Olga Shaffer
Technical Associate

Ata-Ur Rahman
Graduate Student

(13) Analysis of Electrodeposited Epoxy Resin by Laser Raman Microprobe

Principal Investigator: Eugene M. Allen
Professor of Chemistry

(14) Effect of Acid-Base Interaction on Permeability and Mechanical Behavior of Model Protective Coatings

Principal Investigator: John Manson
Professor of Chemistry

Associate: Astrophel Tiburcio
Graduate Student

(15) Diffusion of Ions and Water into Protective Organic Coatings and the Cathodic Delamination Process

Principal Investigator: Henry Leidheiser, Jr.
Professor of Chemistry

Associate: Jeffrey Parks
Graduate Student

Program Concerned with Painting Rusted Steel

(16) An Understanding of the Principles Related to the Application of Paints to Rusted Steel Surfaces with Little or No Surface Preparation

Principal Investigator: John W. Vanderhoff
Professor of Chemistry

Associates: Leonard M. Bennetch
Consultant

Olga Shaffer
Technical Associate

T-C. Clarence Huang
Graduate Student

SECTION 3

A Summary of the Experimental Results Obtained during the Period, September 1, 1982 - September 30, 1983

A summary is given herein of the total research program, the components of which are directed by 9 Lehigh faculty members, a research scientist and a research associate.

The corrosion process which occurs beneath an organic coating is preceded by the development of an aqueous phase at the interface. In some cases this aqueous phase develops over the entire interface and the coating develops what has been termed "poor wet adhesion." This latter phenomenon has been studied on glass substrates and metallic substrates in order to determine if there are correlations which can be drawn among metal/organic coating systems. Acrylic and three different alkyd systems retained good adhesion to aluminum, chromium and tin after immersion in deionized water for 3 days while silver, copper, nickel and silicon exhibited behavior characteristic of the coating system. Measurements of acrylic coatings on glass indicated that the collection of water at the glass/coating interface occurred locally and then the water spread laterally from these nucleation sites.

A second method being used to understand better the initial stages of the corrosion process is based on the change in resistance of a metal film, 150 - 200 A. in thickness, after coating with an organic material and exposure to a corrosive environment. Uncoated metals, such as aluminum, iron and nickel, undergo rapid changes in resistance when exposed to a high relative humidity or to a corrosive environment. Coated metals exhibited slower changes in resistance. The resistance changes occurred before corrosion was visible either as viewed through the coating or as viewed through the thin metal film on a glass base. Large increases in resistance did occur when corrosion was first detected. The method shows promise as a means for studying the very early stages of the corrosion process beneath organic coatings.

The development of an aqueous phase at the coating/metal interface, or possibly within the polymer itself, is being followed by means of high frequency dielectric spectroscopy. A change in the dielectric properties at a frequency of the order of 10^9 Hz has been identified with the presence of water in polyvinyl acetate coatings. The character of the dielectric response in this frequency range is attributed to free and aggregated water molecules in the coating. It appears possible to discriminate between these two types of water.

After water has collected at the metal/organic coating interface, the medium for electrochemical processes is present and the corrosion process can be initiated. Whether or not corrosion occurs is dependent upon the activity of the metal surface. Two studies are being carried out which relate to the surface activity. The first is concerned with activity changes which occur as a consequence of abrasive blasting with alumina. Much of the alumina that

ends up on the surface after blasting is present as embedded particles that impact the surface and plastically deform it. A small fraction of the total aluminum present in the surface is presumed to be incorporated into the oxide film on an atomic scale. The energy released locally during impact is high and some of the aluminum ions or aluminum-oxygen complex enters the surface oxide during its formation as the alumina particles impact the surface. This newly formed oxide is a poorer catalyst for the oxygen reduction reaction and is more resistant to anodic attack.

Means for modifying the surface of the metal to make it a poorer catalyst for the oxygen reduction have already been developed in this study, but additional methods are required. A literature survey suggests that the oxide film on iron can be modified to yield different semiconducting properties which can influence the oxygen reduction reaction. Experimental studies show that anodization of a steel surface in the presence of aluminum ions yields an inhibited electrochemical surface as judged by polarization resistance data.

A quantitative model of cathodic delamination, i.e., the delamination that results because the cathodic reaction occurs beneath the coating, is presented. The model is based on a 2-dimensional application of the model used to explain the precipitation of a solid from a liquid medium. The model predicts reasonable values of the diffusion coefficient for active species.

Laser Raman spectroscopy is being explored as a means for *in situ* studies of the organic coating/metal interface. Iron, zinc and manganese phosphates have been characterized and their spectra have been successfully obtained through organic coatings. It has been possible to follow the attack of the phosphate by strong alkaline solutions, a chemical reaction which mirrors the attack of phosphate during cathodic delamination. Major efforts have been expended to determine if the Surface Enhanced Raman Spectroscopy (SERS) effect can be used to advantage in studying phenomena at the coating/metal interface. Several candidate systems have been selected, but no SERS effect has yet been obtained when the probe molecule is at the coating/metal interface.

The bonding between an organic coating and the substrate metal and between pigment and organic matrix may be interpreted in terms of an acid/base interaction. Three studies are focusing on quantifying these concepts. Flow calorimetry is being used to study the adsorption and desorption of selected organic compounds on iron oxides. Competition between water and the organic molecule for sites on the surface is being determined by using dried solvents and solvents to which small amounts of water are added. The acid/base properties of the oxides on the surface of iron and titanium have been quantitatively appraised by immersing the oxidized metal in KOH at controlled pH. The extent of exchange of potassium ions with protons of the surface hydroxyls is followed by surface analysis techniques. The character of the oxygen atoms in the surface region is simultaneously determined using X-ray photoelectron spectroscopy.

The surface nature of iron oxides is being determined using electrophoresis, surface modification with silicon compounds, gas adsorption, gas adsorption following thermal treatment, and infrared spectroscopy. Hexamethyldisilazane (HMDS) is a very effective reagent for hydrophobing the surface of all iron oxides studied. The surface $^{-}$OH groups are more randomly distributed on γ-FeOOH as compared to α-Fe_2O_3.

Four programs are concerned with the coating. The drying of epoxy resin-curing agent systems was studied as a function of the formulation of the coating and the relative humidity of the air during drying. Water-based systems exhibited a rough surface and cracks after drying while solvent-based systems were comparatively smoother and had fewer cracks on the surface. The drying behavior of the solvent-based systems was independent of the relative humidity of the drying air. The changes in drying rate with time for the water-based systems were attibuted to the formation of a surface skin during the initial stages of drying and its rupture at the end of the drying operation. Increased resistance to cathodic delamination was present in coatings that were dried at higher temperature and lower relative humidity.

The homogeneity of epoxy-amide systems was determined utilizing a Raman microprobe. Emissions characteristic of the epoxy and of the amide were identified and the localized concentration of these two components was then determined. The method shows promise as an analytical technique.

Inverse gas chromatography was adapted to characterize the acid/base nature of untreated glass beads (acidic) and those treated with an aminosilane (basic). Solvent retention, gas permeability and interfacial adhesion (as shown in SEM pictures of fractured coatings) were explained in terms of the surface properties of the glass bead filler material in phenoxy resin.

Radiotracer sodium and chlorine are being used to study the relationship between ionic transport and the disbonding of protective coatings as a function of potential. Coatings with good wet adhesion show a significant increase in the rate of uptake of Na^+ when the substrate metal is made cathodic at -0.8 V vs SCE. Lateral diffusion studies of Na^+ beneath polybutadiene coatings on steel at open circuit potential show that the rate of lateral diffusion is of the same magnitude as diffusion through the coating. Diffusion data are being generated which should be useful in a quantitative analysis of the cathodic delamination process.

Fundamental information on the adsorption of polymers on iron oxide corrosion products is being accumulated in order to understand phenomena related to the painting of rusted steel after the removal of only the loose surface rust. Conductometric and polymer adsorption data indicated that the larger iron oxide particles adsorbed greater amounts of polymer per unit surface area. The larger particles had a greater density of acidic sites. Each of these acidic sites on the oxide particle is attached to a segment of a polymethyl methacrylate molecule and loops of approximately 30 PMMA segments long projected into the solution.

SECTION 4

INDIVIDUAL PROGRAMS

Program #1

Improved Corrosion Resistance of Steel in Mild Media after Abrasive Blasting with Alumina

INTRODUCTION

Many miscellaneous observations of our own and of others during the past few years have made us aware of the important role that surface condition plays in the superficial corrosion of metals. More recently we have noted a very effective inhibition of corrosion of steel which had been subjected to abrasive blast cleaning with alumina. This observation heightened our interest because it had previously been found that the oxygen reduction reaction occurs much less readily on an aluminum surface than on a steel surface [1,2]. Since the rate at which the oxygen reduction reaction occurs is critically important in the cathodic disbonding of an organic coating from a metal substrate under many experimental conditions [3], it appeared worthwhile to explore further the effect of abrasive blasting with alumina on the superficial corrosion of steel. Preliminary studies on the investigation of abrasive blasting with alumina have been reported previously [4]. Initial studies revealed an improved corrosion resistance of steel in distilled water after blasting with alumina [5].

There is much interest at the present time in modifying the surface composition of steels in order to develop superior corrosion resistant behavior. Techniques such as ion implantation, laser surface alloying, and surface diffusion processes are being explored intensively. It appears that another candidate method for modifying the surface composition is non-metallic abrasive blasting. The term, "non-metallic abrasive blasting", is used because there are proprietary processes that utilize metallic-coated abrasives that leave significant amounts of the metallic component on the substrate, a technique which imparts corrosion protection by anodic sacrificial action.

EXPERIMENTAL

Abrasive blasting was carried out using equipment obtained from Hunter Associates, Bridgewater, N.J. The abrasive materials were propelled toward the substrate with compressed air at pressures of 50-68 psi and at angles of 30° or 90°. Table I lists the abrasive materials, mesh size, and several other surface treatments used during the inevestigation. Substrates were stored in a desiccator after blasting and prior to electrochemical investigation. All substrates were washed with methanol and dried using a paper tissue, "Kim-Wipe".

Table I

Material of Surface Preparation	Mesh Size or other	Pressure of Blasting (psi)	Angle of Blasting
Al_2O_3*	280	62	30°
Al_2O_3	60	52	90°
Steel Grit	80	52	90°
Glass Beads*	325	62	30°
Abrasion	600 Grit Silicon Carbide	--	--
Polished	(0.5 μ) Al_2O_3 Finish	--	--

*Powder of finely divided abrasive.

Polarization resistance measurements were carried out with a Princeton Applied Research (PAR) Corrosion Measurement Console, Model 350. A three-electrode system was used and the scan rate was typically 0.1 mv/sec. A previous investigation [5] described studies conducted in distilled water, where compensation for the high resistance of the electrolyte was made in two ways. First, the Luggin capillary was positioned close to the metal surface. Second, a PAR IR compensation module, Model 356, was used to measure the uncompensated resistance of the solution and calculated R_p values were consequently adjusted to account for the high resistance of the solution.

Present studies utilized more conductive and more aggressive solutions. A 0.1M borate buffer solution pH = 8.5 was used initially and later studies involved using a 0.1M borate - 0.1% NaCl solution pH = 8.5.

All measurements were carried out on SAE 1010 Steel.

RESULTS

The experimental data from which the conclusions were drawn are based on polarization resistance measurements, cathodic polarization measurements and cathodic delamination studies of treated and untreated steel substrates. The results from each of these techniques will be reported.

Polarization Resistance Measurements. This technique was adopted as the prime method for comparing corrosion behavior since it was desired to make corrosion measurements at short times in the situation where the metal corrosion loss was minimal. It was also desired to make corrosion measurements as a function of time without removing the samples from the solution. Polarization resistance measurements appeared to meet the required needs. An extensive literature review of the studies utilizing the polarization resistance technique is found in a NACE publication [6].

Early measurements using various surface treatments indicated that steel blasted with alumina, or mixtures of alumina with chromia or silica, yielded significantly lower corrosion rates than steel abrasively polished with silicon carbide or blasted with steel grit. Although these measurements yielded good comparative values, the actual values were not quantitatively correct because of inadequate IR compensation. These values will not be reported herein even though it is felt that they provide convincing support for the efficacy of alumina blasting in developing a surface that has superficial corrosion resistance.

Previous studies provide evidence that steel abrasively blasted with alumina exhibits a lower initial rate of corrosion in distilled water than similar steels balsted with steel grit or abraded with silicon carbide [5]; Table II is a partial summary of the results found.

Table II

Calculated Corrosion Rates from Polarization Resistance Measurements of Steel in Distilled Water after Surfacing in Various Ways [5]

Surface Treatment	Immersion Time (min)	Corrosion Rate (mpy)	E_{corr} (mV) vs. SCE
As received	5	2.35	-624
	35	0.75	-680
	65	0.57	-720
	95	0.52	-736
Abraded, 600 Grit, Silicon Carbide	5	27.30	-586
	35	0.81	-638
	65	0.71	-658
	95	0.67	-674
Blasted, Steel Grit, 80 Mesh	5	3.82	-540
	35	.59	-582
	65	.69	-592
	95	.85	-604
Blasted, Alumina, 60 Mesh	5	0.69	-746
	35	0.35	-736
	65	0.37	-734
	95	0.37	-738

A continuation of these intial studies was conducted during the past year. A decision was made to use a more aggressive environment and one in which the solution conductivity was higher than distilled water. The increase in conductivity of the solution will eliminate 'IR' drop problems. And the use of a more corrosive medium would provide a better way to judge the effectiveness of abrasive blasting with alumina. In addition, several post-abrasion treatments were performed to better enhance the improved corrosion resistance of the alumina-blasted steel. Among the various post-treatments, chromating and anodization gave encouraging preliminary results.

Corrosion data are represented by polarization resistance (R_p) values in ohms/cm^2. The Stern-Geary [7] approach, Equation (1), indicates that a large R_p value corresponds to a low corrosion rate, i.e., small corrosion current densities, as follows:

$$\Delta E/\Delta I = R_p = \frac{\beta_A \beta_C}{2.3\, i_{corr}(\beta_A + \beta_C)} \quad , \qquad (1)$$

where ΔE is the overpotential, ΔI is the current, i_{corr} is the corrosion current density, β_A and β_C are the anodic and cathodic Tafel constants. Values of R_p are preferentially used to compare the corrosion resistance of various substrates. Corrosion rates are not calculated in the usual manner so as to avoid errors caused by uncertainties in the Tafel constants in the mediums investigated. Therefore, the larger the value of R_p, the lower the corrosion rate.

Polarization resistance results for measurements made in 0.1M borate pH=8.5 can be seen in Table III and Figure 1. In Figure 1, a plot of log R_p vs. time shows that alumina blasted steel gave higher values for R_p; however, only slightly better than abraded steel. The maximum difference was observed early in the experiment. A geometric surface area of 0.80 cm^2 was used to calculate R_p values. A discussion of surface area will be approached later in this paper.

Several post-blasting treatments were conducted. First, alumina-blasted steel was anodized in 0.5M borate at pH = 5.50 in an attempt to enhance the surface concentration of aluminum or facilitate its incorporation into the surface oxide. Secondly, alumina-blasted steel was subjected to a chromate dip (Solution composition: 100 g $K_2Cr_2O_7$ + 13 g NaOH/1.0 liter) at 95°C for various immersion times. The chromate dip was applied after blasting and also after anodizing alumina-blasted samples. Polarization resistance results for treated samples can be seen in Table IV and Figure 2. A comparison of the results found in Table IV with those reported in Table III indicates that anodization, chromating, and anodization-chromating gave improved corrosion behavior over those samples treated as indicated in Table III. Survey Auger and XPS scans revealed that chromium remained on the surface after its application and also after exposure to a corrosive environment. The chemical state of chromium has not been determined to date. In addition, chromating of a steel-grit blasted sample did not enhance its corrosion resistance.

Table III

Polarization Resistance Measurements for Abraded and Blasted Samples during Exposure to 0.1M Sodium Borate at pH 8.5

Surface Treatment	Time of Immersion (min)	$R_p(\Omega/cm^2)$	E_{corr}(mV) vs. SCE
Abraded, 600 Grit Silicon Carbide	30	2.17×10^4	-402
	65	4.49×10^4	-380
	100	6.05×10^4	-370
	135	7.18×10^4	-365
	170	8.88×10^4	-360
	205	1.04×10^5	-354
As Received	30	--	--
	65	3.60×10^4	-416
	100	5.74×10^4	-391
	135	6.61×10^4	-384
	170	7.20×10^4	-379
	205	6.48×10^4	-379
Steel Grit, 80 Mesh	30	2.49×10^4	-333
	65	3.76×10^4	-311
	100	4.24×10^4	-297
	135	5.08×10^4	-285
	170	5.21×10^4	-277
	205	6.48×10^4	-269
Alumina*, 280 Mesh (avg.)	30	6.98×10^4	-338
	65	8.55×10^4	-325
	100	8.87×10^4	-320
	135	9.20×10^4	-317
	170	1.01×10^5	-314
	205	9.78×10^4	-314
Glass Beads*, 325 Mesh (avg.)	30	7.94×10^3	-374
	65	1.23×10^4	-356
	100	1.69×10^4	-344
	135	2.20×10^4	-336
	170	2.48×10^4	-331
	205	2.88×10^4	-325

*Powder of finely divided abrasive.

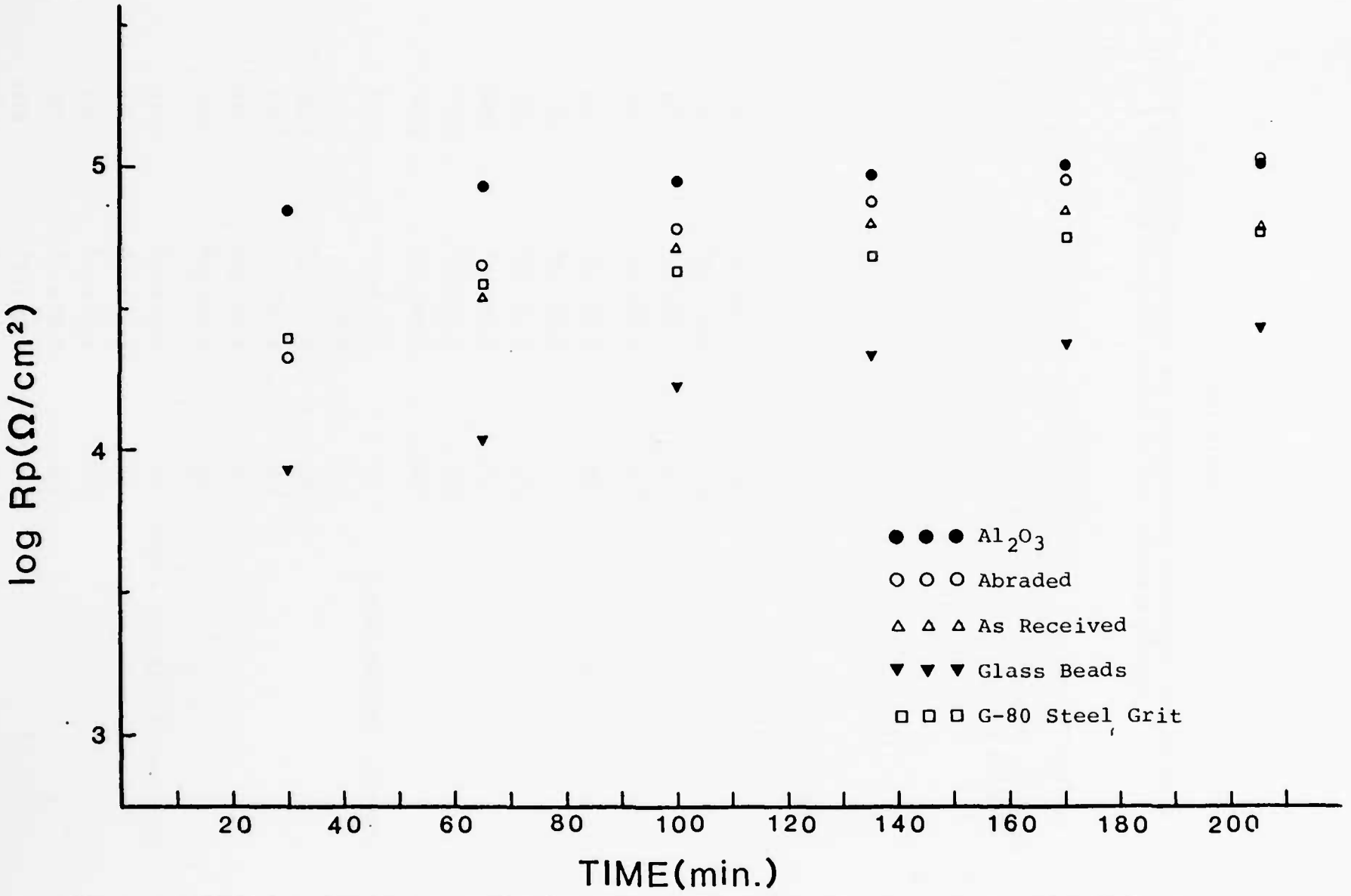

Figure 1. Polarization resistance results for various surface treatments plotted as logarithm R_p vs. immersion time in 0.1M borate pH = 8.5.

Table IV

Polarization Resistance Measurements in 0.1M Sodium Borate of Al_2O_3-Blasted Samples as a Function of Post Treatment

Surface Treatment	Time of Immersion (min)	$R_p(\Omega/cm^2)$	E_{corr}(mV) vs. SCE
Alumina, 280 Mesh, Anodized @ +0.650 V (SCE) for 10 min	30	1.30×10^5	-318
	65	1.50×10^5	-311
	100	1.57×10^5	-307
	135	1.76×10^5	-305
	170	2.08×10^5	-303
	205	1.92×10^5	-302
Alumina, 280 Mesh, Chromate Dip for 3 min	30	6.88×10^4	-392
	65	9.52×10^4	-419
	100	1.16×10^5	-421
	135	1.49×10^5	-409
	170	1.66×10^5	-400
	205	1.90×10^5	-390
Alumina, 280 Mesh, Anodized @ +0.700 V (SCE) for 7 min + Chromate Dip for 6 min	30	5.01×10^4	-424
	65	1.98×10^5	-405
	100	2.20×10^5	-384
	135	2.25×10^5	-373
	170	2.36×10^5	-366
	205	2.58×10^5	-362

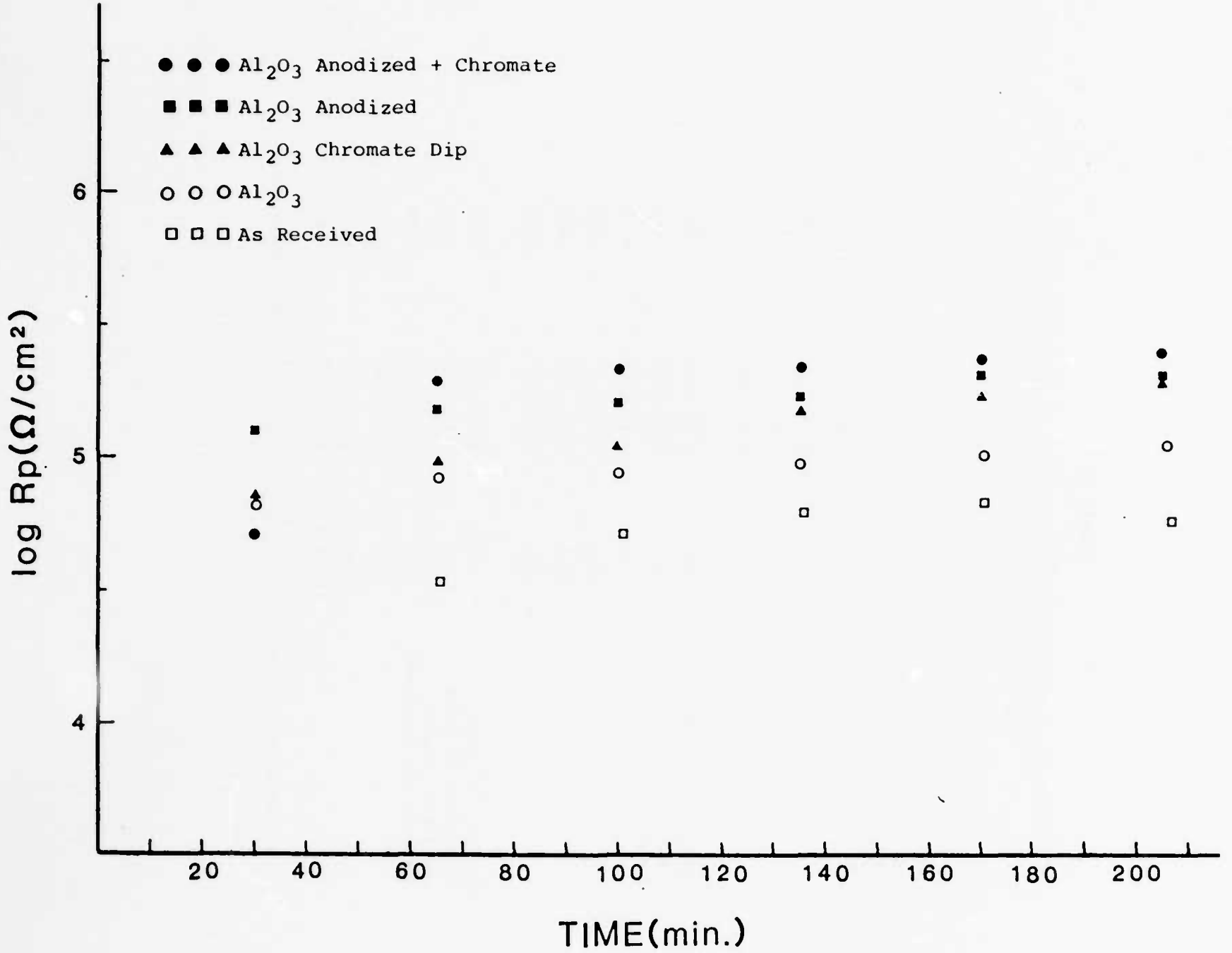

Figure 2. Polarization resistance results for various post-surface treatments plotted as logarithm R_p vs. time of immersion in 0.1M borate pH = 8.5.

Several additional surface treatments were investigated and these results can be seen in Table V. A polished steel surface, an abraded steel surface followed by cathodic treatment, or anodized steel in 0.5M borate pH = 5.50 enhanced the corrosion resistance over that of alumina-blasted steel when tested in 0.1M borate pH = 8.5, see Tables III and IV. Apparently a freshly cleaned or prepared steel surface was easily passivated in the buffered borate solution. An active-passive transition during an anodic scan in 0.5M borate pH = 5.5 was supportive of this conclusion (see Fig. 3).

In addition, an abraded steel surface was subjected to a chromate dip and gave excellent results, i.e., high R_p values (see Table V). Again, survey Auger and XPS scans indicated the presence of chromium before and after exposure to 0.1M borate pH = 8.5.

Although improved corrosion resistance was found for alumina-blasted samples when compared to untreated, steel grit-blasted, glass bead-blasted and, in some cases, abraded steels in buffered borate solution pH = 8.5, some surface treatments revealed that a freshly prepared steel surface was easily passivated. Therefore, it was decided to increase the aggressiveness of the solution by adding 0.1% NaCl to the test medium. Preliminary results can be seen in Table VI and Figure 4. Alumina-blasted steel without post-treatment showed improved corrosion resistance over as received, steel grit-blasted, and glass bead-blasted steels; however, R_p values for abraded steel were higher than for alumina-blasted steel. But, anodization of the alumina-blasted steel in 0.5M borate pH = 5.5 gave better results than all samples tested to date.

Cathodic Polarization

The importance of cathodic reactions on steel substrates, especially the oxygen reduction reaction, has been discussed in previous studies [8-12] concerning cathodic delamination. Also, the investigation and catalytic inhibition of the oxygen reduction reaction has been proposed and its importance defined [13].

Cathodic polarization curves were determined for various surface-treated steels in 0.1M borate-3% NaCl pH = 8.5. Representative polarization curves in the vicinity of the corrosion potential can be seen in Figure 5. For comparison, a polarization curve for 1100 aluminum was included to demonstrate the reduced activity of aluminum surfaces towards the oxygen reduction reaction [1,2]. This reduced activity is characterized by a reduction in the cathodic current density when compared to mild steel substrates. Alumina-blasted surfaces gave lower current density values than did polished or degreased steel samples of almost an order of magnitude. Also, alumina-blasted samples gave lower current density values than either steel grit-blasted or glass bead-blasted steels.

Table V

Polarization Resistance Measurements in 0.1M Borate pH = 8.5
for Various Surface Treatments

Surface Treatment	Time of Immersion (min)	$R_p(\Omega/cm^2)$	E_{corr}(mV) vs. SCE
Abraded, 600 Grit Silicon Carbide, Cathodic Polarization @ -1.300 V (SCE) for 5 min	30	3.49×10^4	-384
	65	7.23×10^4	-356
	100	1.09×10^5	-345
	135	1.35×10^5	-339
	170	1.91×10^5	-332
	205	2.29×10^5	-328
Polished, Alumina Finish (.05 μ)	30	5.97×10^4	-370
	65	1.15×10^5	-347
	100	1.52×10^5	-329
	135	1.69×10^5	-321
	170	1.87×10^5	-319
	205	2.03×10^5	-318
Abraded, 600 Grit Silicon Carbide, Chromate Dip for 4 min	30	1.11×10^5	-521
	65	2.53×10^5	-503
	100	4.10×10^5	-473
	135	4.11×10^5	-461
	170	3.75×10^5	-440
	205	4.92×10^5	-431
Abraded, 600 Grit Silicon Carbide, Anodized @ +.650 V (SCE) for 6 min	30	6.14×10^4	-334
	65	1.08×10^5	-318
	100	1.52×10^5	-305
	135	2.10×10^5	-296
	170	2.46×10^5	-289
	205	3.08×10^5	-284

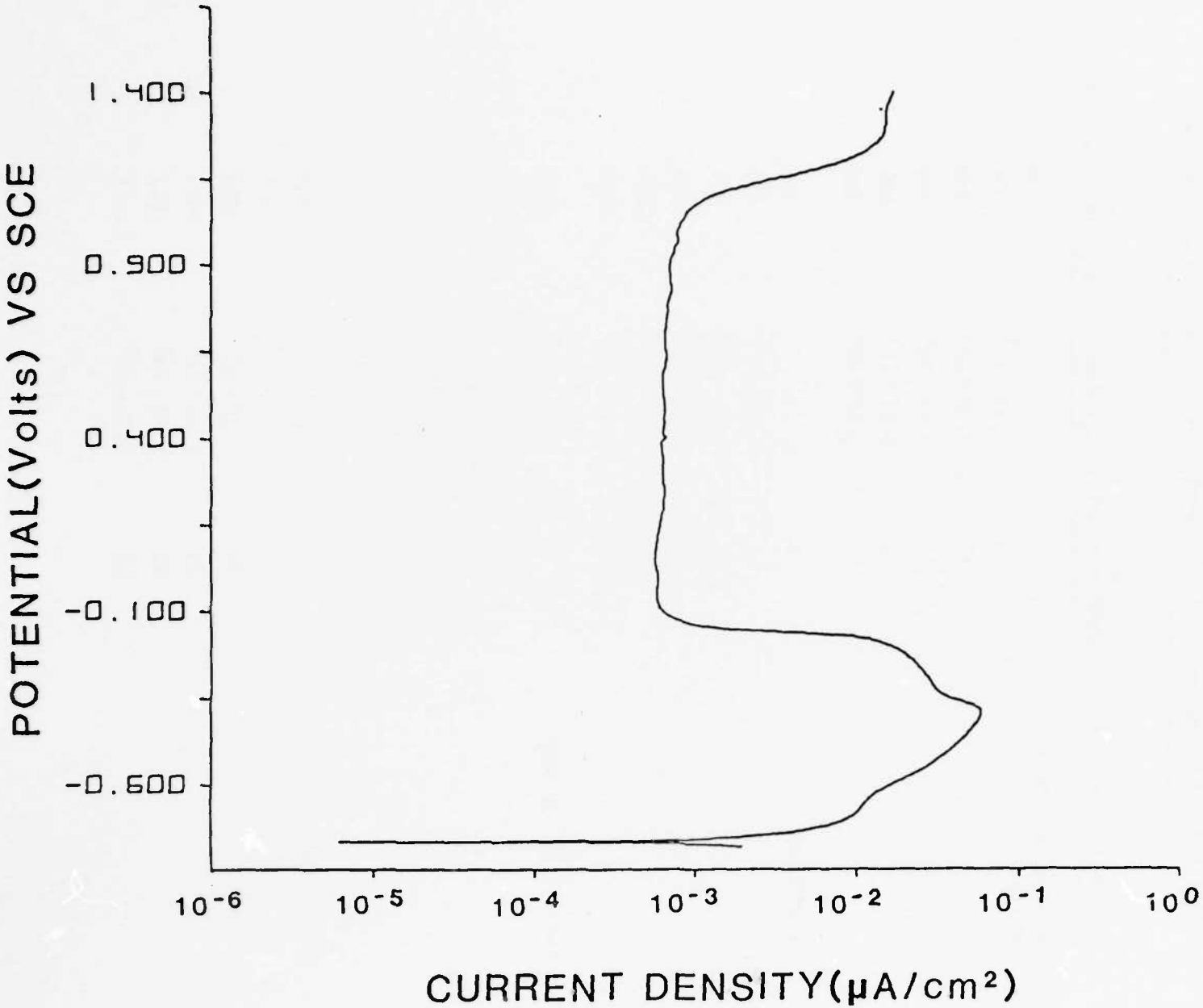

Figure 3. Anodic polarization scan for abraded steel exposed to 0.5M borate pH = 5.5.

Table VI

Polarization Resistance Measurements for Various Surface Treatments during Exposure to 0.1M Borate-0.1% NaCl pH = 8.5

Surface Treatment	Time of Immersion (min)	R_p (Ω/cm^2)	E_{corr} (mV) vs. SCE
Abraded, 600 Grit Silicon	5	--	-424
	15	2.49×10^4	-396
	25	3.78×10^4	-380
	35	4.61×10^4	-369
	45	5.42×10^4	-357
	55	5.47×10^4	-352
As Received	5	--	-399
	15	2.04×10^3	-581
	25	2.51×10^3	-613
	35	3.32×10^3	-625
	45	3.91×10^3	-624
	55	4.37×10^3	-616
Steel Grit, 80 Mesh	5	2.96×10^3	-403
	15	2.80×10^3	-403
	25	2.49×10^3	-404
	35	3.06×10^3	-404
	45	2.73×10^3	-406
	55	2.78×10^3	-407
Glass Beads, 325 Mesh (avg.)	5	8.69×10^2	-818
	15	1.15×10^3	-831
	25	1.27×10^3	-838
	35	1.44×10^3	-842
	45	1.43×10^3	-842
	55	1.41×10^3	-841

Table VI (Contd.)

Surface Treatment	Time of Immersion (min)	R_p (Ω/cm^2)	E_{corr} (mV) vs. SCE
Alumina, 280 Mesh	5	1.15×10^4	-395
	15	1.86×10^4	-388
	25	1.90×10^4	-385
	35	2.24×10^4	-385
	45	1.80×10^4	-382
	55	1.57×10^4	-381
Alumina, 280 Mesh, Anodized @ +.650 V (SCE) for 10 min	5	2.11×10^4	-341
	15	4.59×10^4	-340
	25	5.87×10^4	-339
	35	8.09×10^4	-330
	45	8.17×10^4	-327
	55	1.02×10^5	-323

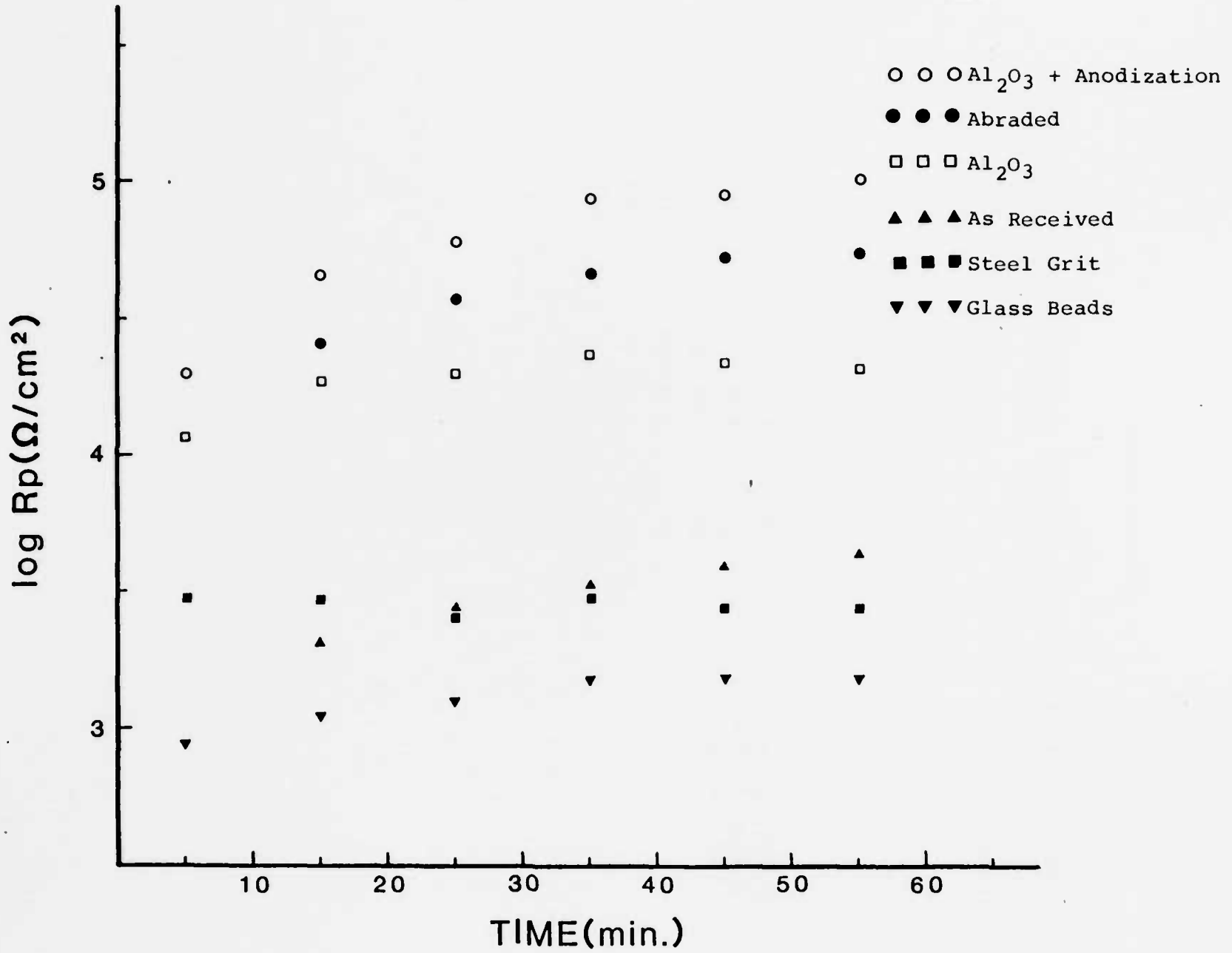

Figure 4. Polarization resistance results for various surface treatments plotted as logarithm R_p vs. immersion time in 0.1M borate-0.1% NaCl pH = 8.5.

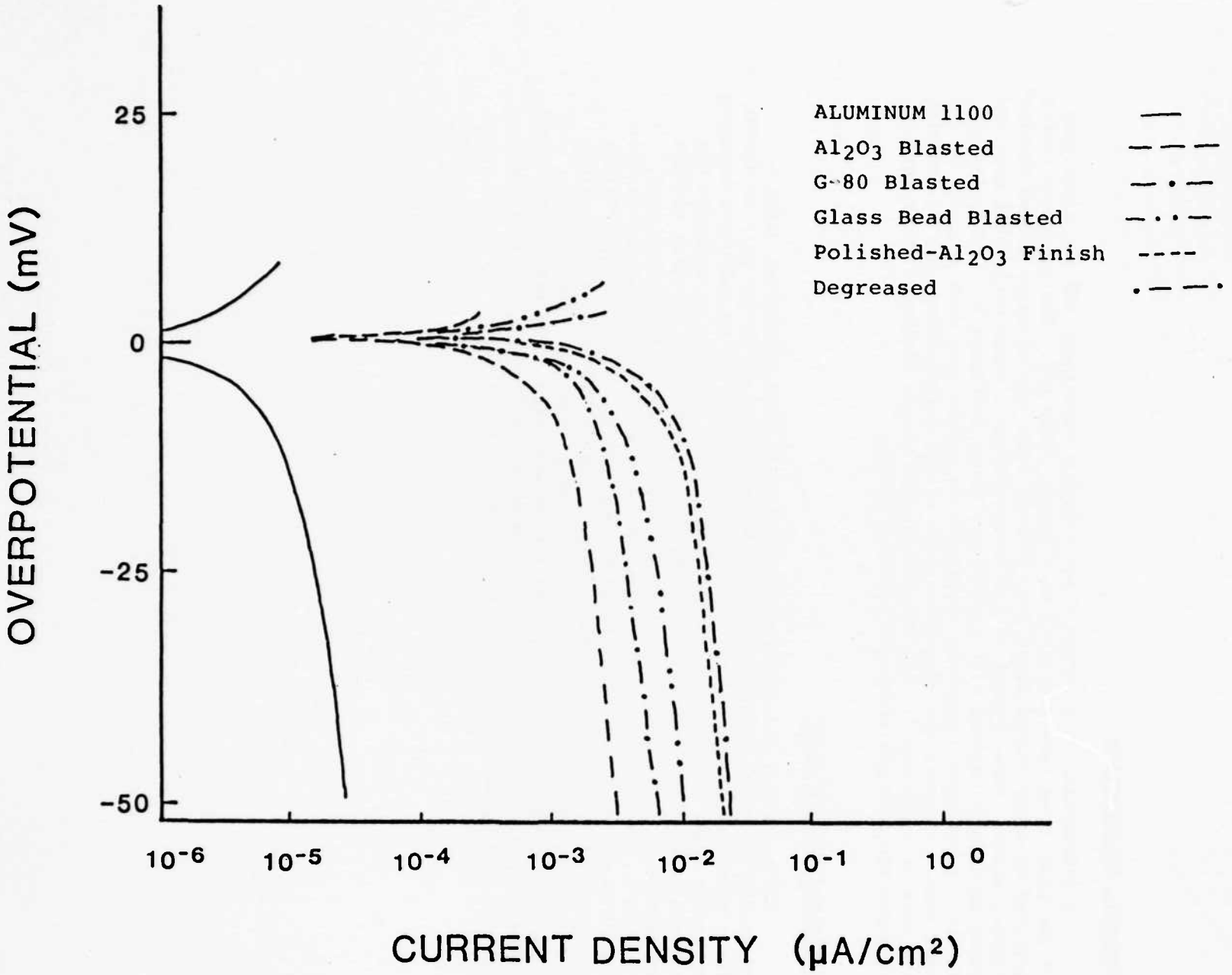

Figure 5. Cathodic polarization scans for various surface treatments exposed to 0.1M borate-3% NaCl pH = 8.5.

Cathodic Delamination

A description of a cathodic delamination experiment and the conditions of the test have been described in a recent study [5]. The specimens tested involved an epoxy coated steel, grit-blasted steel and an epoxy coated alumina-blasted steel. Data typical of panels abrasively cleaned with steel grit and those abrasively cleaned with alumina are given in Figure 6. Each point in Figure 6 represents a separate experiment on panels that were prepared at the same time. Although the absolute values of the delamination rate varied with the type of epoxy powder, the alumina-blasted panels yielded a lower rate of delamination than the steel-grit-blasted panels.

Estimated Surface Areas

Early studies and measurements of R_p data were determined using a geometric value for the surface area, an assumption which may only be useful for a quick comparison and by no means an effective way to calculate accurate corrosion rates or corrosion current densities. In order to estimate the surface area of the substrate of interest, a correlation was used between an average surface roughness value (R_A) and the geometric surface area, 0.80 cm^2. The geometric surface area was assigned to polished and as received steel and direct proportionality was set up to correlate R_A values determined for each of the samples tested. Table VII gives the R_A values and the estimated surface areas for the various samples. The cathodic polarization curves, Figure 5, were determined using these estimated surface areas. Future work on polarization resistance studies will include these surface area values to determine more accurate R_p values.

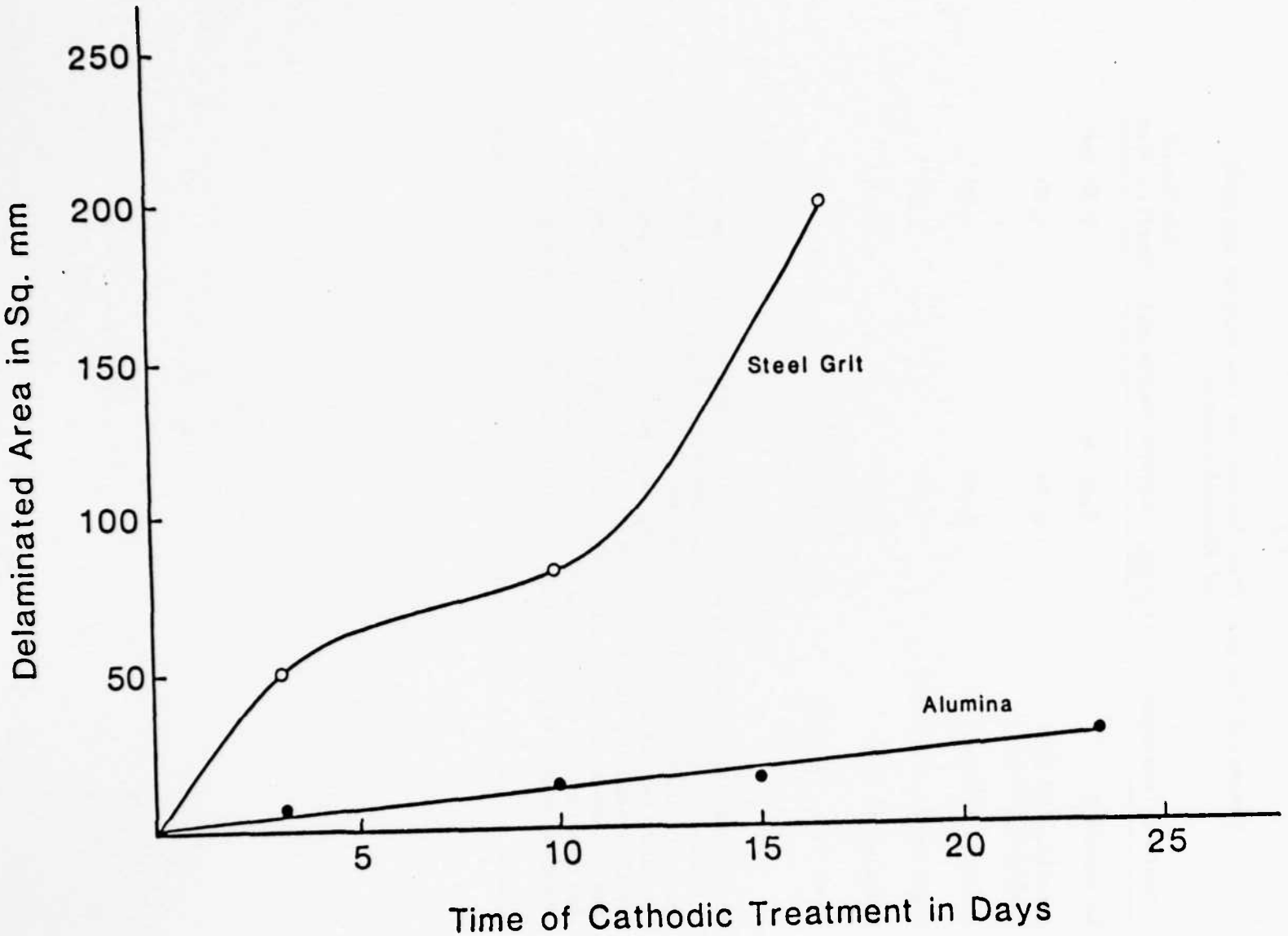

Figure 6. Plot of delaminated area against time for cathodic delamination studies of epoxy-powder coated steel surfaced by abrasive blasting with steel grit and alumina.

Table VII

Estimated Surface Area Values for the Various Abraded and Blasted Samples

Surface Treatment	*R_A(avg. surface roughness)	Estimated Surface Area
As Received	0.25 μm	0.80 cm^2
Abraded, 600 Grit Silicon Carbide	0.34	1.00
Alumina, 280 Mesh	1.03	3.20
Glass Beads, 325 Mesh	0.79	2.50
Alumina, 60 Mesh	2.33	7.40
Steel Grit, 80 Mesh	2.18	7.00

*Roughness values were measured on a "SURTRONIC 3" instrument supplied by Taylor-Hobson of Leicester, England. This instrument provides a numerical assessment of the roughness by what is known as the roughness average, R_A, method. Over a prescribed sampling length, a center line is drawn such that the sum of the areas embraced by the surface profile above and below the line is equal. The R_A value of the surface is then the average height of the surface profile above and below this line.

DISCUSSION

Data from measurements of the polarization resistance and cathodic delamination studies indicate that abrasive treatment of steel with alumina leads to a surface which is less active relative to steel not subject to abrasive treatment. Supporting evidence that the alumina treatment affects the activity of the surface came from Mössbauer studies of the product formed during corrosion in distilled water and from surface analysis which indicated the presence of aluminum [5]. Although we are reluctant to say that the data contained herein conclusively prove that abrasive blasting of steel with alumina leads to a less active steel surface, cathodic delamination and cathodic polarization studies along with information on the reduced activity of steel surfaces implanted with aluminum [14] suggest that the initial corrosion of steel may be reduced by abrasive treatment with alumina.

The most important question raised by this work is "How does alumina blasting reduce the surface activity of the steel?" Both the Auger surface analysis and the electron microprobe analysis showed that the element aluminum was present on the surface after abrasive treatment. However, neither measurement gives conclusive evidence regarding the chemical state of the aluminum. It is likely that the majority is present as finely divided alumina which is embedded in the steel. The local hot spots generated by the impinging alumina particles and the high activity of the abraded steel surface towards oxygen in the air suggest that some aluminum is incorporated in the surface oxide during blasting and that some portion of this aluminum becomes incorporated in the steel at levels below the surface. It is thus proposed that the abrasive blasting of the steel surface with alumina leads to doping of the steel surface with aluminum and that some portion of this aluminum eventually becomes incorporated in the corrosion product at the surface. Under relatively mild corrosion conditions, such as exposure to distilled water [4,5] and exposure to borate solutions with and without chloride, much of the aluminum remains at the surface and the surface film becomes enriched in aluminum. The resulting iron-aluminum oxide is assumed to have a lower activity for both the anodic and cathodic reactions because of the greater thermodynamic stability of aluminum oxide relative to iron oxides and the lower activity of oxided aluminum surfaces for the oxygen reduction reaction [1,2].

Several examples have been found in the literature in which abrasive blasting of a surface altered greatly the corrosion or surface properties of a metal. Such references are difficult to locate because they generally are peripheral to the major purpose of the paper and they are not usually found as index entries.

The most significant article is that by Andziak and Bokszczanin [15] in which it was noted that the anticorrosion properties of powder epoxy coatings on steel were improved when the steel was abrasively blasted with aluminum oxide in the form of corundum.

An outstanding example of the effect of different abrasives on corrosion behavior is shown in the work of van Rooyen, Copson and Berry [16] in experiments carried out with Inconel 600 in borated water at 600°F. They observed that panels grit blasted with alumina exhibited corrosion rates of the order of 50-70 mg/dm^2 whereas panels grit blasted with ferrochrome corroded at the rate of 30 mg/dm^2. Although the authors did not carry out experiments to understand the unusual behavior of the panels abraded with ferrochrome, they did conjecture that the ferrochrome grit blasting increased the chromium content of the surface.

Schwab and Drisko [17] have studied the dry adherence of six different types of organic coatings to steel that was abrasively finished to white metal (NACE 1) as a function of different abrasives. They noted a 0.999 level of significance between the bonding strength and the type of abrasive. Although the profile after abrasion appeared to be an important variable, they also noted that "abrasives may have deposited on surfaces or may have reacted chemically with them."

Present work reported herein strongly suggests and further supports the idea of a chemically mofified surface as a result of abrasive blasting with alumina. Early studies [4,5] revealed an improved corrosion resistance to distilled water when samples had been properly treated by alumina-blasting. Encouraging results in this study indicated that subsequent treatments may further enhance the benefits of alumina-blasting, e.g. anodization, chromating, etc... An area that merits further research and consideration.

SUMMARY

Much of the alumina that ends up on the surface after blasting is present as embedded particles that impact the surface and plastically deform it. Generally these particles act as neutral inclusions which are poor electrical conductors and have little influence on chemical behavior of the steel or iron oxide. However, a small fraction of the total aluminum present in the surface is presumed to be incorporated into the oxide film on an atomic scale. The energy released locally during impact is high and some of the aluminum ions or aluminum-oxygen complex enter the surface oxide during its formation as the alumina particles impact the surface. This newly formed oxide is assumed to be a poorer catalyst for the oxygen reduction reaction and more resistant to anodic attack.

Proof of this hypothesis requires the use of an analytical method to show that aluminum is present in the iron oxide as a component of the oxide on an atomic scale and not as part of an occluded particle of aluminum oxide.

REFERENCES

[1] H. Leidheiser, Jr., Corrosion 38, 374 (1982).

[2] D. R. Gabe and M. Shirkhanzadeh, Br. Corrosion J. 15, 216 (1980).

[3] H. Leidheiser, Jr., Ind. Eng. Chem. Prod. Res. Dev. 20, 547 (1981).

[4] H. Leidheiser, Jr., and J. F. McIntyre, "Corrosion Control through a Better Understanding of the Metallic Substrate/Organic Coating Interface," Third Annual Report, Office of Naval Research, Washington, D.C. (1982).

[5] H. Leidheiser, Jr., S. Music, and J. F. McIntyre, "Improved Corrosion Resistance of Steel in Water after Abrasive Blasting with Alumina," accepted for publication, Corrosion Science (1984).

[6] R. Graver, P. J. Moreland and G. Pini, "A Literature Review of Polarization Resistance Constant (B)-Values for the Measurement of Corrosion Rate," NACE Publication, Houston, Texas (1982).

[7] M. Stern and A. L. Geary, J. Electrochem. Soc. 104, 56 (1957).

[8] H. Leidheiser, Jr., and M. W. Kendig, Corrosion 32, 69 (1976).

[9] H. Leidheiser, Jr., and M. W. Kendig, Ind. Eng. Chem. Prod. Res. Dev. 17, 54 (1978).

[10] H. Leidheiser, Jr., Croat. Chem. Acta 53, 197 (1980).

[11] H. Leidheiser, Jr., and W. Wang, J. Coatings Technol. 53, No. 672, 77 (1981).

[12] H. Leidheiser, Jr., Wendy Wang, and Lars Igetoft, Progress in Organic Coatings 11, 19 (1983).

[13] R. D. Granata and H. Leidheiser, Jr., "Catalysis and Inhibition of the Oxygen Reduction Reaction," ONR Proposal, Program #2 (1983).

[14] B. D. Sartwell, quoted by V. Ashworth, W. A. Grant, and R.P.M. Procter, "Treatise on Materials Science and Technology," J. K. Hirvonen, Ed., Academic Press, New York, 1980, pp. 175-256.

[15] J. Andziak and W. Bokszcyanin, Powlohi Ochr 7(2), 2 (1979).

[16] D. Van Rooyen, H. R. Copson, and W. E. Berry, Corrosion 25, 194 (1969).

[17] L. K. Schwab and R. W. Drisko, Materials Performance 20(5), 32 (1981).

Program #2

Towards an Understanding of the Phenomenon of Poor Wet Adhesion

INTRODUCTION

Some organic coating/metal substrate systems, when immersed in aqueous solutions, show a serious deterioration in the strength of the coating/metal bond. In some systems the adherence becomes essentially negligible within a short period of time whereas in other systems the adherence is unaffected by immersion. Poor wet adhesion is reversible, i.e., the adherence is regained when the coating is permitted to dry. The work reported herein represents a first preliminary step in attempts to understand the origin of poor adhesion in the presence of water.

EXPERIMENTAL RESULTS

The objective of the experiments outlined below was to determine the ubiquitousness of the loss of adhesion when a thin coating/substrate system was immersed in an aqueous solution. These experiments include data obtained on three different types of substrates: (a) glass, (b) solid metals, and (c) evaporated metals on glass and silicon.

Glass Substrates. Fresh glass cover slips were used after flame cleaning and exposure to various organic solvents. Three different coatings were used: an acrylic known as Acryloid B66 manufactured by Rohm and Haas; an alkyd topcoat known as Rustoleum 7791 satin white; and polybutadiene. They were applied using a centrifugal spin coater and the resulting thicknesses were in the range of 5-10 μm. The curing conditions were: acrylic - 30 min in air at 100°; alkyd - 7 days at room temperature; polybutadiene - 30 min in air at 200°.

The coated glass was exposed to deionized water for different periods of time and the adhesion was determined within ten sec after removal from the water using a mask pull-off test. Both the acrylic and the alkyd coating lost adhesion within 15 min after immersion in the water while the polybutadiene remained tightly adherent to the glass after immersion in the water for 2 weeks. Microscopic observations of the glass/coating interface through the glass indicated that small blisters formed and grew in size. The shape of the blister could be determined by measurements of the interference fringes. A dynamic view of the adhesion loss could be obtained by following the blister growth with time. The coating pulled off with the masking tape when approximately one-half of the glass/coating interfacial area was covered with blisters. It should be emphasized, however, that water film thicknesses

at the interface of less than approximately 1000 Å would not be detected.

The effect of solution pH on the deadherence phenomenon was determined with the acrylic coating by immersion of the coated glass in solutions of pH value 0, 2, 4, 6, 8, 10, 12, and 14. The pH was controlled by means of NaOH or HCl. The rate of blister formation was high in all solutions of pH 4 through 10. No blisters were observed at pH 14 and very few blisters were observed within 30 min in solutions whose pH was 0, 2, and 12.

Time-lapse photography was used to examine blister formation and disappearance on acrylic-coated glass. The cell used in this study permitted water to be injected and removed at will. It was also possible to blow dry air over the coating so as to dry it rapidly. Blisters of significant size developed in less than 2 hr. Upon removal of the water and the application of the dry air stream, the blisters disappeared within 1 hr. The dry air was circulated over the surface of the acrylic coating for an additional 17 hr and the coating was re-exposed to water. The blisters formed in the identical locations as previously and grew at approximately 10 times the initial rate. Either the blisters form at specific sites where defects exist in the coating or, once formed and dried, they prevent the coating from regaining all of its initial adhesion.

Solid Metal Substrates. Aluminum, silver, cadmium, copper, nickel, silicon, tin, zinc and zirconium substrates were used in the metallographically polished condition (0.3 μm Al_2O_3 used as abrasive). Four coating systems were studied: the acrylic described previously, the Rustoleum 7791 alkyd, an alkyd coating containing red lead, and an alkyd coating containing zinc chromate. Table I gives the results of adhesion after exposure to deionized water for 3 days at 25°. It will be noted that aluminum and tin both exhibited good adhesion after the immersion while the nickel and silicon exhibited poor adhesion after the immersion in 3 of 4 cases.

Table I

The Adherence of Organic Coatings to Solid Metal Substrates after Immersion in Deionized Water for 3 Days at 25°C

	Coating			
Substrate	Acrylic	Rustoleum Alkyd	Alkyd with Red Lead	Alkyd with Zn Chromate
Aluminum	good	good	good	good
Silver		poor		poor
Cadmium	good			poor
Copper	good	poor	good	good
Nickel	poor	poor	poor	good
Silicon	good	poor	poor	poor
Tin	good	good	good	good
Zinc	good			intermediate
Zirconium	intermediate			poor

Note: All tests are averages of 8 trials.
Blank entries indicate that no experimental data were generated.

Evaporated Metal Substrates. The initial studies were carried out by evaporation of several different metals onto the glass cover slides. However, the metal/glass interface itself exhibited poor adhesion in some cases and this method was abandoned. The glass was then first coated with polybutadiene and the metal was condensed from the vapor state onto the polybutadiene. This method worked moderately well except in the case of copper in which case the acrylic and alkyd coatings led to poor wet adhesion at the glass/polybutadiene boundary. This effect was recognized as strange but an explanation was not pursued. The results obtained with aluminum, silver, copper and silicon substrates after immersion in water for 3 days at 25° are summarized in Table II. The results were consistent with the previous experiments in that aluminum substrates generally exhibited good wet adhesion and silicon exhibited poor wet adhesion.

An additional set of experiments was performed in which silicon single crystal wafers were used as substrates for the metal deposition. Results obtained with organic coatings on silicon coated with aluminum, silver, chromium, copper, nickel and tin as well as uncoated silicon and oxidized silicon are summarized in Table III. In this series as well, the wet adhesion on aluminum and tin was good and the wet adhesion on nickel and silicon was poor.

No interpretation of the experiment results is being offered at the present time pending additional measurements.

Table II

The Adherence of Organic Coatings to Metals Evaporated onto Polybutadiene-Coated Glass after Immersion in Deionized Water for 3 Days at 25°C

	Coating			
Substrate	Acrylic	Rustoleum Alkyd	Alkyd with Red Lead	Alkyd with Zn Chromate
Aluminum	good	poor	good	good
Silver	good	poor	poor	poor
Copper	*	*	good	good
Silicon**	poor	poor	poor	poor

* - No measurements could be made because polybutadiene adherence to glass was poor after water immersion.

** - Silicon wafer was used.

Table III

The Adherence of Organic Coatings to Metals Evaporated onto Silicon Wafers after Immersion in Deionized Water for 3 Days at 25°C

Substrate	Acrylic	Rustoleum Alkyd	Alkyd with Red Lead	Alkyd with Zn Chromate
Aluminum	good	good	good	good
Silver	*	poor	intermediate	poor
Chromium	good	good	good	good
Copper	good	intermediate	good	good
Nickel	poor	poor	intermediate	intermediate
Tin	good	good	good	good
Silicon	good	intermediate	good	poor
Oxidized Silicon	good	poor	poor	poor

* - Silver pulled off silicon during adhesion testing.

Program #3

Interfacial Breakdown in a Coating/Metal System as Studied by Thin Film Conduction Techniques and Optical Microscopy from the Substrate Side

INTRODUCTION

Protective polymer coatings are used to prevent substrate degradation by acting as physical barriers to exclude or reduce aggressive attack by the corrosive environment. The necessary conditions which initiate or propagate underfilm corrosion include: the presence or development of conductive pathways between the substrate and bulk electrolyte, oxygen, water and ions. Elimination of all or some of these conditions at the interface will consequentially impede or inhibit underfilm corrosion.

The study of protective coating failures begin with an attempt to understand the mechanisms which are operative at the metal/coating interface. The use of thin metal films deposited on glass slides enables the investigator to observe changes at this interface by optical as well as electrical methods.

Organic polymeric materials are currently used for dielectrics in the semiconductor industry, electrical protection as insulators, and coatings for metal surfaces. Electrical measurements made on polymers detail changes in the dielectric characteristics of the coating. The electrical properties which are currently measured to observe dielectric changes include: DC resistance, AC resistance, capacitance, AC impedance, and dielectric properties as a function of temperature. In addition, some investigations are concerned with studying the corrosion of painted metals by electrochemical techniques, e.g. potential-time and polarization measurements; reviews of these methods are given by Wolstenholme [1] and Leidheiser [2]. Not only are coating failures recognized by electrical measurements, but mechanisms of coatings failures have been proposed for some systems [3,4].

The primary cause for coating failure results from water penetration to the polymer/substrate interface, i.e., an aqueous phase is needed to support corrosion reactions. A decrease in the resistance of a coating indicates an increase in water penetration, i.e., establishment of conductive pathways. Using resistance values for different polymeric varnish coatings, e.g. erythritol alkyd resins, Kinsella and Mayne [5] have proposed that two types of ionic conduction exist: a given film may exhibit inverse or direct conduction characteristics depending on its composition, mode of preparation, and environment. AC resistance-capacitance studies have been made by Touhsaent and Leidheiser [6] where a model for water penetration and eventual coating breakdown has been postulated. The effective electrical permittivity of polymer-coated steel was measured at various frequencies as a

function of time of exposure to NaCl electrolyte by Kendig and Leidheiser [7]. These measurements were indicative of complete penetration by a conductive phase and correlated well with visible localized corrosion. Also, capacitance measurements have been used to determine the volume % of water in a polymer coating [8]. Capacitance measurements made by O'Brien [9] have been used to predict the lifetime of bituminous type coatings and to calculate the actual depth of water penetration into the coating. Among other electrical phenomena studies, an AC impedance method has been used to detect local defects in polymer coatings [10,11] and a time domain dielectric spectroscopic method is currently being developed in this laboratory to determine the location of aggregates of water in a coating (see Program #6).

Resistance measurements similar to those made by Jedlicka and Geschke [12] and Reidel and Voigt [13] may also prove to be useful. Thin films of iron, either evaporated or in foil form, were coated with a polymer and exposed to corrosive environments. The change in resistance parallel to the surface was indicative of a coating that was converted to a highly resistant material, i.e., rust. These procedures could be modified or extended to include coated corrosion products as a sample and monitoring the change in resistance as water, oxygen, and ions penetrate the organic film. Also, Haruyama and Tsuru [14] performed conductive measurements on evaporated thin films of high purity metal on glass. They used a conventional Wheatstone bridge with a 1000 Hz signal generator. The change in conduction of the film electrode was traced by recording the unbalanced output voltage of the bridge.

The problem at hand is to utilize these various techniques to study the interfacial region between polymer and substrate or polymer/metal oxide/substrate. How does water or electrolytic solution alter the electrical characteristics of the substrate or, better yet, the interface between the substrate and protective coating? Also, what happens to the conduction along this interface when corrosion products are present? In order to seek answers to these questions, the initial work will focus on the electrical properties of thin metallic films coated with an organic polymer.

EXPERIMENTAL

A procedure for measuring the electrical conductivity of dried films was performed by Wallace [16] and for cured films by Henderson [17]. Their set-up will be modified to measure the specific conductivity of a thin metallic film coated with a thin polymeric film. Henderson applied a current of one-microamp across the sample and measured the voltage drop across the measuring probes after one minute. The specific conductivity, L_s, is given by the following equation,

$$L_s = \frac{I}{V} \cdot \frac{\ell}{A} \quad ,$$

where I is the applied current, ℓ is the distance between voltage measuring probes, A is the cross-sectional area of the specimen, and

V is the voltage drop. Using this same experimental design, potential-current behavior can be monitored by applying different currents to the sample and recording the subsequent potential changes. The experimental set-up can be seen in Figure 1. Electrical connections using #32-7/40 extruded teflon wire, obtained from the Alpha Wire Corporation, are made with a low-resistance contact cement supplied by Ernest Fullam, Inc. Voltage measurements were made with a Keithley 600A electrometer and current measurements were made with a Beckman 300 Tech digital multimeter. A variable DC power supply was used as a current source.

At first, only the thin metal film, i.e., no coating, was subjected to high relative humidity, 52% and 88%, to observe changes in the resistance with time of exposure. Additional experiments involved direct contact with either water or 0.1% NaCl. Quantitative results are complete for these initial studies. However, only some qualitative results are available for coated thin metal film specimens. Vinyl ester and epoxy-polyamide coatings were used in these investigations; both coating systems were cured at room temperature over a period of seven days. The coated samples were then exposed to the same relative humidity conditions as the uncoated samples.

RESULTS AND DISCUSSION

The thin metal films studied to date include: aluminum, nickel, and iron. Initial studies involved following the change in resistance with time of exposure to 88% and 52% relative humidity (RH) and, in some cases, direct contact with water or 0.1% NaCl. Quantitative results have been obtained for uncoated systems. Experimental results have revealed that 88% RH is more aggressive than 52% RH. Figures 2-4 give representative plots of change in resistance, ΔR, versus time for the various thin metal films. Aluminum films are more conductive, i.e., lower resistance values, than either iron or nickel. In addition, aluminum is more corrosion resistant, showing the smallest change in resistance with increasing time of exposure. Table I compares the change in resistance with time among the various metal films.

Table I

Uncoated Thin Metal Films Exposed to 88% Relative Humidity.
Change in Resistance at 48 and 220 Hours

Metal	Thickness (Å)	$\Delta R_{48\ hrs}(\Omega)$	$\Delta R_{220\ hrs}(\Omega)$
Aluminum	280	.02	.08
Aluminum	100	2.5	--
Iron	270	1.1	2.1
Iron	250	1.5	5.4
Nickel	390	3.6	7.7
Nickel	110	25	85

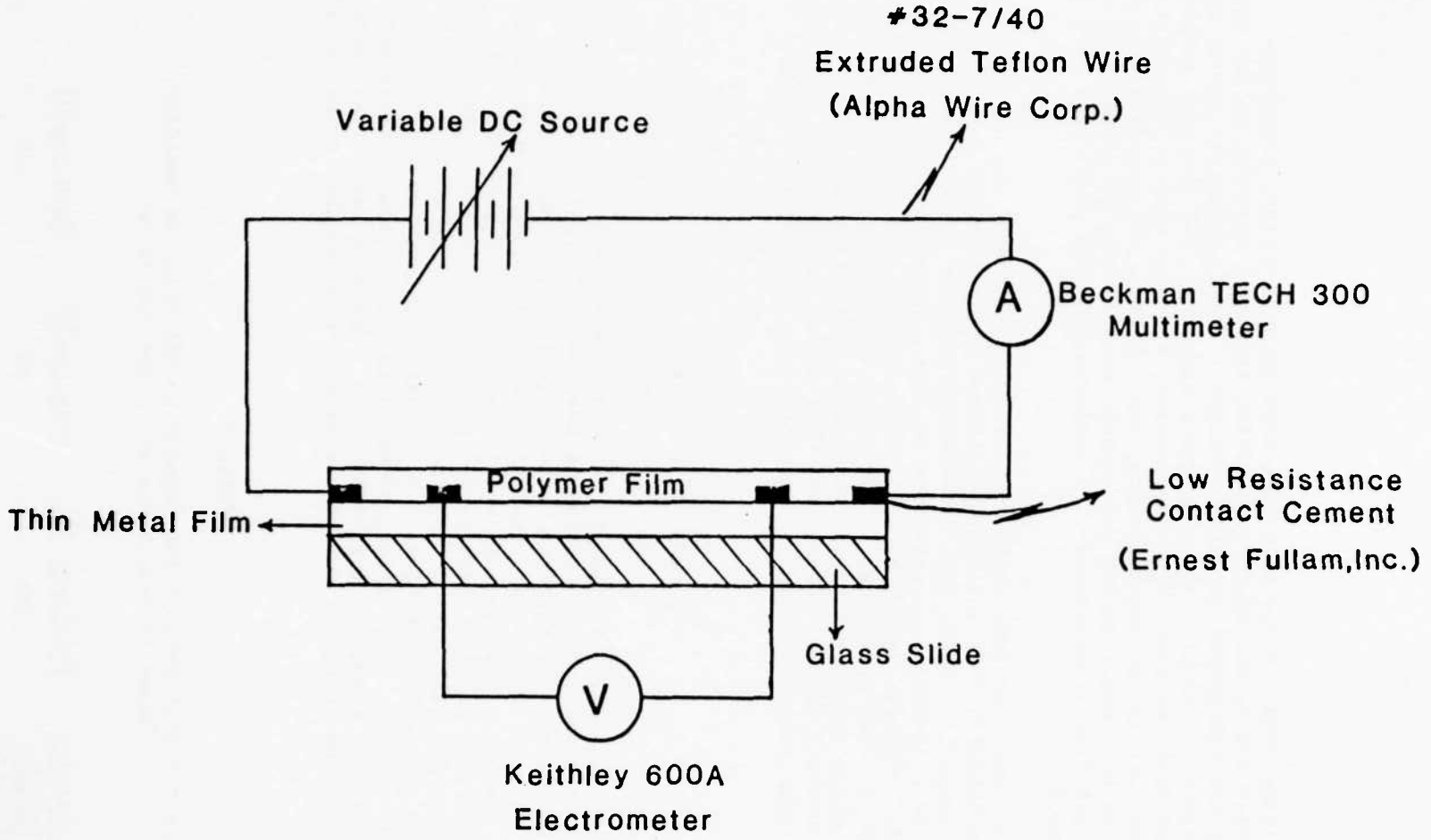
#32-7/40
Extruded Teflon Wire
(Alpha Wire Corp.)
Variable DC Source
A
Beckman TECH 300
Multimeter
Polymer Film
Thin Metal Film
Low Resistance
Contact Cement
(Ernest Fullam,Inc.)
Glass Slide
V
Keithley 600A
Electrometer

Figure 1

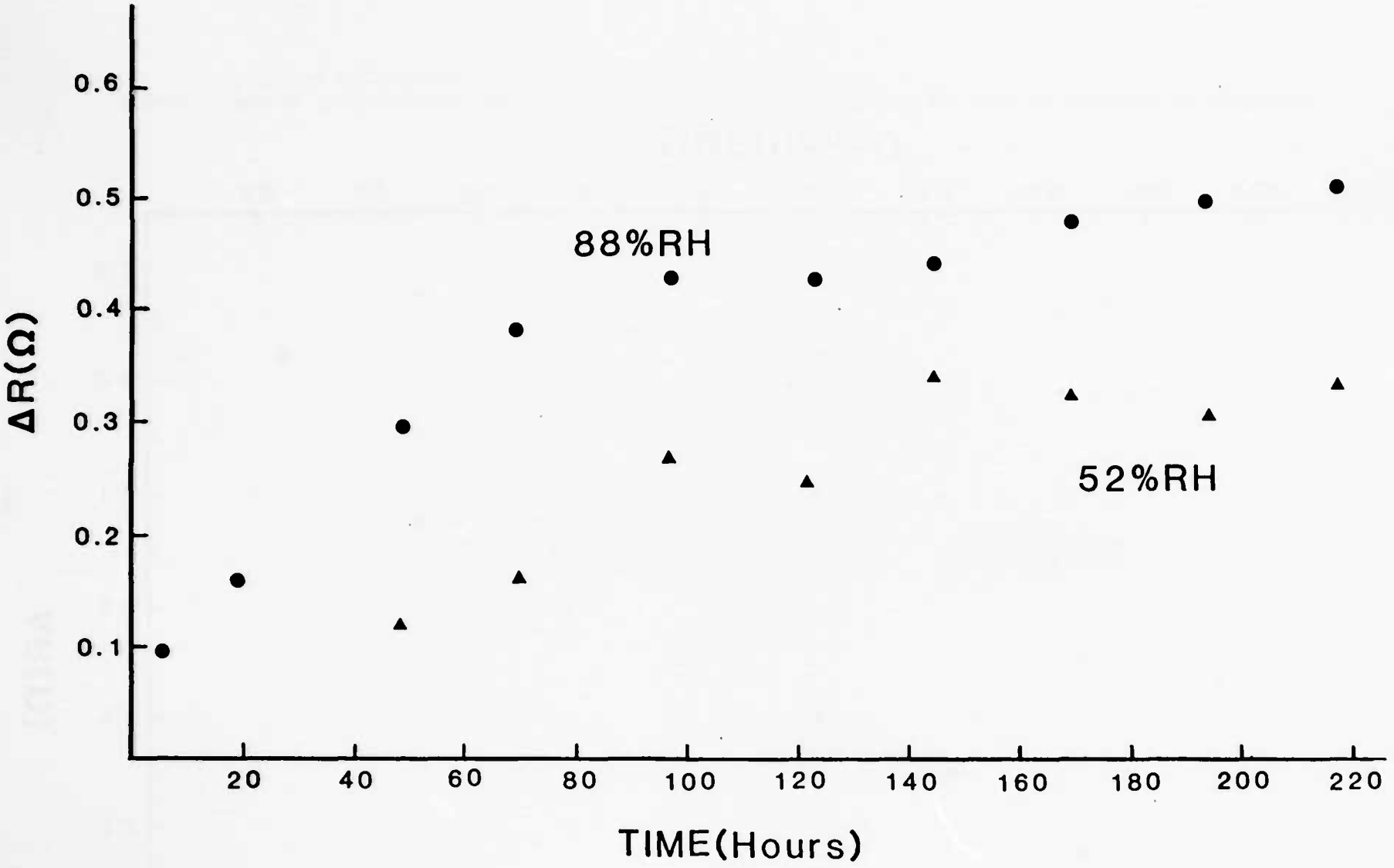

Figure 2. Change in resistance for a thin aluminum film, 160Å, is plotted vs. time of exposure to different relative humidities.

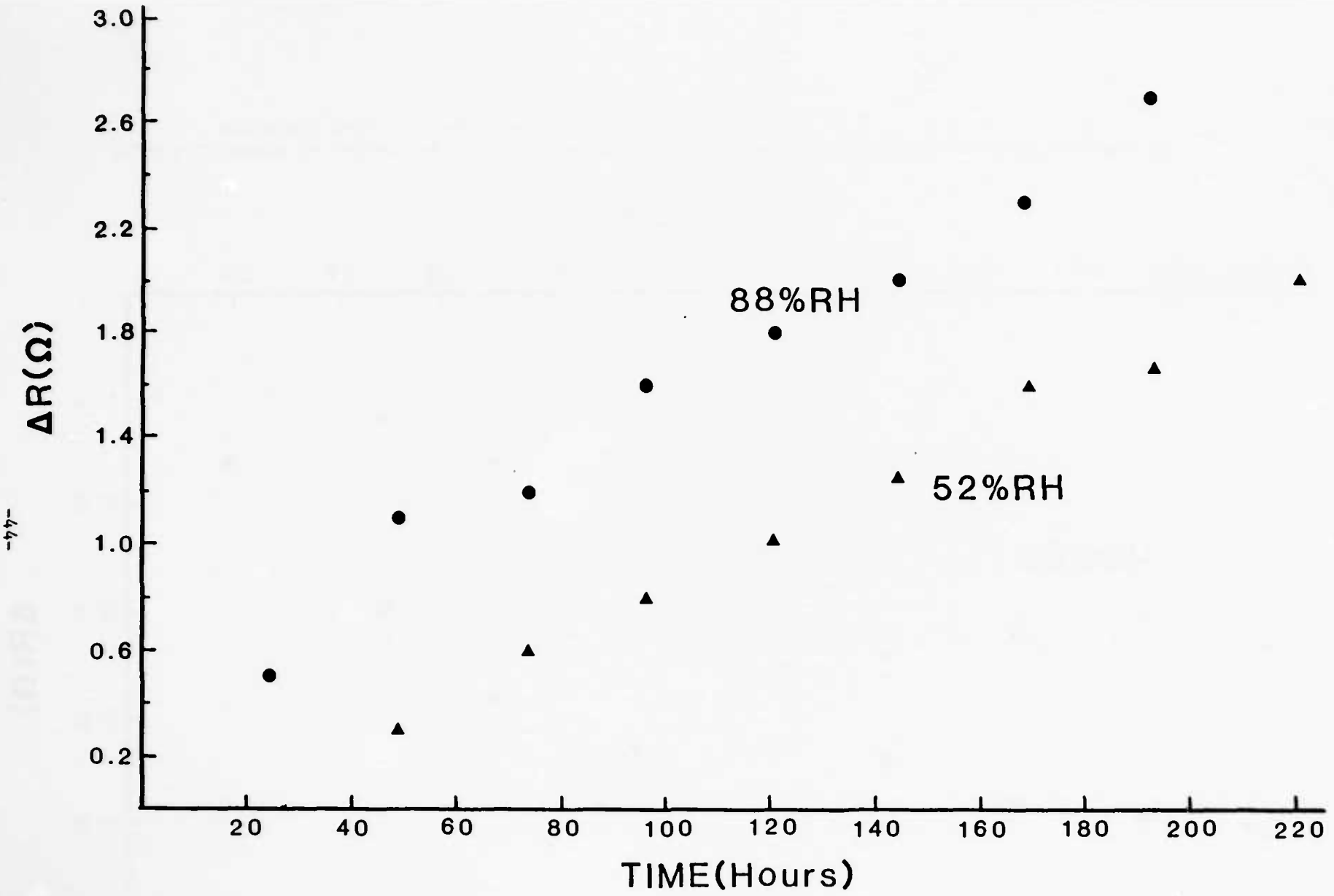

Figure 3. Change in resistance for a thin iron film, 270Å, is plotted vs. time of exposure to different relative humidities.

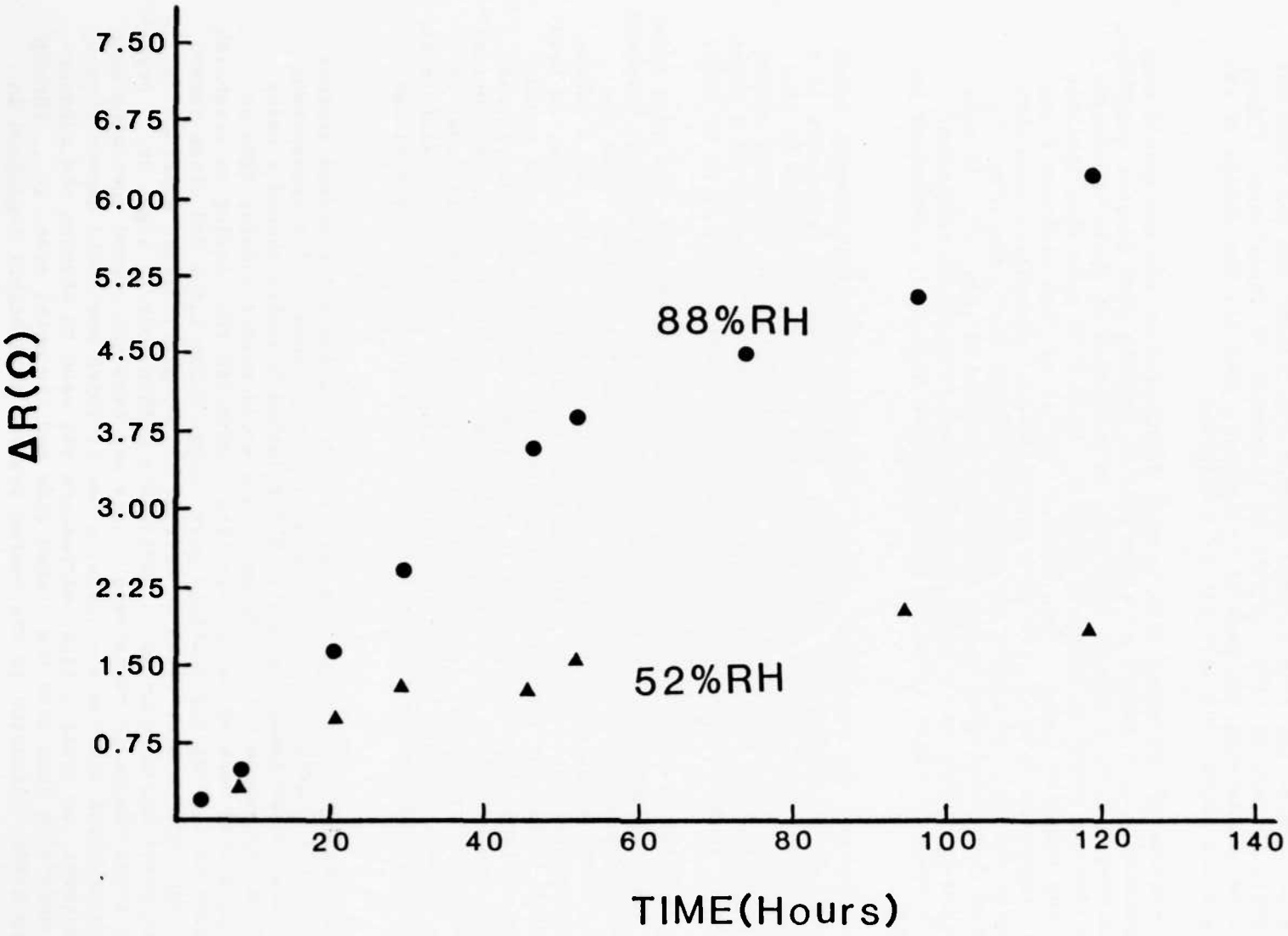

Figure 4. Change in resistance for a thin nickel film, 390Å, is plotted vs. time of exposure to different relative humidities.

Upon examining Figures 2-4 and Table I, it can be seen that resistance values increase as the film thickness decreases. As film thickness becomes of the same order as, or smaller than, the electron mean free path, scattering of electrons at the film surface becomes significant and the effective conductivity is reduced [18]. A plot of thickness vs resistance, Figure 5, shows an exponential increase of resistance, that is, the change of resistance below about 100Å will not be considered.

Corrosion of the metal film is most pronounced at the specimen's edge. This undoubtedly is a result of a decrease in bonding with nearest neighbors, i.e., corrosion in bulk metals generally is initiated at grain boundaries, dislocations and other macroscopic defects. Thin film corrosion exhibits many of the familiar forms. For example: Attack of thin aluminum films (Fig. 6) takes the form of pits or highly localized corrosion; iron thin film attack varies from highly localized to general corrosion (Fig. 7); and nickel thin films show highly localized corrosion (Fig. 9). In some cases, iron corrosion has a similar appearance to "filiform corrosion" (Fig. 9); however, there is no reason to believe that such a mechanism is operative.

In general, the resistance of the film increases within several hours of exposure to an aggressive environment. This increase in resistance is a result of oxide formation, i.e., corrosion product formation which is less conductive than the unattacked metal. Also, the resistance increase occurs before visible signs of corrosion are apparent, even with the aid of a light microscope. However, in most cases, corrosion appears within 48 hr or less.

In addition to exposure at different relative humidities, the thin film samples were exposed directly to water and 0.1% NaCl. The experiment involved taking measurements in the presence of water or salt solution. Then the corrosive environment was removed and the sample allowed to dry and a subsequent measurement was recorded. An increase in resistance was noted, in both cases, with increasing time of exposure; however, the dry film gave higher resistance values. This difference in resistance values can be attributed to an ionic contribution to the overall current. In other words, the current values measured are higher for the wet film which translates into lower resistance values. However, the ionic contribution was small with a difference in resistance between dry and wet films of only 1 to 3Ω for a 160Å nickel film.

Some preliminary qualitative results are available for coated systems. The vinyl ester coating was preferentially used because of its transparent nature. Coated specimens exposed to 88% relative humidity showed a delay time before resistance values changed. One would expect a delay time in the coated system because water must first penetrate the coating to establish a corrosion cell. Thicker coatings gave longer delay times and often showed no resistance change over seven or more days. However, direct exposure to distilled water showed changes in resistance within four to eight hr. Overall, the total change in resistance values was less for coated specimens than found for uncoated specimens -- again, a result which one would expect from a coated system. An optical light microscope was used to observe the advancement of corrosion from both the coated side and the metal side, i.e., through the glass slide. Corrosion in the coated systems were highly localized in

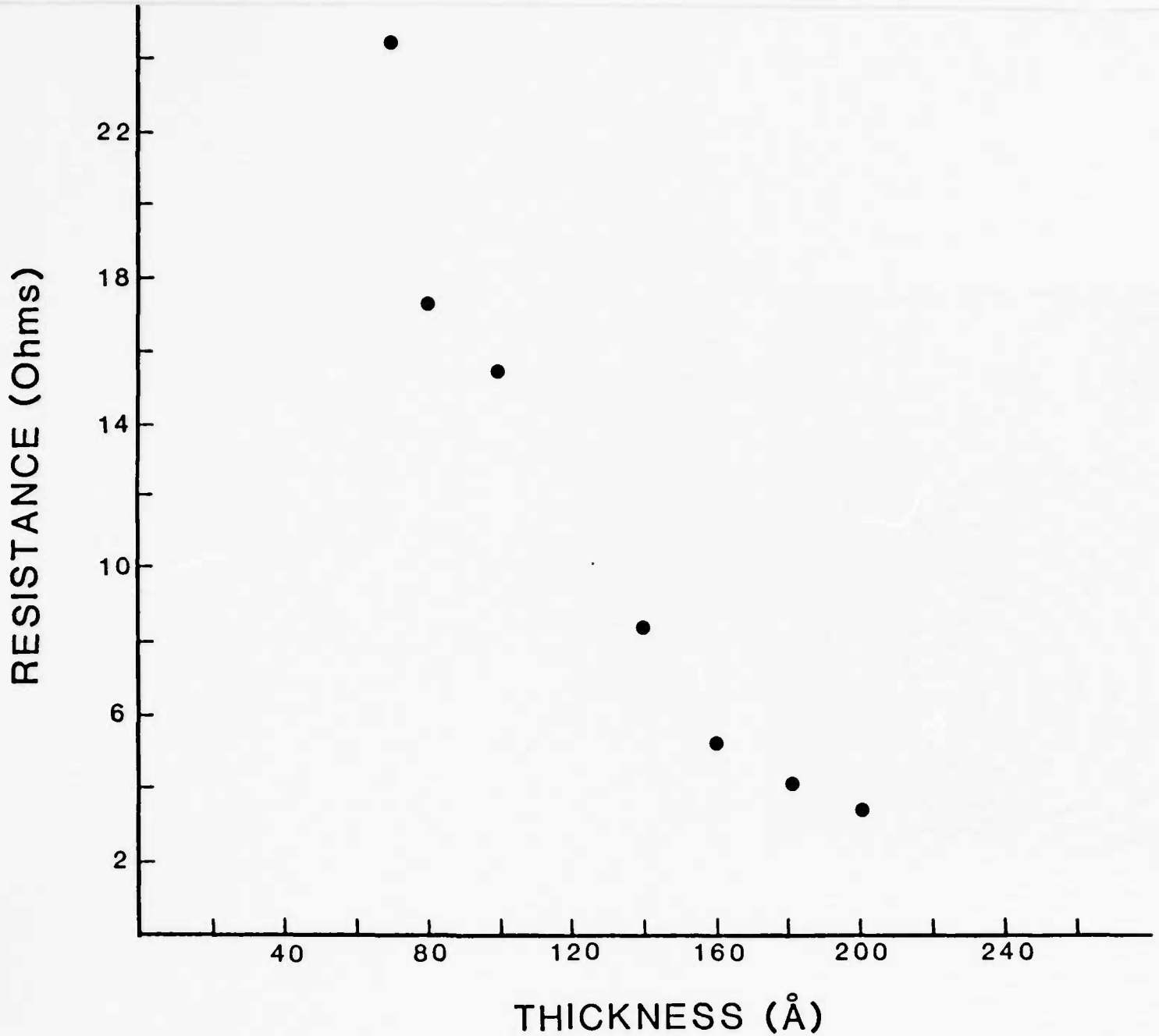

Figure 5. Initial resistance values for thin aluminum films plotted vs. thickness.

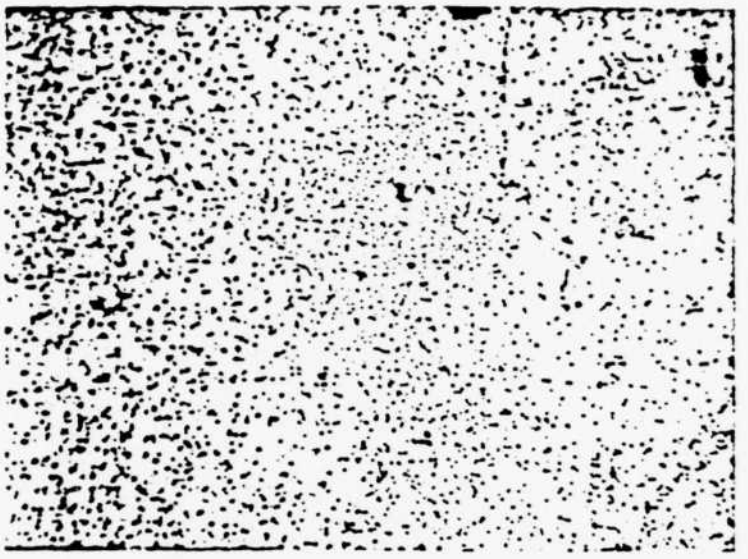

Figure 6. Photograph of a thin aluminum film, 280Å, exposed to 52% R.M. for 19 days (20X).

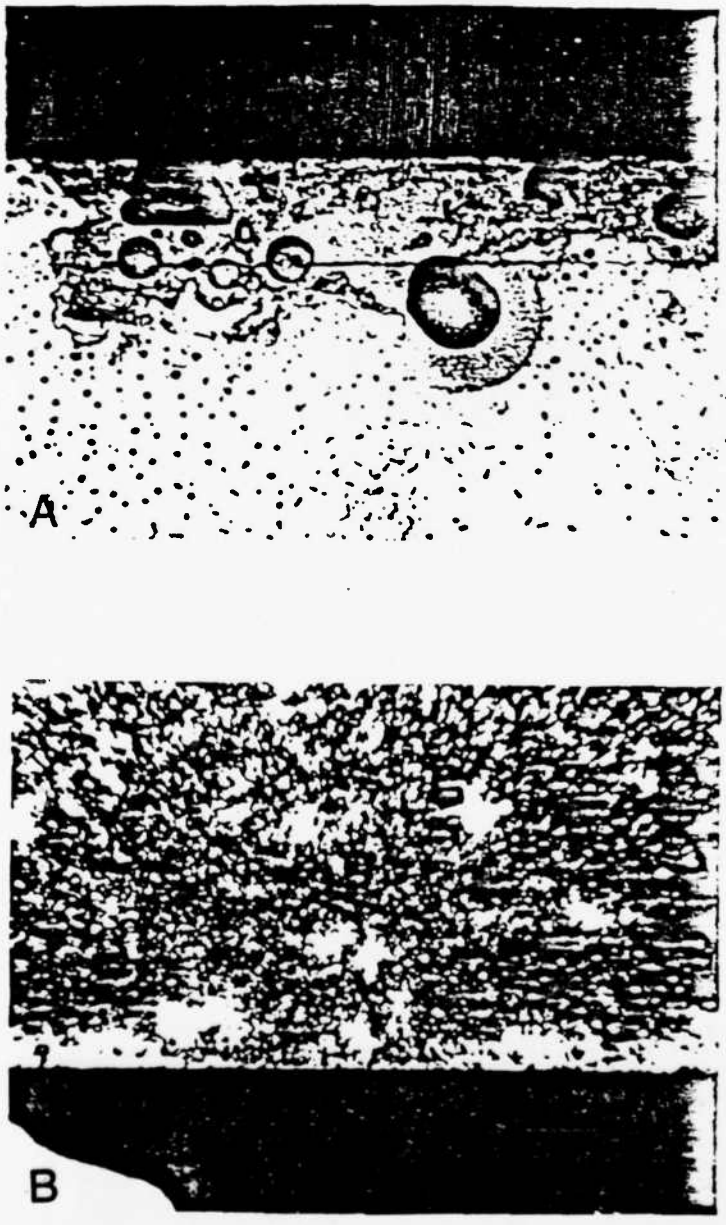

Figure 7. Photographs of thin iron films, 270Å, exposed to 88% R.M. (A), and 52% R.M. (B), for 7 days (10X).

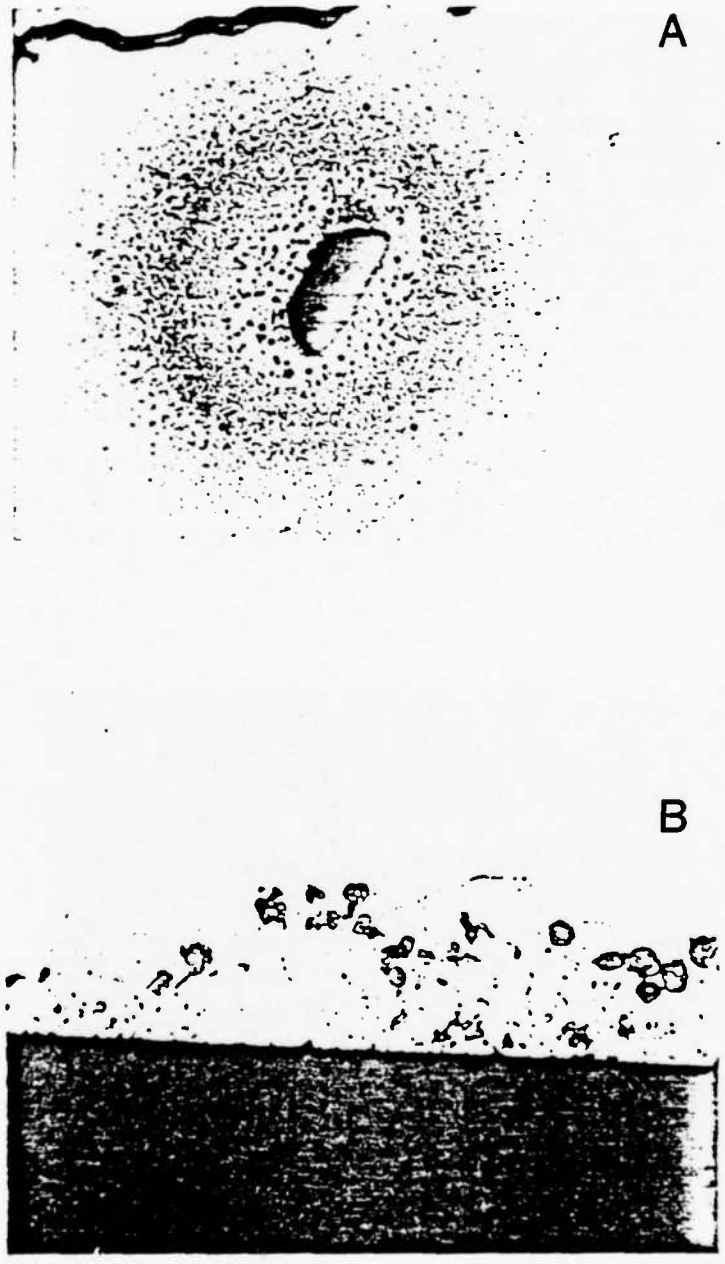

Figure 8. Photographs of thin nickel films, 390Å, exposed to 88% R.M. for 21 days (10X).

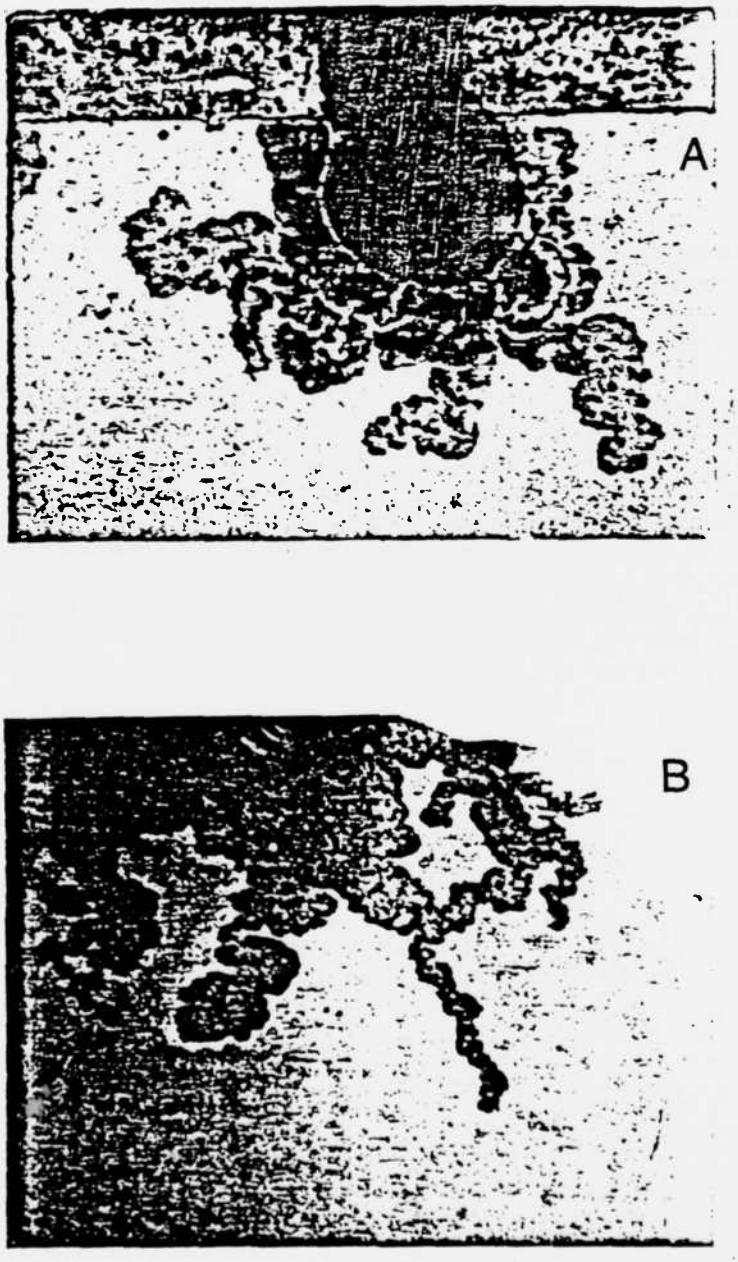

Figure 9. Photographs of 'filiform'-like corrosion on thin iron films, 280Å, exposed to 88% R.M. for 7 days (A-10X and B-4X).

nature where corrosion areas showed radial growth with time until adjacent areas grew together.

SUMMARY

The resistance of the metal film increased with time of exposure to high relative humidity or an aqueous solution. Thinner films gave higher resistance values than did thicker ones and also showed the largest change in resistance with time. There was almost no delay time when uncoated specimens were exposed, that is, resistance values began to change within a few hr. However, the increase in resistance did level off after some time, which was a function of both substrate and thickness. In general, nickel films showed the largest change in resistance, i.e., decreasing conductivity, whereas aluminum films gave the smallest change in resistance, with iron films falling in the middle. It was observed that resistance changes occurred before corrosion was noticeable. Corrosion of uncoated specimens was most pronounced at the specimen edges. Large increases in resistance did occur when corrosion areas, highly localized, became visible. A small ionic contribution to the overall current was observed when the metal thin film was immersed in an aggressive environment. Finally, an induction time was observed for coated samples before resistance values began to change.

REFERENCES

[1] J. Wolstenholme, Corr. Sci. 13, 521 (1973).

[2] H. Leidheiser, Jr., Prog. in Organic Coat. 7, 79 (1979).

[3] D. M. Brasher and T. J. Nurse, J. Appl. Chem. 9, 96 (1959).

[4] H. Leidheiser, Jr., and M. W. Kendig, Corrosion 32(2), 69 (1976).

[5] E. M. Kinsella and J. E. O. Mayne, Br. Poly. J. 1, 1173 (1969).

[6] R. E. Touhsaent and H. Leidheiser, Jr., Corrosion 28(12), 435 (1972).

[7] M. W. Kendig and H. Leidheiser, Jr., J. Electrochem. Soc. 123(7), 982 (1976).

[8] D. M. Brasher and A. H. Kingsbury, J. Appl. Chem. 4, 62 (1954).

[9] H. C. O'Brien, Ind. Eng. Chem. 58(6), 45 (1966).

[10] J. V. Standish and H. Leidheiser, Jr., Corrosion 36(8), 390 (1980).

[11] M. C. Hughes and J. M. Parks, "Corrosion Control by Organic Coatings," Natl. Assoc. Corrosion Engrs., Houston, Texas, 1981, pp. 45-50.

[12] W. W. Jedlicka and T. H. Geschke, J. Paint Tech. 41, 680 (1969).

[13] G. Reidel and C. Voigt, Korrosion-Dresden 5, 13 (1974).

[14] S. Haruyama and T. Tsuru, "Passivity and Its Breakdown on Iron and Iron Base Alloys," Editors R. W. Staehle and H. Okada, NACE, Houston, Texas, pp. 41-46 (1976).

[15] K. L. Chopra, "Thin Film Phenomena," McGraw-Hill Book Co., New York, p. 85 (1969).

[16] R. A. Wallace, J. Crowley and N. W. Vijayaraghavan, J. Poly. Sci.: Polym. Chem. Edition 10, 3447 (1972).

[17] R. S. Henderson, "Electrochemical Properties of Polymeric Films Used in Cathodizing," Master's Thesis, Carnegie-Melon Univ., Pittsburgh, PA (1979).

[18] R. W. Berry, P. M. Hall, and M. T. Harris, "Thin Film Technology," D. Van Nostrand Co., Inc., Princeton, NJ, pp. 2-3 (1968).

Program #4

A Model for the Quantitative Interpretation of Cathodic Delamination

INTRODUCTION

Many coated steel products are subject to scratches or dents with consequent exposure of the steel to the environment. If the coated materials are continuously immersed in an electrolyte, as for example ships, underground pipelines, and the interior of vessels holding an aqueous solution, it is possible to protect the exposed area by means of an applied potential. One of the undesirable aspects of cathodic protection is that the coating adjoining the defect may separate from the substrate metal. This loss of adhesion is known as "cathodic delamination." This type of delamination may also occur in the absence of an applied potential. The separation of the anodic and cathodic corrosion half reactions under the coating provides regions which are subject to the same driving force as when the cathodic potential is applied externally.

The second annual report contained a summary of the experimental data related to cathodic delamination. This report provides a mechanism of the process and predicts some consequences of the mechanism.

PROPOSED MECHANISM OF CATHODIC DELAMINATION

Figure 1 defines some of the terms used in the discussion which follows. The key point about the delamination process is that once the delamination begins, the area delaminated from the substrate metal is a linear function of time. Extrapolation of this linear relationship to zero delamination occurs at a finite time, the so-called "delay time". This delay time is considered to be that time required to establish a steady-state condition.

The concept utilized to interpret the delamination process is one that has been used with success to interpret the growth or dissolution of a precipitate [1]. This concept is outlined below and several of the terms used are shown schematically in Figure 2. The terms used in the discussion are the following:

S = the growth coordinate in cm/sec

D = diffusion coefficient in cm^2/sec

α = the growth coefficient. The value of α is a function of C_o, C_1 and C_∞

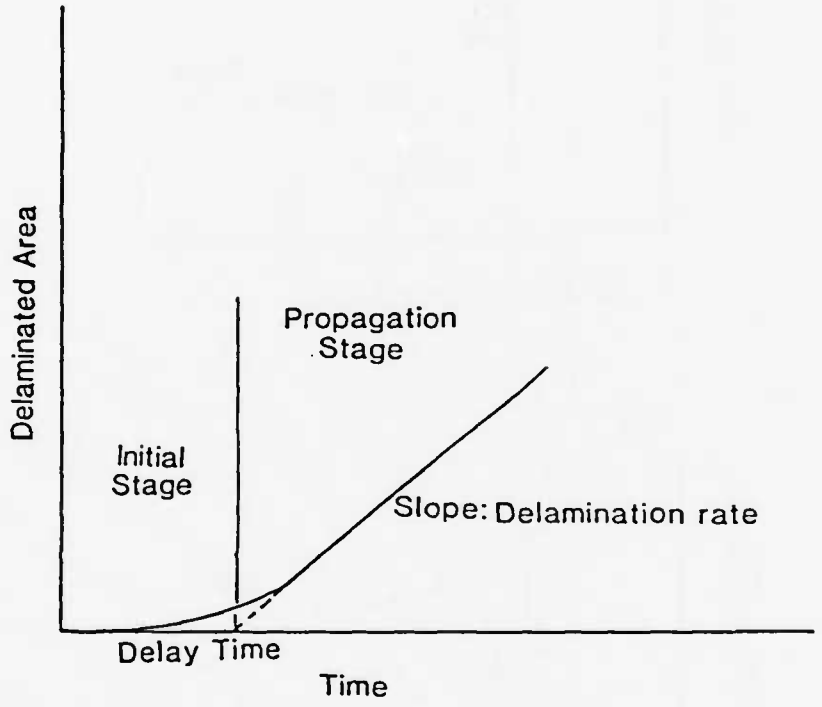

Figure 1. Schematic representation of different stages in the delamination process.

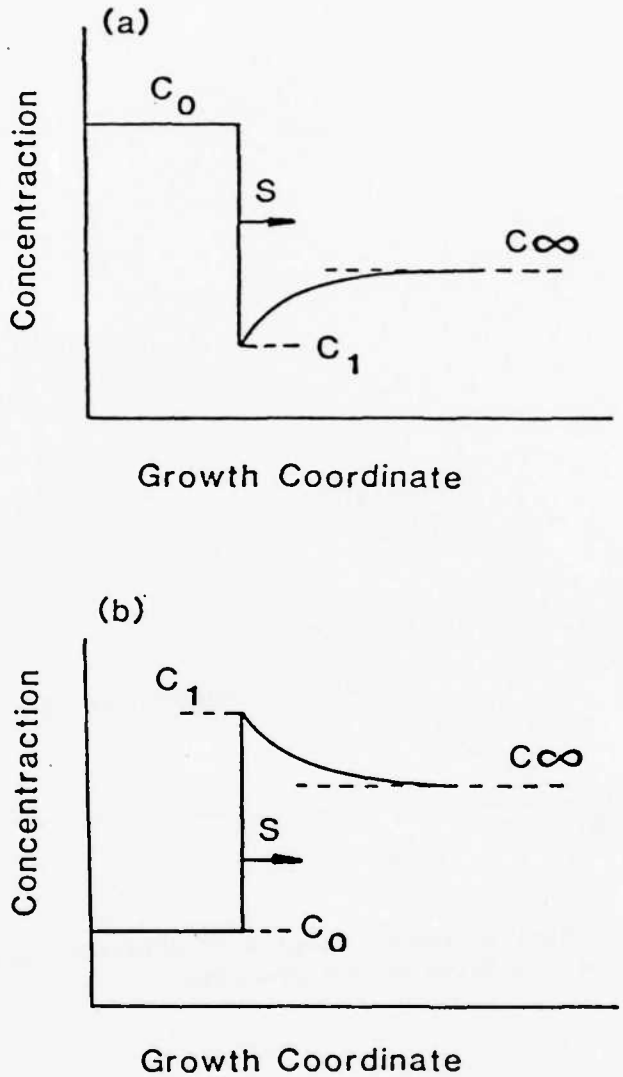

Figure 2. The pertinent concentrations in the precipitation: the advancing interface (a) with the positive precipitation; (b) with the negative precipitation.

C_o = the concentration of the solute atoms in the precipitate

C_1 = the concentration of the solute atoms in the matrix which is in equilibrium with the precipitate

C_∞ = the concentration of the solute atoms in the matrix far away from the precipitate

In our application of these concepts we are concerned with the two-dimensional problem of the radial growth of a circular defect which is made on purpose at the start of the experiment. The component whose concentration is critical is the NaOH which is generated by the cathodic reaction under the coating.

The three essential components that must reach the reaction site are water, oxygen and the metal cation and they can reach the site either by diffusion through the organic coating or by migration through the aqueous phase adjoining the defect underneath the delaminated coating. The cathodic reaction which occurs at the delaminating edge generates hydroxyl ions and causes the very small volume of liquid under the coating to have a high pH. This highly alkaline solution is the destructive influence which results in the delamination of the coating from the metal. We are not concerned in this discussion with the exact mechanism by which the bond is broken. A discussion of this feature can be found in reference [2].

The concentration of the alkaline medium at the delaminating front is determined by the following factors:

(a) The rate of the cathodic reaction

(b) Competition between diffusion of H^+ or Me^+ ions to the delaminating front

(c) The effective volume of liquid at the front

(d) The rate of diffusion of OH^- ions from the delaminating front into the bulk solution

(e) Buffering reactions involving either the metal oxide at the interface or the organic coating which may occur in the liquid under the coating

Many of these factors are difficult to determine. From an experimental point of view, the pH at the delaminating front is about 14 under some circumstances.

The rate of the cathodic reaction is dependent upon the availability of reactants and the catalytic activity of the surface. The rate determines how many OH^- ions are generated per unit time, but the value of the pH at the delaminating front is determined by the factors outlined above.

Evidence summarized previously [2] suggests that both water and oxygen reach the delaminating front by diffusion through the coating. The major question is how do the alkali metal ions, Na^+ for example, reach the front. Is it through the coating or through the liquid at the interface between the metal and the coating? This question remains unanswered but the answer is not necessary before the process can be interpreted mathematically.

An essential reactant in the cathodic reaction, $H_2O + 1/2O_2 + 2e^- = 2OH^-$, is the electron. The flux of electrons at the delaminating front is an important variable. The representation of the electron availability at various locations within the delaminated region is the polarization curve. The possible potential gradient underneath the delaminated coating from the defect to the delaminating front will be described later. The only potential of significance to our concerns is the potential at the delaminating front since this is the site where the reactants are provided.

The metal surface must be catalytically active for the cathodic reaction in order for the delamination process to occur. It has been shown in the case of aluminum surfaces, phosphated steel surfaces, and zinc surfaces inactivated with small amounts of cobalt [3] that the catalytic activity is low and that consequently the rates of delamination of organic coatings on these surfaces are also low.

The counter ions to provide charge transport and to provide charge neutralization for the OH^- ions generated in the cathodic reaction may be either alkali metal ions (Li^+, Na^+, K^+, Cs^+) or the proton. In general, the diffusion of the proton occurs at a faster rate than that of the alkali metal ion both in aqueous solution and in an organic coating. However, in near neutral solutions the ratio of concentration of the metal cation to the proton concentration is very high when the salt concentration is 0.5M. It is reasonable to expect that the diffusion of the alkali metal cation is the determining factor. Experimental proof of this conclusion is the high pH under the coating — the pH would not be high if the H^+ were the main charge carrier.

The Mathematical Model. The following assumptions are made in the derivation of the model:

(a) The coating phase is homogeneous.

(b) The diffusion coefficient, D, is constant in the coating.

(c) The diffusion process obeys Fick's equation.

From Fick's second law:

$$\frac{\partial C}{\partial t} = D\frac{\partial^2 C}{\partial x^2} \qquad (1)$$

with initial conditions: $t=0, \quad C=0$ (2)

with boundary conditions: $t>0,\ x=0,\ C=C_o$ (3)

$x=b,\ C=0$ (4)

b = the thickness of coating

The solution to Eqn. (1) with conditions (2), (3), and (4) is:

$$\frac{C}{C_o} = 1 - \frac{x}{b} - \frac{2}{\pi}\sum_{m=1}^{\infty}\frac{1}{m}\sin\frac{m\pi x}{b}\ \exp\left[\frac{-m^2\pi^2 D}{b^2}t\right] \tag{5}$$

Taking the derivative of Eqn. (5) at x=0,

$$\left.\frac{\partial C}{\partial x}\right|_{x=0} = -C_o\left[\frac{1}{b} + \frac{2}{b\pi}\sum_{m=1}^{\infty}\exp\left[-\frac{m^2\pi^2 D}{b^2}t\right]\right] \tag{6}$$

The mass flux at x=0, i.e., at the coating surface and time t, is given by:

$$F_t\Big|_{x=0} = -D\left.\frac{\partial C}{\partial x}\right|_{x=0} = \frac{DC_o}{b}\left[1 + \frac{2}{\pi}\sum_{m=1}^{\infty}\exp\left[-\frac{m^2\pi^2 D}{b^2}t\right]\right] \tag{7}$$

The total mass flux at x=0 in the range of time T (the delay time) is obtained by:

$$F_T\Big|_{x=0} = \int_o^T F_t\Big|_{x=0}\ dt \tag{8}$$

As $D\ m^2\pi^2 t >> 1$, Eqn. (8) can be expressed as:

$$F_T\Big|_{x=0} = \frac{DC_o}{b}\left[T + \frac{b^2}{3D}\right] \tag{9}$$

After reaching the steady state, the total amount of water in the organic coating is equal to $C_o b/2$, therefore,

$$\frac{C_o b}{2}A = \left\{\frac{DC_o}{b}\left[T + \frac{b^2}{3D}\right]\right\}A \tag{10}$$

$$T = \frac{1}{6D} b^2 \tag{11}$$

A : the area

Equation (11) says that the delay time, T, is proportional to the square of the coating thickness, a result which is in accord with experimental data as shown in Figure 3.

A modification of the mathematical treatment can be developed for the case where the concentration of components at the coating/metal interface is not zero. The equations describing this model are the same Equations (1) through (3) with the following change in the conditions described in Equation (5), namely:

$$x = \infty \qquad C = 0 \tag{12}$$

The solution with Equations (1)-(3) and (12) is:

$$\frac{C}{C_o} = 1 - \text{erf}\left[\frac{x}{2\sqrt{Dt}}\right] \tag{13}$$

The mass flux of water at x=0 equals:

$$F_t\Big|_{x=0} = -D\frac{\partial C}{\partial x}\Big|_{x=0} = \frac{\sqrt{D}}{\sqrt{\pi}\sqrt{t}} C_o \tag{14}$$

Total mass flux of water from t=0 to t=T is obtained by:

$$F_T\Big|_{x=0} = \int_o^T \sqrt{\frac{D}{\pi}} C_o t^{-1/2} \, dt = \sqrt{\frac{D}{\pi}} C_o T^{1/2} \tag{15}$$

When the steady-state is reached, the concentration at the interface is assumed to be controlled by the current flow through the organic coating during the initial stage,

$$i = V/R_o/b \tag{16}$$

F : Faraday's constant

i : the current density, [amp/cm^2]

V : the applied potential, [volt]

R_o : the specific resistance of the organic coating, [ohm-cm]

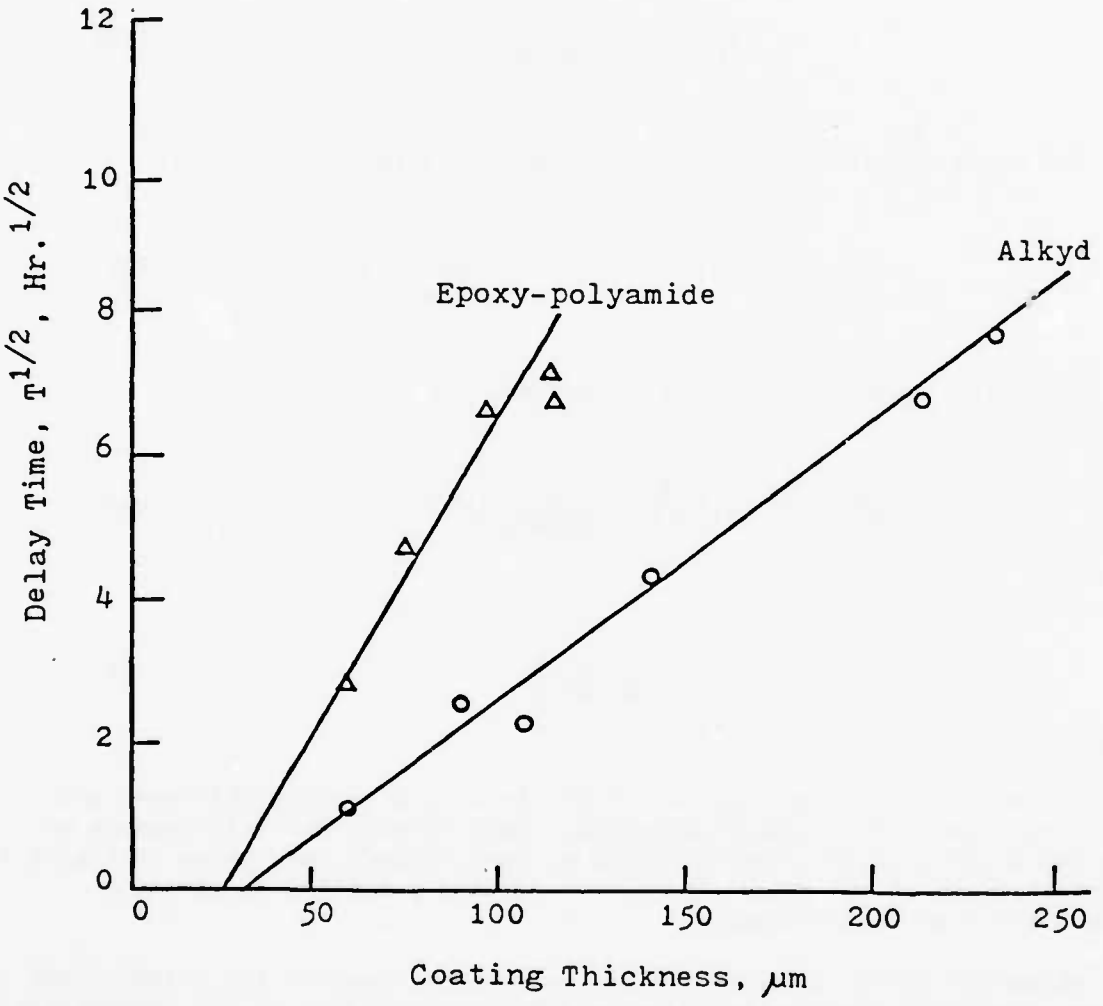

Figure 3. Plot of the square root of the delay time vs. the coating thickness for coated steel panels in 0.5M NaCl solution with an applied potential of -0.8 volt vs. SCE,

$$D\frac{C_b - C_o}{b} = \frac{V}{2R_o bF} \tag{17}$$

$$\frac{C_b}{C_o} = 1 - \frac{V}{2R_o DFC_o} \tag{18}$$

The total amount of water in the organic coating is

$$F_{H_2O} = \left(\frac{C_o + C_b}{2}\right) \cdot b = C_o\left(1 - \frac{V}{4R_o DFC_o}\right) \cdot b \tag{19}$$

Comparing Equations (15) and (19), then

$$2\sqrt{\frac{D}{\pi}}\, C_o\, T^{1/2} = C_o\left(1 - \frac{V}{4R_o DFC_o}\right) \cdot b \tag{20}$$

$$T = \frac{\pi b^2}{4D}\left(1 - \frac{V}{4R_o DFC_o}\right)^2 \tag{21}$$

Therefore, the delay time is a function of the coating thickness and also a function of the applied potential. Data showing the relationship between the delay time and coating thickness have already been given in Figure 3. The relationship of the delay time to the applied potential is given in Figure 4 for 2 coating systems.

Attention is now directed to the propagation stage of the delamination process. The mass flux to the delamination front consists of two components: (1) F_c the flux through the coating and (2) F_d the flux between the coating and the metallic substrate:

$$F_c = -D_c \frac{\partial C}{\partial x} \tag{22}$$

$$F_d = -D_d \frac{\partial C}{\partial Y} \tag{23}$$

The diffusion processes underneath the organic coating will be emphasized. The theory which is applicable to the growth of a precipitation, the rate of which is limited by diffusion, as described previously, is adapted

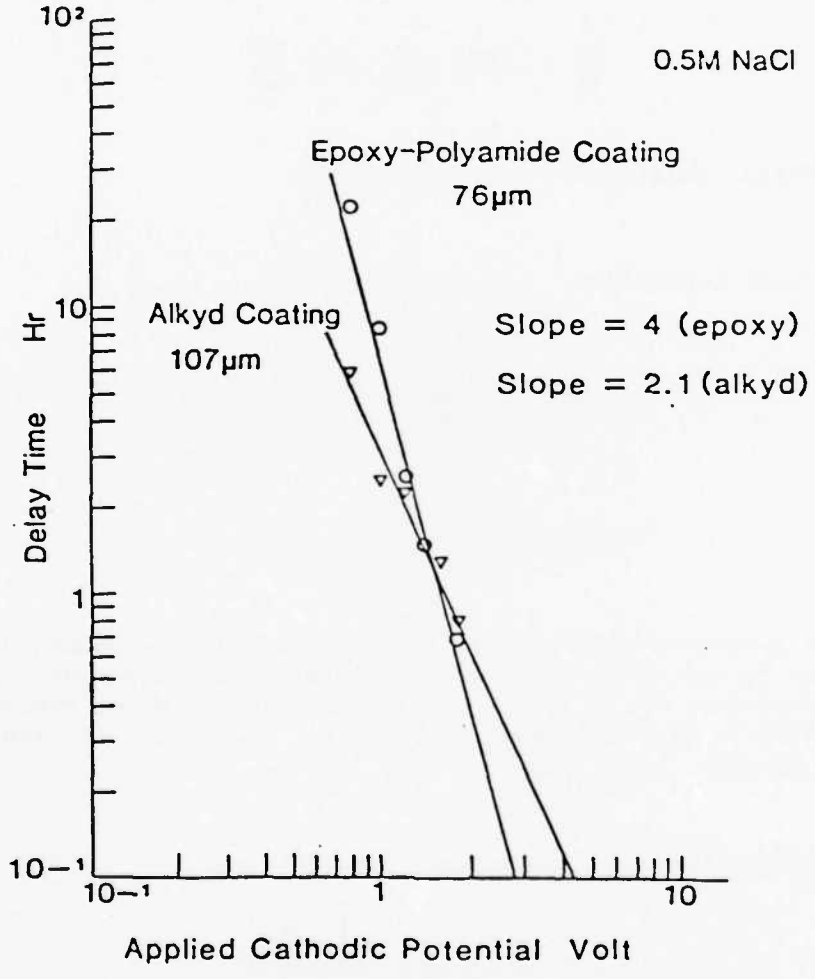

Figure 4. The plot of the logarithms of the delay time vs. the applied potential for the coated steel panel in 0.5M NaCl solution.

to the delamination of an organic coating from a metal substrate.

If the diffusion coefficient D is independent of the concentration, then the concentration distribution will satisfy Fick's second equation.

$$\frac{\partial C}{\partial t} = s^{-n+1} D \frac{\partial}{\partial s} s^{n-1} \frac{\partial C}{\partial s} \tag{24}$$

with initial conditions, $t=0$, $C(0,s)=C_\infty$ (25)

and boundary conditions, $t>0$, $C(t,s[t])=C_1$ (26)

$$C_o \frac{ds}{dt} = C_1 \frac{ds}{dt} + \left(-D\frac{\partial C}{\partial s}\right)_{s=S} \tag{27}$$

$$(C_o-C_1) \frac{ds}{dt} = -\left(D\frac{\partial C}{\partial s}\right)_{s=S} , \tag{28}$$

since both the governing differential equation and all the boundary conditions are homogeneous in the concentrations, the rate of the advancing front S depends on the concentrations, C_o, C_1 and C_∞, only in a dimensionless combination. Furthermore, S(t) is also dependent on D and t. Therefore, the general equation for S(t) becomes $S = \alpha_n [Dt]^{\frac{1}{2}}$

The general solution of Equations (24)-(26) is:

$$C = C_\infty + [C_1-C_\infty] \frac{\phi_n\left[\frac{s}{(Dt)^{\frac{1}{2}}}\right]}{\phi_n(\alpha_n)} \tag{29}$$

where

$$\phi_n(x) = \int_x^\infty e^{-\frac{1}{4}z^2} z^{1-n} dz \tag{30}$$

By using the boundary condition Equation (26), α_n^n can be determined as follows:

$$\frac{1}{2}[C_o-C_1]\,\alpha_n\left[\frac{D}{t}\right]^{\frac{1}{2}} = \frac{-[C_1-C_\infty]\alpha_n^{\,1-n}\exp[-\frac{\alpha_n^2}{4}]}{\phi_n(\alpha_n)Dt} \tag{31}$$

$$\alpha_n^n = \frac{2\beta\,\exp\left[-\frac{\alpha_n^2}{4}\right]}{\phi_n(\alpha_n)} \tag{32}$$

where

$$\beta = \frac{C_\infty-C_1}{C_o-C_1} \tag{33}$$

The counter ions (i.e., either the alkali cation or the proton) to neutralize the negatively charged ions OH^- can be supplied either by diffusion through the organic coating or through the electrolytic solution underneath the delaminated coating, or both. It is assumed that the flux of cations is that necessary to equal the hydroxyl ions generated by the cathodic reaction. The rate of delamination is determined by the migration of MOH from the delaminating front to the attached coating. The most important elements to affect the delamination rate include the diffusion coefficient of MOH underneath the attached coating and a dimensionless growth coefficient α_2 which is a function of the pertinent concentrations. These concentrations C_o, C_1 and C_∞ are defined as follows:

C_1 is the concentration of OH^- at the edge of delaminating front. The determination of this concentration is very complicated because many factors must be considered. These factors have been discussed previously.

C_o is the concentration of OH^- underneath the delaminated coating.

C_∞ is the concentration of OH^- needed to cause the delamination.

The solutions for this diffusion process are obtained in two limiting cases.

(a) In the case of $\frac{C_1-C_\infty}{C_1-C_o} \ll 1$, the approximate solution is:

$$\alpha^* = \sqrt{2}\left[\frac{C_1-C_\infty}{C_1-C_o}\right]^{\frac{1}{2}} = \sqrt{2}\left[\frac{C_1-C_\infty}{C_\infty-C_o}\right]^{\frac{1}{2}} \tag{34}$$

(b) In the case of $\frac{C_\infty - C_o}{C_1 - C_o} << 1$, the approximate solution is:

$$\alpha^* = 2 \frac{[C_1 - C_\infty]}{[C_1 - C_o]^{\frac{1}{2}} [C_\infty - C_o]^{\frac{1}{2}}} \qquad (35)$$

Tests of the Equations Originating from the Model. Equation (11) indicates that the delay time T is related to the coating thickness b by the relationship:

$$T = (1/6D) \times b^2 \ .$$

Figure 3 showed that the coating thickness is linearly related to the square root of the delay time, in conformity with this equation. The equation may also be used to calculate the value of the diffusion coefficient for the species responsible for the delay time. This value turns out to be 3.0×10^{-10} cm^2/sec for the alkyd coating and 5.5×10^{-11} cm^2/sec for the epxoy coating.

These calculated diffusion coefficients correlate moderately well with measured values for the diffusion of water in the coating as shown by the following experimental data. The water permeability of these two coatings was determined by the use of aluminum Payne cups. The interior of the cup was filled with silica gel so as to maintain 0% relative humidity. The free film was used as a cover and the environment exterior to the film was maintained at 50% relative humidity with a saturated solution of $Ca(NO_3)_2$. The equation used to calculate the permeability are the following:

$$\Delta W = P \frac{\Delta p}{b} At$$

$$P = \frac{\Delta W \cdot b}{\Delta p A t}$$

$$P = DS$$

The permeability data obtained by this method for the alkyd and epoxy-polyamide coatings systems are 0.3 and 0.08 $mg\text{-}cm/cm^2/day/atm$, respectively. The solubility of water in these coatings are 2.25% and 2.10% [4]. Therefore, the diffusion coefficient of the water in the alkyd coating is approximately 4 times that of the epoxy-polyamide coatings, in agreement with the

calculated values. The measured values of the diffusion coefficient for water in the two coatings and the calculated values are compared as follows:

	Calculated Value of Diffusion Coeff.	Measured Value of Diffusion Coeff. for Water
Alkyd Coating	3.0×10^{-10} cm^2/sec	1.2×10^{-11} cm^2/sec
Epoxy-polyamide Coating	5.5×10^{-11}	3.4×10^{-12}

The difference between the calculated and the measured values is approximately one order of magnitude, which does not appear to be unreasonable in terms of the crudity of measurements using the Payne cups.

The measurements reported in Program #15 provide a means for comparing the calculated values with the measured values for the diffusion of Na^+ ions into a coating in the absence of any applied potential. The only coating studied in common with the present study is the alkyd. The measured value for the diffusion coefficient of the Na^+ ion into the alkyd coating is 1.9×10^{-11} cm^2/sec, approximately the same as the measured value for the diffusion coefficient of water, but an order of magnitude less than the calculated value.

It remains a critical issue to determine which species is responsible for controlling the delay time. Oxygen is also a critically important species in the cathodic delamination phenomena and we are only now beginning to explore the rate of diffusion of oxygen through coatings in the presence of an aqueous phase.

REFERENCES

[1] C. Zener, J. Appl. Physics 20, 950 (1949).

[2] H. Leidheiser, Jr., W. Wang, and L. Igetoft, Prog. in Org. Coatings 11, 19 (1983).

[3] H. Leidheiser, Jr., and I. Suzuki, J. Electrochem. Soc. 128, 242 (1981).

[4] Pittsburgh Soc. for Paint Technol., Official Digest 33, 1427 (1961).

Program #5

Catalysis and Inhibition of the Oxygen Reduction Reaction

INTRODUCTION

The importance of the oxygen reaction in atmospheric corrosion is well known [1]. This reaction, $O_2 + 2H_2O + 4e^- \rightarrow 4OH^-$, is also firmly established as a fundamental process in coatings failures on metal substrates in cathodic delamination studies [2-8]. It has been proposed that the corrosion rate of a zinc substrate can be decreased by control of the cathodic reaction [9]. It was further shown that such control was possible through use of Co(II) or Ni(II) salts to decrease the rate of the oxygen reduction reaction [10]. It has also been shown that the cathodic reaction on zinc can be inhibited by cathodic treatment of a chromated surface [11]. The cathodic reaction on iron and steel can also be inhibited by anodic treatment of the steel surface in a solution containing an appropriate organic compound [12]. Mechanisms of corrosion inhibition pertaining to organic coatings have been reviewed [13] and control of the oxygen reduction reaction on the interfacial oxide was emphasized. Specifically, control of the electronic properties of the oxide at the interface, particularly with regard to catalytic inactivity towards the cathodic reaction, has been proposed [8].

The general characteristics of oxygen reduction at electrode interfaces have been described [14-18]. Typical observations are that the reduction of oxygen is usually irreversible, that is to say that the reversible potential values are difficult to obtain. A thorough study of the oxygen electrode has yet to be completed and reasons for this situation have been explained by Damjanovic [16]: (1) Most studies have been performed only by noble metals since few materials are stable in the potential range required for study of oxygen reduction. (2) Several steps are involved in the reduction of oxygen and the mechanism changes with test conditions. (3) At the potentials of oxygen reduction, the electrode surface may be covered or partly covered with oxide causing uncertainties in defining the electrode condition. (4) Oxygen exchange currents are usually quite small and are easily affected by solution impurities. Co-workers and Damjanovic [19] suggest that the situation had not changed much in eleven years. However, interest in oxygen reduction mechanisms has increased due to activity in the fuel cell, photoelectrochemistry, and battery research areas. Also, there is a growing interest in electrochemistry at semiconducting electrodes. Reviews of electroanalytical chemistry [20-22] include mention of n-type Fe_3O_4 electrode material studies, covalently modified electrodes for activation or inactivation of electrode surfaces, and polymer coatings which can be activated or inactivated toward the cathodic reaction. Morrison's book [23] broadly treats the subject of semiconductor electrochemistry including oxidized metal surfaces and notes that the iron/iron oxide system is complex.

The studies and areas of research cited above were prelude to the proposal that the kinetics of the oxygen reduction reaction be studied in terms of the semiconductor properties of oxide-covered metal substrates. The objective is the development of better understanding of the proposed area of research such that a substrate/interface/coating system may be designed with knowledge of semiconductor effects applicable to enhanced coating system performance. To achieve the objective, the following specific tasks were proposed: (1) Review the pertinent literature on the kinetics of the oxygen reduction reaction and semiconductor electrochemical properties applicable to oxide-coated metals. (2) Electrochemical evaluation of the catalytic activity as a function of the surface oxide modifications selected on the basis of the literature review. (3) Systems selected on the basis of (1) and (2) will be subjected to cathodic delamination studies [2-6] and correlations will be sought between the activity of the metal surface for the oxygen reduction reaction and the rate of cathodic delamination of a standard coating. (4) Based upon ion selective electrode techniques, a solid state oxygen probe will be designed and constructed to permit monitoring the rate of permeation of water and oxygen through the coating to the reaction sites at the coating/substrate interface to characterize better the oxygen reduction reaction beneath a coating.

The results obtained for tasks (1) and (2) are reported herein. Tasks (3) and (4) will be accomplished during the ongoing phase of this program.

Literature Review

The results of the literature review have been divided into four main areas: (1) The passive oxide film on iron. (2) Semiconductor properties of oxide-covered metal substrates. (3) Chemically modified electrodes for oxygen reactions. (4) Oxygen reduction reactions on electrode surfaces. No literature has been located which directly addresses the objectives of this program. Hence, papers describing these four areas were judged pertinent. The review has been oriented towards the use of iron or steel as the substrate material upon which oxygen reduction takes place. This orientation is most appropriate with regard to the programs of other investigators. However, non-ferrous substrates have not been excluded so that a wide range of ideas can be considered.

(1) Modification of the iron substrate reactivity towards the oxygen reduction reaction requires appraisal of the most current understanding of the nature of the passive film on iron. Much of the current concepts on passive films is derived from Cabrera and Mott [24] in their theory of the oxidation of metals. This work led to a series of papers by Pryor [25], Sewell [26], Nagayama [27,28], Sato [29-34], Bloom [35], Moshtev [36-38], and Markovac [39] which described the properties of the passive film on iron in various media. Generally, the passive film on iron is about 5 nm in thickness, and a bilayer of Fe_3O_4 and gamma-Fe_2O_3 or a mixed oxide of variable composition (Fe_xO_4) where x = 2.67 to 3. More recently, surface analytical techniques have been used to characterize better the passive film on iron. Revie [40], as well as Murphy [41] using SIMS technique, have shown that the passive film formed in aqueous solution is a hydrated ferric oxide whereas an air-formed film showed no evidence of hydration. Mössbauer

studies [42] have shown similar results. Kuroda [43] studied the passive film on iron with electron diffraction and proposed that the film was a fine-grained crystalline spinel oxide with an iron concentration gradient. Long [44] has obtained similar results with EXAFS. Using ESCA and SIMS studies, Tjong and Yeager [45] have determined that protons are probably present in the passive layer. Murphy [46] has observed the penetration of the passive film by chloride and water. Ion migration in the anodic barrier film on iron in acidic phosphate solutions is mainly attributable to the oxide ions rather than the iron ions according to Sato [47]. The passive oxide layer on iron has been considered as a semiconductor by Delnick [48], Stimming [49], and Wilhelm [50]. A series of papers by Cahan and Chen [51-53] provides background for their proposed model of the passive layer on iron being a "chemi-conductor," that is, an insulator which can be variably doped by valency state changes. This most recent proposed model has drawn extensive discussion [54,55]. A satisfactory description of the nature of the passive film on iron has not yet been accepted. However, the current models include consideration of semiconductor principles and a number of investigators are using semiconductor experimental techniques in their studies of the passive layer on iron.

(2) The review area of semiconductor properties of oxide-covered metal substrates is subdivided in order to consider investigations with and without photoresponse effects and with and without iron in the electrode material. Historically (1951), Morin reported electrical properties of alpha-Fe_2O_3 doped with titanium as an n-type impurity [56] and proposed a conduction model for the iron oxide [57]. More recently, Schultze [58] has investigated the tunnel processes at passive iron electrodes and summarizes the work with a statement suggesting that the oxide-covered electrode represents a transition between metal and semiconductor behavior. Stimming [59] reported use of the ferrous/ferric couple to study electron transfer at passivated iron electrodes. Schultze [60] studied a variety of passive oxide films including TiO_2 doped with Pt and an electrode of Au/Au oxide/FeOOH [61]. The electrical properties of calcium borate glasses containing iron oxide revealed n-type semiconductivity with electron conduction attributed to the hopping of electrons between iron atoms with different valence states [62]. The DC conductivity of semiconducting iron phosphate glasses has been investigated by Murawski [63]. Bharati [64] has shown Fe_2WO_6 to be a p-type semiconductor. Schultze [65] discussed the semiconducting behavior of technical electrodes, general considerations of electron transfer on passive films [66], electrocatalysis and inhibition by protective layers [67], and results of capacitance studies of passivated iron electrodes correlated with the band structure of the passive layer [68]. Dogonadze [69] formally considered a theory of electron transfer reactions at film-covered electrodes. The charge transfer process has been reviewed by Memming [70] for semiconducting electrodes. Kapusta [71] has studied passive tin electrodes using capacitive techniques to show that the thin semiconducting film followed Mott-Schottky behavior, noting that problems were encountered with cracking of thick films. Electron transfer reactions were considered at anodized Nb and Ti electrodes [72] in ferro-ferricyanide media. Semiconductor models of the passive iron electrode [48,49] were based, in part, upon the photoresponse of the electrochemical system. Several investigators have studied the photoelectrochemical properties of the passivated iron electrode [50,73-83] and have reported data on the electronic properties, photoinduced charge transfer

characteristics, and semiconductor band structure. Bard [84] and Memming [85] discussed photo-effects at semiconductor electrodes. Many types of metal/film-covered electrodes have been studied for semiconductor and photo-effects including MoS_2 [86,87], iron substituted barium titanates [88], oxidized copper [89], TiO_2 [90], iron-titanium dioxides [91], CdS on a ring-disk electrode [92], and passivating films on tin [93]. Morrison [23] suggested that paint degradation may be a photoelectrochemical process involving OH radical formation on titanium dioxide pigment surfaces.

(3) Chemically modified electrodes have been described and reviewed by Murray [94]. While the original concept of a chemically modified electrode involved covalently bonded surface layers, adsorbed and deposited surface layers have become included. For covalently bonded surface layers, several investigators [95-98] have claimed that the modified surface was stabilized against electrochemical or photochemical degradation. Kobayashi [99] reported that covalently bonded iron and cobalt porphyrins have been studied to determine their catalytic activity for the oxygen reduction reaction. Armstrong [100] treated SnO_2 electrodes to yield a silane-modified surface which was further modified with a variety of metal phthalocyanines and metal cations. Phthalocyanines and porphyrins are often used in oxygen reduction reaction catalysis studies. Rocklin [101] has studied covalently bonded porphyrins metalated with Mn, Fe, Co, Ni, Cu, and Zn to determine the oxygen catalysis properties of the complexes. Numerous investigators [102-126] have studied oxygen reduction on adsorbed or deposited layers of porphyrin, phthalocyanine, or other metal chelant. Other investigators [127-130] have studied redox polymer layers in which the layer serves as an electrochemical link in the electron transfer process. Fan [131] has characterized phthalocyanine thin films on gold contact layers as semiconductor electrodes. Denisevich [132] has reported unidirectional current flow and charge state trapping at redox polymer interfaces constructed from two types of redox polymers forming a junction analogous to a semiconducting np-junction. Tench [133] and Stimming [134] have reported results with iron oxide films anodically deposited from soluble ferrous salt solutions.

(4) Most investigations of the oxygen reduction reaction have been performed on noble metal substrates [135]. Better catalysts and less expensive materials than the noble metals are desirable. Current research on such alternative materials is noted in the following papers cited. Fabjan [136] has compared the reduction reaction of oxygen on Fe, Co, and Ni to that of Pd, Ag, and Au noting that the reaction orders are 0.5 and 1.0, respectively, for each group and correspond to the formation of H_2O_2 as an intermediate for Fe, Co, and Ni. Haruyama [137] has studied oxygen reduction on iron and iron-chromium alloys and reported that the reduction currents were about 10 times lower than expected for a diffusion controlled reaction. Marinich [138] compared oxygen reduction at Fe and Pt electrodes noting a higher ratio of H_2O_2 formation for iron. Takei [139] reported that an Fe coating on an SnO_2/Si electrode was effective in promoting the electroreduction of oxygen. Other investigators have considered the oxygen reduction reaction on Pb [140], dispersed Pt on the tin oxide [141], Ni in alkaline solution [142], copper and brass [143], and Ti [144]. Adzic [145-147] has reported results for noble metals modified with Pb, Bi, Tl, Sn, and Cd in which catalytic effects were observed for Pb and Bi. Bronoel [148] studied the reduction of oxygen on

various oxides of La-Sr-Fe, Cu-Mn, and La-Sr-Co noting that these oxides underwent concomitant reduction. Other materials studied included graphite/cobalt-iron oxides [149], La-Ni oxides containing Fe, Co, or V [150], Ni-Fe oxide mixtures [151], sodium tungsten bronzes [152], and sulfide minerals [153]. A number of studies has related oxygen reduction to corrosion mechanism [154-161]. Vijh [162] has related corrosion potentials in oxygenated solution to the semiconductivity of the corrosion films.

A synopsis of the literature cited above yields the following statements when considered in the framework of this program's objectives:

1. Understanding of the passive layer on iron has progressed to semiconductor models and there is increased use of semiconductor techniques for studies of passive iron layers.

2. The semiconductor properties of oxide-covered metal substrates and modified electrode surfaces are being more intensely studied with the major emphasis on catalysis of oxygen reduction for applications in the energy industry.

3. Chemical modification of electrode surfaces is a powerful technique for tailoring special purpose electrochemical surfaces, especially with respect to catalysis of the oxygen reduction reaction. Inhibition of the oxygen reduction reaction has not been specifically studied.

4. The study of oxygen reduction reactions on the surfaces of bulk materials without surface modification is being pursued more aggressively and the prognosis is for moderate success in the design of materials with desired properties.

EXPERIMENTAL METHODS

Selection of specific modified, oxide-covered surfaces for experimental studies was based upon the cited literature and yielded two major approaches: (1) Doping of the passive layer on iron with various metal ions effecting modification of the semiconductor properties. (2) Developing chemically modified electrode surfaces with appropriately designed electrochemical properties. For the first approach, the techniques developed by Leidheiser [12] and Tench [133] can be used to form oxide layers electrochemically with different compositions. For the second approach, techniques developed by Murray [94] can be used to modify electrodes chemically with inhibited oxygen reduction properties.

The first technique selected for producing modified passive films on steel is an electrochemical anodization technique [12] adapted from the conditions developed by various researchers. The technique consists of abrading the substrate, SAE 1010 steel, with 240 grit silicon carbide paper, rinsing with water, a final rinse with methanol, and allowing the specimen to air-dry.

The specimen is subjected to anodic polarization to produce a passive oxide film. The anodic polarization was conducted in either a glass battery jar fitted with reference, counter electrodes, and a stirrer, or a standard electrochemical cell (Princeton Applied Research Corp. Model K47) with a magnetic stirrer. All potentials are versus the saturated calomel electrode (SCE). A Princeton Applied Research Corp. Model 350 Corrosion Measurement Console or Model 173/376 potentiostat was used for the application of the anodic potential. The solutions and treatment conditions are listed in Table I. The treatment was either a single or two-step anodization process. These treatments have been selected with the intent of growing passive oxide films into which dopants (impurities) such as aluminum, magnesium, and zirconium are incorporated. The specimens were evaluated for corrosion resistance with the polarization resistance technique using a Princeton Applied Research Corp. Model 350 Corrosion Measurement Console with a Model K47 electrochemical cell in a pH 8.5 borate solution. The polarization resistance measurement was conducted on a smaller surface area (1 cm^2) such that edge effects (untreated areas) were avoided.

RESULTS AND DISCUSSION

Table II lists the results obtained. Substantial difficulties occurred in maintaining passivation conditions which were compatible with additions of metal ions to the anodization solutions. The typical problem was determination of an appropriate pH at which the dopant metal, for example, aluminum, was sufficiently soluble and for which passivation conditions could be maintained. For this reason, later efforts concentrated upon use of a combination of chemical and electrochemical passivation. The use of nitrate aids the passivation process. The acetate acts as a buffer in the moderately acidic media and may also promote passivation. The nitrate-acetate medium appears to be a useful system for additional work.

The initial results with magnesium and zirconium showed no improvement in polarization resistance. Either appropriate conditions for passive film formation have not yet been found or the films incorporating these elements offer no improvement in corrosion resistance. Additional tests are being conducted with these and other materials under a variety of anodizing conditions.

The most encouraging results, thus far, have been with anodic oxide films formed in the presence of aluminum. The polarization resistance values for these treated specimens are significantly higher than for specimens similarly treated in the absence of aluminum. The higher polarization resistance values indicate better corrosion resistance for specimens treated under these conditions.

Figure 1 shows the polarization resistance results for three specimens subjected to Treatment G (Table I). These results were plotted as logarithm current density versus the overpotential, that is, the potential axes were normalized to the corrosion potential $E_c = 0$ (overpotential). Note that the oxygen reduction currents in the vicinity of the corrosion potential were substantially lower for specimens treated in the presence of aluminum ion

Table I

Solutions and Treatment Conditions

Treatment	Step	Solution Composition	Electrochemical Potential (volt vs. SCE)	Polarization Time (min)
A	1	0.15M borate, pH 8.5	+1.0	10
	2	add EDTA-$AlK(SO_4)_2$, 0.005M	+1.4	10
B	1	0.1M Na_2SO_4, pH 3.0	No Passivation	
	2	add $AlK(SO_4)_2$, 0.005M		
C	1	0.15M boric acid, pH 3.3	+1.0	10
	2	add $AlK(SO_4)_2$, 0.01M	+1.4	10
D	1	0.1M $NaNO_3$, pH 5	-1.3	5*
			+0.3	10
	2	add $Al(NO_3)_3$	+1.0	10
E	1	0.1M $NaNO_3$, 0.005M NaOAc, pH 5	-1.3	5*
			+0.3	30
	2	add $Al(NO_3)_3$	+1.0	30
F	1	Same as E	-1.3	5*
			+0.5	30
	2	" " "	+1.0	30
G	1	0.1M $NaNO_3$, 0.01M NaOAc, pH 5	-1.3	5*
			+0.8	30
	2	add $Al(NO_3)_3$	+1.0	30
H	1	0.1M $NaNO_3$, 0.02M NaOAc, pH 4	-1.3	5*
			+0.8	15
	2	add $Mg(OAc)_2$	+1.0	10
I	1	0.1M $NaNO_3$, 0.02M NaOAc, pH 4	-1.3	5*
			+0.8	15
		add $Zr(SO_4)_2$	+1.0	10

*No agitation at this potential (cathodic pretreatment).

Note: Solutions were prepared with distilled water.

Table II

Polarization Resistance Values

Treatment (See Table I)	Cation Concentration (M)	Polarization Resistance (kohm/cm^2)
D	0 Al	70
	0.005 Al	240
E	0.015 Al	260
F	0 Al	350
"	0.005 Al	407
"	0.010 Al	2,400
G	0 Al	320
"	0.005 Al	870
"	0.010 Al	990
"	0.015 Al	1,800
H	0 Mg	720
"	0.005 Mg	160
"	0.010 Mg	270
"	0.015 Mg	340
I	0 Zr	840
"	0.005 Zr	200
"	0.010 Zr	140
"	0.020 Zr	80

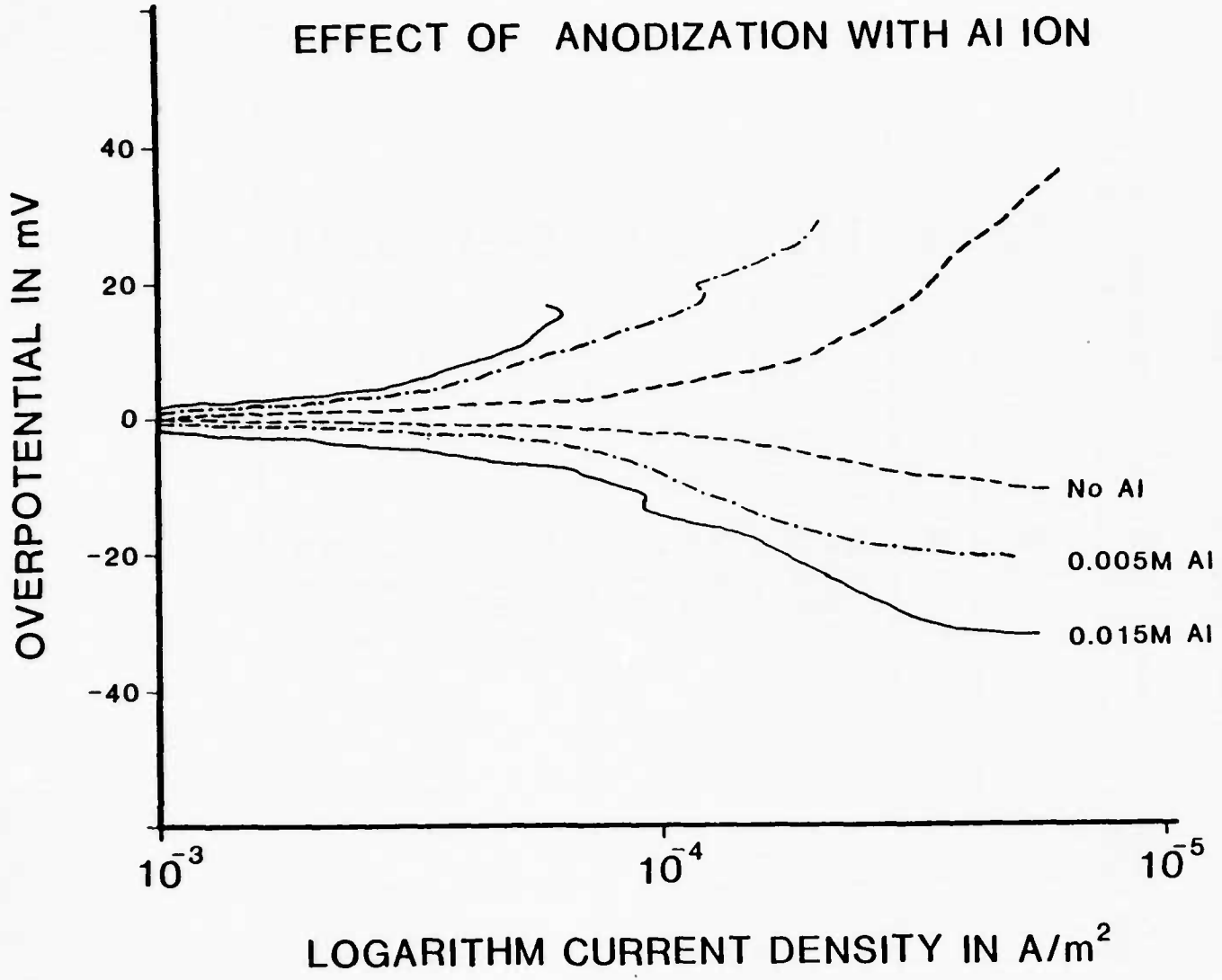

Figure 1. Polarization data in pH 8.5 borate for steel anodized in presence of aluminum ion concentrations of 0M, 0.005M, and 0.015M.

than in its absence. Also, both anodic and cathodic currents were inhibited by the aluminum ion anodization treatment. Additional tests are in progress to determine the extent of the improvement of corrosion resistance under these and related conditions.

SUMMARY AND FUTURE DIRECTIONS

A literature survey of the oxygen reduction reaction has revealed considerable activity in development of electrodes for catalysis of the reaction. Most of the activity is empirical in nature. However, investigations of semiconducting properties are promoting a better understanding of the passive layer on iron and electrocatalysis surfaces for oxygen reduction. Also, techniques for chemically modifying electrode surfaces for specific purposes have demonstrated the ability to create new types of surfaces for electrochemical reactions. These developments suggest that the passive oxide layer on iron can be modified to yield different semiconducting properties which can influence the oxygen reduction reaction. Additional property changes can be affected by chemical modification of the surface. Moreover, these modification methods can be combined to produce new interfacial properties for ferrous substrates.

Modification of a steel substrate by anodization in the presence of aluminum has yielded an inhibited electrochemical surface as judged by polarization resistance data. Additional tests will pursue the ability of this technique and surface chemical modification techniques to influence the rates of cathodic delamination on treated surfaces coated with organic layers.

Some efforts will also be devoted to development of a solid state oxygen probe for use beneath organic layers in cathodic delamination studies.

REFERENCES

[1] J. C. Scully, "The Fundamentals of Corrosion," 2nd Edition, Pergamon Press, Ltd., New York, 1975.

[2] H. Leidheiser, Jr., M. W. Kendig, Corrosion 32, 69 (1976).

[3] M. W. Kendig, H. Leidheiser, Jr., J. Electrochem. Soc. 123, 982 (1976).

[4] H. Leidheiser, Jr., M. W. Kendig, Ind. Eng. Chem. Prod. Res. Dev. 17, 54 (1978).

[5] H. Leidheiser, Jr., Croat. Chem. Acta 53, 197 (1980).

[6] H. Leidheiser, Jr., W. Wang, J. Coatings Technol. 53, No. 672, 77 (1981).

[7] R. A. Iezzi, H. Leidheiser, Jr., Corrosion 37, 28 (1981).

[8] H. Leidheiser, Jr., Ind. Eng. Chem. Prod. Res. Dev. 20, 547 (1981).

[9] H. Leidheiser, Jr., I. Suzuki, Corrosion 36, 601 (1980).

[10] H. Leidheiser, Jr., I. Suzuki, J. Electrochem. Soc. 128, 242 (1981).

[11] H. Leidheiser, Jr., Y. Momosa, R. D. Granata, Corrosion 38, 178 (1982).

[12] H. Leidheiser, Jr., H. Konno, J. Electrochem. Soc. 130, 747 (1983).

[13] H. Leidheiser, Jr., J. Coatings Technol. 53, No. 678, 29 (1981).

[14] T. Erdey-Gruz, "Kinetics of Electrode Processes," Wiley Interscience, New York, 1972

[15] J. P. Hoare, "Oxygen," in "Encyclopedia of Electrochemistry of the Elements," A. J. Bard, Editor, Marcel Dekker, Inc., New York, 1974.

[16] A. Damjanovic, "Mechanistic Analysis of Oxygen Electrode Reactions," in "Modern Aspects of Electrochemistry - Vol. 5," J. O'M. Bockris and B. E. Conway, Editors, Plenum Press, New York, 1969.

[17] J. O'M. Bockris, A.K.N. Reddy, "Modern Electrochemistry - Volume 2," Plenum/Rosetta Edition, Plenum Press, New York, 1970.

[18] J. Koryta, J. Dvořák, V. Boháčková, "Electrochemistry," Methuen & Co., Ltd., London, 1970.

[19] D. B. Sepa, M. V. Vojnovic, A. Damjanovic, Electrochimica Acta 25, 1491 (1980).

[20] W. R. Heineman, P. T. Kissinger, Anal. Chem. 52, 138R (1980).

[21] D. C. Johnson, Anal. Chem. 54, 9R (1982).

[22] M. D. Ryan, G. S. Wilson, Anal. Chem. 54, 20R (1982).

[23] S. R. Morrison, "Electrochemistry at Semiconductor and Oxidized Metal Electrodes," Plenum Press, New York, 1980.

[24] N. Cabrera, N. F. Mott, Rep. Prog. Phys. 12, 163 (1949).

[25] M. J. Pryor, M. Cohen, J. Electrochem. Soc. 100, 203 (1953).

[26] P. B. Sewell, C. D. Stockbridge, M. Cohen, Can. J. Chem. 37, 1813 (1959).

[27] M. Nagayama, M. Cohen, J. Electrochem. Soc. 109, 781 (1962).

[28] M. Nagayama, M. Cohen, J. Electrochem. Soc. 110, 670 (1963).

[29] N. Sato, M. Cohen, J. Electrochem. Soc. 111, 512 (1964); 111, 519 (1964).

[30] N. Sato, K. Kudo, T. Noda, Corrosion Science 10, 785 (1970).

[31] N. Sato, K. Kudo, Electrochimica Acta 16, 447 (1971).

[32] N. Sato, K. Kudo, T. Noda, Electrochimica Acta 16, 1909 (1971).

[33] N. Sato, T. Noda, K. Kudo, Electrochimica Acta 19, 471 (1974).

[34] N. Sato, K. Kudo, T. Noda, Z. Phys. Chemie 98, 271 (1975).

[35] M. C. Bloom, L. Goldenberg, Corrosion Science 5, 623 (1965).

[36] R. V. Moshtev, Berichte Der Bunsengesellschaft 71, 1079 (1967).

[37] R. V. Moshtev, Electrochimica Acta 15, 657 (1970).

[38] R. V. Moshtev, Electrochimica Acta 16, 2039 (1971).

[39] V. Markovac, M. Cohen, J. Electrochem. Soc. 114, 674 (1967).

[40] R. W. Revie, B. G. Baker, J. O'M. Bockris, J. Electrochem. Soc. 122, 1460 (1975).

[41] O. J. Murphy, J. O'M. Bockris, T. E. Pou, D. L. Cocke, G. Sparrow, J. Electrochem. Soc. 129, 2149 (1982).

[42] W. E. O'Grady, J. Electrochem. Soc. 127, 555 (1980).

[43] K. Kuroda, B. D. Cahan, Gh. Nazri, E. Yeager, T. E. Mitchell, J. Electrochem. Soc. 129, 2163 (1982).

[44] G. G. Long, J. Kruger, D. R. Black, M. Kuriyama, J. Electrochem. Soc. 130, 240 (1983).

[45] S. C. Tjong, E. Yeager, J. Electrochem. Soc. 128, 2251 (1981).

[46] O. J. Murphy, J. O'M. Bockris, T. E. Pou, L. L. Tongson, M. D. Monkowski, J. Electrochem. Soc. 130, 1792 (1983).

[47] N. Sato, T. Noda, Electrochimica Acta 22, 839 (1977).

[48] F. M. Delnick, N. Hackerman, J. Electrochem. Soc. 126, 732 (1979).

[49] U. Stimming, J. W. Schultze, Electrochimica Acta 24, 859 (1979).

[50] S. M. Wilhelm, K. S. Yun, L. W. Ballenger, N. Hackerman, J. Electrochem. Soc. 126, 419 (1979).

[51] C. T. Chen, B. D. Cahan, J. Electrochem. Soc. 129, 17 (1982).

[52] B. D. Cahan, C. T. Chen, J. Electrochem. Soc. 129, 474 (1982).

[53] Ibid., 921.

[54] U. Stimming, J. Electrochem. Soc. 129, 2868 (1982).

[55] C. Gabrielli, M. Keddam, J. Electrochem. Soc. 129, 2872 (1982).

[56] F. J. Morin, Phys. Rev. 93, 1195 (1954).

[57] F. J. Morin, Phys. Rev. 83, 1005 (1951).

[58] J. W. Schultze, U. Stimming, Z. Phys. Chem. (Frankfurt am Main) 98(1-6), 285 (1975); cf. C. A. 84, 171417e.

[59] U. Stimming, J. W. Schultze, Ber. Bun. Ges. 81 (10), 1116 (1977).

[60] J. W. Schultze, Met. Corros., Proc.: Int. Congr. Met. Corros./8th, 1, 1 (1981); cf. C. A. 96, 149387w.

[61] J. W. Schultze, Chem.-Ing.-Tech. 51(6), 643-44, 649 (1979).

[62] M. N. Saleh, M. M. Gawish, J. Appl. Phys. 51(1), 459 (1980).

[63] L. Murawski, O. Gzowski, Phys. Stat. Sol. (a) 19, K125 (1973).

[64] R. Bharati, R. A. Singh, J. Mater. Sci. 16(2), 511 (1981).

[65] J. W. Schultze, S. Mohr, DECHEMA-Monogr. 90(1851-1870, Elektrochem. Elektron.), 231 (1981); cf. C. A. 95, 71540y.

[66] J. W. Schultze, Passivity Met., Proc. Int. Symp., 4th 1977, 82 (1978); cf. C. A. 93, 194155t.

[67] J. W. Schultze, M. A. Habib, J. Appl. Electrochem. 9, 255 (1979).

[68] U. Stimming, J. W. Schultze, Ber. Bundesges. Phys. Chem. 80(12), 1297 (1976).

[69] R. R. Dogonadze, A. M. Kuznetsov, J. Ulstrup, Electrochimica Acta 22(9), 967 (1977).

[70] R. Memming, "Charge Transfer Processes at Semiconductor Electrodes," in "Electroanalytical Chemistry, Volume 11," A. J. Bard, ed., Marcel Dekker, New York, 1979.

[71] S. Kapusta, N. Hackerman, Electrochimica Acta 25(7), 949 (1980).

[72] K. E.Heusler, K. S. Yun, Electrochimica Acta 22(9), 977 (1977).

[73] A.M.T. Olmedo, R. Pereiro, D. J. Schiffrin, J. Electroanal. Chem. 74, 19 (1976).

[74] S. V. Koshcheev, A. E. Cherkashin, Izv. Akad. Nauk SSSR, Neorg. Mater. 16(7), 1239 (1980); cf. C. A. 93, 101648t.

[75] P. Iwanski, J. S. Curran, W. Gissler, R. Memming, J. Electrochem. Soc. 128(10), 2188 (1981).

[76] K. L. Hardee, A. J. Bard, J. Electrochem. Soc. 123(7), 1024 (1976).

[77] M. Gori, H. R. Grueniger, G. Calzaferri, J. Appl. Electrochem. 10(3), 345 (1980).

[78] R. A. Fredlein, A. J. Bard, J. Electrochem. Soc. 126(11), 1892 (1979).

[79] N. C. Debnath, A. B. Anderson, J. Electrochem. Soc. 129(10), 2169 (1982).

[80] R. M. Candea, Electrochimica Acta 26(12), 1803 (1981).

[81] W. Bowen, T. Hurlen, Acta Chem. Scanda., Ser. A A 35(5), 359 (1981).

[82] W. Paatsch, J. Phys. (Paris), Colloq. 1977(5), 151 (1977).

[83] W. Paatsch, Proc. Int. Vac. Congr., 7th 2, 911 (1977).

[84] A. J. Bard, Science 207(4427), 139 (1980), cf. C. A. 93, 213225j.

[85] R. Memming, Top. Surf. Chem., (Proc. Int. Symp.) 1977, E. Kay, P. S. Bagus, Editors, Plenum Press, New York, 1978, pp.1-28.

[86] L. F. Schneemeyer, M. S. Wrighton, J. Am. Chem. Soc. 101(22), 6496 (1979), cf. C. A. 91, 219337c.

[87] S. M. Ahmed, H. Gerischer, Electrochimica Acta 24(6), 705 (1979), cf. C. A. 92, 29117d.

[88] D. M. Schleich, C. Derrington, W. Godek, D. Weisberg, A. Wold, Mat. Res. Bull. 12, 321 (1977).

[89] W. Paatsch, Ber. Bunsenges. Phys. Chem. 81(7), 645 (1977).

[90] R. N. Noufi, P. A. Kohl, S. N. Frank, A. J. Bard, J. Electrochem. Soc. 125(2), 246 (1978).

[91] B. Morosin, R. J. Baughman, D. S. Ginley, M. A. Butler, J. Appl. Cryst. 11, 121 (1978).

[92] R. Memming, Ber. Bunsenges. Phys. Chem. 81(8), 732 (1977), cf. C. A. 88, 128181u.

[93] S. Kapusta, N. Hackerman, Electrochimica Acta 25(8), 1001 (1980).

[94] R. W. Murray, Acc. Chem. Res. 13(5), 135 (1980).

[95] M. S. Wrighton, A. B. Brocarsly, J. M. Bolts, M. G. Bradley, A. B. Fischer, S. N. Lewis, M. C. Palazzotto, E. G. Walton, Adv.Chem. Ser. 184 (Interfacial Photoprocesses: Energy Convers. Synth.), 269 (1980), cf. C.A. 92, 200818j.

[96] C. P. Jester, R. D. Rocklin, R. W. Murray, J. Electrochem. Soc. 127(9), 1979 (1980).

[97] A. B. Bocarsly, E. G. Walton, M. G. Bradley, M. S. Wrighton, J. Electroanal. Chem. Interfacial Electrochem. 100, 283 (1979), cf. C. A. 92, 49369r.

[98] J. M. Bolts, A. B. Bocarsly, M. C. Palazzotto, E. G. Walton, N. S. Lewis, M. S. Wrightman, J. Am. Chem. Soc. 101(6), 1378 (1979), cf. C. A. 90, 194672x.

[99] N. Kobayashi, T. Matsue, M. Fujihira, J. Electroanal. Chem. Interfacial Electrochem. 103(3), 427 (1979), cf. C. A. 92, 66658b.

[100] N. R. Armstrong, V. R. Shepard, Jr., J. Electroanal. Chem. Interfacial Electrochem. 115(2), 253 (1980), cf. C. A. 94, 92574g.

[101] R. D. Rocklin, R. W. Murray, J. Electroanal. Chem. Interfacial Electrochem. 100, 271 (1979), cf. C. A. 91, 148464d.

[102] D. Astruc, J. R. Hamon, G. Althoff, E. Roman, P. Batail, P. Michaud, J. P. Mariot, F. Varret, D. Cozak, J. Am. Chem. Soc. 101(18), 5445 (1979).

[103] A. Bettelheim, R.J.H. Chan, T. Kuwana, J. Electroanal. Chem. Interfacial Electrochem. 110(1-3), 93 (1980).

[104] F. Beck, J. Appl. Electrochem. 7(3), 239 (1977), cf. C. A. 87, 75524d.

[105] H. Behret, H. Binder, G. Sandstede, G. G. Scherer, J. Electroanal. Chem. Interfacial Electrochem. 117(1), 29 (1981).

[106] A. Bettelheim, T. Kuwana, Anal. Chem. 51(13), 2257 (1979).

[107] J. P. Collman, M. Marrocco, P. Denisevich, C. Koval, F. C. Anson, J. Electroanal. Chem. Interfacial Electrochem. 101(1), 117 (1979).

[108] O. Contamin, E. Levart, M. Savy, J. Electroanal. Chem. Interfacial Electrochem. 115(2), 267 (1980), cf. C. A. 94, 38624k.

[109] G. A. Deborski, Patent, U.S. 4,179,350, Dow Chemical Co. (1979).

[110] K. Hiratsuka, H. Sasaki, S. Toshima, Chem. Lett. 1979(7), 751 (1979).

[111] A. Kaisheva, Elektrokhimiya 15(10), 1539 (1979), cf. C. A. 92, 49335b.

[112] T. Kikuchi, H. Sasaki, T. Shinobu, Chem. Lett. 1980(1), 5 (1980).

[113] N. Kobayashi, M. Fujihira, Chem. Lett. 1982(4), 575 (1982), cf. C. A. 96, 225256v.

[114] L. Kreja, R. Dabrowski, J. Power Sources 6(1), 35 (1980), cf. C. A. 94, 54745f.

[115] L. Kreja, A. Plewka, Electrochimica Acta 25, 1283 (1980).

[116] C. Kretzschmar, K. Wiesener, I. Iliev, A. Kaisheva, Ext. Abstr., Meet. - Int. Soc. Electrochem., 28th 1977, 2, 286 (1977), cf. C. A. 89, 96926t.

[117] C. Kretzschmar, K. Wiesener, M. Musilova, J. Mrha, R. Dabrowski, J. Power Sources 2(4), 351 (1978), cf. C. A. 89, 119508z.

[118] G. Magner, M. Savy, G. Scarbeck, J. Riga, J. J. Verbist, J. Electrochem. Soc. 128(8), 1674 (1981).

[119] B. Z. Nikolic, R. R. Adzic, E. B. Yeager, J. Electroanal. Chem. Interfacial Electrochem. 103(2), 281 (1979), cf. C. A. 92, 11663u.

[120] M. Savy, P. Andro, C. Bernard, Croat. Chem. Acta 44(1), 107 (1972), cf. C. A. 77, 28234t.

[121] M. Savy, C. Bernard, G. Magner, Electrochimica Acta 20(5), 383 (1975), cf. C. A. 83, 154486p.

[122] E. Yeager, J. Zagal, B. Z. Nikolic, R. R. Adzic, Proc. - Electrochem. Soc. 1979, 80-3, 436 (1980), cf. C. A. 93, 212340f.

[123] J. Zagal, P. Bindra, E. Yeager, J. Electrochem. Soc. 127(7), 1506 (1980).

[124] M. R. Van de Mark, L. L. Miller, J. Am. Chem. Soc. 100(10), 3223 (1978), cf. C. A. 89, 7655p.

[125] H. Tachikawa, L. R. Faulkner, J. Am. Chem. Soc. 100(14), 4379 (1978), cf. C. A. 89, 119628p.

[126] J. C. Sturm, J. Zagal, Bol. Soc. Chil. Quim. 27(1), 215 (1982), cf. C. A. 96, 225278d.

[127] C. P. Andrieux, J. M. Saveant, J. Electroanal. Chem. Interfacial Electrochem. 111(2-3), 377 (1980).

[128] C. P. Andrieux, J. M. Dumas-Bouchiat, J. M. Saveant, J. Electroanal. Chem. Interfacial Electrochem. 114(1), 159 (1980), cf. C. A. 94, 22143s.

[129] J. E. Dubois, P. C. Lacaze, M. C. Pham, J. Electroanal. Chem. Interfacial Electrochem. 117(2), 233 (1981), cf. C. A. 94, 129419p.

[130] P. Daum, J. R. Lenhard, D. Rolison, R. W. Murray, J. Am. Chem. Soc. 102(14), 4649 (1980), cf. C. A. 93, 43713q.

[131] F. R. Fan, L. R. Faulkner, J. Am. Chem. Soc. 101(17), 4779 (1979).

[132] P. Denisevich, K. W. Willman, R. W. Murray, J. Am. Chem. Soc. 103(16), 4727 (1981), cf. C. A. 95, 69824a.

[133] D. Tench, L. F. Warren, J. Electrochem. Soc. 130(4), 869 (1983).

[134] U. Stimming, J. Electroanal. Chem. Interfacial Electrochem. 136(2), 354 (1982), cf. C. A. 97, 46436c.

[135] J. P. Hoare, "The Electrochemistry of Oxygen," John Wiley and Sons, New York, 1968.

[136] Ch. Fabjan, M. R. Kazemi, A. Neckel, Ber. Bunsenges. Phys. Chem. 84(10), 1026 (1980).

[137] S. Haruyama, H. Fukayama, K. Nagasaki, Denki Kagaku 40(9), 637 (1972).

[138] M. A. Marinich, L. I. Antropov, M. R. Tarasevich, Ukr. Khim. Zh. (Russ. Ed.) 44(4), 357 (1978), cf. C. A. 89, 50432a.

[139] T. Takei, H. A. Laitinen, Surf. Technol. 16(3), 185 (1982), cf. C. A. 97, 171160j.

[140] E. A. Khomskaya, N. F. Gorbacheva, N. B. Tolochkov, Sov. Elec. 16(1), 48 (1980).

[141] M. Watanabe, S. Venkatesan, H. A. Laitinen, J. Electrochem. Soc. 130(1), 59 (1983).

[142] V. S. Bagotskii, N. A. Shumilova, G. P. Samoilov, E. I. Khrushcheva, Electrochimica Acta 17(9), 1625 (1972).

[143] K. Balakrishnan, V. K. Venkatesan, Electrochimica Acta 24, 131 (1979).

[144] A. Caprani, I. Epelboin, P. Morel, J. Less-Common Met. 69(1), 37 (1980).

[145] R. Adzic, A. Tripkovic, R. Atanasoski, J. Electroanal. Chem. Interfacial Electrochem. 94(3), 231 (1978).

[146] R. R. Adzic, N. M. Markovic, A. V. Tripkovic, Glas. Hem. Drus. Beograd 45(10), 399 (1980), cf. C. A. 94, 73479p.

[147] R. R. Adzic, Isr. J. Chem. 18(1-2), 166 (1979).

[148] G. Bronoel, J. C. Grenier, J. Reby, Electrochimica Acta 25, 1015 (1980).

[149] J. R. Goldstein, A. C. C. Tseung, J. Phys. Chem. 76(24), 3646 (1972).

[150] Y. Matsumoto, H. Yoneyama, H. Tamura, J. Electroanal. Chem. Interfacial Electrochem. 79(2), 319 (1977), cf. C. A. 87, 45849w.

[151] N. F. Razina, A. Kamalova, Izv. Akad. Nauk Kaz. SSR, Ser. Khim. 28(4), 30 (1978), cf. C. A. 89, 170788t.

[152] D. B. Sepa, A. Damjanovic, J. O'M. Bockris, Electrochimica Acta 12, 746 (1967).

[153] D.A.J. Rand, J. Electroanal. Chem. Interfacial Electrochem. 83(1), 19 (1977).

[154] K. Ogura, N. Hackerman, J. Electrochem. Soc. 121(8), 1013 (1974).

[155] K. Bohnenkamp, Arch. Eisenhuettenwes. 47(4), 253 (1976), cf. C. A. 85, 26684f.

[156] N. F. Razina, A. Kamalova, Tr. In-ta Org. Kataliza i, Elektrokhimii. AN KazSSR 1978, (18), 49 (1978), cf. C. A. 90, 94242p.

[157] T. Nigorikawa, K. Kojima, G. Okamoto, Boshoku Gijutsu 26(2), 67 (1977), cf. C. A. 88, 96537w.

[158] K. Kojima, T. Yamada, T. Nigorikawa, K. Tachivana, G. Okamoto, Boshoku Gijutsu 23(12), 595 (1974), cf. C. A. 84, 168038b.

[159] M. D. Getmanskii, N. I. Savitkin, A. A. Gonik, K. R. Nizamov, Korroz. Zashch. Neftegazov. Prom-sti 1978, (2), 7 (1978), cf. C. A. 88, 179320w.

[160] R. J. Chin, K. Nobe, Corrosion 33(10), 364 (1977).

[161] A. Caprani, C. Deslouis, M. Keddam, Ph. Morel, B. Tribollet, Electrochimica Acta 22(11), 1231 (1977).

[162] A. K. Vijh, Corr. Sci. 12, 105 (1972).

Program #6

Detection of Aggregated Water in Polymer Coatings

ABSTRACT

The technique of high frequency dielectric spectroscopy has been advanced to the stage where meaningful data may now be obtained on polymer systems. The advances are as follows:

- Unwanted reflections in the measurement system have been removed.
- Data processing programs have been fine tuned.
- A new cell for coating work was designed, tested, and characterized.
- Unwanted "losses" occurring previously have been removed.

Measurements on polyvinyl acetate have shown a distinct loss mechanism for an absorbed non-aggregated phase of water. Experiments in progress have indicated a loss mechanism for an aggregated phase of water within the polymer.

REVIEW OF TIME DOMAIN SPECTROSCOPY

In previous reports the technique of time domain spectroscopy was introduced as a method for obtaining high frequency (GHz) dielectric information [1]. In time domain spectroscopy a dielectric system is perturbed with a fast rise time pulse and the response in time is noted. Each pulse, incident and reflected, is Fourier transformed to obtain the frequency response of the system. The Fourier transforms of the pulses can be combined mathematically to obtain dielectric information over a frequency range. A diagram of the experimental setup is shown in Figure 1. The advantages of time domain spectroscopy over conventional frequency domain techniques are the speed at which measurements can be made and the continuous nature of the resulting frequency information. The intent of dielectric measurements is to provide translational information about water molecules in polymer systems.

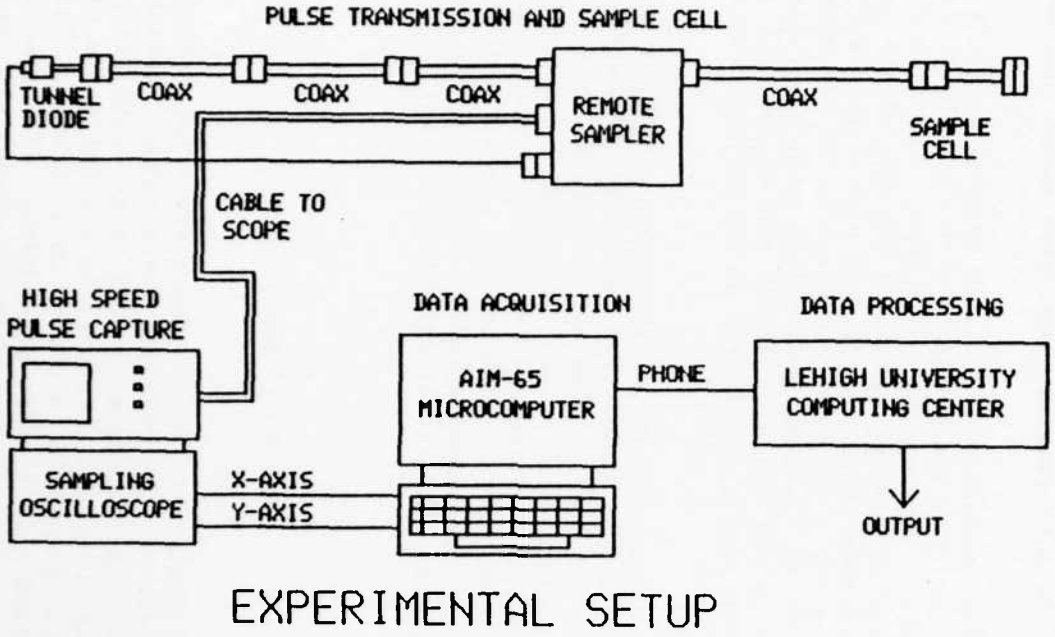

Figure 1. Diagram of experimental setup used for high frequency dielectric measurements.

DISCUSSION OF EXPERIMENTAL ADVANCES

In the last report, mention was made of several problems including the unexplained loss mechanism and unwanted reflections within the measurement system. The removal of unwanted reflections was accomplished using two methods. The existing coaxial lines were replaced with new higher precision lines thereby minimizing reflections. For those reflections that could not be removed, the computer programs were modified in order to include only time data that were important to the experiment. In simple terms, the time data were truncated immediately after time response was finished. Although these changes help improve the data quality, the unexplained loss was still present.

The source of the unexplained loss was assumed to be in the cell used for the coatings. A new cell was designed with the help of Dr. Nikoli Eberhardt from the Electrical Engineering Department. The cell was constructed out of one of the replaced coaxial lines. A diagram of the new cell is shown in Figure 2. One important change is the use of a thin flexible metal foil substrate. The reason for a flexible substrate is to accommodate different coating thicknesses and at the same time ensure good electrical contact with the outer conductor. A bolt was also placed behind the foil substrate to allow the pressure of the sample dielectric on the center conductor to be adjusted.

A very careful characterization was performed after the new cell was constructed. A theoretical response for Teflon was calculated and compared with results from the new cell. Cause and effect information was then compiled for the whole experimental process. During the characterization, it was noted that the unexplained loss occurred when a short circuit reflection was used for the incident pulse. When an open circuit reflection was used as the incident pulse, the loss disappeared.[1] Results of the cell characterization have shown an excellent fit of experimental data with theoretical calculations.

WHAT DO ε' AND ε'' MEAN?

The results of dielectric measurements are often stated in terms of ε' and ε''. In the context of this research these values represent the translational response of a polar molecule (water) to an oscillating electric field. When the frequency of the field increases to a point where the molecule can no longer keep up with the field, a change in ε' occurs. This type of change is appropriately called a dielectric relaxation. If the molecule's oscillation is below the relaxation frequency it can reversibly return the energy input to it by the field, acting as a perfect capacitor. Once the molecule's oscillation is above the relaxation frequency it can no longer return all the energy to it and ε' decreases. The energy that can not be returned is measured by ε''. One of the factors contributing to the relaxation frequency is the surrounding environment. The frictional loss of energy due to the surroundings contributes to ε'', the dielectric loss. A spectroscopic measure of energy can be given by the following:

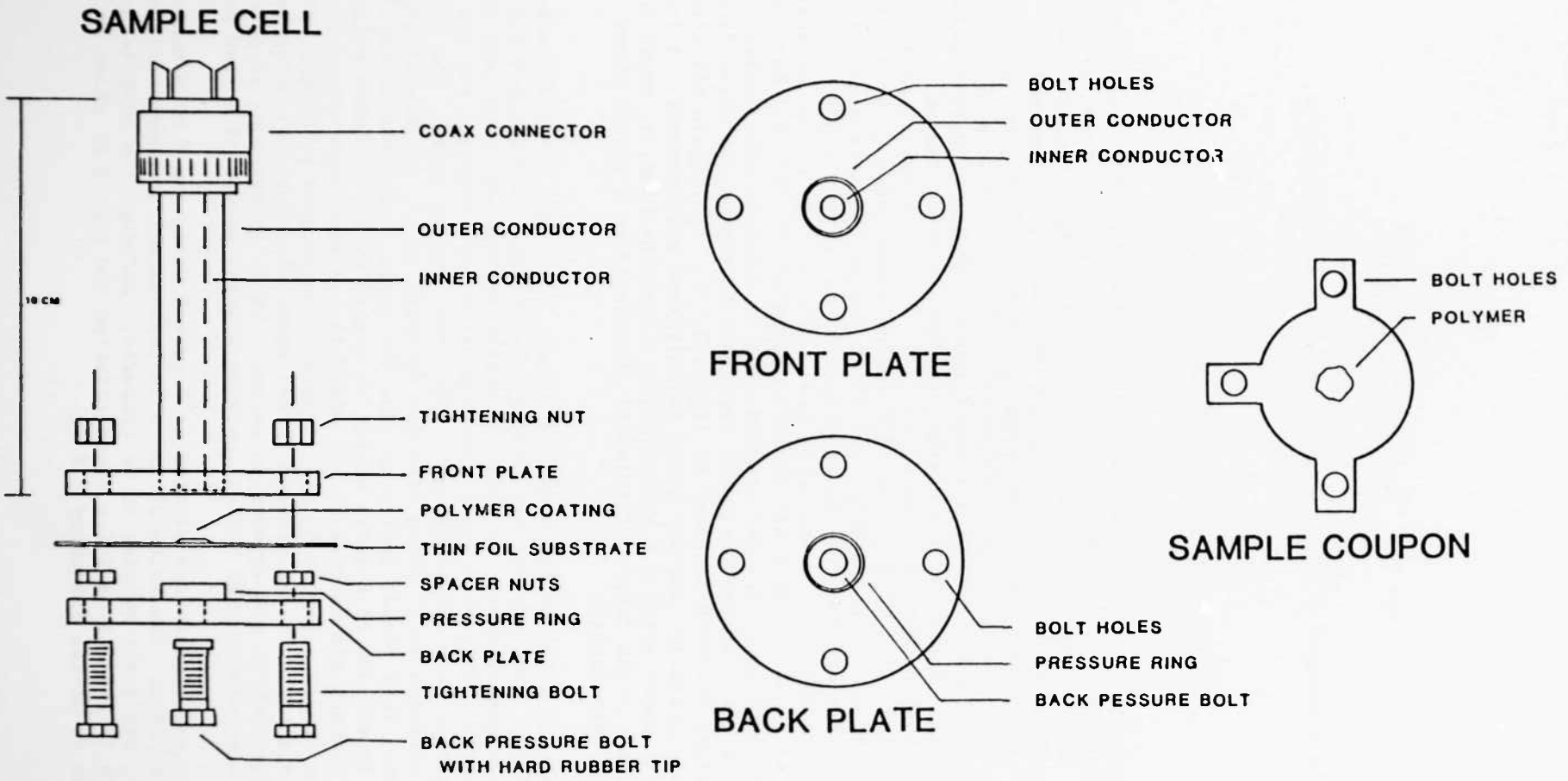

Figure 2. Diagram of sample cell and sample coupon.

$$\tan \delta = \frac{\varepsilon'' \text{ (energy dissipated)}}{\varepsilon' \text{ (energy returned)}}$$

Thus tan δ is a measure of the energy absorbed by the dielectric.

RESULTS AND DISCUSSION FOR POLYMER SYSTEMS

Measurements on dry Teflon and polyvinyl acetate (PVAc) were repeated using the improvements described above. Both samples were free films and were stored under vacuum overnight before testing. The dielectric response of Teflon is shown in Figure 3. The predicted dielectric response, ε' value, of Teflon is 2.1 across the entire frequency range. (If ε' does not change, ε'' is zero.) The results clearly illustrate this type of response except for a small loss at about 8.8 Hz on the log frequency scale. Figure 4 gives the results for PVAc. Again, no dielectric response is predicted at these frequencies and an experimental value of $\varepsilon' = 3.2$ is within experimental error of the calculated value of 3.0. As with Teflon there seems to be a slight loss at log frequency equal 8.8 Hz. At first glance the loss might seem to be some negligible artifact of the experiment. On further study, however, the loss, albeit small, is found to be real. The loss is due to an absorbed non-aggregated phase of water within both polymers. Studies [2] have been performed at low frequencies and temperatures on other polymer systems and have indicated that careful drying is necessary to remove all water from the sample. Further evidence is given in Figure 5 [3]. The figure illustrates a generalized relaxation map for water in different environments. A loss maximum at log frequency equal 8.8 Hz gives log relaxation time, τ, equal to -8.8 sec. According to the figure, this would correspond to a sorbed phase of water at room temperature.

In order to identify the loss positively, water was carefully added to samples of PVAc. The samples were soaked in warm water and weighed before and after each measurement.[2] A range of weight percent was then used for each measurement. Figures 6 and 7 give the dielectric response for the percent water ranges of 0.55%-0.84% and 2.78%-2.92%, respectively. The obvious change, the increase in ε'' along with the decrease in ε', is seen at log frequency 8.8 Hz. This result indicates that the small loss found in the "dry" samples was indeed due to a small amount of sorbed water. Further evidence is given by Johnson and co-workers [4] where it has been reported that water exists in two separate phases in PVAc. Below five percent by weight, water is present as a sorbed non-clustered phase; above five percent, water begins to form clusters which are aqueous in nature. It is interesting to note that a hydrophobic substance like Teflon contains a small amount of sorbed water.

Further experiments are plotted in Figure 9 using tan δ as a measure of dielectric response. The value of tan δ is independent of sample thickness, thus allowing different samples to be compared. Although the plot is not linear, there is still a definite trend relating the amount of water in the sample to tan δ, at log frequency 8.8 Hz.

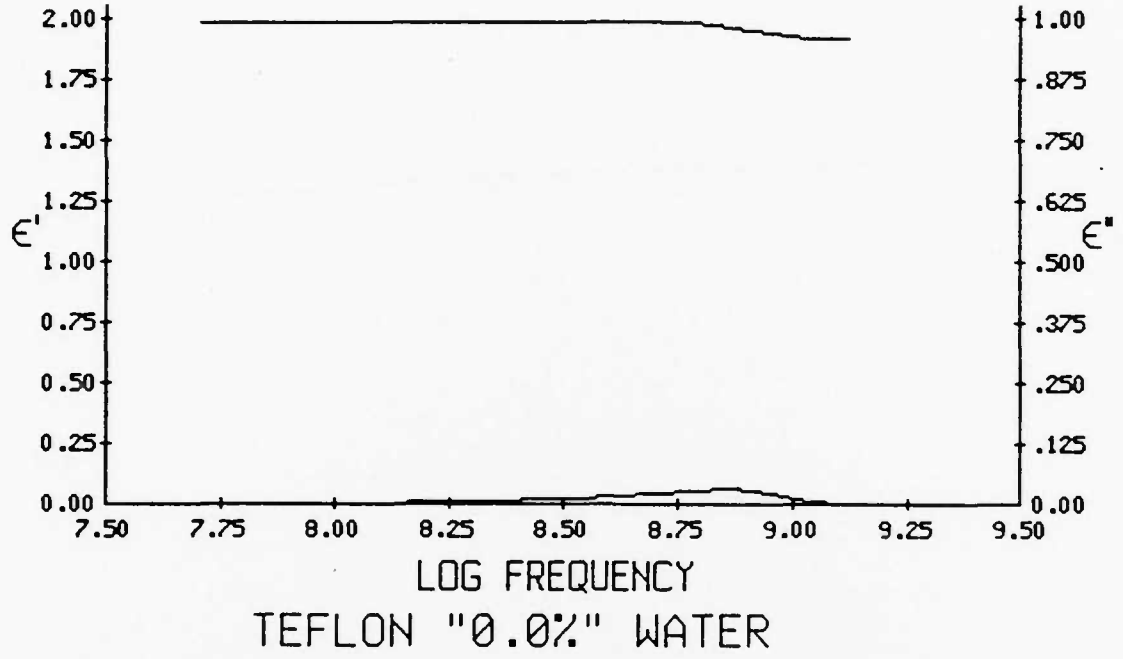

Figure 3. Teflon Dielectric Data. (Note: ε' is upper curve, ε" is lower curve.)

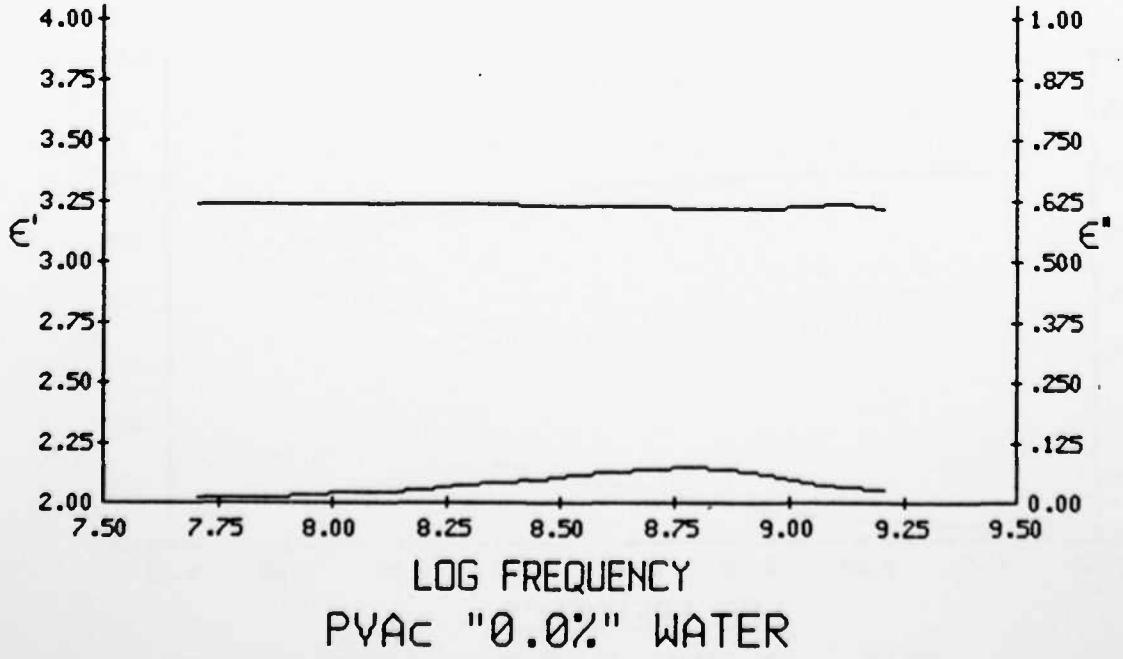

Figure 4. Polyvinyl Acetate Dielectric Data.

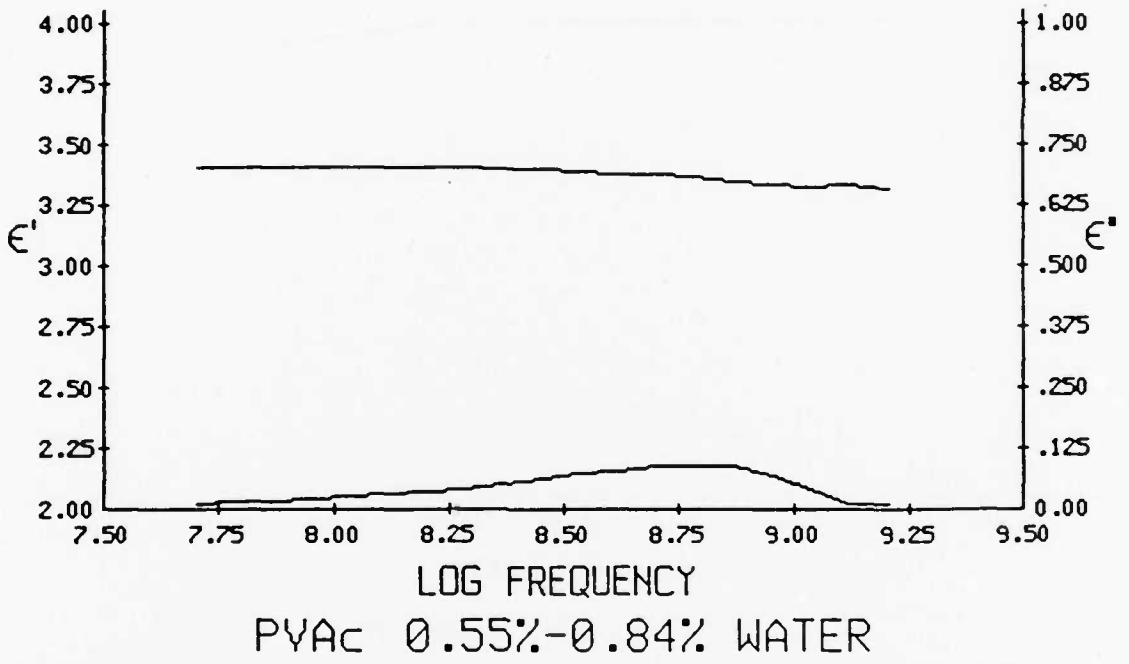

Figure 5. Polyvinyl Acetate and Water Dielectric Data.

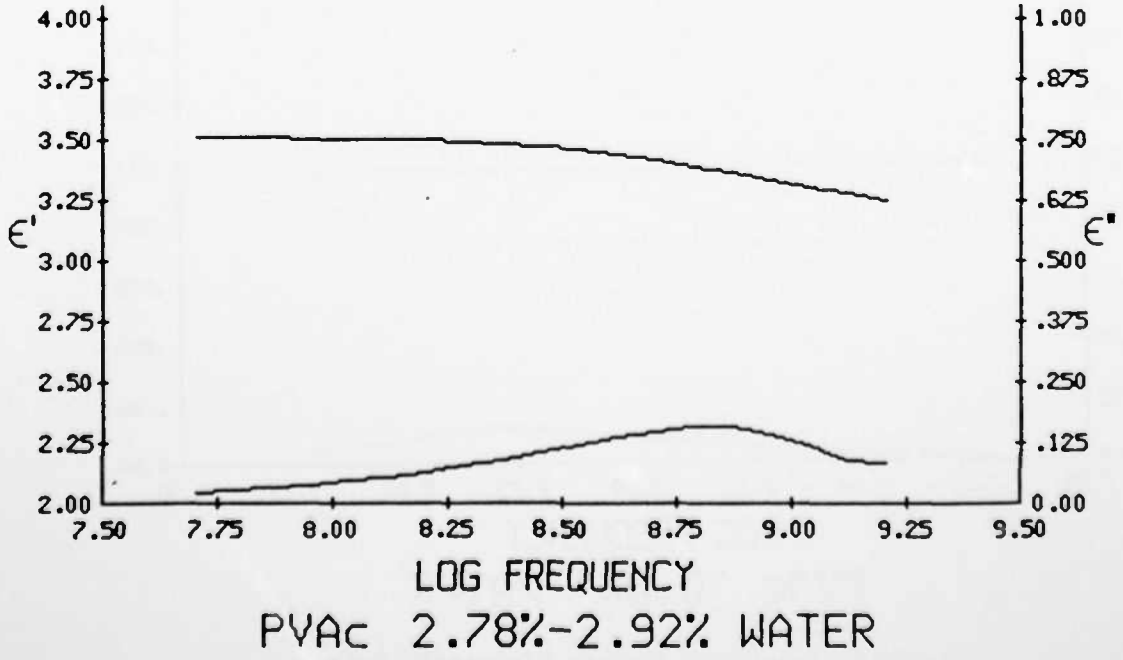

Figure 6. Polyvinyl Acetate and Water Dielectric Data.

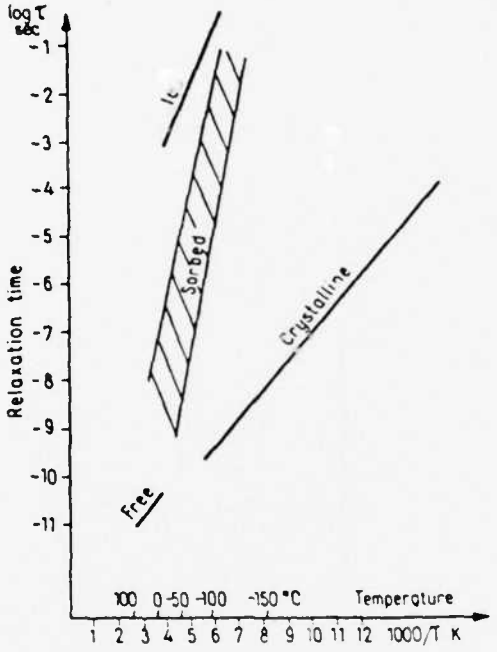

Figure 7. Relaxation map for water in different environments, from Ref. [3]. (Note: Relaxation time $\tau = 1/2\pi f$, where f is the frequency at which ε'' is at a maximum.)

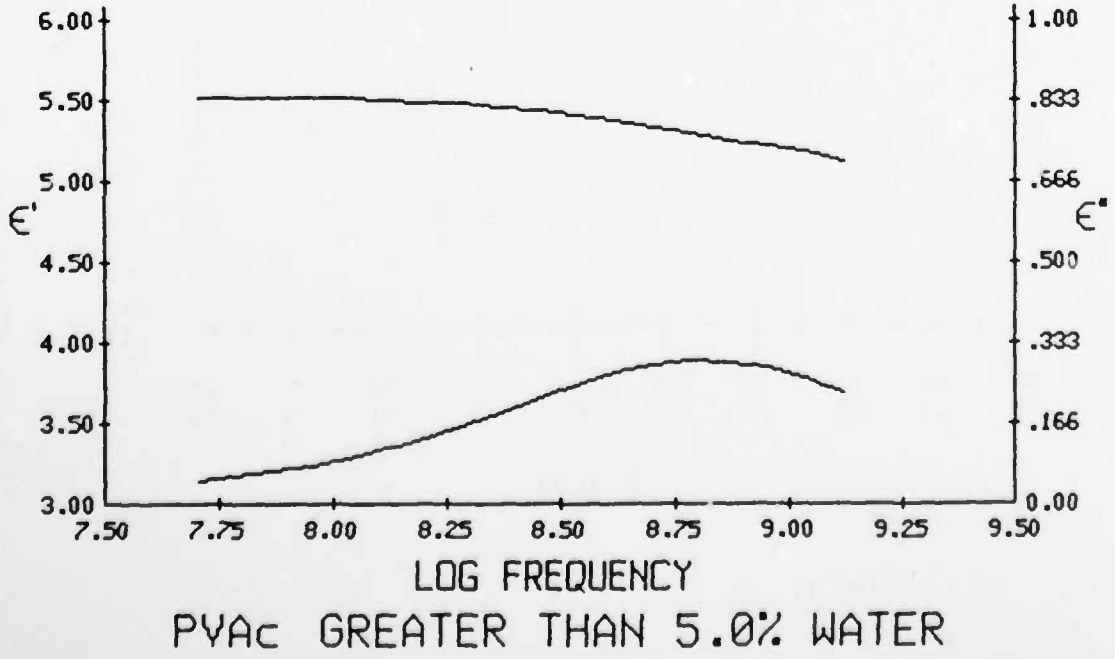

Figure 8. Polyvinyl Acetate and Water Dielectric Data.

AD-A139 086 CORROSION CONTROL THROUGH A BETTER UNDERSTANDING OF THE METALLIC SUBSTRAT..(U) LEHIGH UNIV BETHLEHEM PA CENTER FOR SURFACE AND COATINGS RESE.. H LEIDHEISER ET AL. 2/3

UNCLASSIFIED 01 JAN 84 N00014-79-C-0731 F/G 11/6 NL

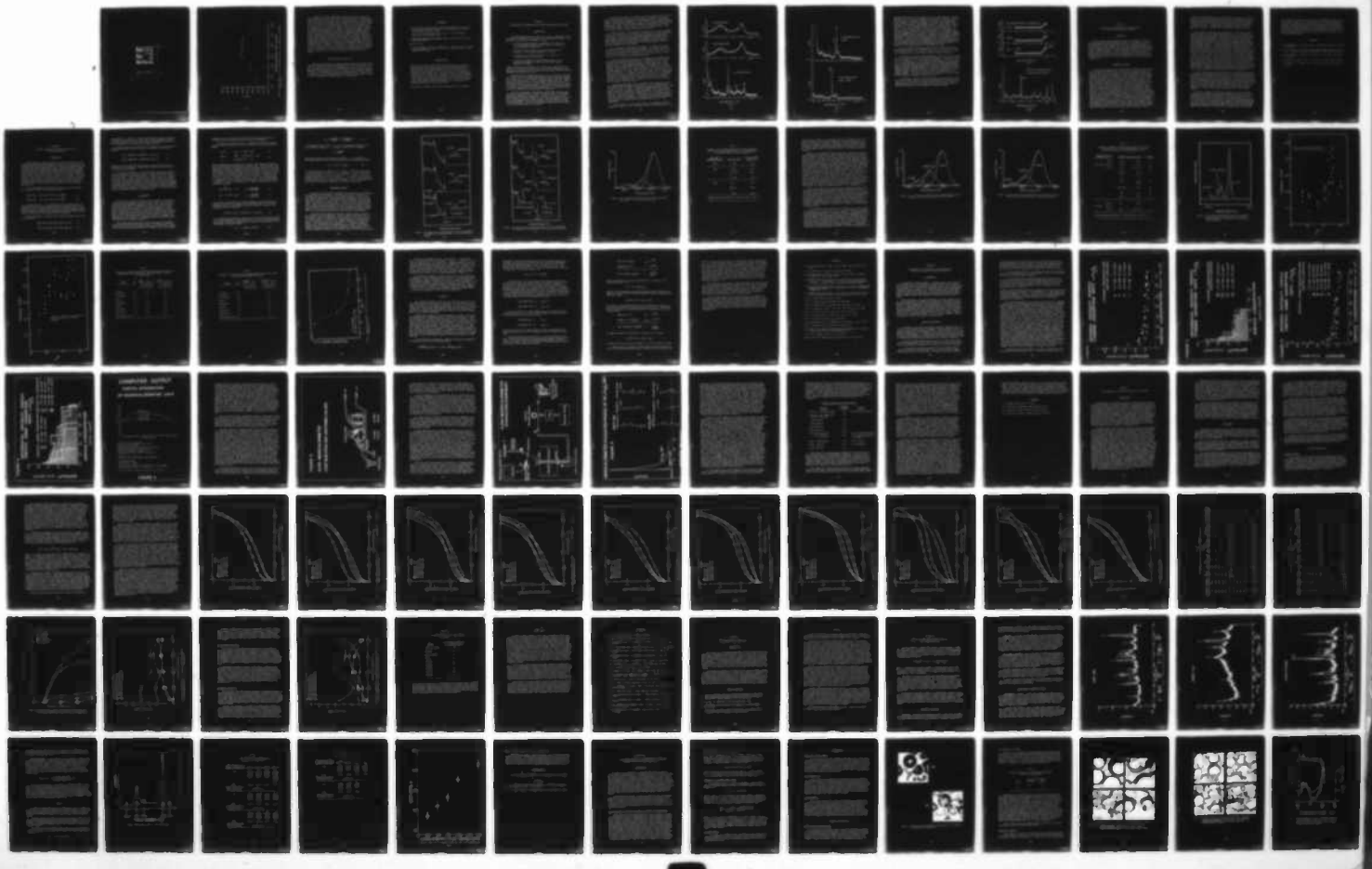

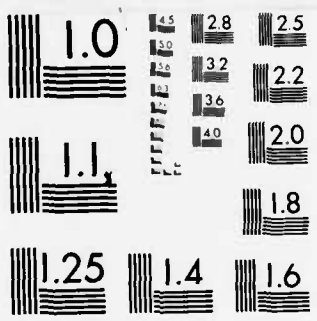

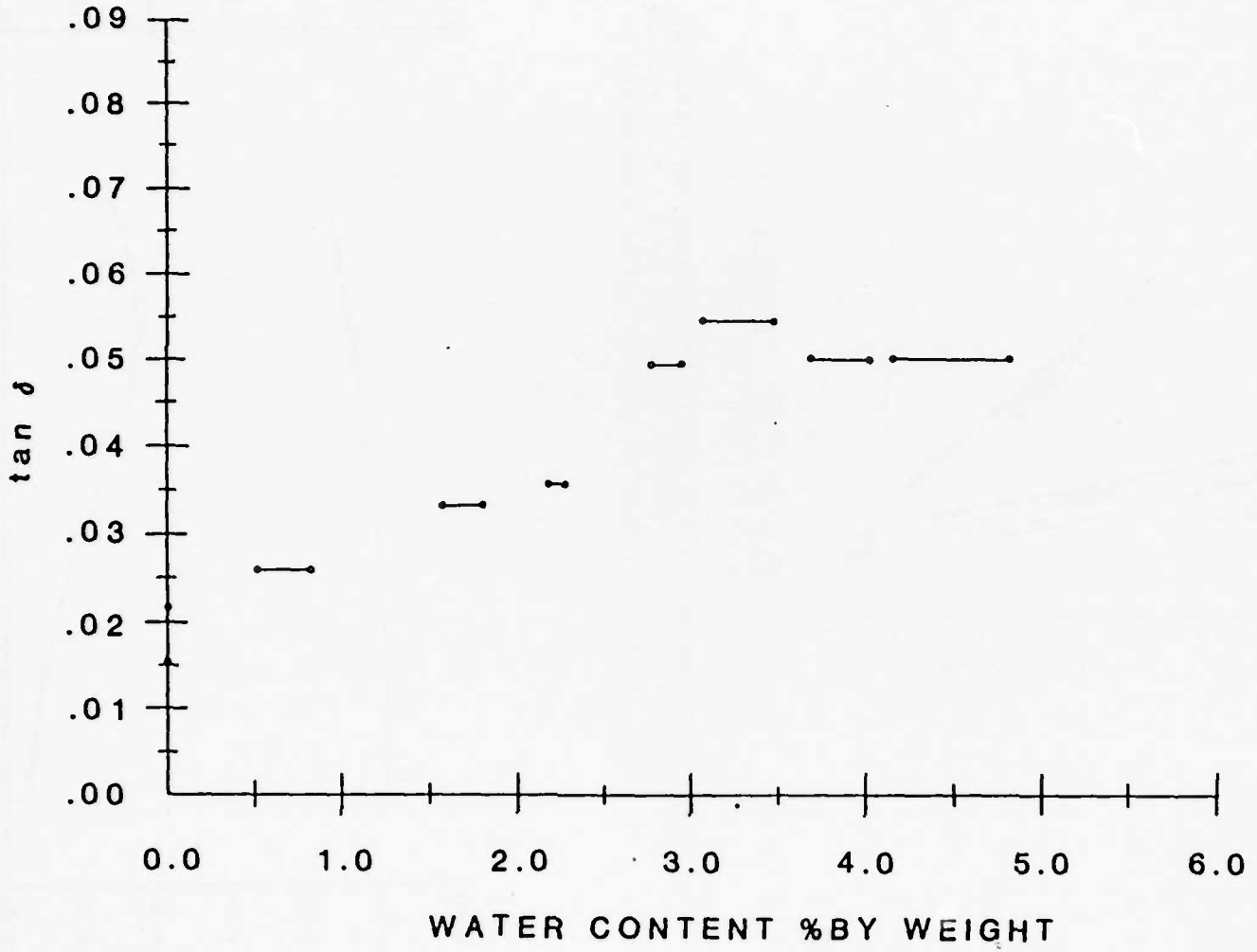

Figure 9. Water content vs. tan δ for polyvinyl acetate at a frequency of 7.0×10^8 Hz, log = 8.8 Hz.

A sample of PVAc was "saturated" with water at a water content well above five percent. Clustering of water causes the PVAc to turn milky white. Figure 8 is the dielectric response for the saturated sample. Several interesting observations can be made. First, the value of tan δ max (log frequency $\simeq$ 8.8) is 0.056, which coincides with low temperature and low frequency work by Johnson [4] for a "saturated" sample of PVAc. Several experiments have shown the value of tan δ to remain between 0.050 and 0.060 as water content is increased above four percent. Second, if Figure 8 is compared to Figure 6, one notes the broadening of the loss peak at the higher water content. This effect is attributed to the presence of clustered or aggregated water within the polymer, such water having a loss higher than that of sorbed water. Supporting this conclusion is the fact that in Figure 7 free water is shown to have a higher ε'' max than sorbed water. The frequency limitations of the method do not allow the ε'' max to be seen for free water. What is observed is the beginning of the loss for free water overlapping the loss for sorbed water. (Low temperature studies now in progress may allow ε'' max for clustered water to be seen.) A second source of support for this conclusion is again the work of Johnson [4]. Studies at low temperature and frequencies indicate a second loss due to clustered water at a higher frequency than the loss for sorbed water. It should be noted that the temperatures were low enough to freeze the water, thus the relaxation time is that of ice in Figure 7.

CONCLUSIONS AND FUTURE PLANS

Aside from completing and characterizing the measurement system, several important conclusions have been reached in the past year. The detection of a loss for sorbed water in PVAc at room temperature is scientifically new data. On-going research indicates that a different loss can be attributed to an aggregated or clustered phase of water. The application to coating systems is the next step. The technique has worked on model systems of Teflon and PVAc. It is hoped that enough information has been gained on these systems to enable a study of the metallic substrate/organic coating/interface.

REFERENCES

[1] See "Corrosion Control Through a Better Understanding of the Metallic Substrate/Organic Coating/Interface," Third Annual Report, Office of Naval Research, December 1, 1982.

For a survey of time domain techniques see: M.J.C. van Germert, Philips Res. Repts. 28, 530, 1973.

[2] Dielectric Spectroscopy of Polymers, Hedvig, John Wiley and Sons, New York, 1977, p.295.

[3] Ibid., p.294.

[4] G. E. Johnson, H. E. Blair, S. Matsuoka, E. W. Anderson, and J. E. Scott, Water in Polymers, ACS Symposium Series 127, American Chemical Society, Washington, DC, 1980.

REFERENCE NOTES

[1]The "short" or "open" reflection indicates how the cell is terminated when the incident pulse is recorded. A short circuit termination is simply the cell with no sample between the inner conductor and foil substrate, thus the signal is "shorted out" and an exact reflection of the incident pulse should result. An open circuit is one where no foil is present at the cell end, thus the signal is "open" to the atmosphere, a reflection will also result. Intuitively one would expect the short circuit would give a better representation of the incident pulse because an open would have an impedance associated with it from the atmosphere. it turns out, however, that the unexplained loss is the result of an impedance associated with the short circuit.

[2]PVAc tends to lose water quite rapidly when exposed to the atmosphere.

Program #7

Investigation of Phosphated Steel Surfaces by Laser Raman Spectroscopy

INTRODUCTION

Laser Raman Spectroscopy was shown to be a useful technique for the investigation of phosphated steel systems in the previous annual report. Four goals were set forth and are outlined as follows:

1. To record the Raman spectra of phosphated steels using zinc, iron and manganese phosphates and to compare the spectra with their mineralogical counterparts.

2. To find a suitable organic coating which will permit the examination of the phosphate beneath the coating.

3. To identify some corrosion products of steel and build up a reference library of their spectra.

4. To expose the organically coated phosphate samples to aggressive environments and identify the corrosion products which may have formed.

Progress concerning this research over the past year is discussed in this report in the context of each objective. Laser Raman Spectroscopy has the advantages of providing molecular information with sample analysis at ambient temperature and pressure or *in situ*.

Twenty commercial phosphating systems have been studied with the major goal of selecting two representative systems for use in continuing research. As a result, iron, zinc, and manganese phosphated samples have been characterized by their Raman spectra. The iron phosphate sample resulted in a Raman spectrum having one broad band in the phosphate active region (1000 cm^{-1}). This band is indicative of an amorphous structure which structure is generally accepted in the phosphating industry. Zinc phosphates were characterized by a two-phase system of hopeite and phosphophyllite. The manganese system resulted in a Raman spectrum characteristic of hureaulite.

The latter two systems, zinc phosphate and manganese phosphate, were chosen for future research for a number of reasons. First, zinc phosphate and manganese phosphate coatings are very crystalline and, as such, give Raman spectra with distinct signatures. They are both presently used in industry and their spectra are easily recorded. Uniform phosphate coatings of zinc and manganese could not be produced in the laboratory due to lack of proper equipment. For this reason phosphated samples have been provided by two leading manufacturers in the field.

The restrictions placed on an organic coating to be used in this project have been discussed in detail in the last report. Essentially one wants an organic coating which is transparent to the phosphate coating. The polyester-melamine coating studied previously is a good candidate for manganese phosphate systems. In the zinc phosphate system, however, the polyester-melamine obscures the phosphate signal. Two new organic coatings investigated, Eponol (SHELL) and Epon 1001 (SHELL), permit one to record the zinc phosphate signal. Thus, three different organic coating systems are now available.

The third objective in continuing this research was to build a reference library of Raman spectra to be used in the identification of corrosion products. This library, over the past year, has become an extensive data bank which includes spectra of all the iron oxides and oxyhydroxides, phosphate mineral spectra which correspond to most phosphating products, and inorganic and organic compound spectra associated with the phosphating process. Recently added to this library are some corrosion and thermal degradation products of manganese phosphate and zinc phosphate.

The remaining objective deals with changes of the organically coated phosphate as a function of aggressive environments. Although no experiments were carried out on an organic coating/phosphate system, the effects of an aggressive environment on the phosphate coating and the organic coating have been carried out separately. We view this as a preliminary step to the investigation of an organic coating/phosphate system.

The two phosphate systems selected, zinc phosphate and manganese phosphate, were characterized as stated earlier. Samples from one of the manufacturers gave additional Raman signatures at approximately 1350 cm^{-1} and 1600 cm^{-1} shift, for both manganese phosphate and zinc phosphate. These features were not characteristic of hureaulite, phosphophyllite or hopeite moieties. The two peaks were finally attributed to carbon. Figure 1 shows the Raman spectrum for A. zinc phosphated steel, B. the 1200 cm^{-1} - 1800 cm^{-1} region expanded for the sample, and C. activated carbon. Two sources of this carbon are proposed: (1) improper cleaning of the steel prior to phosphating, implying that the source of carbon was the rolling mill oil, or (2) improper rinsing after cleaning in which case the carbon may be due to residual surfactants of the cleaning solution. The effects of this carbon, whether deleterious or advantageous to the phosphate coating's corrosion resistance, will be studied in future research.

Thermal transformations for both phosphate systems have been studied. Phosphated samples were heated under argon for 1/2 hr at temperatures of 100°C, 200°C, 400°C and 600°C. The manganese phosphated steels show no change at 200°C (see Fig. 2); however, at 400°C the phosphate peak in the Raman spectrum broadened and shifted to higher wavenumbers. The sample heated at 600°C (see Fig. 2) resulted in the appearance of two peaks at 970 cm^{-1} and 1041 cm^{-1}. The peak at 970 cm^{-1} is characteristic of a phosphate structure known as wolfeite [$(FeMn)_2PO_4OH$]. The structure responsible for the peak at. 1041 cm^{-1} has yet to be identified. Preliminary data on the zinc phosphate coating indicate a similary type transformation which occurs at lower temperatures.

Under conditions of cathodic delamination, the delaminating front usually has a pH of 13 to 14. With this in mind zinc phosphated steel and

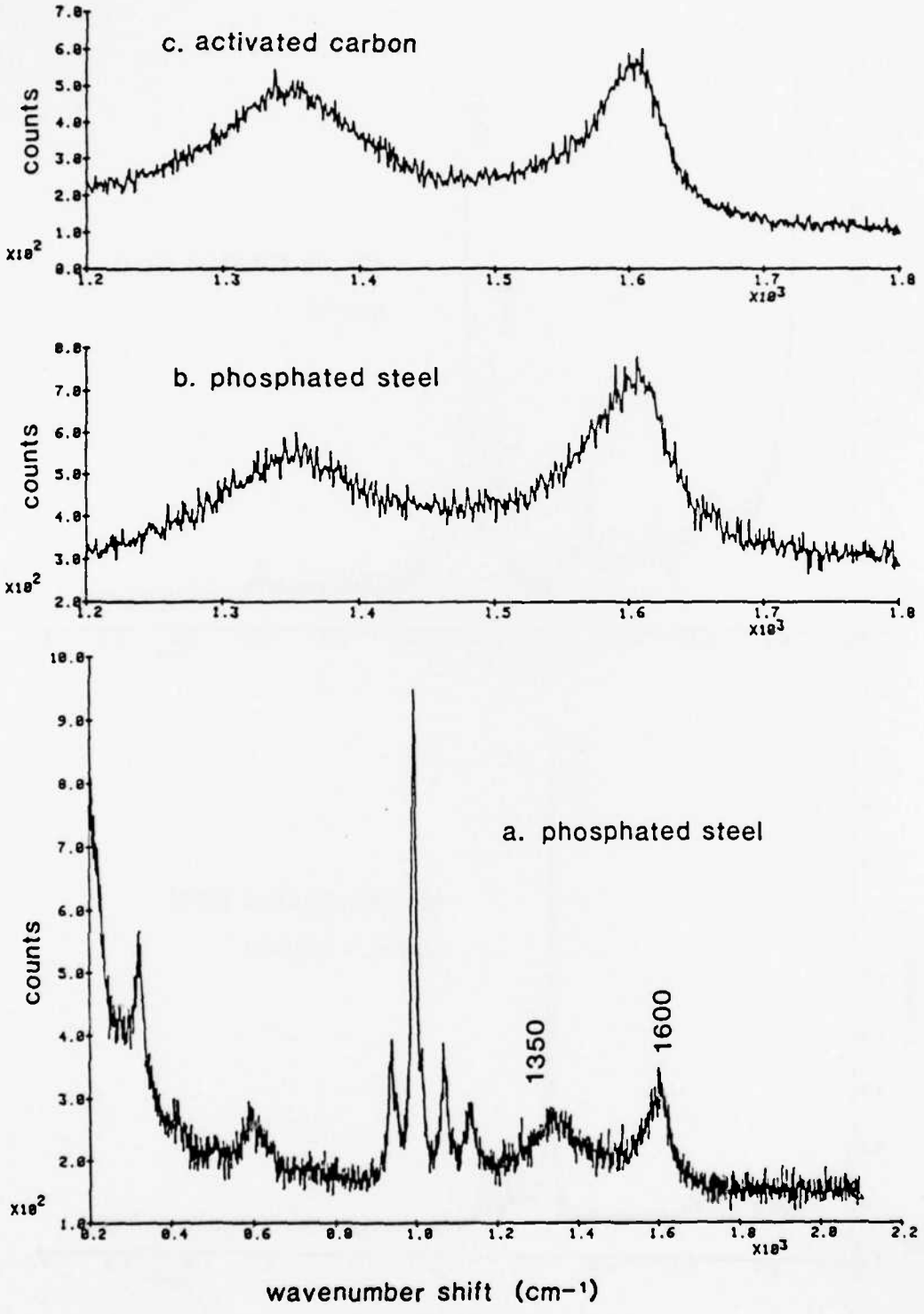
c. activated carbon
counts
X10²
X10³
b. phosphated steel
counts
X10²
X10³
a. phosphated steel
counts
X10²
X10³
1350
1600
wavenumber shift (cm⁻¹)

Figure 1.

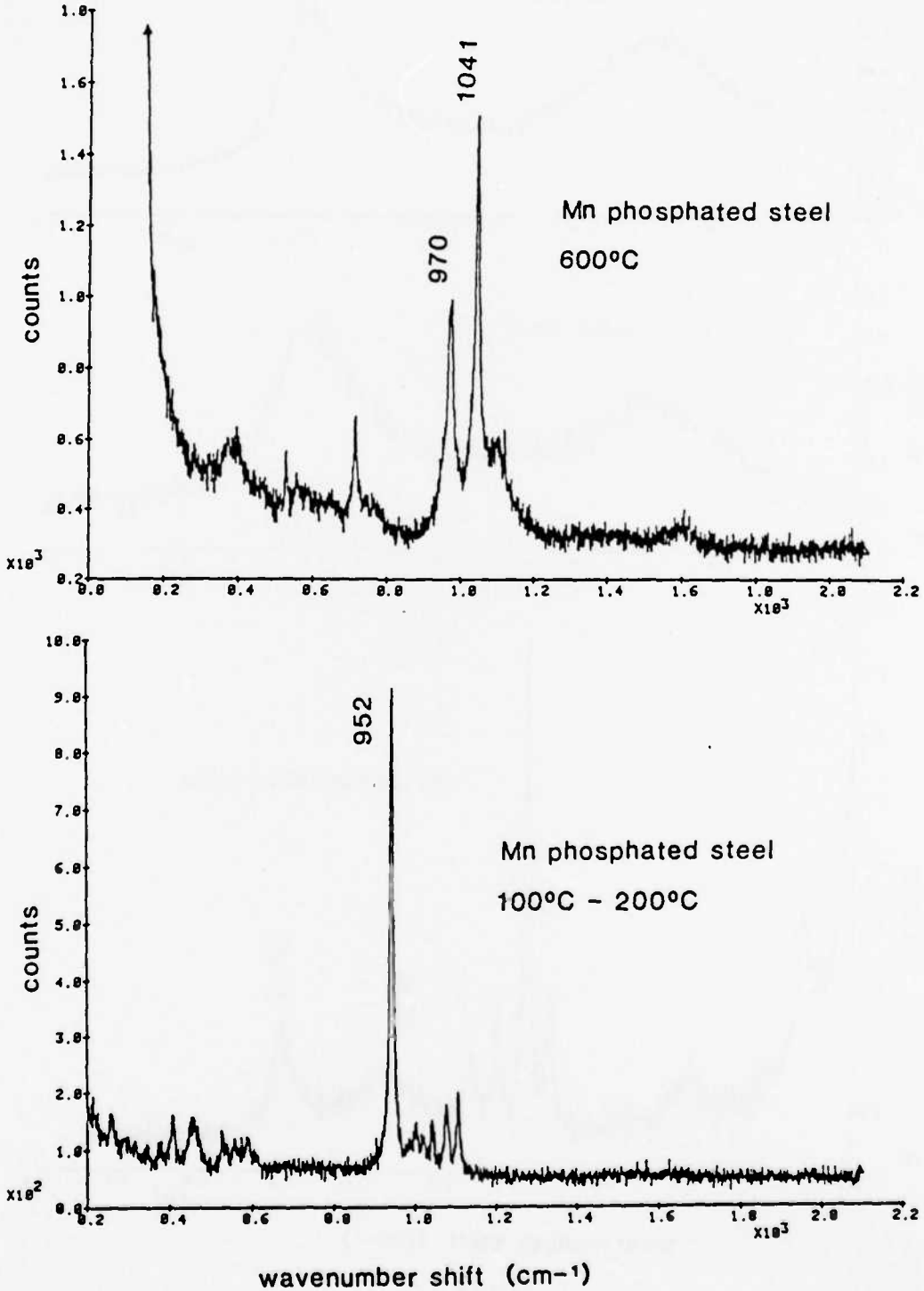
1041
970
Mn phosphated steel
600°C
counts
X10³
952
Mn phosphated steel
100°C - 200°C
counts
X10²
wavenumber shift (cm⁻¹)

Figure 2.

manganese phosphated steel were immersed in a 0.1M NaOH solution. Using the hydroxide ion as an internal standard, one can ratio the intensity of the Raman peak due to hydroxide ion against the intensity of the Raman peak due to the phosphate. Using this technique one can get a semi-quantitative measure of what happens to the phosphate coating. Figure 3 shows a typical experiment in which the manganese phosphate peak is monitored over a time frame of 3 hr. The intensities or the counts for the phosphate peak at 952 cm^{-1} and the hydroxyl peak at 3395 cm^{-1} are given in the figure. One striking feature of Figure 3 is that the intensity of the phosphate peak (952 cm^{-1}) degenerates over the course of three hr to a peak which is almost indistinguishable from the background. The hydroxyl peak intensity remains essentially the same due to the great concentration of hydroxide in the test cell setup. One can interpret the degeneration of the phosphate peak as being due to dissolution of the phosphate coating. This is supported by the fact that during the course of the experiment a brownish-black film appears on the remaining coating. This film was identified to be an oxide of manganese, a major building block of the phosphate coating.

The zinc phosphate coatings degenerate under the same conditions at a generally faster rate, with subsequent formation of a milky white film on the remaining coating. The film is believed to be some form of zinc oxide, also a building block of the coating for that particular phosphate.

Three organic coatings, polyester-melamine, Eponol, and Epon 1001, were applied on steel substrates using a spinner technique. The average thickness of each coating was 10 μm. The samples were immersed in 0.1M NaOH for one day. Upon examination, all the polymers had delaminated from the substrate. In each case no detectable difference was noted on comparing the Raman spectrum of the delaminated coating, except in the case of polyester-melamine. Figure 4 presents the Raman spectrum of the bound and delaminated polyester-melamine coatings. The Raman signature at 1000 cm^{-1} characteristic of the polymer backbone vibration is seen to be shifted approximately 5 cm^{-1} to higher frequency. This shift could be a result of added freedom in the polymer backbone. It should be noted that this research is in early stages and more work has to be done to confirm this shift.

In conclusion, three of the four objectives have been realized. The major thrust of future research will be concerned with the fourth objective, namely, to study the effects of aggressive environments on an organic coating/phosphate system in order to gain insight into the organic coating/phosphate interface and its relationship to corrosion science.

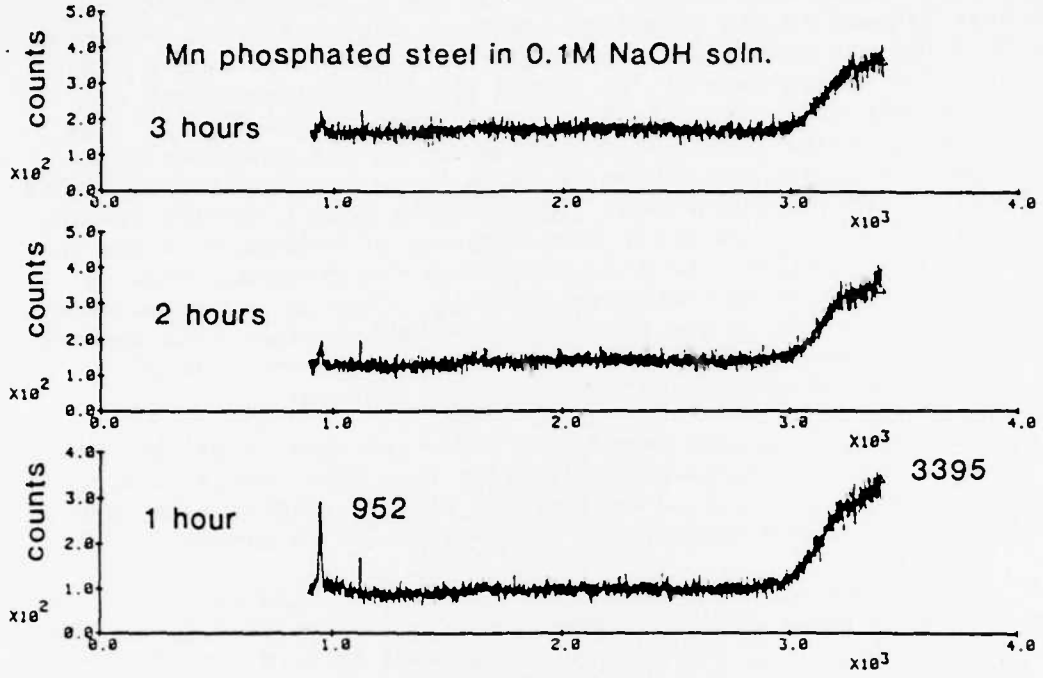

Figure 3.

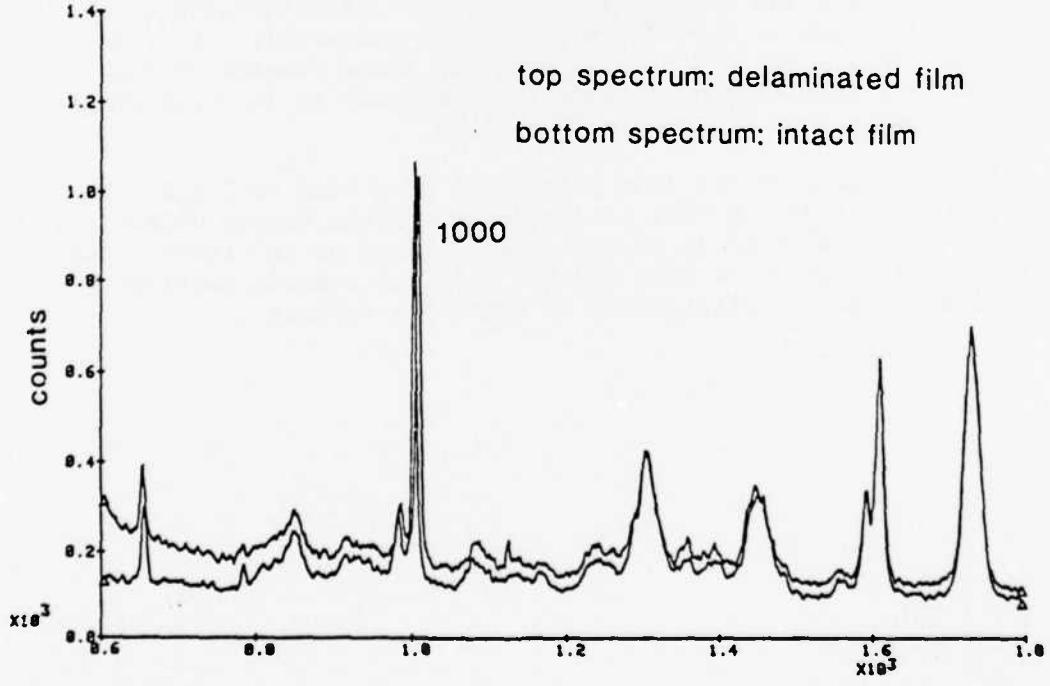

Figure 4.

Program #8

Studies of the Coating/Substrate Interface Using
Surface Enhanced Raman Spectroscopy

INTRODUCTION

SERS or Surface Enhanced Raman Scattering is a phenomenon of Raman spectroscopy whereby surface-adsorbed molecules or ions exhibit a 10 to 10^6-fold enhancement of their vibrational spectra due to their interaction or association with a metal surface. Since our research involves the study of the metal-coating interface and it has already been demonstrated that several organic coatings have fairly large Raman windows, application of this surface specific technique should be a logical extension. The first step was the demonstration of the SERS effect on our equipment and then the finding of a suitable probe molecule or ion with a strong Raman signal different from our available coatings that would exhibit frequency shifts in different aqueous environments.

EXPERIMENTAL RESULTS

The most well characterized system by SERS is the pyridine/silver system first studied by Fleischmann et al. [1] and later by Van Duyne et al. [2]. Since corrosion occurs in an oxygen atmosphere, cells were not purged with nitrogen after the initial experiments. With this adaptation and the Raman microprobe, the results of Van Duyne [2] were demonstrated. A rather strong signal was detected and all major and most minor peaks were found. It was noted that the peak at 1008 cm^{-1}, assigned to the pyridine ring breathing mode, varied with electrode potential and shifted to lower frequency as the applied potential became more cathodic. A pronounced "continuum" occurred from 400-1700 cm^{-1} and increased in intensity with increasing cathodic potential. Monitoring peak intensity as a function of potential, therefore, became meaningless unless a background correction could be made. Strong peaks at 621 and 1271 cm^{-1} appeared to increase in intensity with applied potential. In the low frequency region, one to two broad bands are observed from 200 to 260 cm^{-1} in KCl supporting electrolyte. It is disputed that these peaks are not attributed to the Ag-N stretch but rather due to Ag-Cl. In our work the size of the peak was dependent on chloride concentration; however, beyond a potential of -.5 to -.6 V (vs. Ag/AgCl) these "peaks" disappeared and another peak reappeared at potentials of -.7 V and beyond. Recent work by Fleischmann et al. [3] indicates that these "peaks" are a composite of both Ag-N and Ag-Cl stretching and their results along with ours seem to reinforce the thought that a desorption of Cl^- occurs as the potential of zero charge (PZC) is approached and at potentials more negative than this pyridine

nitrogen is the adsorbed species. Peaks also tend to increase in intensity with time, a phenomenon that might be attributed to the development of a much steeper concentration gradient since no stirring was used as this movement might affect the electrode and cell optics. A sharp peak of weak intensity is found at 1650 cm^{-1}, a region where adsorbed water is known to exhibit a stretching frequency. The peak might be expected to grow in intensity as supporting electrolyte concentration (anion specific adsorption) increases [3].

Major new work using SERS involved observation of the SERS spectrum for pyridine on nickel. While the peaks observed are not as intense as those found for silver, they do exhibit some of the same features. The major peak the ring breathing mode, appears at 1003 cm^{-1}: however, the frequency shifts with potential are less dramatic. The intensity of the 1270 cm^{-1} peak increases sharply with potential while the 1040 cm^{-1} peak disintegrates much more rapidly than in silver. The Ni-X (Ni-Cl or Ni-Cl/Ni-N) band is present at low frequency; however, it is much weaker when compared to silver. The broad continuum present in silver also is present in the nickel-pyridine spectrum and is also a function of applied potential. Previous work [4] had indicated a SERS effect could be observed on both Ni and NiO surfaces; however, the potential dependence had not been demonstrated. Nickel electrodes were masked, as were other electrodes previously used, and a potential varying from -1.350 V (vs. SCE) to +0.65 V, cycled continuously, was applied for periods of 10-20 min using a nickel counter electrode and 1M KCl supporting electrolyte and saturated $NiCl_2$. Treated electrodes were green in color but metallic after rinsing with ethanol and then distilled water. Electrodes were fashioned from both 99.99% Ni wire and Ni-2000 foil (99% Ni, Fe and C impurities). Treated electrodes showed slightly stronger signals than untreated ones. One phenomena more apparent on Ni than Ag is that upon use (exposure to the laser beam) signals got stronger either due to the radiation or due to oxide formation on aging. Current work entails defining the electrode preparation procedure so that production of the SERS signal on Ni is reproducible.

Prior to starting work on nickel electrodes, copper electrodes were prepared and the Cu/pyridine system was examined. A very weak SERS spectrum was obtained, but laser excitation was at 514 nm and previous work has shown the most intense signal appears with 647 nm excitation. It is uncertain what effect this change in excitation source might have on the spectra observed using nickel. Again because of the excitation source no discernable signal could be detected in the Cu/benzotriazole system; however, two broad peaks at 1370 and 1590 cm^{-1} were observed with the Cu/8-hydroxyquinoline system. It was concluded that, without a krypton laser source for the MOLE Raman Microprobe, examination of copper-coating interfaces would produce at best marginal results.

While dry specimens of Ni-2000 electrochemically treated in NaCN and 8-hydroxyquinoline exhibited no detectable Raman spectra, the silver/NaCN system looked promising for further study. Silver treated in basic cyanide solutions is reported to exhibit different SERS signals indicative of a surface composition which is a function of cation type and electrode washing [5]. Difficulty has been experienced in producing a Ag/pyridine signal under an acrylic coating. An aqueous environment under the coating might be demonstrated by the presence of only one peak at 2143 cm^{-1} due to a rather homogeneous chemi-adsorbed CN^-, whereas the dry environment would be indicated

by two peaks (if from KCN) at 2108 and 2148 cm^{-1} ($K[Ag(CN)_2]$, solid – 2148, 2145.5 and 2147 cm^{-1}) or (if from NaCN) 2117 and 2155 cm^{-1} ($Na[Ag(CN)_2]$, solid – 2155 cm^{-1}). Unfortunately, prepared samples first seemed to produce a composite spectrum with little indication of two peaks on unrinsed samples causing us to consider abandoning the attempt; however, isolated samples of Ag treated in 0.57M NaCN have shown two scattering peaks. Rinsed samples exhibit very weak signals and thus far it has been difficult to produce consistently the treated, unrinsed sample, but the Ag/CN^- system still appears the most promising system.

REFERENCES

[1] M. Fleischmann, P. J. Hendra, and A. J. McQuillan, Chem. Phys. Lett. 26, 163 (1974).

[2] R. P. Van Duyne, in "Chemical and Biochemical Applications of Lasers, Vol. 4," C. B. Moore, Editor, Academic Press, New York, 1979, pp.101-85.

[3] M. Fleischmann, J. Robinson, and R. Waser, J. Electroanal. Chem. 117, 257 (1981).

[4] H. Yamada, Y. Yamamoto, and N. Tani, Chem. Phys. Lett. 86, 397 (1982).

[5] G. Lauffer, J. T. Huneke, and T. F. Schaaf, Chem. Phys. Lett. 82, 571 (1981).

Program #9

Acid/Base Properties of Hydrated Oxides on Iron and Titanium Surfaces

INTRODUCTION

Metals exposed to ambient atmosphere are readily oxidized and in the presence of moisture the outer surface of the metal oxide is hydrated [1-3]. In the absence of surface contamination, the interaction between a metal and a polymer is on this hydrated oxide surface. Bolger and Michaels [4] have proposed that polymer coatings bond to metal surfaces via hydrogen bonding of polar groups in the polymer with the hydroxyls present on the hydrated metal oxide surface. Fowkes [5,6] has shown that the strength of adhesive bonds between a polymer and a filler (an oxide such as silica) can be correlated with the relative acidic or basic strength of the polymer, filler, and solvent. If the bonding of polymer coatings to metal surfaces is indeed by hydrogen bonding, it should be possible to predict not only the relative strengths of the bonding between different coatings and metal surfaces but also the stability of the coating in the presence of water at different values of pH.

The surface hydroxyl (-MOH) interaction with an organic acid (HXR) and an organic base (XR) can be depicted as follows:

$$\text{ORGANIC ACID} \quad -\text{MOH} + \text{HXR} \longrightarrow -\text{MO}\overset{\text{H}}{\cdots}\text{HXR} \longrightarrow -\text{MO}\overset{+}{\text{H}}_2\overset{-}{\text{X}}\text{R} \qquad (1)$$

$$\text{ORGANIC BASE} \quad -\text{MOH} + \text{XR} \longrightarrow -\text{MOH}\cdots\text{XR} \longrightarrow -\text{MO}\overset{-+}{\text{H}}\text{XR} \qquad (2)$$

In these reactions, X is an oxygen, sulfur or nitrogen atom. The bond energy increases as the equilibrium shifts to the right and the bond becomes more ionic. Maximum strength of the bond between an organic coating and metal surface would then be obtained when the surface hydroxyl acts as a strong base and the polar group as a strong acid or when the surface hydroxyl acts as a strong acid and the polar group as a strong base.

Water can displace or interrupt hydrogen bonds according to the following interactions:

$$-\text{MO}\overset{\text{H}}{\cdots}\text{HXR} + 2\text{H}_2\text{O} \longrightarrow -\text{MO}\overset{\text{H}}{\cdots}\text{HOH} + \text{H}_2\text{O}\cdots\text{HXR} \qquad (3)$$

$$-\text{MOH}\cdots\text{XR} + 2\text{H}_2\text{O} \longrightarrow -\text{MOH}\cdots\text{OH}_2 + \text{HOH}\cdots\text{XR} \qquad (4)$$

Poor adhesion of a polymer to a metal surface would be expected if the water, acting either as a base or as an acid, forms a stronger hydrogen bond with the surface hydroxyl or with the polar groups in the polymer than the hydrogen bond between the polar group and the surface hydroxyl.

The pH of water at the interface is also expected to interfere with the hydrogen bonding between the polar group in the polymer and the surface hydroxyl.

$$MOH + \overset{+}{H}XR \xleftarrow{H^+} MO\cdot\cdot H\cdot\cdot XR \xrightarrow{OH^-} MO^- + HOH + XR \qquad (5)$$

$$MOH_2^+ + HXR \xleftarrow{H^+} M\text{-}\overset{H}{O}\cdot\cdot H\cdot\cdot XR \xrightarrow{OH^-} MOH + HOH + \bar{X}R \qquad (6)$$

The range of pH over which the coating would be expected to be stable is a function of the effective pK_a of the surface hydroxyls and the pK_a of the polar groups in the polymer.

The acid/base properties of polar groups that are typically present in polymer coatings are relatively well known. Acid/base properties of metal oxides have also been studied extensively for oxides in the form of high surface area powders. Less well known, however, is the nature of the hydrated oxide surface on flat metal surfaces that are usually coated for corrosion protection. The principal objective of our part of the ONR research program is to characterize the hydrated oxide surfaces present on metals, to determine the presence and number of hydroxyls and to determine the acid/base strengths of these hydroxyls. Based on the results of this study it may be possible to predict the relative stabilities of different coatings on different metal surfaces in the presence of water as a function of pH.

EXPERIMENTAL

Details of the technical approach and the development of experimental procedures have been presented in earlier reports. Thus, only the salient features of these experimental methods will be described. Auger electron spectroscopy (AES) and X-ray photoelectron spectroscopy (XPS) were used to characterize the elemental composition and chemical composition of metal surfaces which have been oxidized in a controlled environment to promote growth of a hydrated oxide and at the same time to minimize surface contamination. Titanium and iron surfaces have received the most extensive study. These two metals were chosen for study not only because of their practical importance, but also because their acid/base properties were expected to be different owing to differences in charge/radius ratio of the Ti^{+4} and Fe^{+3} ions present in the respective oxides [7].

The presence and concentration of surface hydroxyls were determined directly by X-ray photoelectron spectroscopy. The acid/base properties of these hydroxyls were then determined by following the adsorption or exchange of K^+ on the titanium and iron surfaces as a function of pH. The following

considerations of surface/solution equilibria are the basis on which the acid/base properties of hydrated oxide surfaces were determined.

The hydrated metal oxide on iron for example, when exposed to aqueous solutions, would be expected to behave as a function of pH in the following manner:

$$\text{Low pH} \qquad -FeOH + H^+ \rightleftharpoons -FeOH_2^+ \tag{7}$$

$$\text{High pH} \qquad -FeOH + OH^- \rightleftharpoons -FeO^- + H_2O \tag{8}$$

$$\text{or} \qquad -FeOH \rightleftharpoons -FeO^- + H^+$$

These equilibria have been established for metal oxide powders from measurements of electrophoretic mobility as a function of pH. The pH at which oxide particles do not move in either direction in an applied field is known as the isoelectric point and is a measure of surface acid/base properties. Although electrophoretic mobility measurements are not applicable for low surface area metal surfaces, the equilibria given above can be used to determine the acid/base character of the hydrated oxide on metal surfaces by following the adsorption of anions on the $-FeOH_2^+$ surface at low values of pH and adsorption of cations on the $-FeO^-$ surface at high values of pH. The following example is considered for cation exchange with the hydrogen of the surface hydroxyl on hydrated iron oxide as a function of pH. Similar arguments apply for the adsorption of anions.

$$-FeOH \xrightarrow{K_{a2}} -FeO^- + H^+ \qquad K_{a2} = \frac{[-FeO^-][H^+]}{[-Fe^-OH]} \tag{9}$$

$$-FeO^- + M^+ \xrightarrow{K} -FeO^-M^+ \qquad K = \frac{[-FeO^-M^+]}{[-FeO^-][M^+]} \tag{10}$$

At any value of pH the sum of the surface hydroxyls, ionized hydroxyls and hydroxyls for which the hydrogen has been exchanged with M^+ is a constant representative of the total number of hydroxyls originally present on the surface N_o (units of sites/m^2).

$$[-FeOH] + [-FeO^-] + [-FeO^-M^+] = N_o \text{ (sites/m}^2\text{)} \tag{11}$$

It is assumed that equilibrium is reached during the 300 sec immersion period. It is further assumed that all ionized sites at a given pH will react with the cation since the solution concentration of cations is in large excess of the total number of surface hydroxyls.

$$N_o = [-FeOH] + [-FeO^-M^+] \tag{12}$$

$$K_{a2} = \frac{[-FeO^-][H^+]}{[-FeOH]} = \frac{[-FeO^-M^+][H^+]}{[-FeOH]} \qquad (13)$$

For convenience, the fraction, θ , of the total available hydroxyls which have undergone exchange, i.e., coverage, is defined by the following:

$$\theta = \frac{[-FeO^-M^+]}{N_o} \quad .$$

Using this definition of the fraction of exchange, θ , in Equation (12) and, substituting the result into Equation (13), gives the following result.

$$pH = pK_a - \log \frac{\theta}{1-\theta} \qquad (14)$$

In this equation, $pH = -\log[H^+]$ and $pK_a = -\log K_a$. The pK_a of the hydroxyls can thus be obtained by plotting, θ , as a function of pH. The pH at which this fraction equals 0.5 (i.e., $\theta = 0.5$) is the pK_{a2} of -FeOH. Similar experiments using anions would give the pK_{a1} of $FeOH_2^+$ for the equilibrium shown in Equation (7). In our studies of the surfaces of iron and titanium, we have used AES and XPS to measure the coverage, θ , of K^+ after exposure of these metals to solutions containing K^+ at different values of pH.

EXPERIMENTAL RESULTS

Typical XPS spectra taken of specimens after preparation of the hydrated oxide surfaces, after immersion in distilled water and after immersion in potassium containing solutions at pH are shown in Figures 1 and 2 for iron and titanium, respectively. These spectra show the expected oxygen and oxidized metal peaks and, for the specimens that were immersed in the potassium solution, the expected potassium peaks. In addition, carbon and sodium were found. Comparison of the spectra shows that the carbon peak intensity was lowest on the as-prepared specimens and that the intensity increased slightly after immersion in distilled water and in the potassium containing solutions. Sodium, on the other hand, was present on the as-prepared specimens, and the amount of sodium remained essentially constant after further treatments.

A high resolution carbon (1s) spectrum is shown in Figure 3 which has been resolved into three components. The most intense peak at 284.6 eV is attributed to carbon in $-CH_2-CH_2-CH_2-$ and the peaks at 285.9 eV and 288.2 eV are oxidized carbon. The carbon (1s) binding energies of different oxygenated carbon that may be present in the organic contamination are shown in Table I. Although unequivocal identification of the specific organic compound(s) that is present on these specimens is not possible, the carbon spectrum does indicate that the organic compound(s) contains polar group(s). The polar group(s) can account for the propensity for the adsorption of organic contamination observed on the hydrated oxides of the iron and titanium

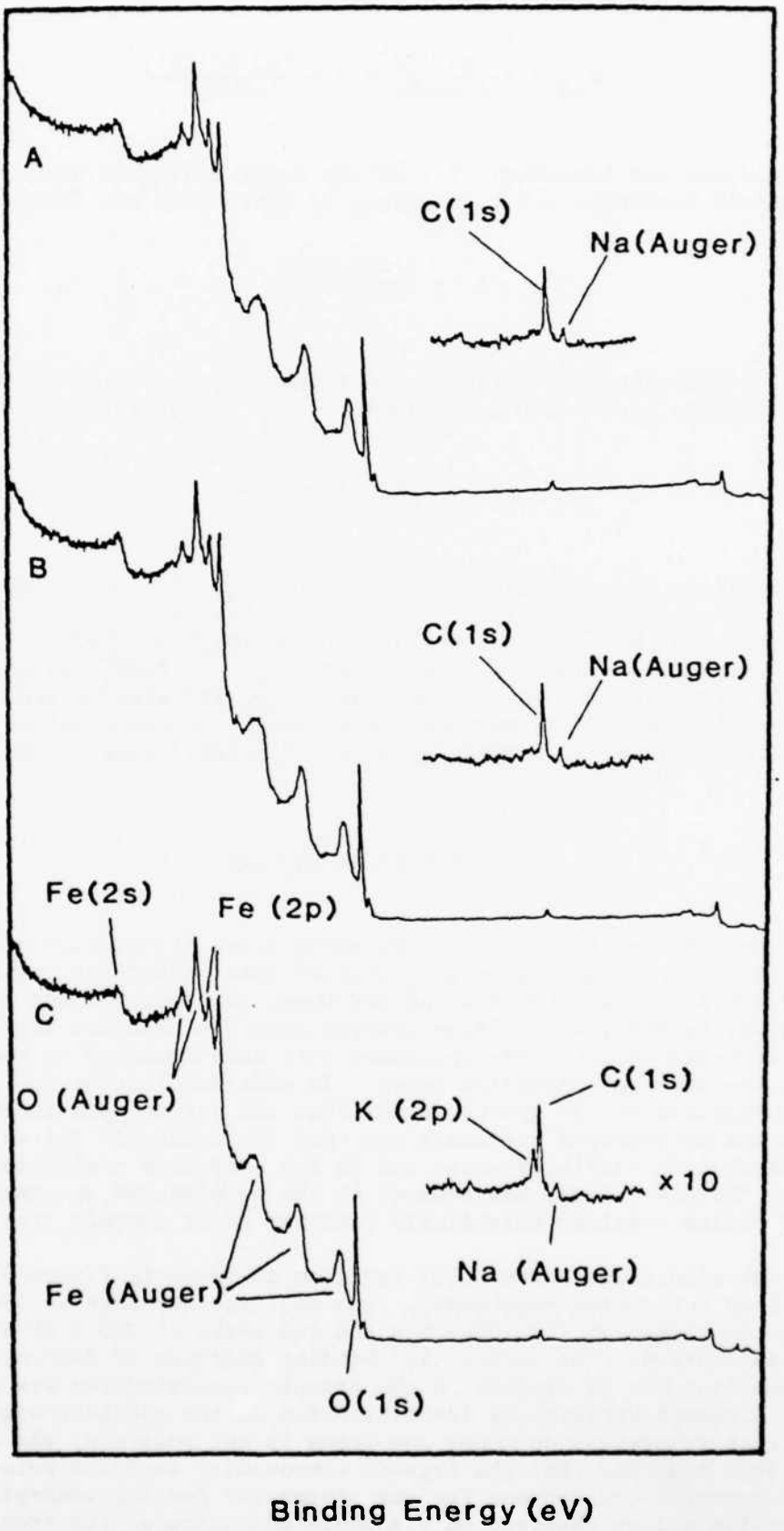

Figure 1. XPS survey scans of iron specimens: (A) after preparation; (B) immersion in distilled water; (C) after potassium exchange.

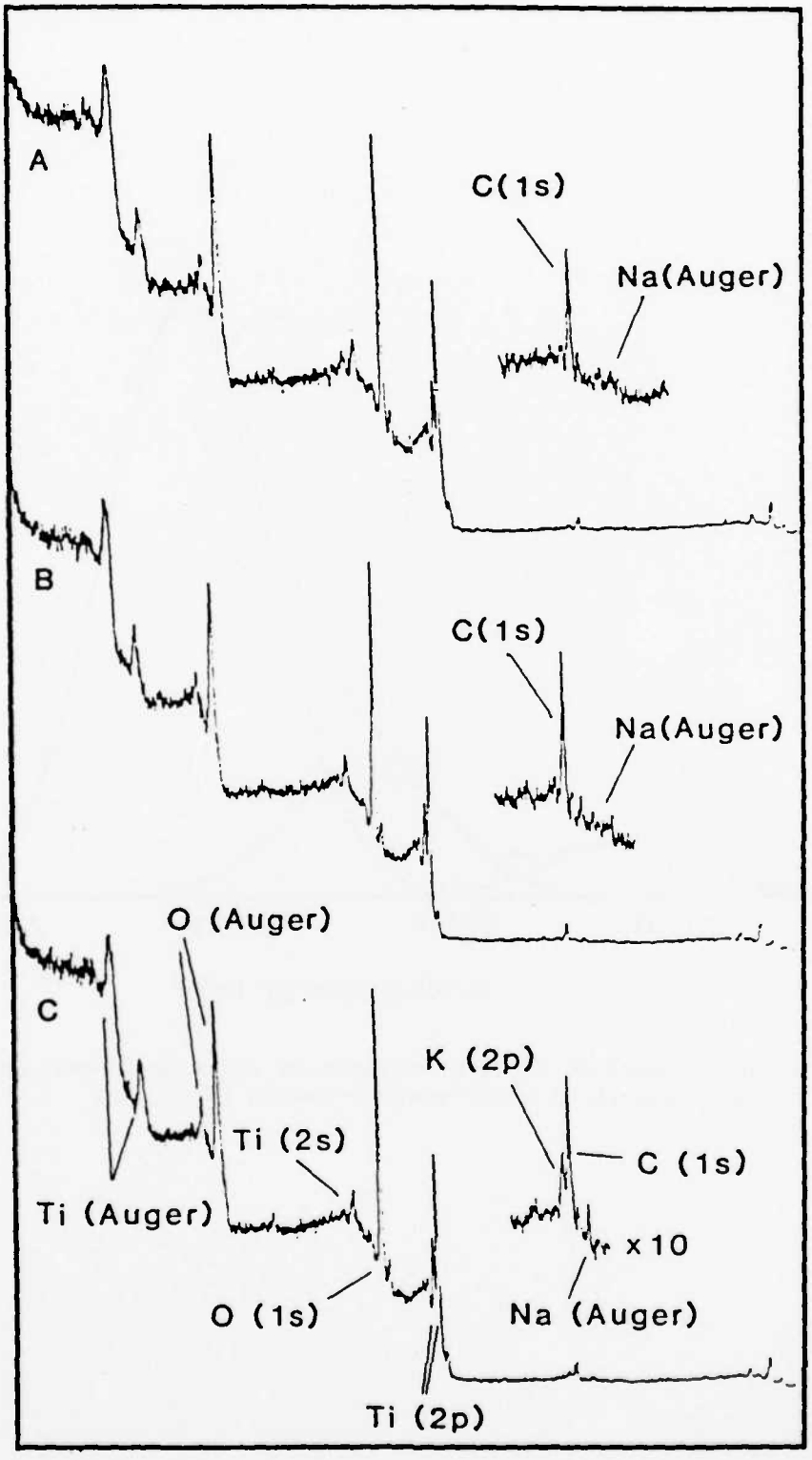

Figure 2. XPS survey scans of titanium specimens: (A) after preparation; (B) immersion in distilled water; (C) after potassium exchange.

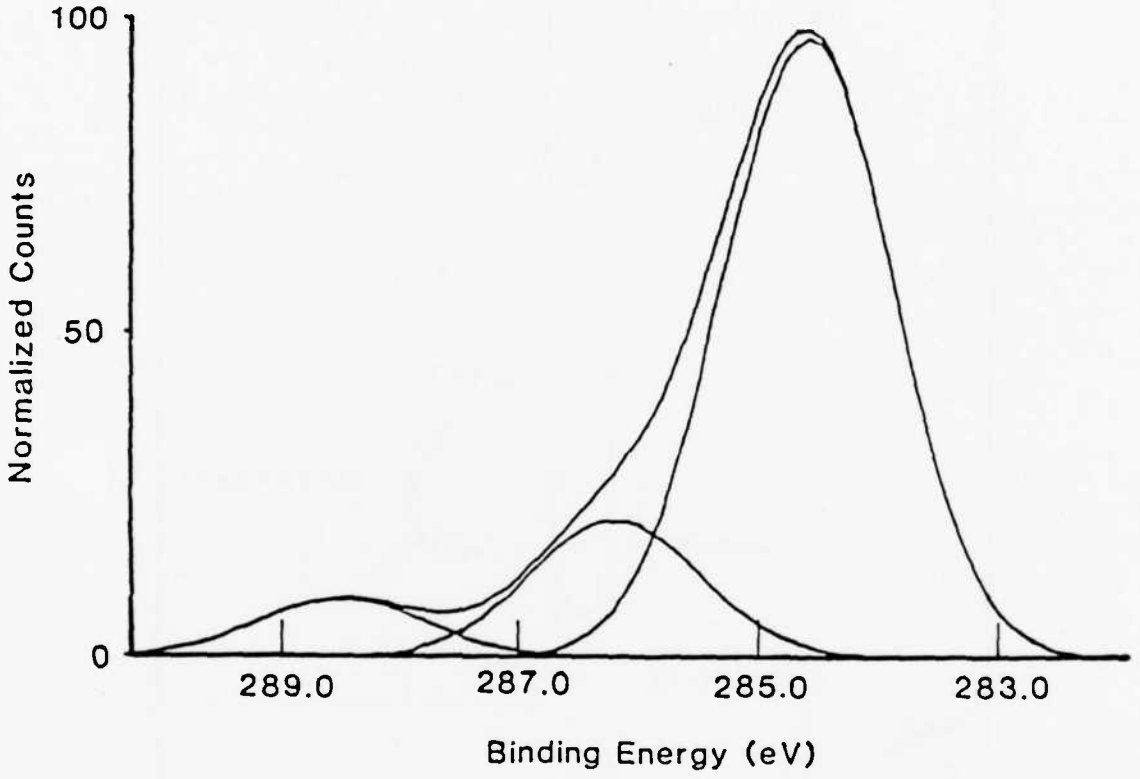

Figure 3. Curve resolved C(1s) photoelectron spectrum illustrating the presence of three surface carbon forms.

Table I

Comparison of C(1s) Binding Energies of Carbon Contamination on Iron and Titanium Specimens with C(1s) Binding Energies of Different Organic Functional Groups [10]

Experimental Binding Energy (eV)	Functional Group	Reported Binding Energy, eV
284.6	$-CH_2-$	284.6
286.1	$-CH_2OH$	286.2
	$-CH_2-O-CH_2-$	286.1
	$-\overset{O}{\overset{\|}{C}}-O-\overset{*}{C}H-$	286.2
288.6	$>C=O$	287.5
	$-\overset{O}{\overset{\|}{C}}-O-CH-$ (*)	288.8
	$-\overset{O}{\overset{\|}{C}}-OH$	288.7

*Binding energies referenced to ($-CH_2-$) carbon (1s), 284.6 eV.

specimens after exposure to the atmosphere and to the solutions used in this study. Oxidation of the "organics" present in the distilled water used to prepare the potassium solutions by ultraviolet radiation was found to reduce the amount of organic contamination orginating from the solutions. Indeed, only small increases in the carbon peak intensity were observed after specimens were immersed either in the distilled water or in solutions containing potassium.

Figures 4 and 5 show high resolution oxygen (1s) spectra for iron and titanium specimens, respectively. These spectra show at least three resolved peaks at 529.9 eV, 531.5 eV and 532.8 eV. The most intense peak at 529.9 eV is attributed to the oxygen in the respective metal oxide, the lower intensity peak at 531.5 eV is believed to be the oxygen in a surface hydroxyl, and the relatively small peak at 532.8 eV can be attributed to adsorbed molecular water and/or to the oxygen present in the organic contamination. These assignments for the oxygen (1s) components observed for the iron specimen are in agreement with those reported for studies of the oxidation of iron in water vapor [1,8, 9] cf. Table II. It is assumed that a similar assignment can be made for the oxygen (1s) components found on the titanium specimen. The intensities of the hydroxyl and molecular water peaks were found to increase relative to the oxide peak as the angle between the analyzer and the surface normal was increased. This result is direct evidence that the hydroxyls and molecular water are present on the outermost part of the specimen surfaces. The integrated hydroxyl peak intensity was quantified by a method proposed by Dreiling [13]. On this basis the hydroxyl surface concentration was found to be 4.5 hydroxyls/nm^2 for iron specimens and 6.1 hydroxyls/nm^2 for titanium specimens. These values are comparable to those found on iron oxide powders of 5.6 hydroxyls/nm^2 [14] and on titanium oxide powder of 7-14 hydroxyls/nm^2 [15].

Since it was shown earlier that the organic compound(s) present on the specimens contains oxygen, the possible overlap of the spectrum of this oxygen with that of the hydroxyl and/or molecular water spectra was considered. The binding energies of oxygen (1s) in several organic functional groups are summarized in Table II. If it is assumed that the interaction between the surface and the organic compound(s) does not significantly influence the binding energy of oxygen (1s), it is apparent that the oxygen (1s) peak from the organic contamination does not overlap the oxygen (1s) peak from the hydroxyl. The binding energies of the oxygen (1s) peak of functional groups in organic compounds, however, are similar to the oxygen (1s) binding energy in molecular water.

A high resolution XPS spectrum of the potassium ($2P_{3/2}$, $2P_{1/2}$), carbon (1s) and sodium (KL L_{23}) Auger peaks from a titanium specimen after immersion in potassium solution at pH 11.0 is shown in Figure 6. The integrated areas of the potassium peaks shown in this spectrum and the integrated area of the hydroxyl component of the oxygen spectrum were used in the determination of the fraction of the hydroxyls that have undergone exchange with potassium as a function of pH. The integrated peak areas were put on the same basis by using the appropriate sensitivity factors. Figure 7 summarizes the results obtained for iron and Figure 8 the results from titanium. In these figures, the fraction of hydroxyls that have undergone exchange, θ , at different values of solution pH is defined by the ratio, θ = (K peak area/OH peak area).

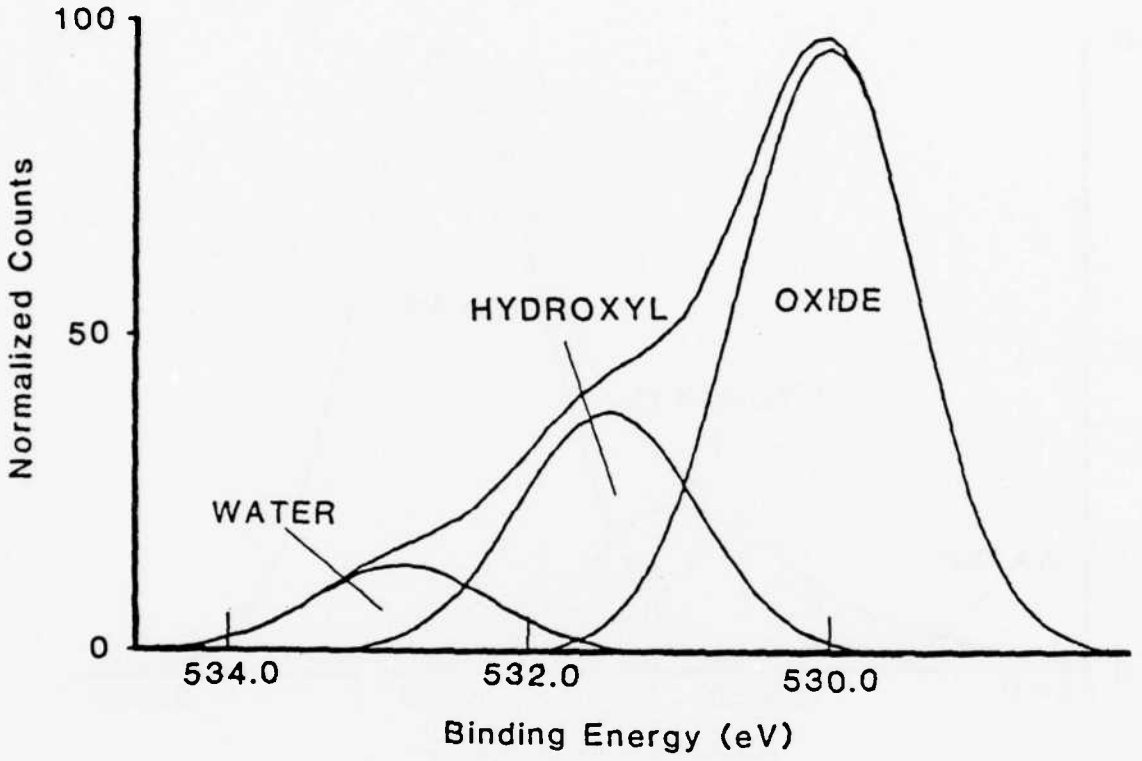

Figure 4. Curve resolved O(1s) photoelectron spectrum showing the oxide, hydroxyl. and adsorbed water peaks on an iron specimen.

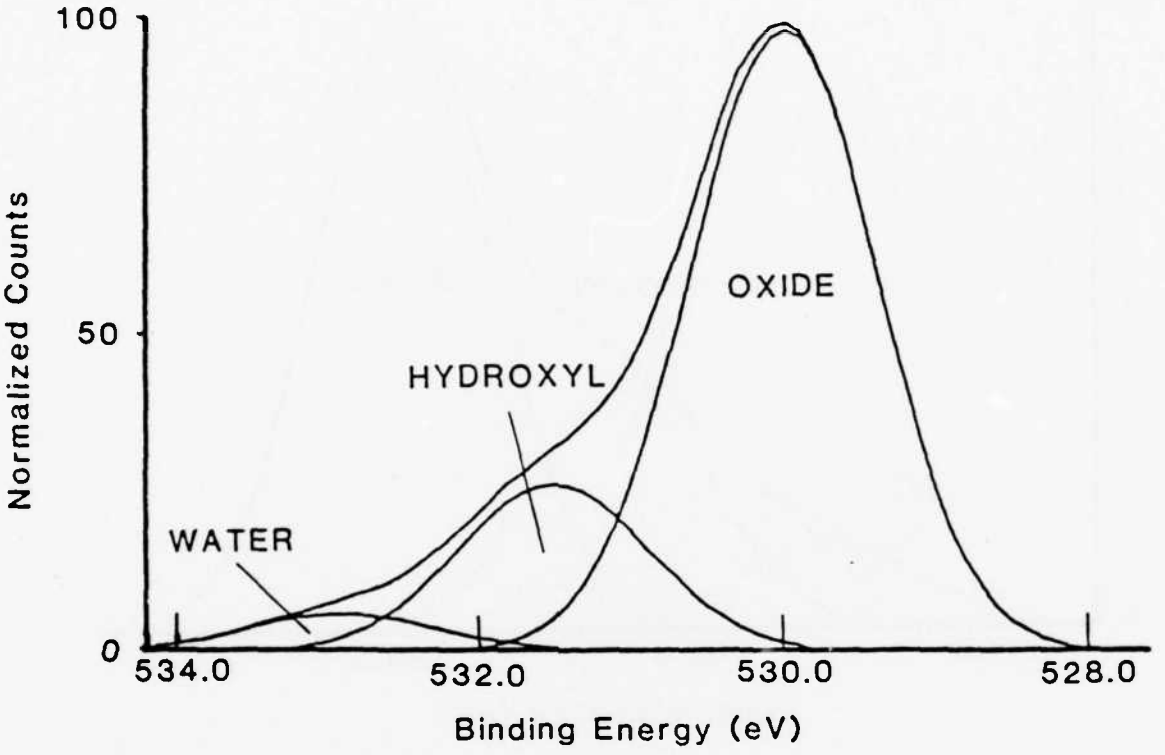

Figure 5. Curve resolved O(1s) photoelectron spectrum showing the oxide, hydroxyl, and adsorbed water peaks on a titanium specimen.

Table II

Comparison of Energies of Binding O(1s) Obtained from Iron and Titanium Surfaces with ((1s) Binding Energies of Oxygen in Oxide, Hydroxide, and Organic Fundtional Groups

Experimental O(1s) Binding Energy (eV)		Reported Binding Energy (eV)		Reference
Iron Surfaces	529.9	Fe_2O_3	530.0	11
	531.5	-Fe-OH	531.4	11
	532.8	H_2O	532.0 - 534.0	1,8,11
		$-\overset{O^*}{\overset{\|\|}{C}}-O-CH-$ †	532.6*	10
			534.0†	
		$-\overset{O^*}{\overset{\|\|}{C}}-OH$ †	533.0*	10
			533.9†	
		$-CH_2-O-CH_2-$	533.2	10
		$>C=O$	533.2	10
		$-CH_2OH$	533.2	10
Titanium	529.7	TiO_2	530.2	12
	531.5			
	532.3	H_2O	532.0 - 534.0	8

*Binding energies referenced to ($-CH_2-$) carbon (1s), 284.6 eV.

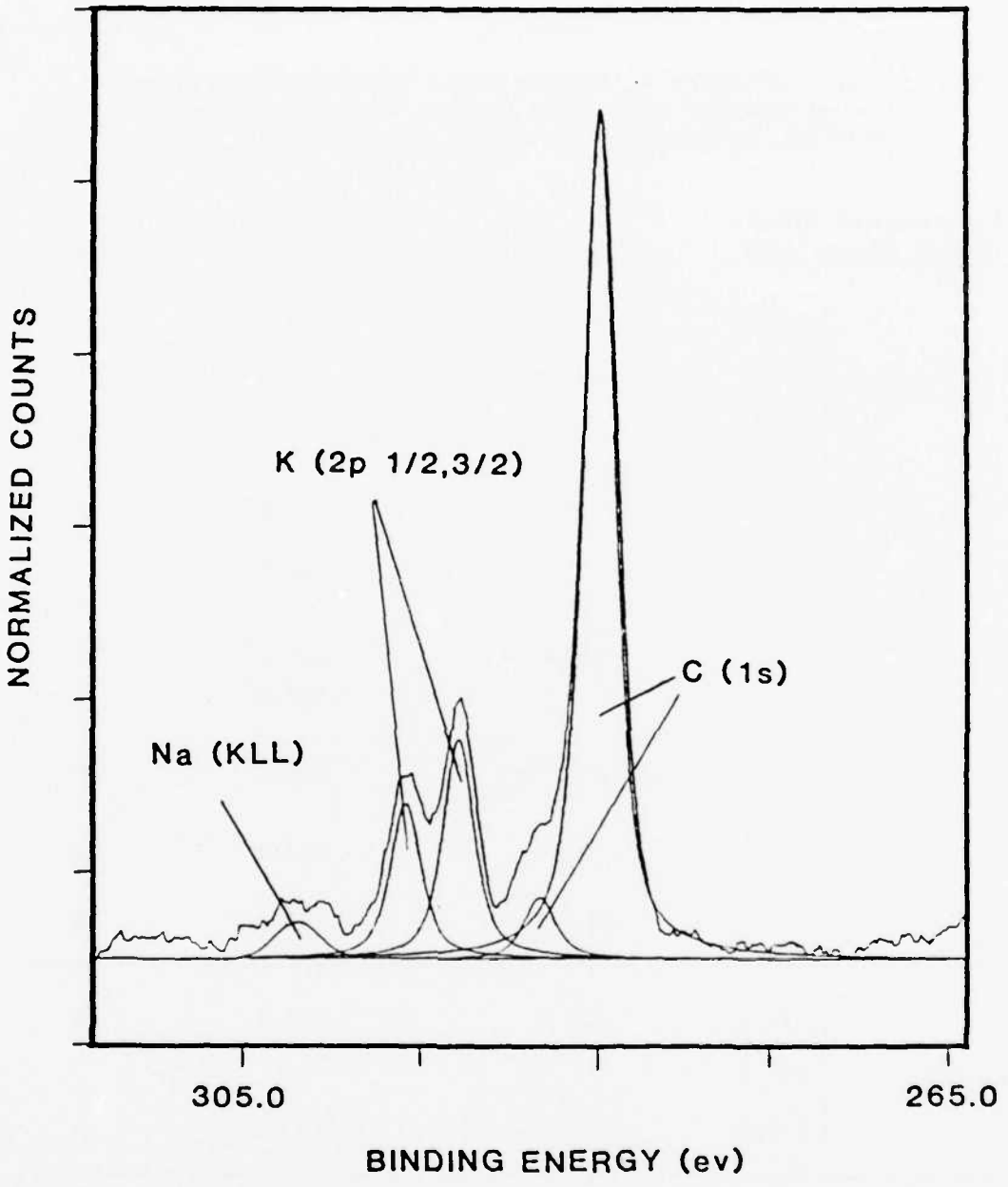

Figure 6. Curve resolved photoelectron spectrum of potassium on an iron surface following exposure to a potassium-containing solution. Sodium and two forms of carbon are also observed.

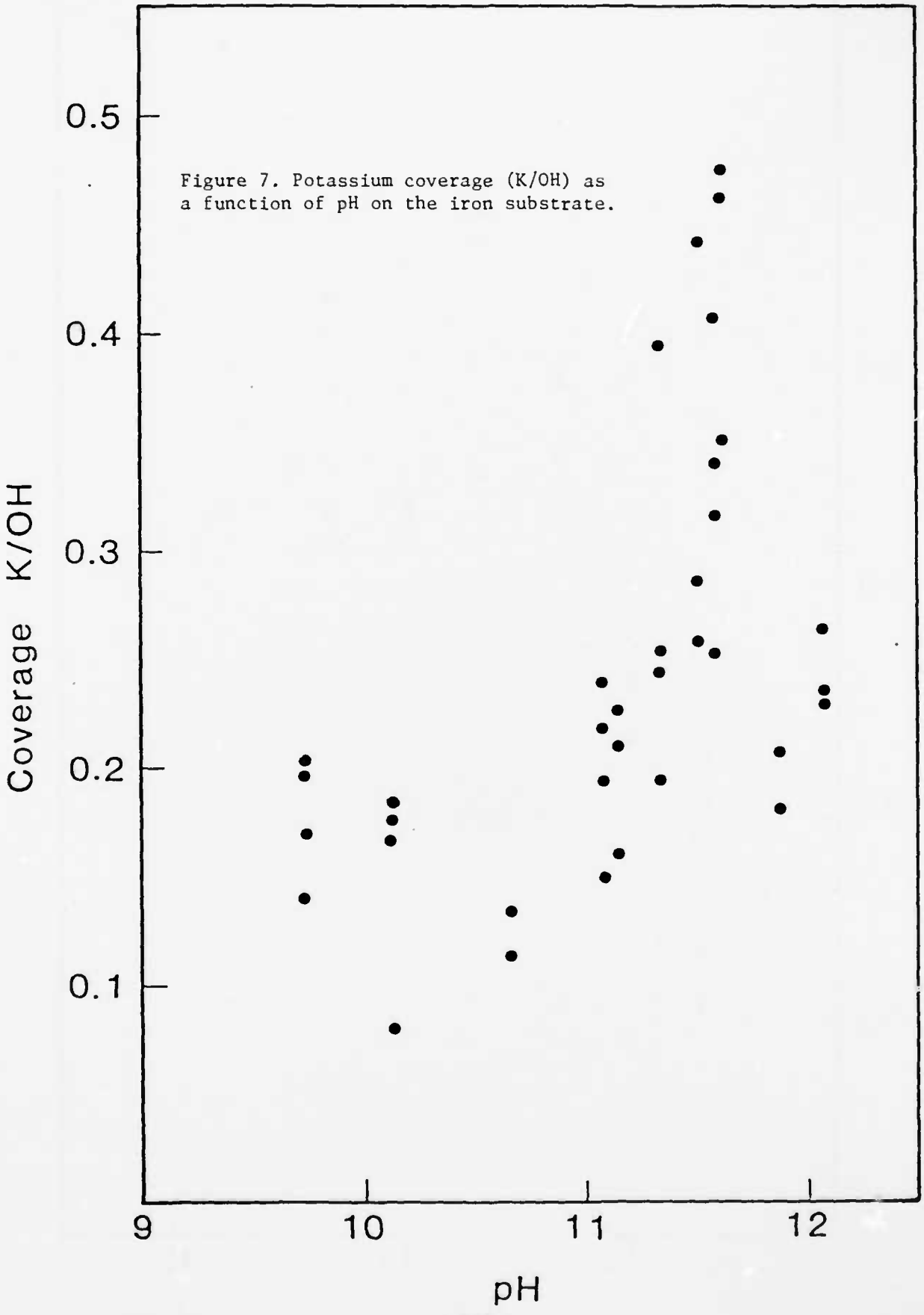

Figure 7. Potassium coverage (K/OH) as a function of pH on the iron substrate.

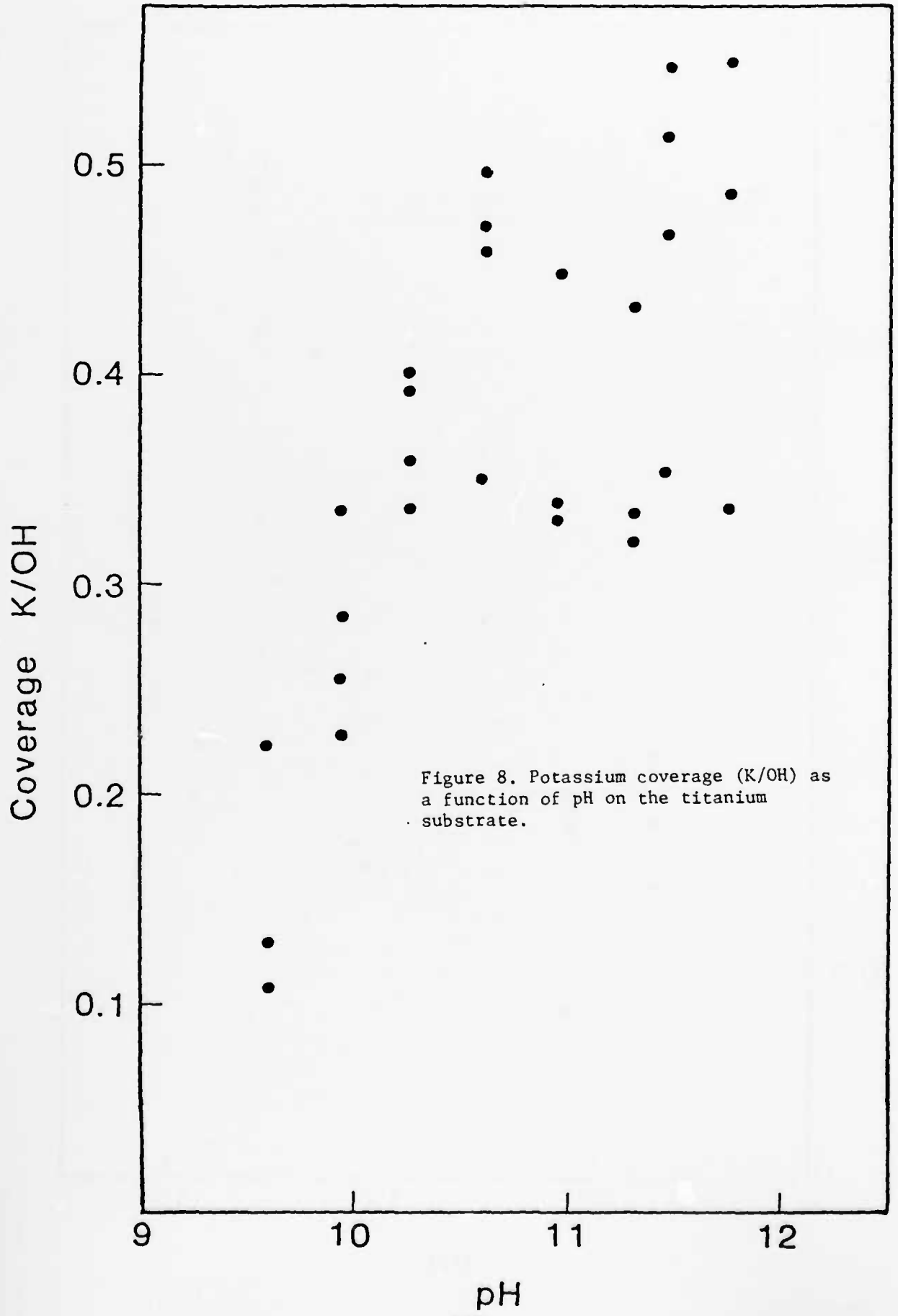

Figure 8. Potassium coverage (K/OH) as a function of pH on the titanium substrate.

Table III

Estimates of the Relative Bond Strengths between Organic Polar Groups and Hydrated Iron Oxide Surfaces. The Bond Strength Increases with Decreasing Δ.

Organic	pK_a	Iron Surface $pK_{a1} = 8.5$	Iron Surface $pK_{a2} = 11.2$
		$\Delta_B = pK_a - pK_{a1}$	$\Delta_A = pK_{a2} - pK_a$
Ethylamine	11.0	2.5	0.2
Triethylamine	10.8	2.3	0.4
Phenol	9.9	1.4	1.3
Benzylamine	9.3	0.8	1.9
Pyridine	5.7	-2.8	5.5
Acetic Acid	4.8	-3.7	6.4
Benzoic Acid	4.2	-4.3	7.0
Trichloracetic Acid	0.7	-7.8	10.5

Table IV

Estimates of the Relative Bond Strengths between Organic Polar Groups and Hydrated Titanium Oxide Surfaces.

Organic	pK_a	Titanium Surface $pK_{a1} = ?$	Titanium Surface $pK_{a2} = 9.7$
		$\Delta_B = pK_a - pK_{a1}$	$\Delta_A = pK_{a2} - pK_a$
Ethylamine	11.0		-1.3
Triethylamine	10.8		-1.1
Phenol	9.9		-0.2
Benzylamine	9.3		0.4
Pyridine	5.7		4.0
Acetic Acid	4.8		4.9
Benzoic Acid	4.2		5.5
Trichloroacetic Acid	0.7		9.0

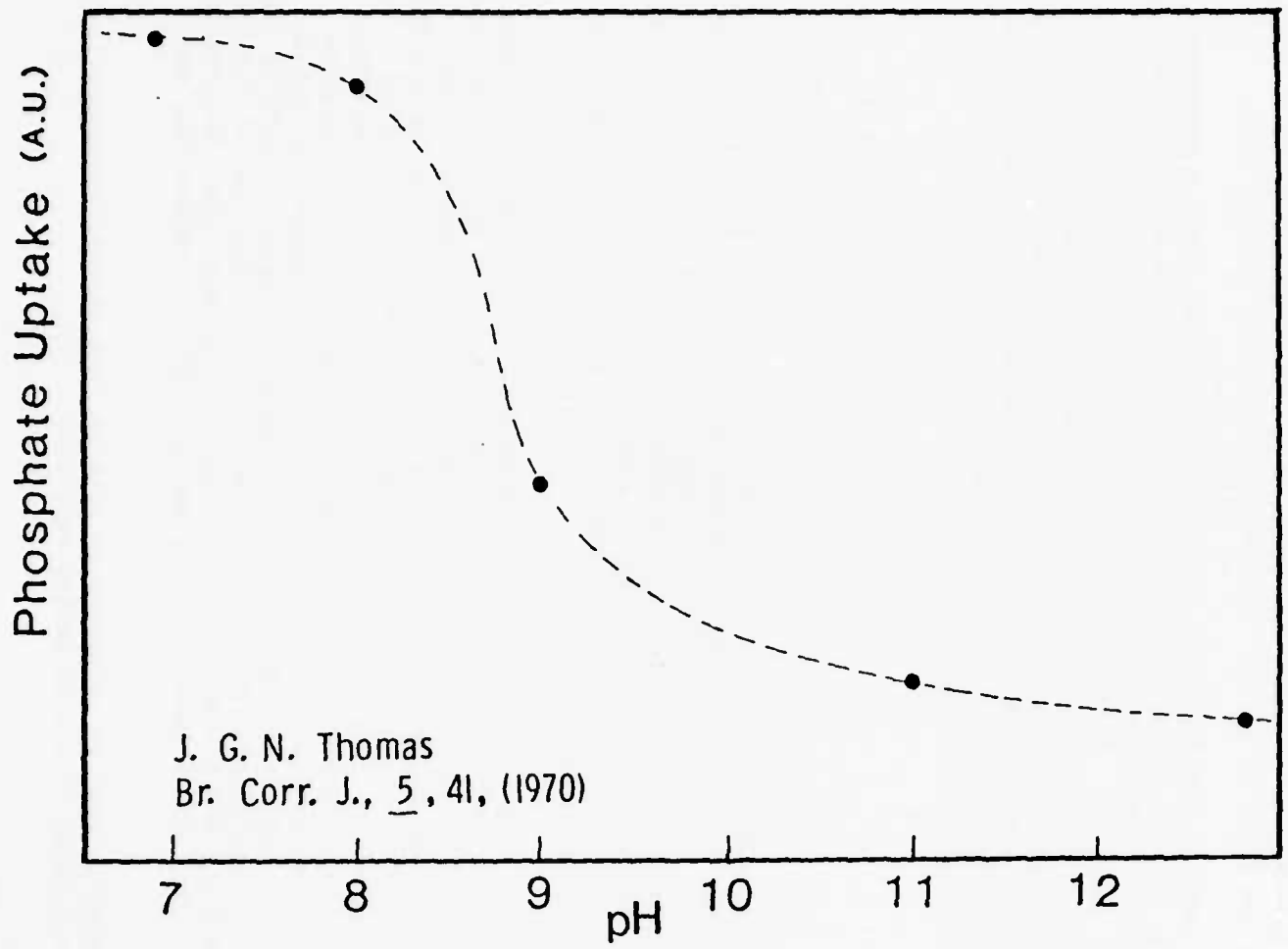

Figure 9. Phosphate anion uptake on mild steel as a function of pH by radiotracer measurements [17].

For the iron specimens, Figure 7, the coverage, θ, increased as a function of pH as expected for pH values up to pH = 11.7. Above pH = 11.7, however, an unexpected drop in θ was observed. A maximum coverage of 0.45 was observed suggesting that either some of the hydroxyls are not available for exchange or do not undergo exchange over this range of pH. Although a saturation coverage at high pH is not apparent because of the "anomalous" behavior, the maximum observed value was used to estimate a value of pK_{a2} for the hydrated iron oxide on iron. The pH at which the coverage is half the maximum value was found to be ~11.2 which corresponds to a $pK_{a2} = 11.2$.

The coverage increased as a function of pH for the titanium specimens and appeared to reach a saturation value at pH $\geq$10.8. This saturation value, as was found for iron, indicated that only ~45% of the available hydroxyls have undergone exchange. A decrease in coverage at high pH comparable to that found with iron, however, was not found for titanium. The pH at which the coverage was one half the maximum value gave an estimated value of $pK_{a2} = 9.7$ for hydrated oxide on titanium. The lower pK_{a2} value for titanium compared to that for iron is consistent with the larger charge/radius ratio of Ti^{4+} in titanium oxide compared to that for Fe^{3+} in iron oxide.

DISCUSSION

High resolution oxygen (1s) spectra of the hydrated oxide on both iron and titanium indicated the presence of hydroxyls with concentrations on the order of 5-10/nm^2. It was shown that the oxygen (1s) line for the oxygen in organic contamination had a higher binding energy than the oxygen (1s) line of the hydroxyl. The area under the hydroxyl line was, therefore, taken as a measure of the hydroxyl concentration, since there was no apparent interference from the carbon contamination.

Although the coverage vs. pH results presented in Figures 7 and 8 show the expected trends, considerable scatter in the data was observed. Furthermore, deviations in the ideal behavior was seen for iron at high pH. The varying amounts of sodium and carbon contamination were considered as possible causes for the scatter in the data and the deviation from ideal behavior. No correlations were found, however, between coverage, θ, and either the total carbon signal or the sodium signal. The organic contamination, on the other hand, may have been bound to the surface by interaction between the organic polar group(s) and the surface hydroxyl. The number of surface hydroxyls tied up by the organic contamination would be expected to be a function of the intensity of the polar group component of the carbon (1s) spectrum. No correlation, however, was found between coverage and the 288.6 eV carbon (1s) peak intensity.

It is possible that in solutions at high pH, the organic contamination is displaced according to the following reaction:

$$-FeOH_2^+\overset{O}{\overset{\|}{O}}C(CH_2)_nCH_3 + OH^- \longrightarrow -FeOH + \overset{O}{\overset{\|}{O}}C(CH_2)_nCH_3 + H_2O$$

Consequently, the surface hydroxyls would be free to undergo exchange with potassium. Recontamination by organics may have then occurred during subsequent specimen rinsing and exposure to air. The possible role of sodium contamination during the exchange, on the other hand, is not clear. The deviation from ideal behavior at pH > 11.7 for iron specimens may be attributed to instability of iron oxide at this pH [16].

$$Fe_2O_3 + H_2O + 2e^- \longrightarrow 2HFeO_2^-$$

Our studies have not yet included the anion exchange reactions at low pH that would provide a pK_{a1} value for $-MOH_2^+$. The uptake of phosphate iron by oxide films on mild steel, however, has been reported by Thomas [17]. The exchange of phosphate with the oxide surface was followed by radioactive phosphate over a pH range of 7-13, and the results are reproduced in Figure 9. The highest phosphate uptake was estimated to be on the order of a monolayer at pH 7 and decreased with increasing pH. One half the maximum uptake occurred at pH 8.5 suggesting that the pK_{a1} for $-FeOH_2^+$ has a value of 8.5. On the basis of Thomas's results and the results of our study, the acid/base properties of the hydrated oxide on iron can be summarized as follows:

$$-FeOH_2^+ \rightleftharpoons -FeOH + H^+ \qquad pK_{a1} = 8.5$$

$$-FeOH \rightleftharpoons -FeO^- + H^+ \qquad pK_{a2} = 11.2$$

We are not aware of any anion exchange studies for hydrated oxide on titanium surfaces. From our study of cation exchange we propose the following acid/base properties for titanium surface.

$$-TiOH_2^+ \rightleftharpoons TiOH + H^+ \qquad pK_{a1} =$$

$$-TiOH \rightleftharpoons TiO^- + H^+ \qquad pK_{a2} = 9.7$$

The more acidic nature of titanium compared to iron is consistent with the higher charge/radius ratio of Ti^{4+} compared to Fe^{3+} in the respective metal oxide.

Bolger and Michaels [4] and Noller et al. [16] have proposed that the pK_a of the surface and the pK_a of the polar groups in organic coatings can be used to predict the strength of the hydrogen bonding between surface and coating. For example, the interaction between an organic acid and a hydrated metal surface can be considered as follows:

$$-MOH + H^+ \rightleftharpoons -MOH_2^+ \qquad K_{a1} = 10^{-pK_{a1}}$$

$$RCOOH \rightleftharpoons RCOO^- + H^+ \qquad K = 10^{+pK_{a(A)}}$$

$$-MOH + RCOOH \rightleftharpoons -MOH_2^+ \,\overset{-}{O}OR \qquad K = \frac{10^{pK_{a(A)}}}{10^{pK_1}}$$

Since the standard free energy of this interaction is a function of the equilibrium constant, i.e.,

$$\Delta G^\circ = -RT \ln [K_{a1}/K_{a(A)}] \ ,$$

then the relative strength of the hydrogen bonding between the surface and coating is a function of the difference between the surface and organic polar group pK_a values.

$$\Delta(\text{organic acid}) = pK_{a(A)} - pK_{a1} \ .$$

On the basis of the equilibria shown above the coating would be expected to be stable in solutions over the pH range $pK_{a1} > pH > pK_{a(A)}$. Similar arguments are applicable for interaction between the hydrated metal surface and an organic base.

$$-MOH \rightleftharpoons MO^- + H^+ \qquad K_{a2} = 10^{+pK_{a2}}$$

$$RCH_2NH_2 + H^+ \rightleftharpoons RCH_2NH_3^+ \qquad K_{a(B)} = 10^{-pK_{a(B)}}$$

$$-MOH + RCH_2NH_2 \rightleftharpoons -MONH_3CH_2R \qquad K = \frac{10^{pK_{a2}}}{10^{pK_{a(B)}}}$$

The relative strength of interactions, in this case, is as follows:

$$\Delta(\text{organic base}) = pK_{a2} - pK_{a(B)}$$

Interactions of this type would be expected for the pH range $pK_{a2} < pH < pK_{a(B)}$.

The pK_a values for a number of organic acids and bases are listed in Table III, along with calculated values of Δ(Organic acid) and Δ(Organic base)

for iron. On the basis of the pK_{a1} = 8.5 derived from Thomas's study and the pK_{a2} = 11.2 from our studies of iron, it is possible to predict which organic functional groups are likely to form strong hydrogen bonds with iron surfaces. For organic acids strong bonds are favored where the acid $pK_{a(A)}$ is less than pK_{a1} = 8.5 [i.e., Δ(organic acid) < 0]. Thus, stronger surface bonding would be expected for carboxylic acids than that for phenols. Organic bases that would form strong surface bonds should have $pK_{a(B)}$ greater than pK_{a2} = 11.2. Since there are not many organic bases with $pK_{a(B)}$ higher than this value, basic functional groups in organic coatings would not contribute to strong hydrogen bonding with the surface of iron. Furthermore, the stronger bond expected via organic acid interaction would not be expected to be stable outside the pH range of 4 - 8.5.

Since the pK_{a1} of titanium has not been determined, predictions of relative bond strengths are restricted to organic base interaction. The hydrated oxide on titanium was found to be more acidic (pK_{a2} = 9.7) than for the oxide on iron (pK_{a2} = 11.2). Consequently, there are several organic bases that would interact more strongly with titanium than with iron, cf. Table IV. Additions of base functionality to organic coatings should, therefore, be more effective in promoting bonding to a titanium surface.

The interactions between metal surfaces and organic coatings are undoubtedly more complex than the simple model presented in this report. The experimental approach and the results that were obtained have shown, however, that surface hydroxyls are present on hydrated metal oxide surfaces and that their hydroxyls exhibit acid/base properties. The predictions of the relative strengths and stabilities of the interactions between organic coatings and metal surfaces on the basis of relative pK_a values need to be evaluated experimentally.

REFERENCES

[1] M. W. Roberts and P. R. Wood, J. Elect. Spect. and Rel. Phen. 11, 431 (1977).

[2] J. Kruger and H. T. Yolken, Corrosion 20, 29 (1964).

[3] "Thermodynamics of Wetting of Solids," W. H. Wade and N. Hackerman, Adv. Chem. Ser. #43, c. 1964, p.222.

[4] "Molecular Structure and Electrostatic Interactions at Polymer-Solid Interfaces," J. C. Bolger and A. S. Michaels from Interface Conversion, P. Weiss and D. Cheever, Editors, Elsevier Publishing Co. (1969).

[5] "Donor-Acceptor Interactions at Interfaces," F. M. Fowkes in Adhesion and Adsorption of Polymers, Part A, Leing Huang Lee, Editor, Plenum Press, c. 1980, p.43.

[6] "Pigment-Matrix Interactions," F. M. Fowkes, in Proceeding of Corrosion Control by Coatings Conference, Lehigh University, Nov. 13-15, 1978.

[7] G. A. Parks, Chem. Rev. 65, 177 (1965).

[8] A. G. Akimov, Soviet Electrochem. 15, 1301 (1980).

[9] N. S. McIntyre and D. G. Zetaruk, Anal. Chem. 49, 1521 (1977).

[10] D. T. Clark and A. Dilks, J. Poly. Sci., Poly. Chem. 17, 957 (1979).

[11] K. Asami and K. Hasimoto, Corros. Sci. 17(7), 559 (1977).

[12] N. R. Armstrong and R. K. Quinn, Surf. Sci. 67, 451 (1977).

[13] M. J. Dreiling, Surface Sci. 71, 231 (1978).

[14] E. McCafferty and A. C. Zettlemoyer, Dis. Faraday Soc. 52, 239 (1971).

[15] G. D. Parfitt, Prog. Surf. Mem. Sci. 11, 181 (1976).

[16] "Atlas of Electrochemical Equilibria in Aqueous Solution," M. Pourbaix, National Association of Corrosion Engineers (1974).

[17] J. G. N. Thomas, Br. Corro. J. 5, 41 (1970).

[18] H. Noller, B. Mayerbock, and G. Zundel, Surf. Sci. 33, 82 (1972).

Program #10

Determination of the Acidity of Iron Oxide Surfaces. Acid Sites on Hematite Using Flow Calorimetry

INTRODUCTION

The adhesion of organic polymers to inorganic oxides, such as those on steel surfaces and iron oxide pigments, has been shown to result entirely from acid/base interactions between the polymer and the oxide. Hydrogen bonds have been shown to be a subject of acid/base interactions and dipole/dipole interactions have been shown to be so negligibly small that no experimental evidence for them has yet been found. It is therefore important to find a method of measuring and predicting acid/base interactions in the bonding of organic polymers to metal oxide surfaces, especially the oxide layers of steel.

Results detailed in the Annual ONR Report for 1981-82 suggested that the poor reproducibility obtained for the adsorption of pyridine from cyclohexane (at concentrations less than 20 mM pyridine) onto a hematite surface was due to water contamination. Samples tested with a reduced evacuation time (i.e., inadequate water removal) showed essentially a constant enthalpy with increasing surface coverage by pyridine while samples tested using the standard evacuation time (ten min) generally showed an initial coverage of highly active sites with decreasing enthalpy at further coverage. These results were not reproducible, however, so a Karl Fischer automatic titrimeter was obtained to permit routine water content analysis.

RESULTS AND DISCUSSION

The Aquatest IV automatic Karl Fischer titrimeter (PHOTOVOLT CORP., New York, NY) is now routinely used to determine the water content of the non-aqueous solvents used in the microcalorimeter. Good reproducibility (± 1 ppm) has been obtained with a 20 ml sample of cyclohexane by allowing a 30 sec premix prior to the titration. By testing both the solvent and solution for use in each microcalorimeter run, any gross increase in the water content obtained by introducing the hydroscopic probe molecule can readily be determined.

Initial cyclohexane samples analyzed for water content using the Karl Fischer titrimeter pointed to two major sources of error which could lead to the poor reproducibility observed for the enthalpy of pyridine adsorption:

1. Much higher water contents were found in the pyridine solution compared to the pure cyclohexane, especially for "dried" pyridine samples stored longer than two to three weeks. A "mismatch" in the water contents

of the solvent and probe solution appears to be a relevant parameter which determines whether "wet" behavior occurs. So-called "wet" behavior occurs when the final baseline of the enthalpy curve against the pyridine solution is below the initial baseline observed for the pure cyclohexane carrier solvent due to transfer of water from the powder surface into the solution.

2. A lack of reproducibility in the absolute water contents of different batches of cyclohexane carrier solvent even though treated in the same manner and aged under the same apparent conditions.

3. Previous reported water contents obtained using the same type of Karl Fischer apparatus but for cyclohexane samples which were stored 16 hr or longer prior to testing were found to be significantly higher than those obtained with freshly sampled cyclohexane (15 to 20 ppm vs. 3 to 10 ppm). This result is due to water pickup from the glass containers during the storage time prior to testing [1].

Standard laboratory sampling and handling procedures were judged to be acceptable for maintaining the dryness of the cyclohexane, i.e., the probability of inadvertent contamination was low. Modification of the vacuum system and use of the microcalorimeter to obtain an evacuation profile (detailed below) have minimized the likelihood that sample contamination due to atmospheric moisture will go undetected.

Work completed immediately after receipt of the Karl Fischer titrimeter was restricted to the characterization of the surface acidity of a commercial hematite powder (R-1299 Lot E9036, PFIZER INC., Easton, PA) using 3 mM pyridine or triethylamine in cyclohexane. A low adsorbate concentration was desirable in order to examine the adsorption on a relatively long time scale suitable for the "cut and weigh" technique of peak integration. Examining the pyridine and triethylamine data for the enthalpy and number of moles adsorbed as a function of time by a "time slice" technique has revealed a heterogeneous distribution of acidic surface sites on the hematite powder. This distribution of adsorption strength is illustrated in two ways: an "integral" and a "differential" form. The integral curve is obtained using the total enthalpy divided by the total number of moles adsorbed over the entire time interval up to the given surface coverage. The differential curve plots the adsorption enthalpy divided by the moles adsorbed for a given one min time interval at the mean surface coverage for the time interval. Limited work done at higher concentrations suggests that the differential enthalpy distribution is a continuous smooth function extending to higher concentrations. Figures 1 and 2 show the integral and differential enthalpy distributions, respectively, for pyridine adsorption, while Figures 3 and 4 show the comparable plots for triethylamine adsorption onto the same hematite surface as a function of increasing surface coverage. Further exploration and refinement of this procedure has been deferred pending implementation of our laboratory computer and writing of the appropriate software to simultaneously collect data from both the microcalorimeter and the UV flow detector, and then process this data in the appropriate "time slice" integration. The software is approximately 90% completed at this writing. An example of the computer output for the microcalorimeter is presented in Figure 5.

Two HPLC switching valves (VALCO Inc., Houston, TX) were added to the microcalorimeter flow system this year: a four-port switching valve and a

FIGURE 1

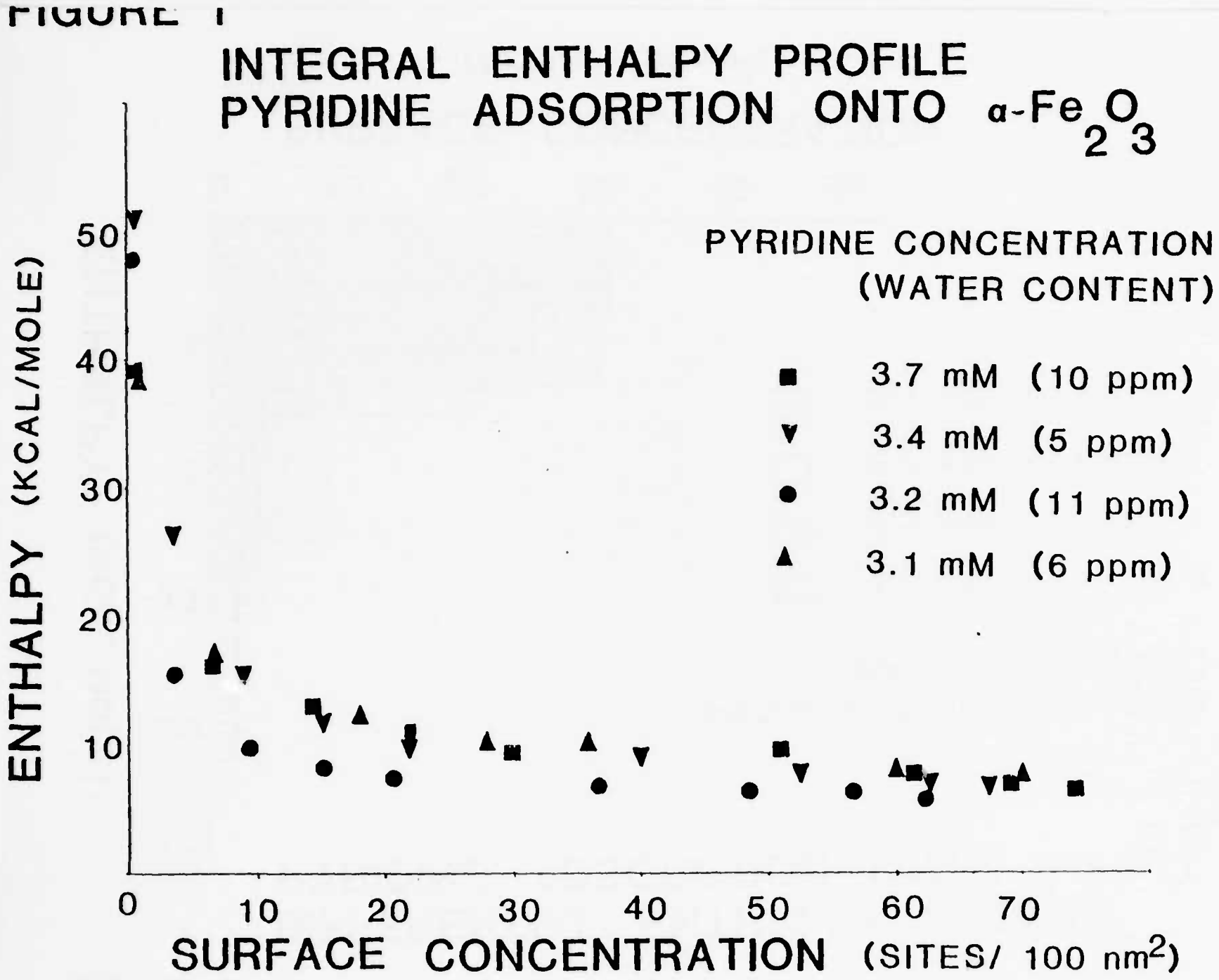
INTEGRAL ENTHALPY PROFILE
PYRIDINE ADSORPTION ONTO α-Fe2O3
PYRIDINE CONCENTRATION
(WATER CONTENT)
3.7 mM (10 ppm)
3.4 mM (5 ppm)
3.2 mM (11 ppm)
3.1 mM (6 ppm)
ENTHALPY (KCAL/MOLE)
50
40
30
20
10
0
10
20
30
40
50
60
70
SURFACE CONCENTRATION (SITES/ 100 nm2)

FIGURE 2

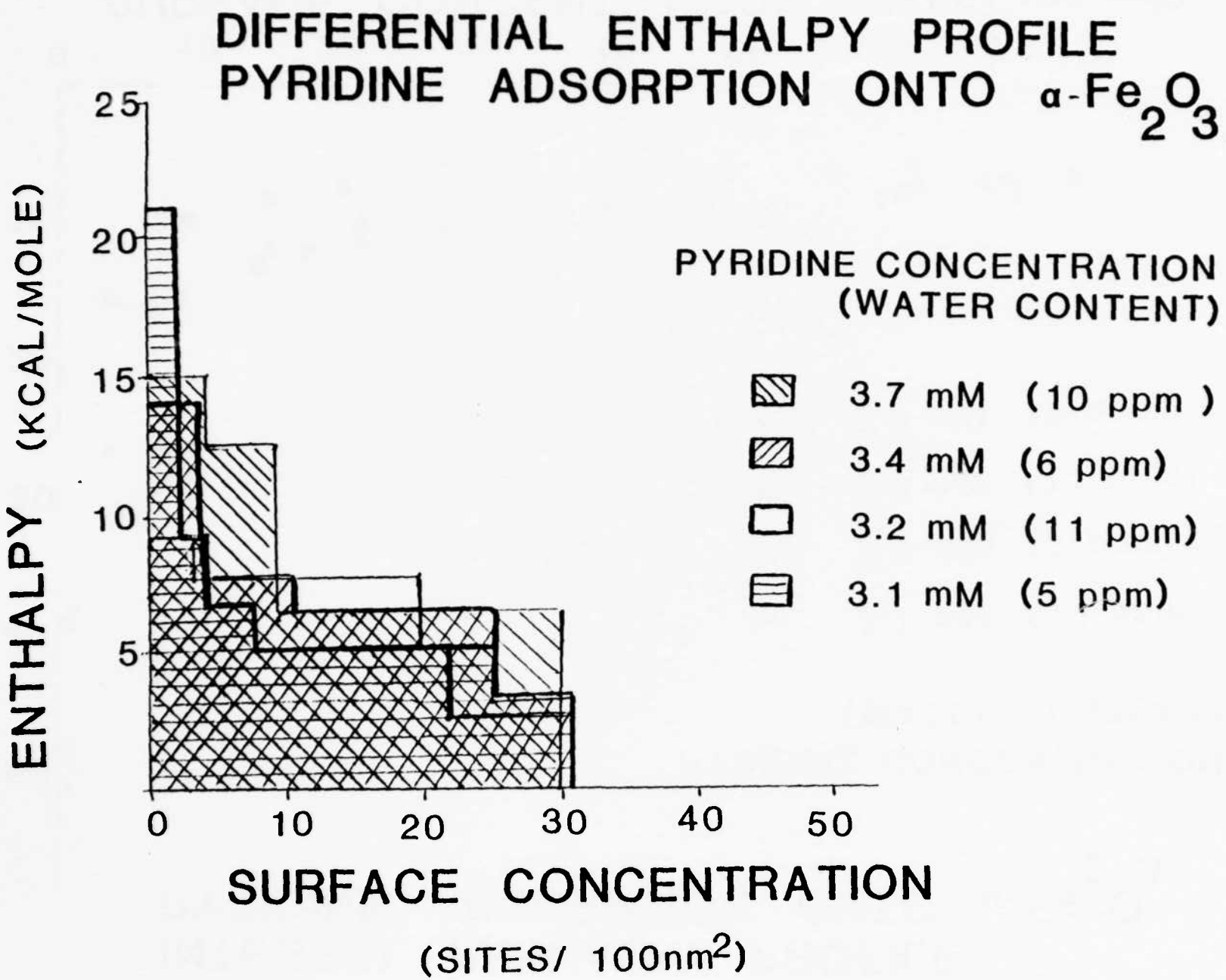
DIFFERENTIAL ENTHALPY PROFILE
PYRIDINE ADSORPTION ONTO α-Fe2O3
ENTHALPY (KCAL/MOLE)
25
20
15
10
5
0
10
20
30
40
50
SURFACE CONCENTRATION
(SITES/ 100nm2)
PYRIDINE CONCENTRATION
(WATER CONTENT)
3.7 mM (10 ppm)
3.4 mM (6 ppm)
3.2 mM (11 ppm)
3.1 mM (5 ppm)

FIGURE 3 INTEGRAL ENTHALPY PROFILE
TRIETHYL AMINE ADSORPTION
ONTO α-Fe_2O_3

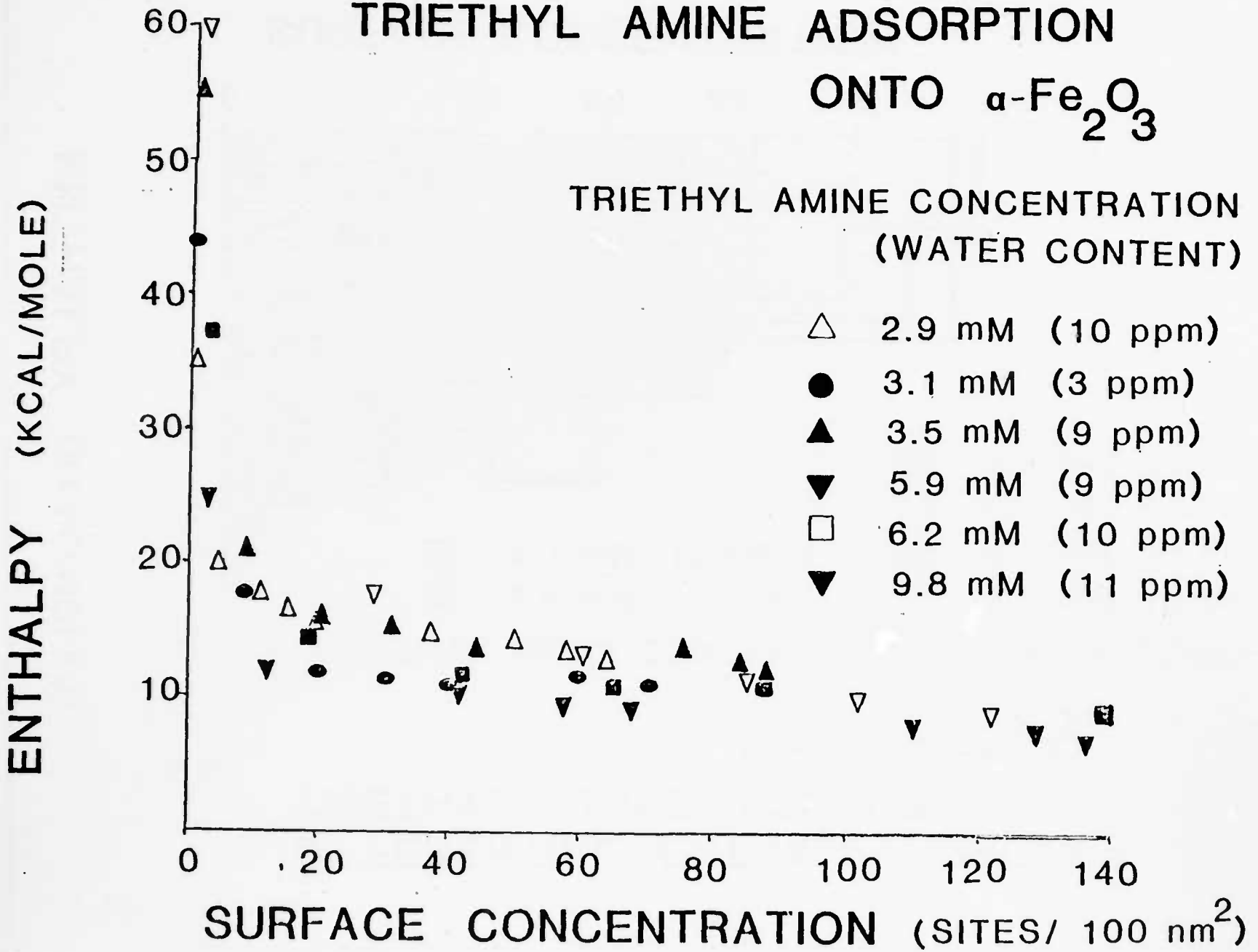

FIGURE 4

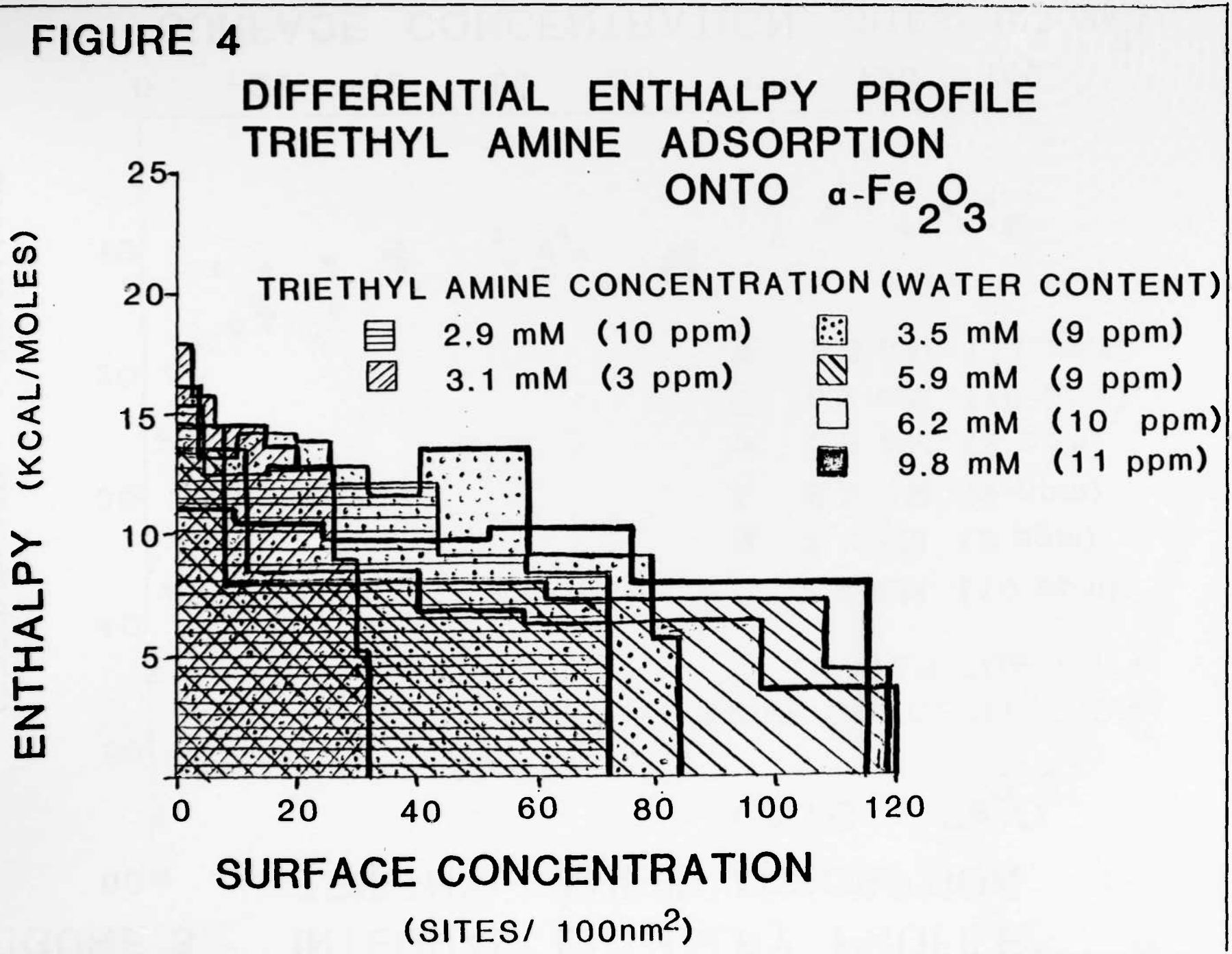
DIFFERENTIAL ENTHALPY PROFILE
TRIETHYL AMINE ADSORPTION
ONTO α-Fe2O3
TRIETHYL AMINE CONCENTRATION (WATER CONTENT)
2.9 mM (10 ppm)
3.1 mM (3 ppm)
3.5 mM (9 ppm)
5.9 mM (9 ppm)
6.2 mM (10 ppm)
9.8 mM (11 ppm)
ENTHALPY (KCAL/MOLES)
25
20
15
10
5
0
20
40
60
80
100
120
SURFACE CONCENTRATION
(SITES/ 100nm2)

COMPUTER OUTPUT

PARTIAL INTEGRATION

OF MICROCALORIMETER DATA

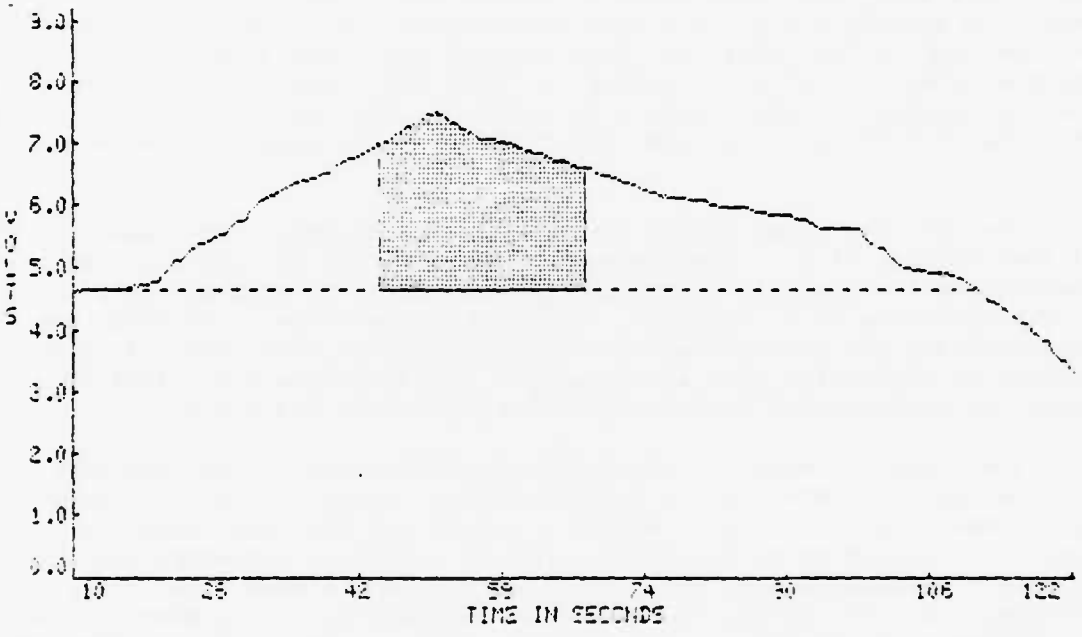


```
THE DATA FILE IS TESTDATA
THE DATA WAS RECORDED ON 20-OCT-83
THE TIME WAS 13:58:55
THE CONVERSION RATE IS 4 POINTS PER SECOND
THE ARRAY DIMENSION OF THE DATA IS  1
THE MULTI-D CHANNEL NUMBER IS  1
THE EXPERIMENT FILE NAME IS MICROCAL.S

COMMENTS:
 TEST DATA FOR STRIPCHART AND DATAPENCIL

INTEGRATION DATA:
 LIMIT ONE =  44.25
 LIMIT TWO =  87.25
 BASELINE POINT ONE = 15.75 SECONDS, 4.6784 VOLTS
 BASELINE POINT TWO = 111.5 SECONDS, 4.6784 VOLTS

 THE INTEGRATED AREA = 55.3359218 VOLT-SECONDS
```

FIGURE 5

six-port valve with an internal fixed volume flow loop (Fig. 6). The four-port switching valve changes the source of the inlet stream to the micro-calorimeter from one syringe pump to another with a minimal fluctuation in the flow rate or pressure in the flow lines. The six-port valve incorporates a fixed volume flow loop which can be filled with adsorbate solution while the powder bed is equilibrated against the carrier solvent. The flow path of the carrier solvent can then be altered to pass through the flow loop to introduce a known volume of adsorbate solution into the flow stream. This equipment has classically been used to introduce very small quantities of adsorbate (approximately 10 µl) in a "pulse" experiment; however, use of a relatively large loop volume (two to five ml) permits saturation adsorption experiments which are independent of any potential variation between syringe pumps. In addition, computer-controlled experiments can be performed using the flow loop by upgrading the current manual switch to an electronic switch. Computer control would prove useful for obtaining reproducible desorption times in a series of experiments, for example. The current 20 ml syringes limit the flow time to approximately three hr at the present flow rate (6 ml/hr).

The two loop sizes tested for saturation adsorption experiments to date are two and five ml in volume, respectively. The two ml loop has been used to characterize the pyridine adsorption isotherm over the concentration range 15 to 40 mM pyridine in cyclohexane. The five ml flow loop is suitable for characterizing the strength and distribution of the acidic surface sites on hematite by adsorption of a 3 mM pyridine from cyclohexane to yield the integral and differential enthalpy profiles previously discussed.

The number of moles of adsorbate removed by flowing the adsorbate solution through the powder bed is determined by alignment of the UV concentration curves obtained for the adsorption trial and the calibration run, respectively, according to the initial drop in adsorbate concentration which represents breakthrough of the carrier solvent in the desorption cycle. The difference in area between the two curves corresponds to the number of moles of adsorbate removed from the bed as a function of time. The interface between two solutions of different concentration flowing consecutively through a tube exhibits a concentration gradient of finite width. This frontal zone results from the parabolic velocity gradient of the fluid across the tube cross-section (since the velocity of the fluid at the wall is zero), as well as any mixing which occurs where there are changes in the tube diameter. The relative "broadness" of the concentration front can be characterized by the time interval (at a given flow rate) from an initial concentration to where the concentration is midway between the initial and final value. This time interval is constant and the same regardless whether from low to high concentration or vice versa when examined using the four-port switching valve and the two micropumps. Using the six-port valve and the flow loop (containing the high adsorbate concentration), the broadness of the low to high concentration front is essentially the same as in the previous case; however, the broadness of the high to low concentration front is markedly longer using the flow loop system.

Two possible explanations for the increased broadening in the flow loop system are adsorption of the solute molecule onto the stainless steel flow loop or increased mixing due to changes in the tubing diameters between the flow loop and the Teflon tubing. Adsorption on the stainless steel interior

FIGURE 6

FLOW MICROCALORIMETER

LOOP INJECTION AND SWITCHING VALVES

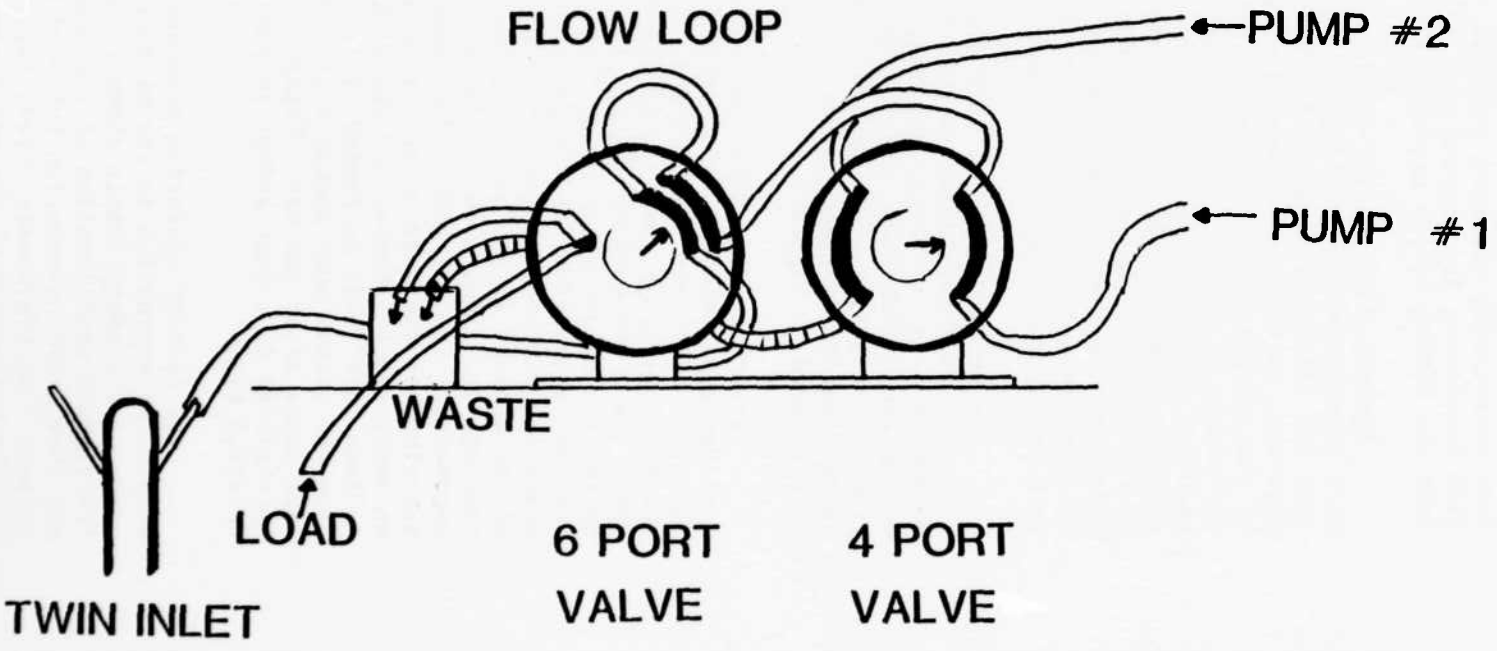

is calculated to be a relatively minor effect due to the small amount of material involved, i.e., about .2% of the adsorbate in a 3 mM pyridine solution for the five ml flow loop. In addition, the two and five ml flow loops have essentially the same internal surface area, yet significantly greater flow broadening is observed with the larger diameter five ml loop, suggesting that the mixing effect predominates.

Increased broadening of the concentration front in the desorption cycle is a significant disadvantage of using the flow loop system due to the necessity for alignment between the UV trial and calibration curves. As the front broadens, it becomes increasingly difficult to determine the breakthrough time of the solvent in the desorption cycle, particularly when the concentration difference is small. Reproducible results for the number of moles of pyridine adsorbed onto hematite were obtained using the two ml flow loop with a lower concentration limit of 10 mM pyridine but could not be obtained using the five ml flow loop. Computerization should extend the useful range of the flow loop system as the breakthrough time of the desorption cycle could be more accurately characterized by observing the rate of change of concentration (derivative) as a function of the time coordinate.

The primary focus of work over this year has been a refinement of the procedure to remove moisture from the hydrophilic powder by evaporation under vacuum in order to obtain reproducible surface water contents. A Hastings vacuum gauge (TELEDYNE HASTINGS-RAYDIST, Hampton, VA) has been added to the flow microcalorimeter to permit vacuum monitoring above the powder bed. The current equipment assembly for *in situ* vacuum drying of the hematite powder is presented in Figure 7.

Vacuum readings were made to compare the readings obtained from the Hastings gauge and the McLeod gauge manometer when the Hastings gauge was attached at different points within the system. At points A and B in Figure 7, the Hastings gauge readings differed only slightly from the McLeod gauge readings, i.e., the Hastings gauge placed at point B read 1.45 mm Hg vs. 1.1 mm Hg for the McLeod gauge after a nine min pumpdown period (a typical time scale for the evacuation of the powder samples used in this work). At point C, where the narrow diameter Teflon tubing assembly must be incorporated to permit attachment to the microcalorimeter inlet tube, the Hastings gauge vacuum readings are significantly higher than those taken using the McLeod gauge manometer. Typical vacuum differences are presented in Figure 8 with the superimposed microcalorimeter traces representing the evacuation profile of an empty sample chamber and the packed hematite powder bed, respectively. A "leak rate" test performed by isolating a pre-evacuated empty sample chamber from the vacuum pump showed little or no loss of vacuum measured by the Hastings gauge after two min. Water contamination due to atmospheric moisture is observed as a heat effect in the evacuation profile of the hematite bed as detailed below.

The current operating procedure for preparation of a hematite powder sample for evaluation in the microcalorimeter involves the preliminary evacuation of the empty sample chamber, release of vacuum and sample loading, temperature equilibration of the powder with the microcalorimeter (40°C), and then sample evacuation followed by wetting with the appropriate carrier solvent. As previously noted, Figure 8 presents the microcalorimeter traces for the evacuation of the empty sample chamber and the packed powder bed,

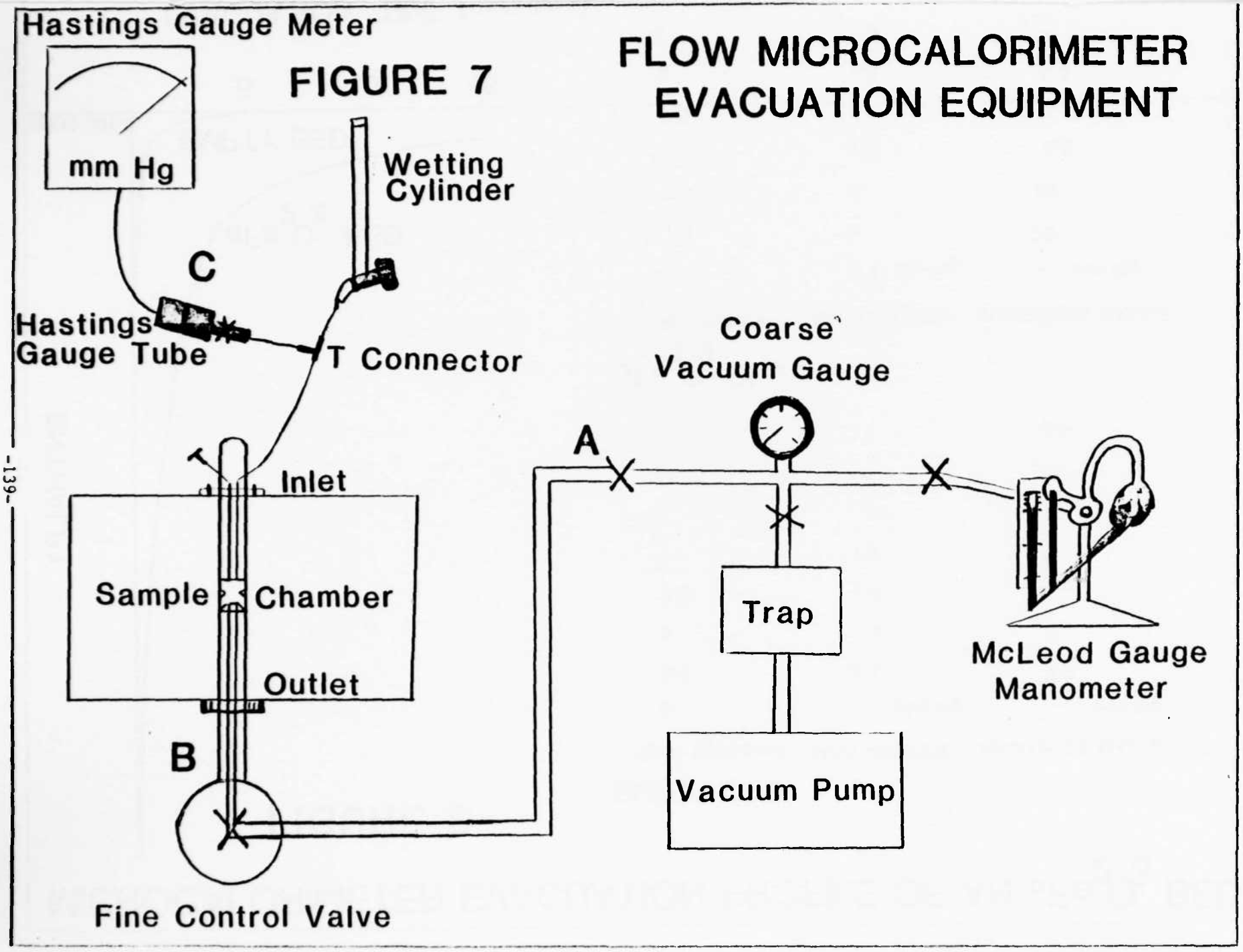

FIGURE 7

FLOW MICROCALORIMETER EVACUATION EQUIPMENT

MICROCALORIMETER EVACUATION PROFILE OF AN αFe_2O_3 BED

FIGURE 8

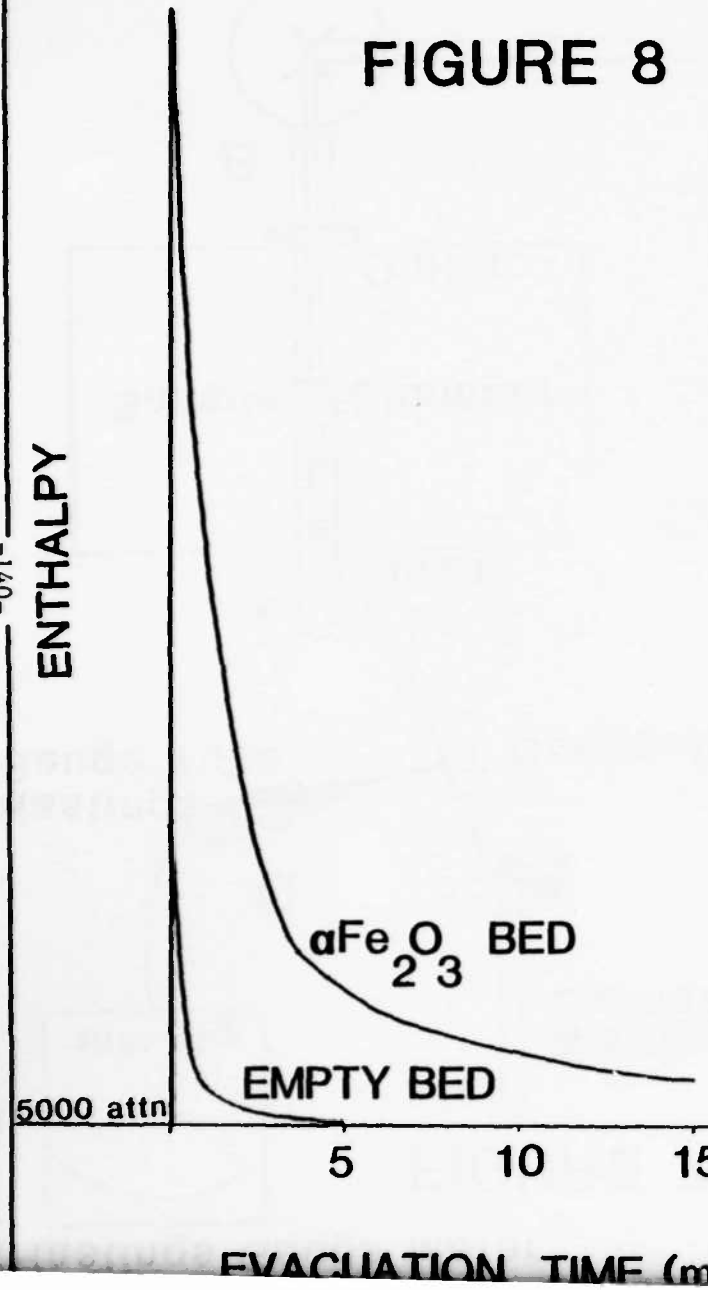

EMPTY BED

TIME (minutes)	MANOMETER	HASTINGS GAUGE
0	1.1 mm Hg	– mm Hg
2.5	3.1	6.5
5	1.9	5
7.5	1.4	4.5
9	1.2	4.25
15	.95	4
30	.8	3.5
60	.8	3.4

αFe_2O_3 BED

TIME (minutes)	MANOMETER	HASTINGS GAUGE
0	1.4 mm Hg	– mm Hg
1.5	–	20
2.5	3	10
5	1.7	6.5
7.5	1.2	5.75
9	1.2	5.5
15	.9	5

respectively. Evacuation and opening the empty bed to the atmosphere gives essentially equal and opposite temperature effects while the cooling observed upon evacuating the 150 mg hematite powder bed is substantially larger than the heating observed upon readmission of the atmosphere. Previous work with one to three g hematite powder samples evacuated overnight at 25°C in a vacuum oven to 1 mm Hg gave a net weight loss of between .25% and .5% when re-weighed after capping under a flow of dried nitrogen gas. Immediate sample removal after evacuation gave weight losses close to the .5% value. Equilibrating the evacuated powder with dry gas (nitrogen gas passed through a Drierite column, i.e., with equilibrium water content of 1 to 2 ppm per ℓ of gas) for one hr resulted in weight losses close to the .25% value, suggesting strong water re-adsorption under these low relative humidity conditions. Reweighing the samples equilibrated for an hr against the dry gas, it was found that the sample vials with three g of powder had a greater observed weight loss compared to vials containing one g, indicating that availability of water vapor for diffusion into the powder was a factor determining the ultimate weight. Evacuated hematite samples with a .25% weight loss that were capped using Teflon septa and aluminum caps while under a dry nitrogen flow showed no further weight increase when stored overnight.

The amount of water remaining on the hematite surface when it ultimately is exposed to pyridine for adsorption is determined by the evacuation conditions as well as both the water content and equilibration time with the non-aqueous solvent. The experimental design in this project has been to evaluate the hematite surface under controlled conditions at surface water contents that are representative of the strongly-bound first layer of "physisorbed" water. Water vapor adsorption isotherms on hematite at 35°C by McCafferty [2] show a relatively flat region for strongly bound water with increasing water vapor pressure with completion of the first monolayer of "strongly bound" water in the pressure range of 4 to 10 torr. His work also demonstrates that a single curve is obtained as a reduced relative pressure isotherm for data obtained at 5°, 15°, 25°, and 35°C. This plot shows that one layer (or less) of strongly held water is found for samples equilibrated with water vapor below 15% RH. In McCafferty's work, all of the physisorbed water was removed by 48 hr evacuation at 25°C and 10^{-6} torr prior to starting the water vapor adsorption isotherm. Our procedures designed to reach this region of interest have involved short-term *in situ* evacuation of the hematite powder at 40°C to remove multilayer water condensed between the powder particles followed by equilibration of the powder with a non-aqueous solvent of known water content within this desired humidity region, i.e., cyclohexane containing 3 to 10 ppm of water roughly corresponding to 3 to 10% relative humidity. Our previous work showed that the amount of water removed by overnight evacuation of 1 to 3 g samples of hematite powder was .25% to .50% by weight or equivalent to approximately .8 to 1.75 layers of water. Assuming that the samples with a net weight loss of .25% represent those that have physisorbed water but contain no multilayer water, then examination of the adsorption properties of a hematite powder sample which has been dried and stored to prevent multilayer water condensation should indicate whether our evacuation procedure is capable of removing only multilayer water or also a portion of the underlying "strongly bound" physisorbed water.

In a recent publication, Heal and McEwen [3] have stressed the importance of pretreatment conditions in determining the surface area of powders using adsorption of n-butanol from heptane in the flow microcalorimeter.

They demonstrated that the heat of butanol adsorption onto rail rust is increased by removal of the physisorbed water by sixteen hr pretreatment at 120°C or by room temperature evacuation. Their evacuation technique required the use of individual pre-weighed rail rust samples in vials which were capped after evacuation while under a stream of dry gas and then transferred to the microcalorimeter. We have examined the effect of short term *in situ* evacuation of the heat of .2% v/v n-butanol adsorption from heptane using our hematite sample. Our work has demonstrated the different contributions water can make to the enthalpy of n-butanol adsorption as determined using the flow calorimeter.

n-Butanol Adsorption onto Hematite Powder

Condition	Enthalpy ($\times 10^5$ KCAL)	Comments
Wet Load - "As Received" Sample	4.30	Poor Baseline Definition
Wet Load - "Dry" Sample Oxide Stored in Desiccator	3.70	
1 Min Evacuation	3.53	
5 Min Evacuation	3.52	
10 Min Evacuation	4.72	
20 Min Evacuation	6.19	
10 Min Air-Contaminated	3.60	Air in Tubing after Wetting
Air-Contaminated	3.97	Leak in Hastings Gauge Cut-off Valve
10 Min - Increased Flow	4.21	2 hr vs. 30 min
10 Min - Stop Flow	3.41	2 hr "relaxation"
10 Min - Wet BuOH	5.14	

These results will be interpreted by considering the type and amount of water present under the given experimental conditions. It should be noted that n-butanol is <u>not</u> a preferred probe for adsorption studies since it can behave as either an acid or a base. No information on the number of moles of n-butanol adsorbed is available for our studies since this probe is not UV sensitive; however, Allen and Patel's microcalorimeter study of fatty alcohol adsorption from heptane onto a water-covered alpha ferric oxide powder [4] gave an area per adsorbed n-butanol molecule of 22 $Å^2$.

First, examine the results obtained using the "wet loading technique". (<u>Note</u>: The "wet loading" technique involves transfer of powder sample directly into the wetting liquid previously placed in the flow microcalorimeter sample

chamber. The evacuation technique previously discussed involves a dry loading step with subsequent sample wetting after removal of water by evacuation. We observe that the "as received" sample has a greater enthalpy of interaction with n-butanol than the sample which was dried and then stored in the desiccator prior to testing. When a nonporous hydrophilic powder is brought into contact with atmospheric moisture, liquid water condenses at the contact points between adjacent particles at a critical humidity less than that required for condensation on a flat surface. N-butanol addition to the hydrocarbon carrier solvent increases the water solubility in the flowing stream and thus is capable of extracting this multilayer water from the "as received" powder. If the multilayer water remained trapped between the hydrophilic particles in the "as received" powder, less total water surface area would be available for interaction with the n-butanol and a decreased enthalpy would be observed compared to the water-covered surface represented by the sample stored in the desiccator. Thus, the effect of the multilayer water condensed between hydrophilic particles clearly is to enhance the apparent enthalpy of n-butanol adsorption due to the interaction of n-butanol with free (solubilized) water extracted from the powder bed as well as the water-covered surface.

If we examine the effect of *in situ* evacuation, we observe that short evacuation times of one and five min give a water-covered surface apparently equivalent to the "wet loaded" sample from the desiccator, indicating the absence of bulk water. Examination of the evacuation profile shows that a large amount of heat is removed from the sample in this time, indicating appreciable water evaporation. At longer evacuation times, the increasing enthalpy of n-butanol adsorption is similar to the trend observed by Heal and McEwen as they removed physisorbed water. Presumably, water removal from the hematite surface permits specific adsorption of n-butanol giving a greater molar enthalpy of adsorption than the interaction of n-butanol with surface water. Intrusion of atmospheric moisture quickly covers the active sites before or after the hematite is wetted with the carrier solvent.

The enthalpy obtained for n-butanol adsorption onto hematite after 10 min evacuation using a two hr "stop flow" technique vs. a two hr flow show the importance of solvent water content on the amount of surface water present. The heptane used in this study was not dried and had a nominal water content of 40 ppm or approximately 40% RH since n-heptane has a water solubility of 100 ppm at this temperature. Note that the sample exposed to a two hr "stop flow" had an enthalpy equivalent to a water-covered surface suggesting that this time period was sufficient to allow readsorption of water from the solvent within the sample chamber. Rough calculations indicate that the water available in the sample chamber would be approximately equal to a monolayer on the powder sample. An alternate possibility is that the two hr time interval permitted "relaxation" of the existing surface water that had been perturbed by the evacuation step. (Note: Our pyridine adsorption work using a 10 min evacuation time has been performed after a two hr solvent equilibration; however, for lower water contents in the solvent. Pyridine adsorption did not give reproducible enthalpies for the active sites after one hr equilibration but good reproducibility was observed after two hr. The same number of water molecules is passed through the hematite bed in the two hr equilibration time for the pyridine adsorption studies as in the thirty min flow time for the n-butanol studies. A two hr flow period for the n-butanol/n-heptane system resulted in the formation of multilayer water at the highly curved interface

between the hydrophilic powder particles so that the observed enthalpy exceeds that of the water-covered surface, similar to the "as received" wet loaded sample. The use of "wet" n-butanol when preparing the adsorbate solution increased the total water content of the solution by approximately 50% compared to the carrier solvent. Exposure of the evacuated powder to the "wet" solution resulted in rapid readsorption of water (in addition to adsorption of n-butanol) onto the dried surface which enhanced the apparent enthalpy of adsorption.

REFERENCES

[1] J. Gedemer, American Lab, Oct. 1975.

[2] E. McCafferty, PhD Thesis, Lehigh University, 1968.

[3] G. Heal and I. McEwen, Powder Tech. 30, 243 (1981).

[4] T. Allen and R. Patel, J. Applied Chem. 20, 165 (1970).

Program #11

Characterization of the Surface Properties of Iron Oxides

INTRODUCTION

The development of protective coatings for corrosive materials requires a knowledge not only of the physical properties of the coating, but also the nature of the interaction of the coating with the substrate and the affinity of the metal oxide/coating interface for water. Water plays an essential role in the corrosion of iron [1]. The growth of rust layers on ferrous metals in the atmosphere where water vapor is present, or the retention of water by certain soils are additional examples of the importance of the interaction of iron oxide with water. In addition, an understanding of the iron oxide-water system should provide insight into the broader problem involving adsorption of polar gas on an ionic solid. The experimental approaches used to study the surface properties of materials require high-surface-area, small-particle-size samples. Mössbauer spectroscopic and X-ray diffraction techniques have shown that α-Fe_2O_3, Fe_3O_4, γ-FeOOH, and β-FeOOH, among others, are present as corrosion products on iron exposed to the atmosphere [2].

Although a large body of literature exists in the area of gas adsorption on metal oxide surfaces, relatively little has been published for the adsorption of gases on iron oxides. Previous investigations in this laboratory by McCafferty and Zettlemoyer [3] studied the interaction of water vapor with α-Fe_2O_3 using heat of immersion [4], dielectric techniques [5,6], and adsorption thermodynamics. They concluded [7] that water vapor chemisorbs on bare α-Fe_2O_3 by a dissociative mechanism to form two hydroxyls per water molecule, the hydroxyl group adsorbing on a surface Fe^{3+} ion and the proton forming a second hydroxyl with an adjacent surface O^{2-} ion. The first layer of physically adsorbed water vapor on the hydroxylated substrate is localized by double hydrogen bonding of a single water molecule to adjacent hydroxyl groups, as was shown by energetic, thermodynamic, and dielectric arguments. The multilayer adsorption was proposed to develop in an ordered ice-like structure. Blyholder and Richardson [8] applied infrared spectroscopy to the investigation of the α-Fe_2O_3/water system. They concluded that physically adsorbed water was completely removed by prolonged outgassing at 25°C and that underlying surface hydroxyls were totally removed at 475°C. Jurinak [9] investigated the interaction of water with α-Fe_2O_3 at various activation temperatures. He showed that about 1/3 of the α-Fe_2O_3 surface is covered with chemisorbed or strongly adsorbed water which, unless removed by high temperature activation, blocks water adsorption sites on the surface. Morimoto et al. [10] studied the amounts of chemisorbed and physisorbed water on α-Fe_2O_3. They took the hydroxyl groups remaining on the oxide surface into account and reported the ratio of the number of water molecules in the first physisorption layer to that of underlying hydroxyl groups to be about 1:2.

Modifications of surface properties by addition of surface active materials to the surface hydroxyls of silica is relatively common. Hexamethyldisilazane (HMDS) was chosen for this investigation because it reacts quantitatively with surface hydroxyls from the vapor phase even at room temperature. The interaction of HMDS was first reported by Stark et al. [11] and the reaction kinetics have been explored by Hertl and Hair [12,13]. Kiselev and his co-workers [14] examined the reaction of trimethylchlorosilane (TMCS) with silica, as did Hair and Hertl [15] for all the methyl chlorosilanes. Zettlemoyer and Hsing [16,17] first examined water interaction with silane-treated silica by a NIR technique. They explored the possibility of the NH_3 adsorption on HMDS-treated silica. Kiselev and co-workers [18] also investigated the interaction of water with TMCS-treated silicas.

The objectives of this study are concerned with the characterization of the intrinsic surface properties of corrosion products, and the extent and manner in which the surface properties can be changed by pretreatment conditions such as high temperature and chemisorption of surface active materials. The rationale for carrying out this investigation is related to the fact that the concentration and types of surface groups present on the iron substrate surface can have the capability of affecting both the adhesion properties of protective coatings and the concentration of water at the substrate/coating interface. Both of these factors, furthermore, can be influential for reducing the rate of corrosion of iron under different environmental conditions.

EXPERIMENTAL

Gas adsorption measurements are the primary technique used to evaluate the concentration of surface polar groups and the effectiveness of different surface modifications. Additional experimental techniques, such as heats of immersion, electrophoresis, and near infrared reflectance spectroscopy, have been used in this investigation in order to determine the nature of these polar groups under different conditions.

The iron oxide samples used in this investigation, α-Fe_2O_3, α-FeOOH, and γ-FeOOH, were precipitated from solution according to experimental techniques described in the Second Annual Report, page 161, November 1, 1981. Previous work had investigated Fe_3O_4 and α-Fe_2O_3 obtained from Pfizer Inc. The current and future experiments are expected to investigate iron oxide samples prepared and characterized in this laboratory.

The argon gas adsorption isotherms for specific area determination were obtained at liquid nitrogen temperatures using a classical BET volumetric vacuum rig. The residual pressure of 10^{-6} torr differential pressure transducer (Datametrics, Inc.) was used to measure the argon gas pressure with a sensitivity of 10^{-3} torr. Specific areas were calculated for argon molecular cross-section of 17 $Å^2$. The water adsorption isotherms were measured on a quartz spring (Worden Quartz Co.) balance with a sensitivity of 10 µg/g of sample. The equilibrium water vapor pressure was measured with a 100 torr capacitive differential manometer (Datametrics, Inc.).

The heats of immersion were measured in a thermistor type adiabatic calorimeter. The temperature changes in the calorimeter vessel were followed by measuring the change in resistance of the thermistor in a Wheatstone bridge and recording the off-balance of the bridge after amplification by a Hewlett-Packard DC Numm Voltmeter 419A. The workable sensitivity was 1×10^{-4}°C with a background noise of 2×10^{-4}°C in water. The sources of error in this calorimeter, i.e., instrument sensitivity, reproducibility of heat of bulb breaking, and reproducibility of heat capacity determination led to a cumulative error of +0.2J for each heat of immersion measurement.

A particularly sensitive technique for investigating adsorbate interactions with active surface sites and the nature of surface modifications is near infrared diffuse reflectance spectroscopy, NIR. A Cary 14R spectrometer with a double beam reflectance attachment provided the means for this investigation. Minimal sample heating was experienced due to the use of dispersed, diffuse illumination with spectra obtained for the range of 2.0 to 1.2 μm. A repetitive scan attachment permitted multiple scanning (typically 8 cycles from 2.0 to 1.2 back to 2.0 μm), thus enabling spectral averaging, a means of background noise reduction which results in signal enhancement. An AVIV computer interface was set to read the reflectance at 1.0 nm intervals, the value being encoded and recorded on a cassette tape for computer input.

Data processing for NIR was via a computer program which averaged both the baseline and the measured spectrum. The baseline was subtracted from the spectrum, the results being plotted either as an absorbance, reflectance or transformed into a transmission spectrum as a function of wavelength using the Schuster-Kubellca-Munk theory. The standard reference for this investigation was dehydrated MgO (J. T. Baker) which was dehydrated at 700°C at 5×10^{-6} torr. The reflectance cell was 2.5 cm diameter by 0.1 cm deep all quartz tube. The sample cell window was a low hydroxyl content Infra-Sil I (Dell Optics Co.), which was transparent over the useful wavelength range.

Electrophoretic mobility of the different iron oxide samples prepared in this laboratory, as well as samples obtained from Pfizer Inc., were measured on the Pen Kem System 3000. This instrument has the advantage of operating automatically while maintaining a high degree of precision and presenting the results in the form of electrophoretic mobility distribution curves.

RESULTS AND DISCUSSION

Solid/Gas Interface

Water adsorption results had previously been reported on α-Fe_2O_3 and Fe_3O_4 samples obtained from Pfizer Inc. and on α-FeOOH prepared in this laboratory. The approach has been to characterize the hydrophilic character of the different iron oxide samples, which have been identified as corrosion products, as a function of pretreatment conditions such as high temperature activation and chemisorption of trimethysilicon with surface hydroxyls via interaction with hexamethyldisilazane, HMDS. This approach has been continued with α-Fe_2O_3 and γ-FeOOH prepared in this laboratory.

The experimental approach adopted here, which utilizes gravimetric techniques for measuring water adsorption isotherms, is designed to determine the degree of surface hydrophilicity of iron oxides as a function of activation temperature in the range of 25° to 400°C under high vacuum, and after hydrophobing the surface with HMDS. The procedure measures the weight loss as a function of activation temperature, the water adsorption isotherms at 25°C after activation at the specified elevated temperature, and a second series of isotherms which follows the previous series after activation at 25°C. The intent is to compare the weight loss results to the amount of irreversibly adsorbed water after each isotherm, and also the decrease in monolayer capacity of the second isotherm activated at 25°C compared to the first isotherm which was activated at the elevated temperature. Since the intrinsic surface properties of the iron oxide sample are sought in this approach, the specific surface area, as determined from a BET analysis of argon adsorption isotherms at -195°C, was measured as a junction of activation temperature.

One approach to hydrophobe iron oxide is by chemical treatment of the surface. Since surface hydroxyl groups on iron oxides are primarily responsible for the adsorption of water, the approach was to chemically treat these hydroxyls so as to render them hydrophobic. Silanes, in general, are known to react with the proton of hydroxyls whether they are part of the surface or of an organic or inorganic molecule. Hexamethyldisilizane, HMDS, was used to treat α-Fe_2O_3 and Fe_3O_4 according to the following reaction:

$$2ROH + (CH_3)_3\,Si\text{-}\overset{\overset{H}{|}}{N}\text{-}Si(CH_3)_3 \longrightarrow NH_3 + 2ROSi(CH_3)_3$$

where R represents the iron oxide surface. HMDS adsorption isotherms were measured on α-Fe_2O_3 and γ-FeOOH at 25°C after sample activation at 400°C. The amount of irreversibly adsorbed HMDS, after subsequent activation at 25°C and 10^{-6} torr, was assumed to be due to the above chemical reaction where one molecule of HMDS reacts with two surface hydroxyl groups to yield two molecules of chemisorbed trimethylsilicon and one molecule of ammonia. The results show that the concentration of adsorbed trimethylsilicon was 1.5 and 2.5 groups/100 $Å^2$ for α-Fe_2O_3 and γ-FeOOH, respectively. Since the cross sectional area of trimethylsilicon is expected to be about 40 $Å^2$, 2.5 groups/100 $Å^2$ represents close packing and hence a maximum value.

There has been a question concerning the disposition of NH_3 after interaction of HMDS with the surface. Zettlemoyer and Hsing [19] have shown by near infrared diffuse reflectance spectroscopy measurements that NH_3 remains adsorbed after activation at 25°C under 10^{-6} torr, and is essentially removed after 170°C activation. Since the nitrogen atom is a proton acceptor, NH_3 can be expected to be strongly physically adsorbed with available surface hydroxyls in competition with water. If all the NH_3 produced by HMDS interaction with the surface interacts in this fashion, then the surface concentration of NH_3 would be 0.75 and 1.25 molecules/100 $Å^2$ for HMDS treated α-Fe_2O_3 and γ-FeOOH, respectively. The analysis of results will be based on this interpretation of HMDS interaction with the iron oxide surfaces under investigation.

The water adsorption isotherm results on α-Fe_2O_3 are presented in

Figures 1-5. Each figure contains the first and second water adsorption isotherms measured at 25°C for the untreated sample and the sample which has been treated with HMDS after 400°C activation for the designated activation temperatures which are in the range of 25 to 400°C. The first isotherm represents the measurement which is carried out immediately after activation at the designated temperature, and the second isotherm represents the measurement which is carried out by activating the sample at 25°C immediately after completion of the first isotherm. The HMDS treated samples have all been exposed to 400°C activation prior to adsorption of HMDS. Figures 6-10 present the same results for γ-FeOOH.

The gas adsorption results are summarized in Tables I and II for α-Fe_2O_3 and γ-FeOOH, respectively. The specific surface areas were calculated from a BET analysis of argon adsorption isotherms at -196°C in order to express the adsorption isotherms in terms of molecules adsorbed per unit area, i.e., in order to determine the intrinsic properties of the surface. The weight loss measurements represent the equilibrium loss in weight at the designated temperature compared to the weight at 25°C with a nominal pressure of 10^{-6} torr. The effective monolayer values for the first and second isotherms, W_{m1} and W_{m2}, were obtained from the inflection point of the water adsorption isotherms, i.e., the B point. The irreversibly adsorbed water represents the water which was adsorbed in the first isotherm and was not desorbed after activation at 25°C.

The surface area results show that both α-Fe_2O_3 and γ-FeOOH increase in surface area to a maximum value at 200°C followed by a decrease. Since there is no apparent change in particle size as a function of activation temperature, the decrease in surface area at the higher activation temperature is assumed to be due to surface sintering. The increase in surface area at 200°C is due to decreased surface porosity brought about the desorption of water from the interior of the sample. This latter effect is much more pronounced for γ-FeOOH which undergoes a dehydration conversion to α-Fe_2O_3. The theoretical amount of water loss in this conversion is 101 mg per gram of sample. Figure 11 presents the bulk weight loss as a function of activation temperature for all the iron oxide samples investigated, where the bulk weight loss is calculated by subtracting the surface water from the total weight loss. The indication is that γ-FeOOH contains the stoichiometric amount of water while the other samples contain excess water to varying degrees.

Figure 12 presents the reversible and irreversible surface polar site concentration as a function of activation temperature for α-Fe_2O_3, where the reversible sites are calculated by subtracting the measured irreversibly adsorbed water from the water monolayer values of the first isotherms presented in Table I. The indication for the untreated sample is that the reversible site concentration decreases from 8 sites/100 $Å^2$ to 5.5 sites/100 $Å^2$ at activation temperatures above 100°C, and that the irreversible site concentration increases from zero to about 2.5 sites/100 A^2 at activation temperature above 25°C. The indication for the HMDS treated α-Fe_2O_3 is that the reversible water has been reduced to a relatively constant value of 3.5 sites/100 $Å^2$, and that the irreversible site concentration increases above 100°C activation. The interpretation of these results is that HMDS interacts with the surface, with a measured value of 1.5 trimethylsilicon groups/100 $Å^2$, to reduce the reversible water by 2 to 3 sites/100 $Å^2$, but that the irreversible water increases primarily due to the desorption of adsorbed NH_3 at activation temperatures above 100°C.

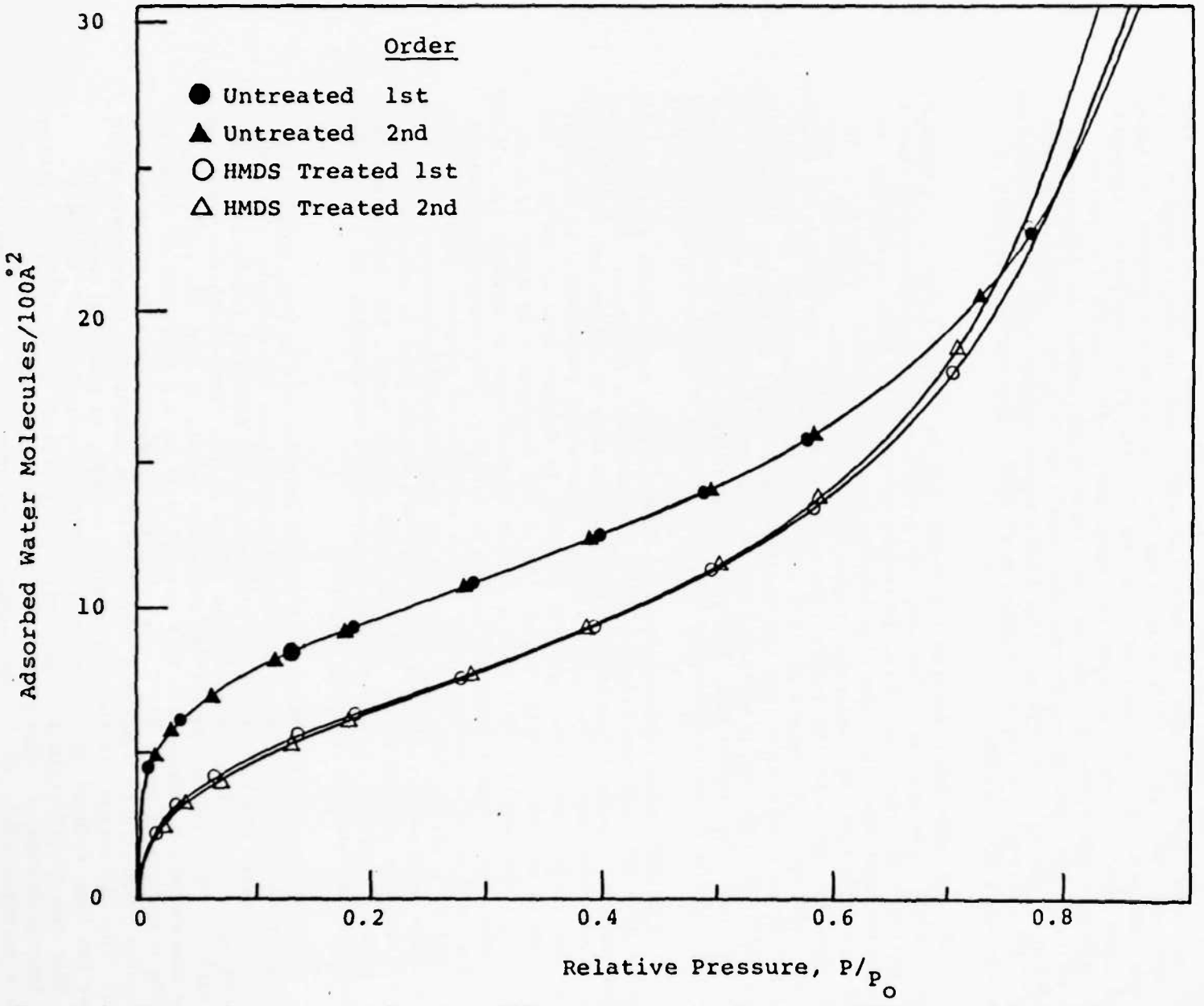

Figure 1. Water adsorption isotherms at 25°C on untreated α-Fe_2O_3 and HMDS treated α-Fe_2O_3 (400°C) after 25°C activation.

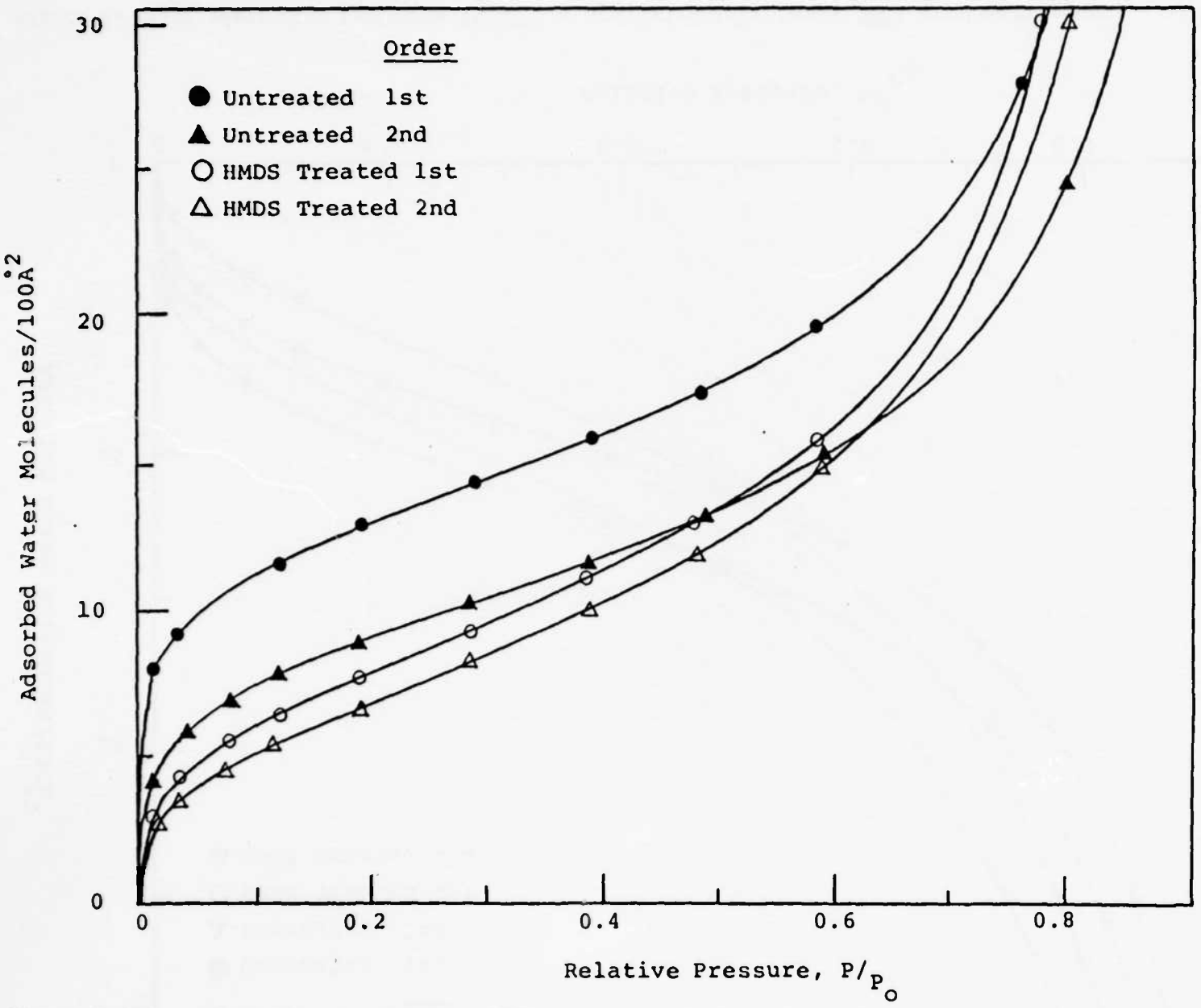

Figure 2. Water adsorption isotherms at 25°C on untreated α-Fe_2O_3 and HMDS treated α-Fe_2O_3 (400°C) after 100°C activation.

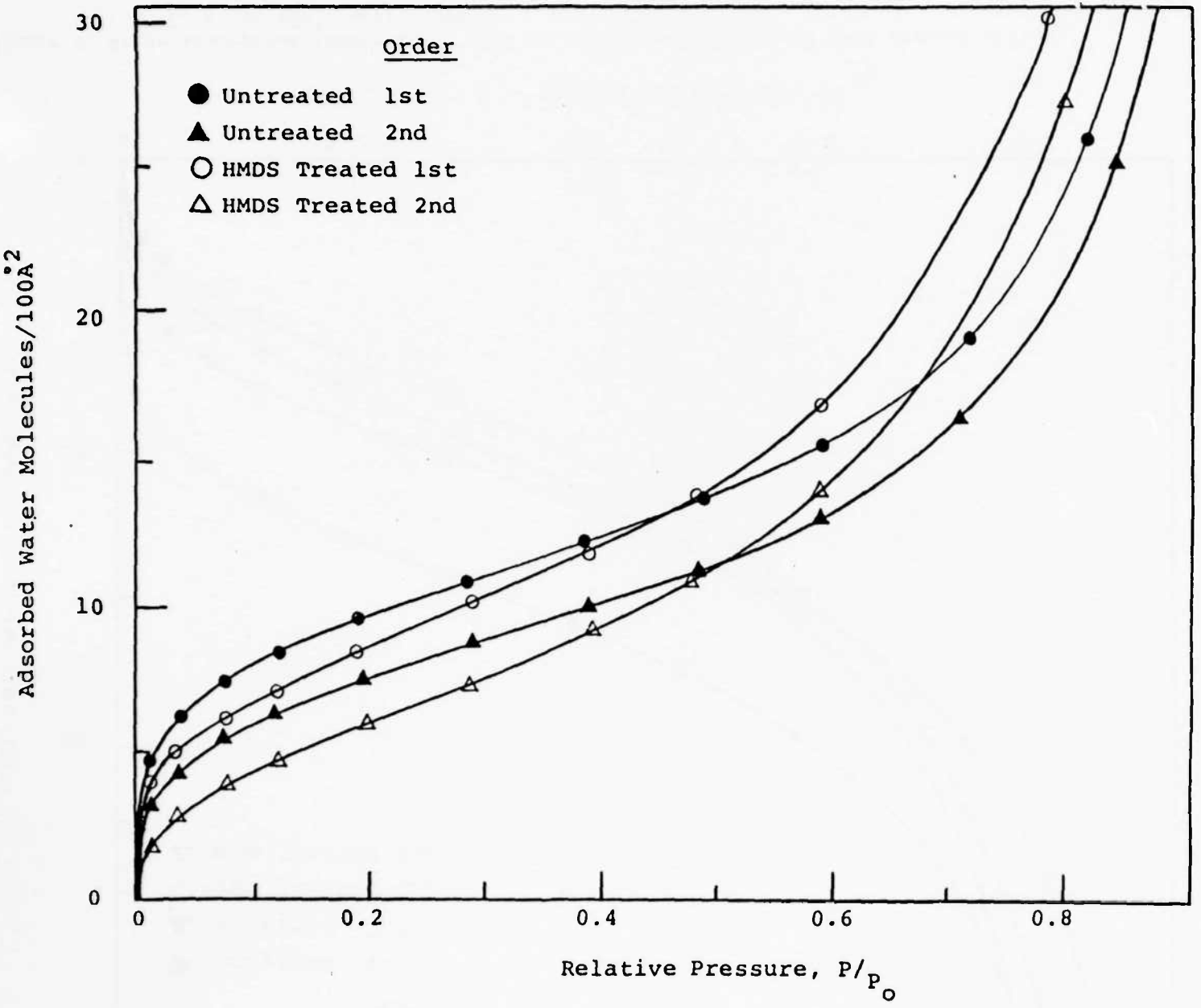

Figure 3. Water adsorption isotherms at 25°C on untreated α-Fe_2O_3 and HMDS treated α-Fe_2O_3 (400°C) after 200°C activation.

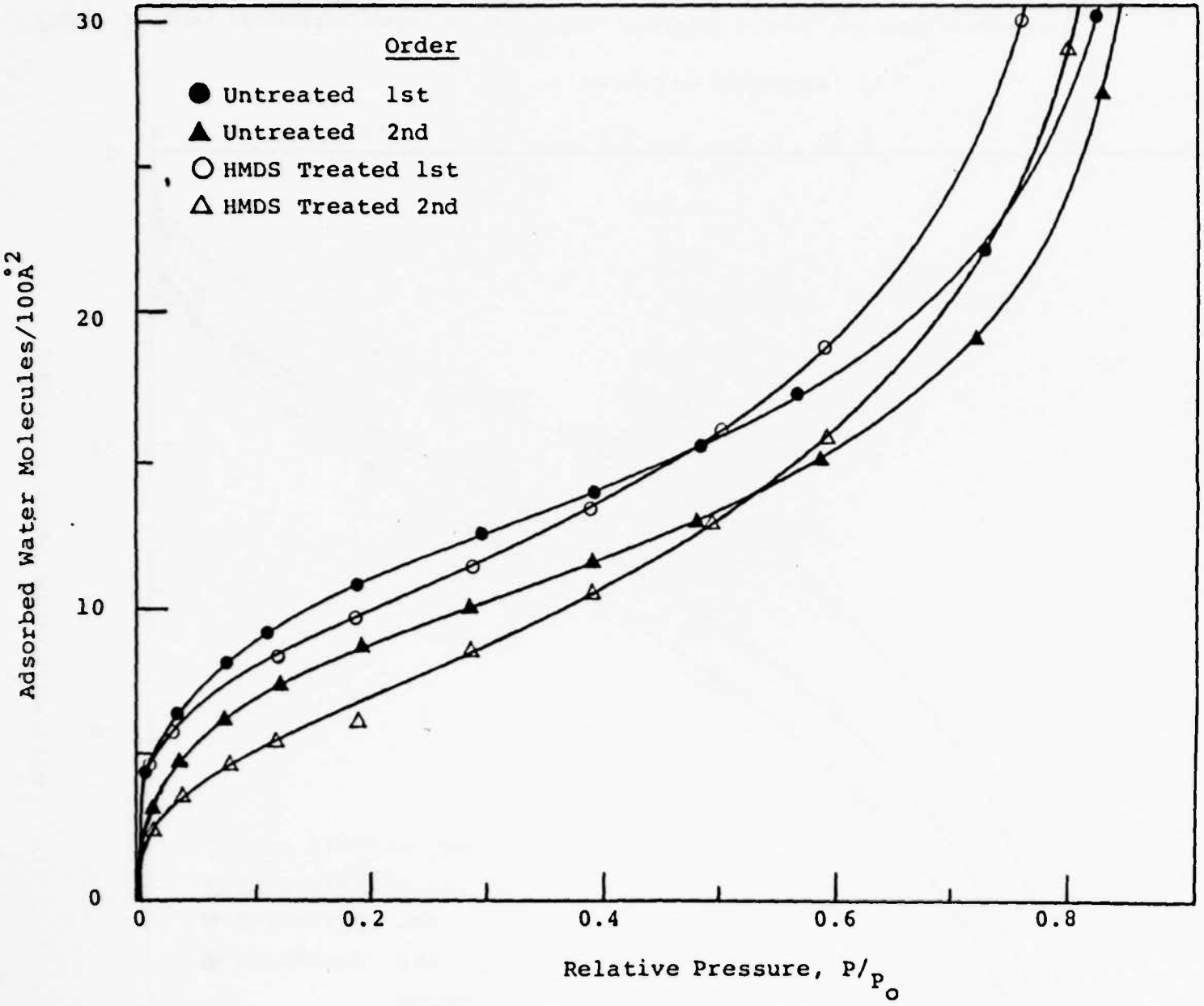

Figure 4. Water adsorption isotherms at 25°C on untreated α-Fe_2O_3 and HMDS treated α-Fe_2O_3 (400°C) after 300°C activation.

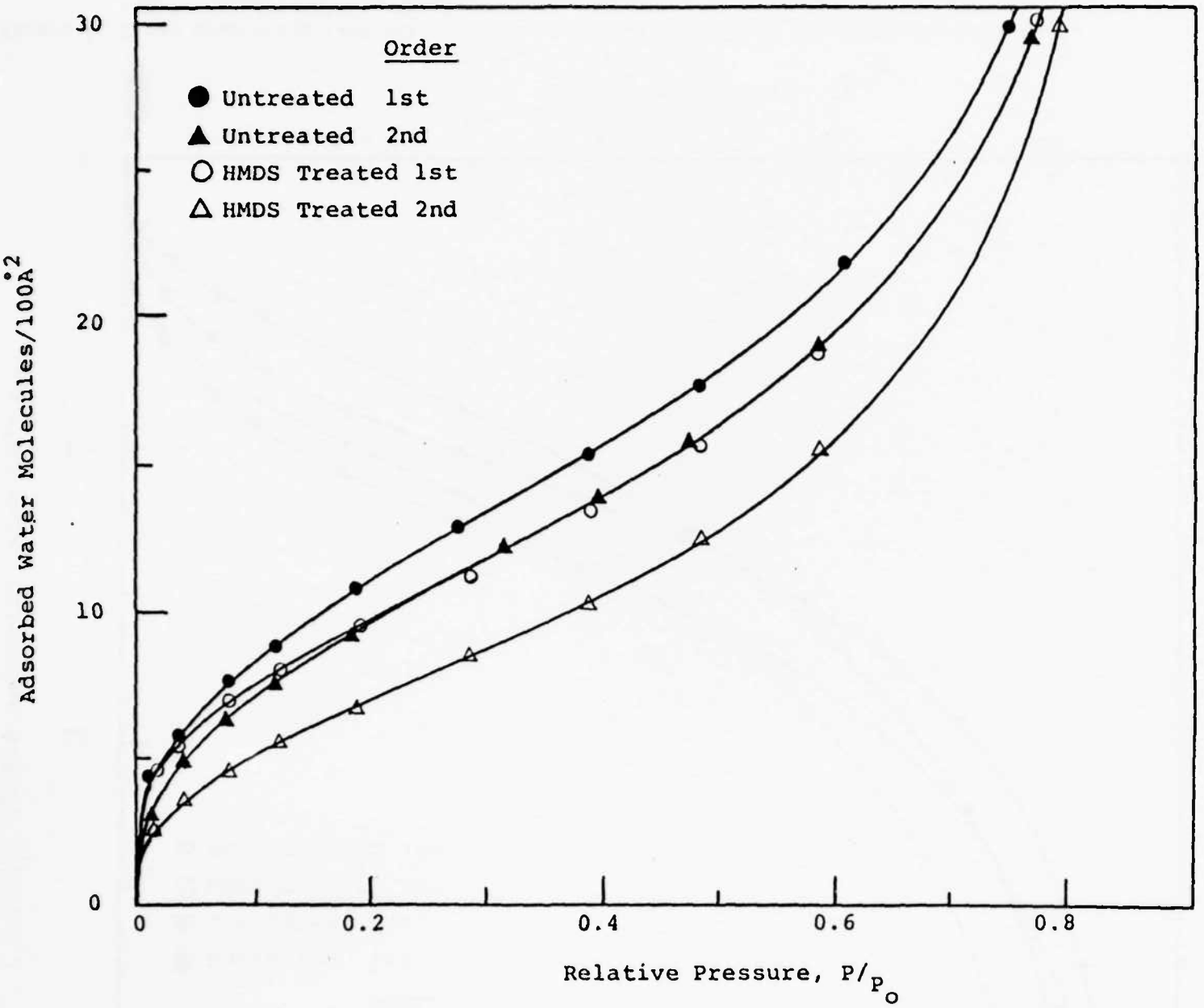

Figure 5. Water adsorption isotherms at 25°C on untreated α-Fe_2O_3 and HMDS treated α-Fe_2O_3 (400°C) after 400°C activation.

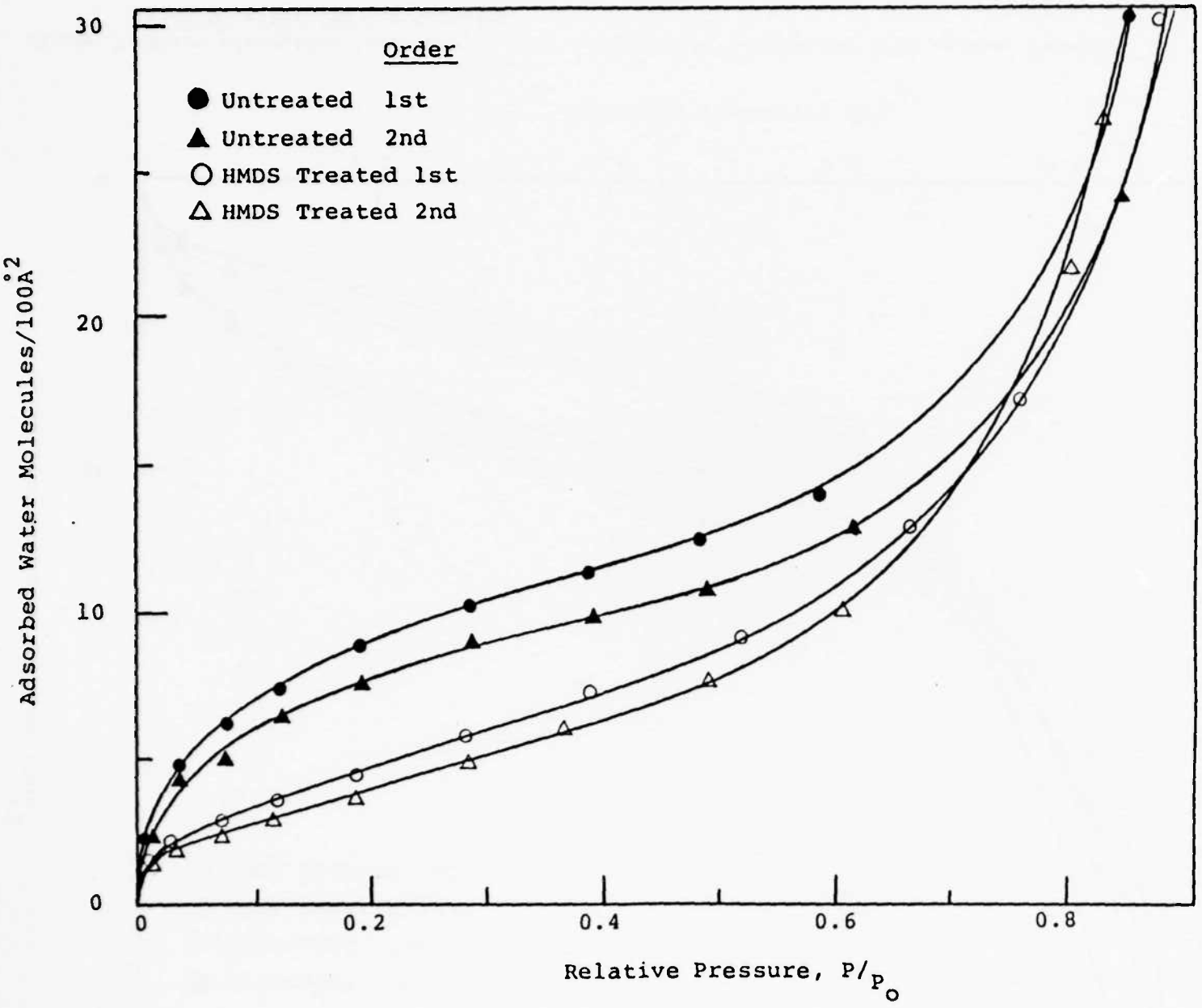

Figure 6. Water adsorption isotherms at 25°C on untreated γ-FeOOH and HMDS treated γ-FeOOH (400°C) after 25°C activation.

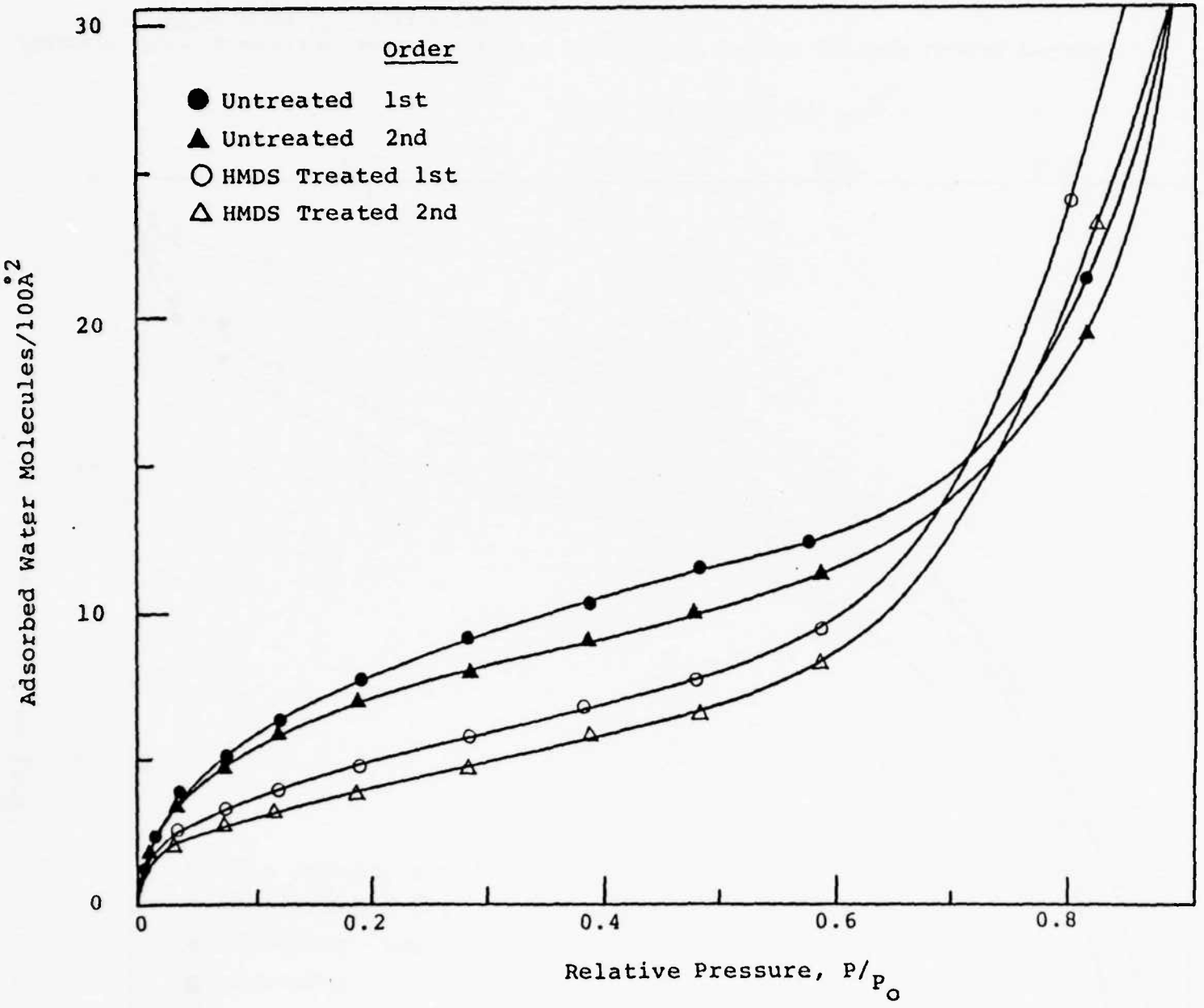

Figure 7. Water adsorption isotherms at 25°C on untreated γ-FeOOH and HMDS treated γ-FeOOH (400°C) after 100°C activation.

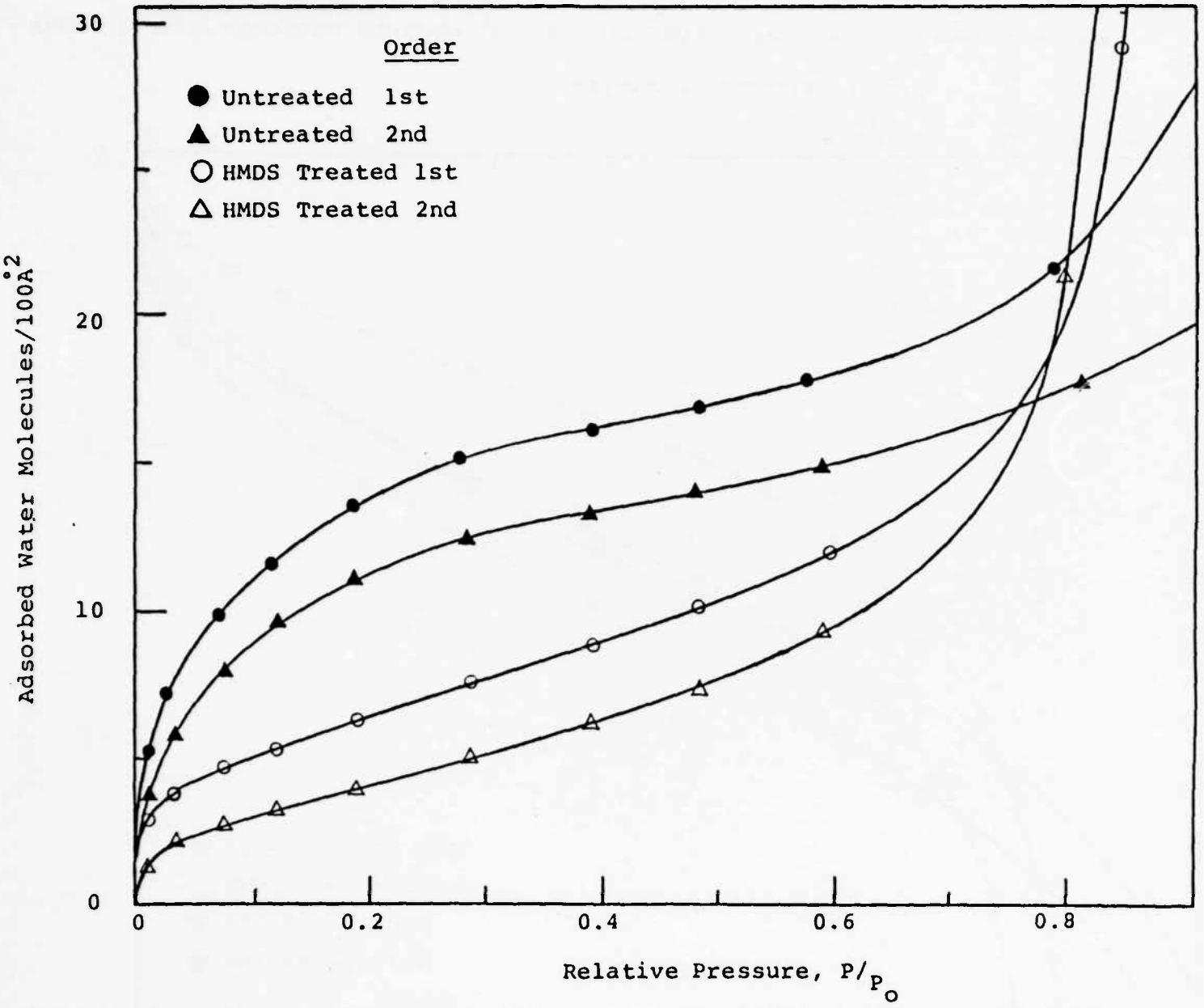

Figure 8. Water adsorption isotherms at 25°C on untreated γ-FeOOH and HMDS treated γ-FeOOH (400°C) after 200°C activation.

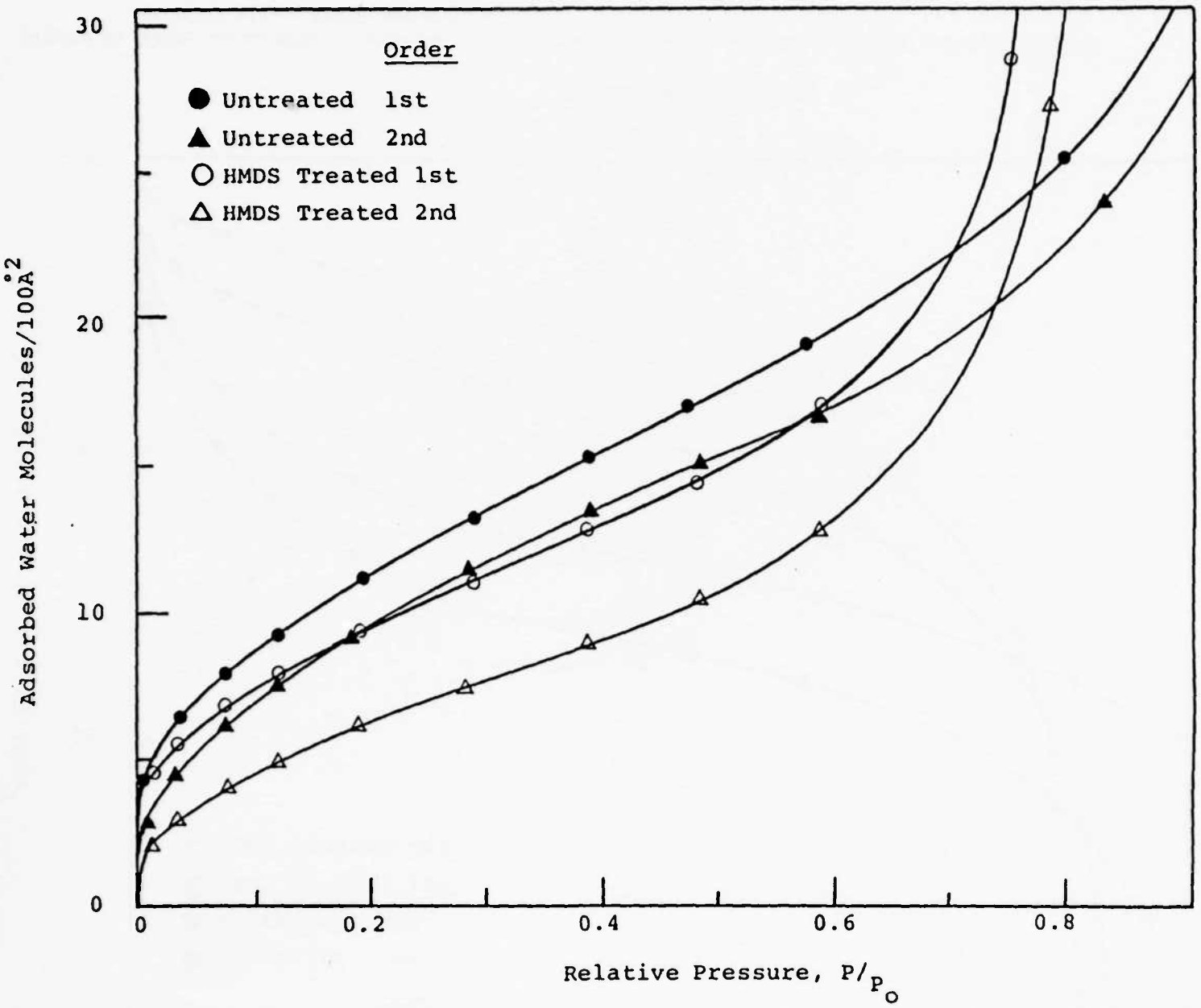

Figure 9. Water adsorption isotherms at 25°C on untreated γ-FeOOH and HMDS treated γ-FeOOH (400°C) after 300°C activation.

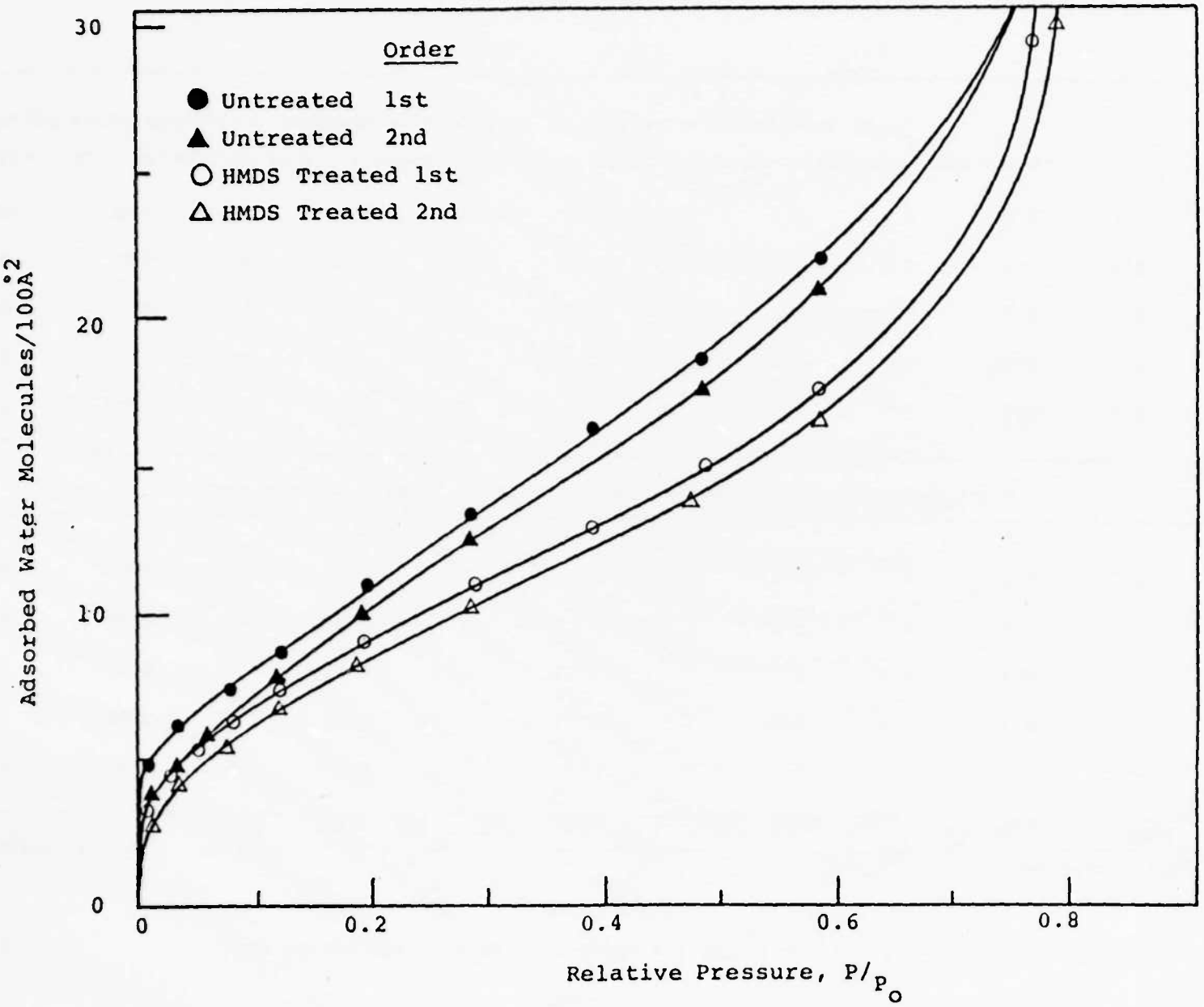

Figure 10. Water adsorption isotherms at 25°C on untreated γ-FeOOH and HMDS treated γ-FeOOH (400°C) after 400°C activation.

Table I

Gas Adsorption Results on α-Fe_2O_3 and HMDS Treated α-Fe_2O_3

Activation Temp, °C	Surface Area, m^2/g	Wt.Loss mg/g	α-Fe_2O_3 W_{m1}* mg/g	W_{m1}* Mol./100Å^2	W_{m2}** mg/g	W_{m2}** Mol./100Å^2	$W_{m1}-W_{m2}$ mg/g	$W_{m1}-W_{m2}$ Mol./100Å^2	Irrev. Adsorbed H_2O mg/g	Irrev. Adsorbed H_2O Mol./100Å^2
25	56.3	--	13.3	7.9	--	--	--	--	--	--
100	59.6	11.3	20.0	11.2	13.4	7.5	6.6	3.7	7.3	4.1
200	69.2	19.7	16.3	7.9	12.6	6.1	3.7	1.8	4.9	2.4
300	61.3	25.5	16.1	8.8	12.6	6.9	3.5	1.9	5.7	3.1
400	36.6	30.3	9.1	8.3	7.8	7.1	1.3	1.2	2.9	2.7
HMDS Treated α-Fe_2O_3 after 400°C Activation (1.5 Groups/100 Å^2)										
25	36.6	--	5.4	4.9	5.1	4.7	0.3	0.2	1.2	1.1
100	36.6	2.1	6.7	6.1	5.7	5.2	1.0	0.9	1.9	1.8
200	36.6	4.4	7.3	6.7	4.9	4.5	2.4	2.2	3.9	3.6
300	36.6	6.0	8.7	7.9	5.6	5.1	3.1	2.8	5.4	4.9
400	36.6	5.7	8.2	7.5	5.7	5.2	2.5	2.3	4.1	3.7

*First water adsorption isotherm monolayer at 25°C after indicated activation temperature.

**Second water adsorption isotherm monolayer at 25°C after activation at 25°C.

Table II

Gas Adsorption Results on γ-FeOOH and HMDS Treated γ-FeOOH

γ-FeOOH

Activation Temp, °C	Surface Area, m^2/g	Wt.Loss mg/g	W_{m1}*		W_{m2}**		$W_{m1}-W_{m2}$		Irrev. Adsorbed H_2O	
			mg/g	Mol./100Å^2	mg/g	Mol./100Å^2	mg/g	Mol./100Å^2	mg/g	Mol./100Å^2
25	20.4	--	4.3	7.0	--	--	--	--	--	--
100	22.0	0.9	3.4	5.6	3.3	5.4	0.1	0.2	1.5	2.2
200	26.5	89.2	6.7	11.0	5.4	8.9	1.3	2.1	9.9	3.8
300	40.5	96.8	5.3	8.7	4.6	7.5	0.8	1.3	4.0	3.3
400	14.1	100.1	5.0	8.2	4.4	7.2	0.6	1.0	0.6	1.2
HMDS Treated γ-FeOOH after 400°C Activation (2.5 Groups/100 Å^2)										
25	14.1	--	2.1	3.4	1.7	2.8	0.4	0.6	0.5	1.2
100	14.1	0.2	2.3	3.7	1.9	3.1	0.4	0.7	0.5	1.2
200	14.1	1.7	3.2	5.2	1.8	3.0	1.3	2.2	1.3	3.2
300	14.1	0.9	4.1	6.8	2.8	4.6	1.3	2.2	2.0	4.6
400	14.1	0.2	4.3	7.0	3.8	6.3	0.4	0.7	0.7	1.7

*First water adsorption isotherm monolayer at 25°C after indicated activation temperature.

**Second water adsorption isotherm monolayer at 25°C after activation at 25°C.

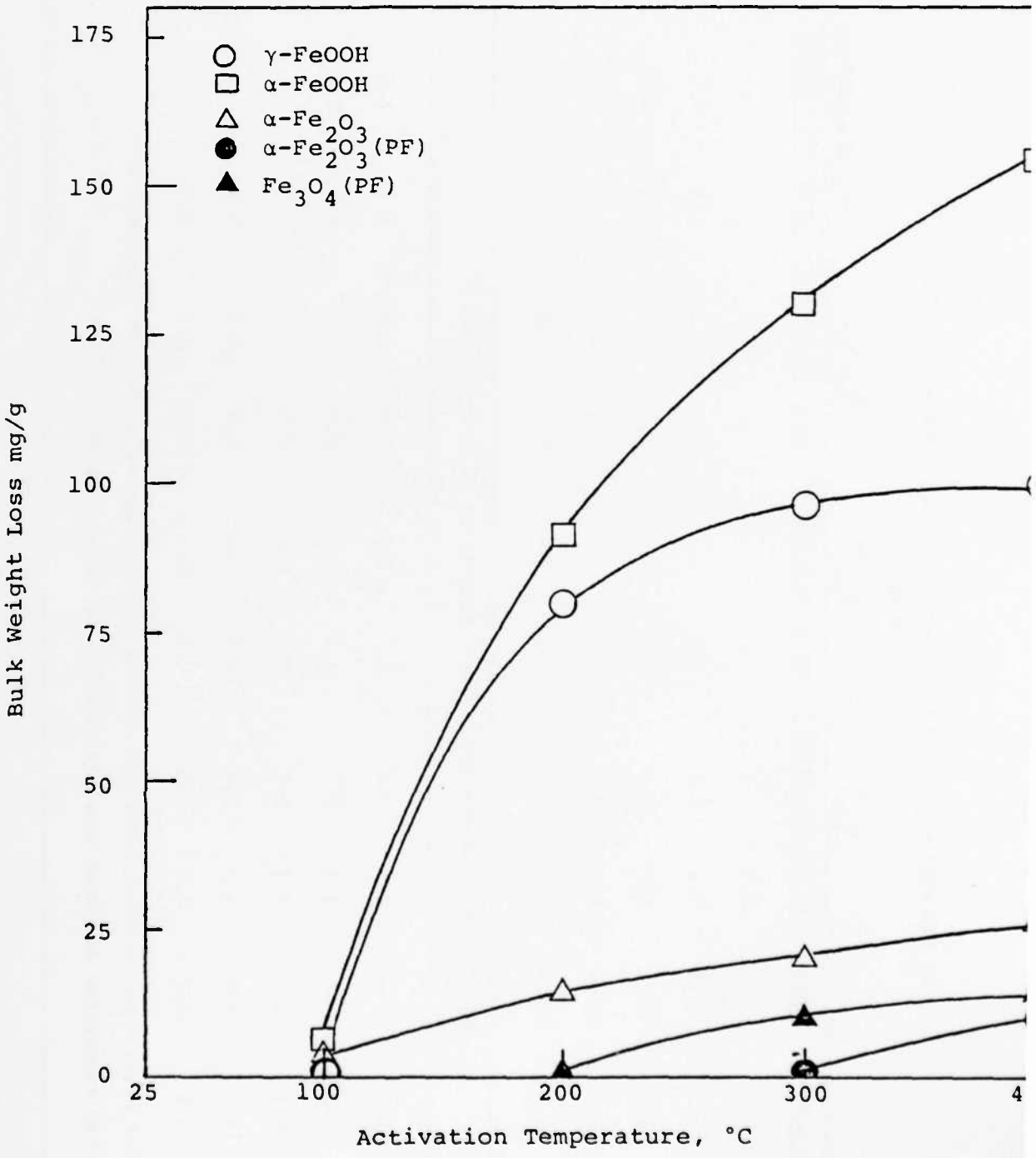

Figure 11. Bulk weight loss calculated from measured total weight loss of iron oxide samples as a function of activated temperature.

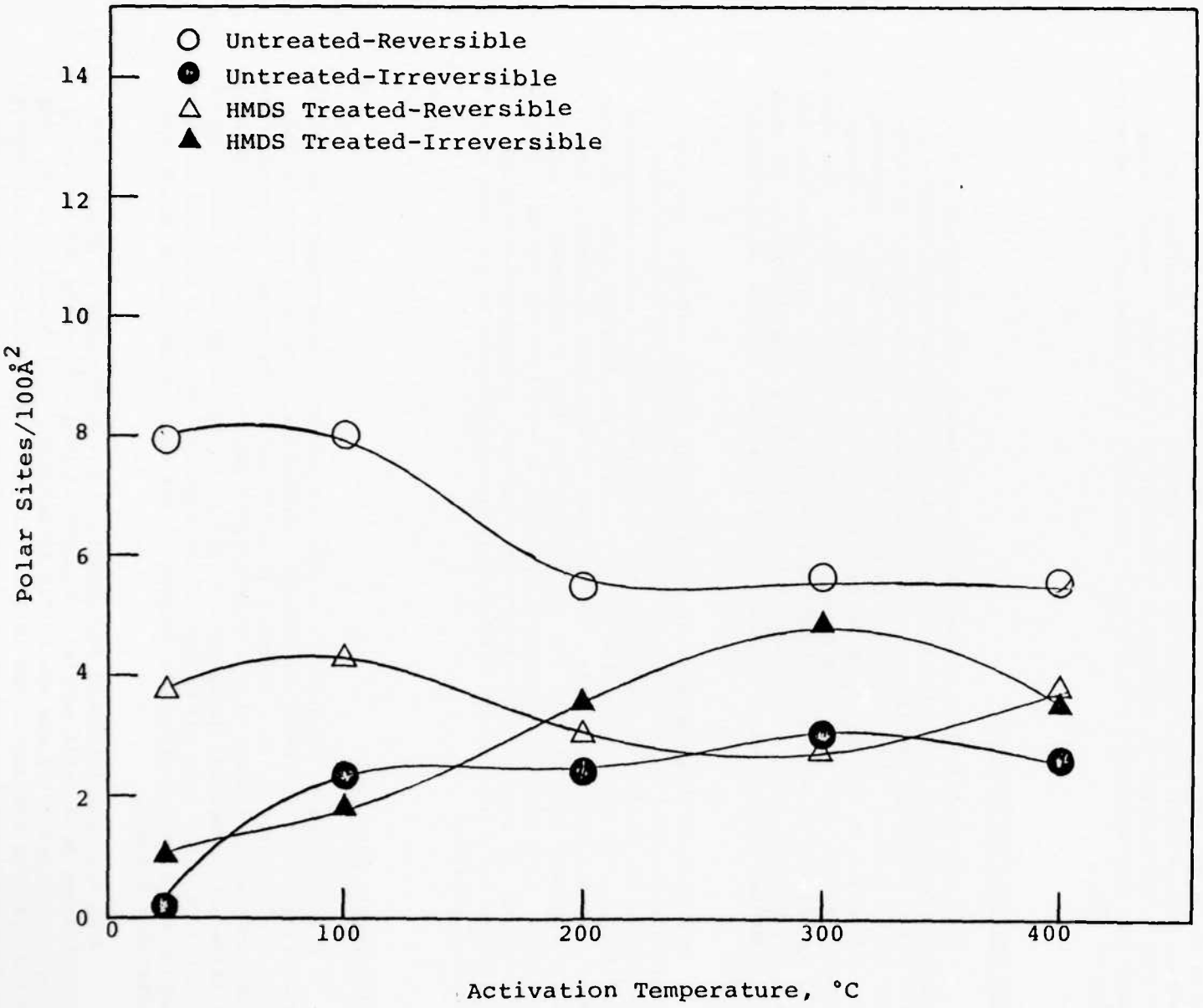

Figure 12. Polar site concentration as a function of activation temperature on untreated α-Fe_2O_3 and HMDS treated α-Fe_2O_3 after 400°C activation.

Figure 13 presents the reversible and irreversible surface polar site concentration as a function of activation temperature for γ-FeOOH. Although there is large scatter for the reversibly adsorbed water of the untreated sample, the results for γ-FeOOH are very similar to those obtained with α-Fe_2O_3. The scatter is especially prevalent for the HMDS treated sample, which has been converted to α-Fe_2O_3 by the 400°C activation prior to adsorption of HMDS.

Near Infrared Reflectance

Near infrared diffuse reflectance spectroscopy, NIR, represents a sensitive technique for qualitative investigation of the groups present on iron oxide surfaces, and the nature of interaction of adsorbate molecules with those groups. This technique is considered to be especially important for understanding the nature and extent of surface modification. Although measurements of this type have been carried out in this laboratory, the sample cell and method of activation have been modified, and the data treatment has been upgraded in order to increase the resolution of peak definition by means of a computer program which is designed to reduce the effects of background noise.

Preliminary measurements have been carried out on α-Fe_2O_3 over the wavelength range of 1.18 to 2.0 microns in the diffuse reflectance mode. The sample was loaded in the cell and a spectrum measured under atmospheric conditions, 10^{-6} torr activation at 25°C, and in equilibrium with 1 mm water vapor. Data processing of the original spectra has been hindered by bugs in the computer program with the result that the data enhancement is not yet complete. Although molecular water has been detected in the raw data at 1.9 microns, the OH peak at 1.36 microns requires data enhancement for peak evaluation. The preliminary measurements are expected to be improved in the near future.

Solid/Liquid Interface

Electrophoretic mobility techniques represent an experimental method for evaluating the proton donor or acceptor tendencies of surface polar groups, which are amphoteric, as a function of their ionic environment in water. Previous studies have shown that electrokinetic potential — i.e., zeta potential — of different commercial grade iron oxides at different pH values are a function of the iron oxide type and method of preparation. Complete analysis of these samples was somewhat difficult because of the surface impurities which were invariably present.

Work has been initiated for studying the electrophoretic mobility of the different iron oxide samples, prepared in this laboratory and currently under investigation by gas adsorption techaniques, as a function of pH. The initial results are summarized in Table III where the electrophoretic mobilities are presented for a pH value of 1.8. It should be noted that all the samples have a positive charge at this pH, and that α-Fe_2O_3 (Pfizer) and γ-FeOOH exhibit the highest positive charges with electrophoretic mobilities

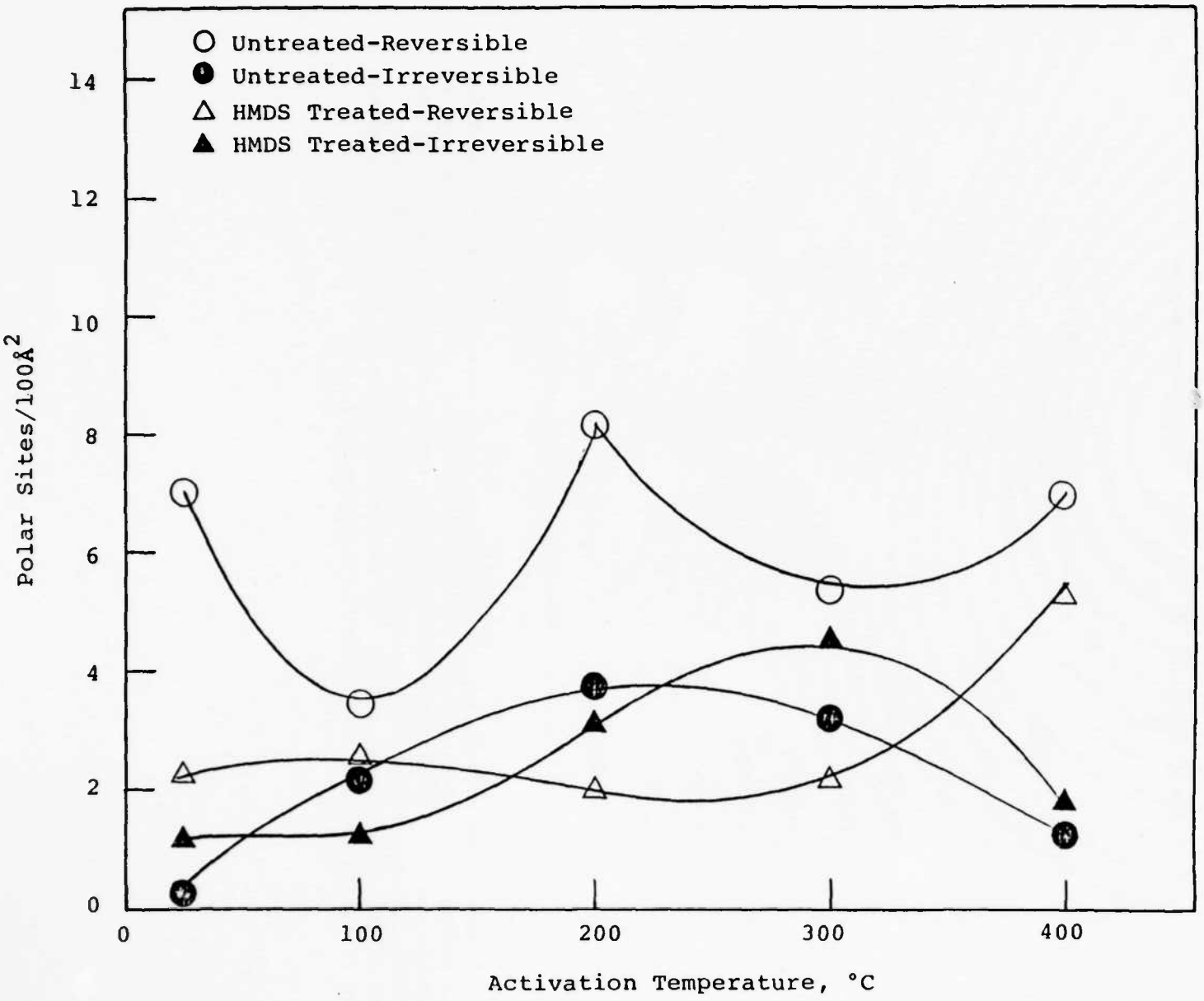

Figure 13. Polar site concentration as a function of activation temperature on untreated γ-FeOOH and HMDS treated γ-FeOOH after 400°C activation.

Table III

Electrophoretic Mobility of Iron Oxide Samples at pH 1.8

Sample	Electrophoretic Mobility μm cm/volt sec
α-Fe_2O_3 (Pfizer)	2.9
α-Fe_2O_3	2.0
Fe_3O_4 (Pfizer)	2.2
Fe_3O_4	2.0
γ-Fe_2O_3	2.4
α-FeOOH	2.3
β-FeOOH	2.0
γ-FeOOH	2.8
δ-FeOOH	2.2

of 2.9 and 2.8 μm cm/volt sec, respectively, which corresponds to a calculated zeta potential of about 50 mV. The suspicion for the Pfizer sample is that it contains surface impurities which contribute to the surface charge, while the γ-FeOOH contains a high concentration of surface OH groups which adsorb protons at low pH. Further results are required in order to determine the mechanism of ion adsorption as a function of OH concentration.

CONCLUSIONS

The HMDS treatment has been shown to have a measurable effect on decreasing the surface hydrophilicity of α-Fe_2O_3 and γ-FeOOH, as well as from previous results, α-FeOOH and Fe_3O_4. The proposed mechanism for this HMDS interaction is chemisorption of the trimethylsilicon group with the oxygen of the surface OH. Although both α-Fe_2O_3 and δ-FeOOH exhibited about the same degree of surface hydrophilicity from water adsorption isotherm results, α-Fe_2O_3 irreversibly adsorbed 1.5 trimethylsilicon groups/100 $\AA^2$ as compared to 2.5 trimethylsilicon groups/100 $\AA^2$ for γ-FeOOH. Since the cross sectional area of trimethylsilicon is of the order of 40 A^2, the value of 2.5 groups/100 $\AA^2$ represents a maximum value due to close packing. The interpretation of these results is that the surface OH groups are more randomly distributed on γ-FeOOH as compared to α-Fe_2O_3. This interpretation is consistent with the electrophoretic mobility results at a pH value of 1.8 where γ-FeOOH exhibits a higher positive charge than α-Fe_2O_3, where the latter contains clusters of surface OH groups and proton adsorption is limited by localized coulombic repulsion.

All of the iron oxide surfaces investigated thus far interact with HMDS to yield chemisorbed trimethylsilicon which effectively hydrophobes the surfaces to varying degrees. There is no doubt that this silane type interaction, which is basically replacement of the OH proton with a silicon containing group, will occur on a corroded iron oxide surface with a variety of different silane molecules containing different functional groups. The implication is that this type of chemisorption can be used to decrease surface hydrophilicity of iron oxide and at the same time increase adhesion of a protective coating through selection of the appropriate silane molecule.

Experiments are currently underway to verify the above interpretation of results by means of NIR techniques. Further experiments are also being designed to increase the degree of hydrophobing the surface through interaction of smaller hydrophobic molecules with surface polar sites present on the iron oxide surfaces. This approach will require determination of the appropraite experimental conditions which will result in the irreversible adsorption of small molecules, such as methanol, with surface OH groups.

REFERENCES

[1] T. A. Banfield, Progress in Organic Coatings 7, 253 (1979).

[2] M. J. Graham and M. Cohen, Corrosion 32, 432 (1976).

[3] E. McCafferty and A. C. Zettlemoyer, J. Colloid Interface Sci. 34, 452 (1970).

[4] A. C. Zettlemoyer and E. McCafferty, Z. Phys. Chem. N. F. 64, 41 (1969).

[5] E. McCafferty and A. C. Zettlemoyer, Trans. Faraday Soc. 66, 1720 (1970).

[6] E. McCafferty and A. C. Zettlemoyer, Trans. Faraday Soc. 66, 1732 (1970).

[7] E. McCafferty and A. C. Zettlemoyer, Disc. Faraday Soc. 52, 239 (1971).

[8] G. Blyholder and E. A. Richardson, J. Phys. Chem. 66, 2597 (1962).

[9] J. J. Jurinak, J. Colloid Sci. 19, 477 (1964).

[10] T. Morimoto, M. Nagao, and F. Tokuda, J. Phys. Chem. 73, 243 (1968).

[11] F. O. Stark, O. K. Johannson, G. E. Vogel, R. G. Chaffee, and R. M. Lacefield, J. Phys. Chem. 72, 2750 (1968).

[12] W. Hertal and M. L. Hair, J. Phys. Chem. 75, 181 (1971).

[13] M. L. Hair, J. Colloid Interface Sci. 60, 154 (1977).

[14] V. Y. Davydov, A. V. Kiselev, and L. T. Zhuravlev, Trans. Faraday Soc. 60, 2254 (1964).

[15] M. L. Hair and W. Hertl, J. Phys. Chem. 73, 2372 (1969).

[16] A. C. Zettlemoyer and H. H. Hsing, J. Colloid Interface Sci. 55, 637 (1976).

[17] A. C. Zettlemoyer and H. H. Hsing, J. Colloid Interface Sci. 58, 263 (1977).

[18] A. V. Kiselev, B. V. Kuzhetsov, and S. N. Lanin, J. Colloid Interface Sci. 69, 148 (1979).

[19] H. H. Hsing and A. C. Zettlemoyer, Prog. Colloid & Polymer Sci. 61, 54 (1976).

Program #12

Drying and Curing of Epoxy Films

INTRODUCTION

Air drying is the most widely used method in removing solvent from coatings films. Temperature, relative humidity and air flow velocity are the drying parameters studied in this connection. Usually, drying rate curves for a given coating formulation, i.e., flux of solvents vs. drying time, are generated as a function of the above drying parameters. These drying rate curves are valuable: (i) in predicting drying patterns especially under intense drying environments, (ii) in providing information about the mechanism of film formation and its consolidation, (iii) in reflecting the formation of certain types of defects during the drying step such as skin formation, blisters, and cracks.

Recognizing the important role played by the rates of drying of organic coatings in corrosion protection, it was decided to conduct a systematic study on drying of five different systems of epoxy resin-curing agent mixtures: (i) solvent-based Epon 1001 and Emerez 1511, (ii) aqueous-based latex of Epon 1001 and Emerez 1511 [Lehigh Formula], (iii) modified aqueous-based latex of Epon 1001 and Emerez 1511 [Lehigh Formula]; (iv) modified Epi-Rez 510 liquid epoxy resin and Epi-Cure W-50-8535 [Celanese formulation], and (v) modified Epi-Rez 510 liquid epoxy resin and Epi-Cure WC-60-8537 [Celanese formulation].

OVERALL OBJECTIVES

1. To generate drying curves for the above five systems of epoxy-curing agent (unpigmented and pigmented) under different drying parameters (temperature, relative humidity and air flow velocity).

2. To study the morphology of the above dried epoxy films.

3. To study the corrosion protection performance of the above dried epoxy films.

4. To correlate the effect of drying conditions on the morphology and corrosion protection performance of epoxy coatings.

PROGRESS

During this period an M.S. Research Report was completed, submitted to and accepted by the Department of Chemical Engineering at Lehigh. The Conclusions of this work as outlined in the M.S. Report are as follows:

Drying studies of epoxy resin-curing agent systems indicate distinct drying trends in water-borne and solvent-based formulations. For a given set of drying conditions, solvent-based and aqueous-based systems exhibit highest and lowest values of flux (average and instantaneous), respectively, while the Celanese formulations have values intermediate between them. The drying rates of aqueous-based, modified latex and Celanese formulations decreased with drying time until most of the water in the film was removed. In most cases the flux (average and instantaneous) increased towards the end of the drying operation and, in some cases, dropped after attaining a maximum value. This increase in drying rate at the end of the drying process is explained in terms of skin formation during the initial stages of drying and its rupture at the end of the drying operation. In general, the drying rates increased with increased temperature and reduced relative humidity. The drying behavior of solvent-based systems was found to be independent of the relative humidity of the drying air.

Morphology studies showed a rough surface and the presence of cracks in almost all the water-borne coatings. Solvent-based films were comparatively smoother and had fewer cracks in their surface. The surface morphology of epoxy films is affected by the nature of the substrate. Films on glass substrates showed greater cracking tendency as compared to films cast on steel panels. Also, the films formed from low initial solid content appear to have a rough surface, with the surface becoming smoother as the initial solids content was increased. Baking of films already dried in the wind tunnel resulted in a comparatively smooth surface. However, when wet films were dried in an oven preheated to 145-150°C, cracks appeared in the films of all the coating formulations including the solvent-based system. The cracking tendency of epoxy systems increased with increasing film thickness.

Cathodic disbonding studies revealed that for a given set of drying and curing conditions, Celanese formulation 24-174 was most resistant to delamination and solvent-based system the least, while Celanese formulation 24-180 was found to have values in-between the two. The resistance to cathodic delamination increased when the films were dried at higher temperature and lower relative humidity. Best results in terms of corrosion protection performance were obtained when the films were baked in the oven at 150°C for 30 min after drying them in the wind tunnel under known drying conditions. However, no definite trend in the delamination behavior of epoxy coatings was observed when they were allowed to cure at room temperature for 8 weeks.

The corrosion protection performance of epoxy coatings was explained in terms of their drying and curing behavior.

Program #13

Analysis of Electrodeposited Epoxy Resin by Laser Raman Microprobe

In the preparation of epoxy films on steel, aqueous emulsions of Epon 1001 (diglycidyl ether of bisphenol A) and Emerez 1511 (a polyamide prepared from dimer acids and a diamine) are mixed and cathodically electrodeposited on the steel. The Emerez 1511 serves as the curing agent for the Epon 1001, presumably by reaction of the residual free amine groups of the Emerez with the epoxy groups of the Epon:

$$A-CH\underset{O}{\diagdown\diagup}CH_2 + B-\underset{H}{N}-R \longrightarrow A-\underset{OH}{CH}-CH_2-\underset{R}{N}-B \ ,$$

where A represents the residue attached to the epoxy group in Epon 1001, and B represents the residue attached to the amine group in Emerez 1511. The symbol R stands for either H, if the reactive amine is primary, or an organic moiety, if it is secondary.

The intent is to electrodeposit the Epon and Emerez in stoichiometric ratio, but this is very hard to achieve. The amount deposited depends strongly on the diffusion characteristics of the two reactants. One is likely to get layering and uneven film formation. We therefore wished to have a method of spot checking the deposited film, to determine whether the film is homogeneous or, if not, the degree of variation from spot to spot. Chemical analytical methods are not applicable because such methods are destructive, and too large a sample is required to furnish the required point-to-point information.

We investigated the applicability of the laser Raman microprobe to this problem, since this instrument is capable of examining areas as small as several μm^2. In order for such examination to be effective, spectra must be obtained which are capable of indicating the ratio of Epon to Emerez deposited. In this report we describe studies of films cast from solvent rather than electrodeposited, since only in this way can the ratio of the reactants be controlled easily.

MATERIALS AND METHODS

Materials. Films were cast by mixing solutions of Epon 1001 and Emerez 1511 in 1:1 methyl isobutyl ketone/toluene solvent. The mixtures were placed in aluminum evaporating dishes, and the solvent was allowed to evaporate at

room temperature for several days. The samples were then heated at 150°C for one hour to complete the cure. Filings from the samples were placed on microscope slides for microprobe analysis.

Instrument. To obtain the Raman spectra, we used a "Molecular Optics Laser Examiner" (MOLE), which is the trade name for the Raman microprobe manufactured by Instruments S.A., Inc. The excitation source was the 5145 Å line emitted by a Spectra Physics Model 164 Argon ion laser. In this instrument, the laser beam is focused down to a very small area of the order of several μm^2 by means of an NPL Leitz objective, and the scattered light is collected over a large angle by means of the same objective. The scattered light was detected by an RCA 31034 photomultiplier tube cooled to -30°C by means of a thermoelectric housing made by Products for Research (Model TE-104 RF).

Fluorescence Quenching. We were successful in obtaining Raman spectra of the starting materials, Epon 1001 and Emerez 1511, but found it impossible at first to get spectra of the cured reaction products. A large amount of fluorescence, generated by the laser beam, completely swamped the Raman spectra of the cured samples. We found, however, that we could quench most of the fluorescence by heating the samples to 140°-150°C while the spectrum was being run. The drop in fluorescent emission was roughly one order of magnitude, enough to make the Raman peaks easily measurable.

We used a microscope slide heater consisting of a thin plastic-imbedded heating element sandwiched between a copper block on top and an insulating pad on bottom. The copper block was drilled for the insertion of a thermometer, and had a machined recess into which a microscope slide could be placed. We connected the heating element to a Variac transformer.

We chose a long focus objective lens of 50X magnification in the microscope, because we wished to avoid damage to the lens that might be caused by proximity to the heated microscope slide.

DEVELOPMENT OF ANALYTICAL METHOD

Raman Spectra. Figures 1, 2 and 3 show, respectively, Raman spectra of Epon 1001, Emerez 1511, and a solvent cast film obtained by mixing stoichiometric amounts of the two reactants. (The stoichiometry was based on reacting one gram-equivalent of epoxy from Epon 1001 with one gram-equivalent of amine from Emerez 1511.) Each spectrum, of course, represents only a few μm^2 at most of the surface of each sample, but repeat spectra on different areas showed no significant differences.

A strong peak at 1609 cm^{-1} exists for Epon which is absent in the Emerez spectrum. The strongest peak in the Emerez spectrum occurs at 1442 cm^{-1}; this peak is not apparent in the Epon spectrum, although there is a minor peak close by at 1460 cm^{-1}. The 1:1 stoichiometric mixture displays the 1609 cm^{-1} Epon peak, and also a composite peak at 1448-1461 cm^{-1} that coincides roughly with both the Emerez 1442 cm^{-1} peak and the Epon 1460 cm^{-1} peak. It is

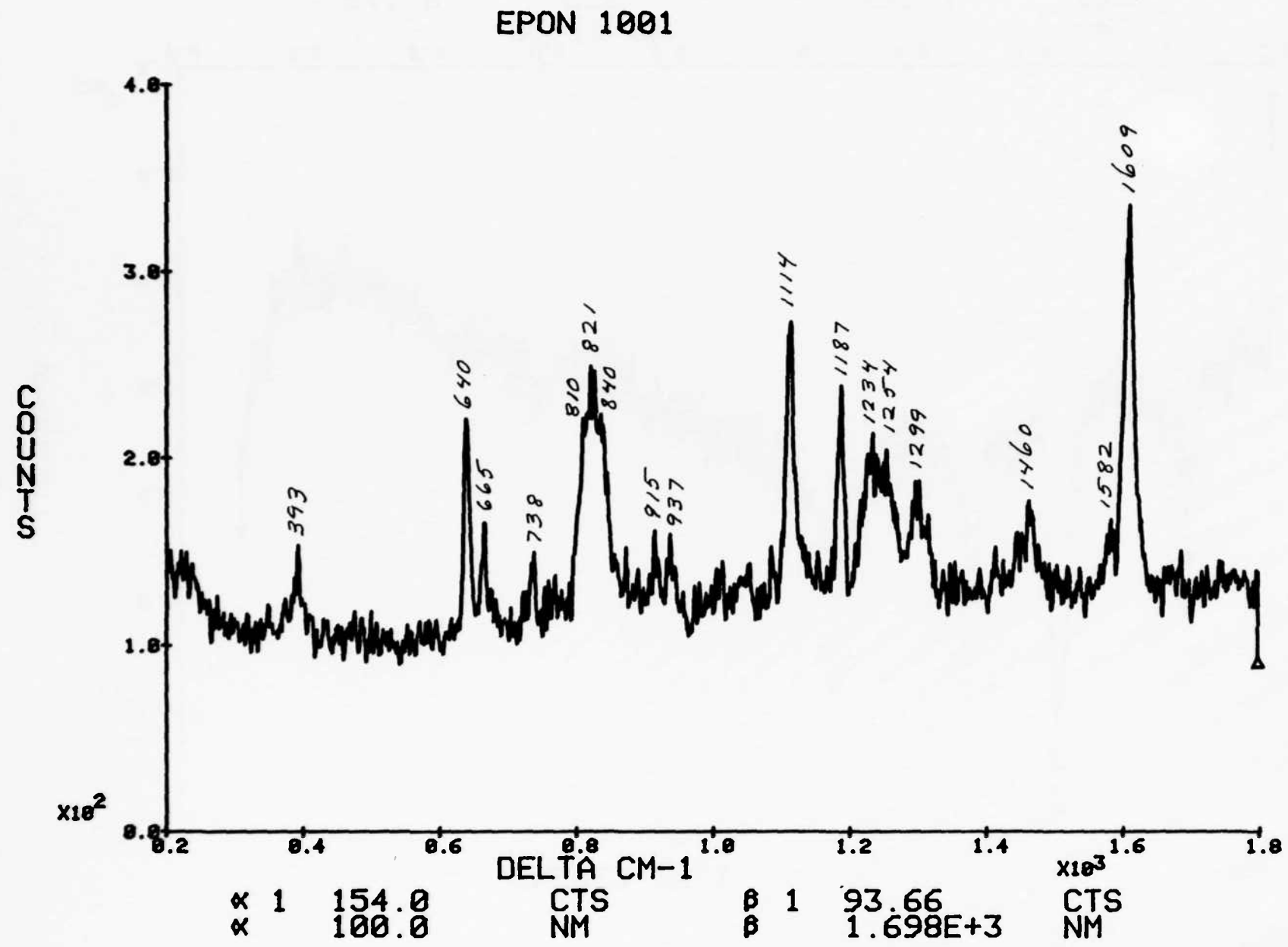

Figure 1. Raman spectrum of Epon 1001.

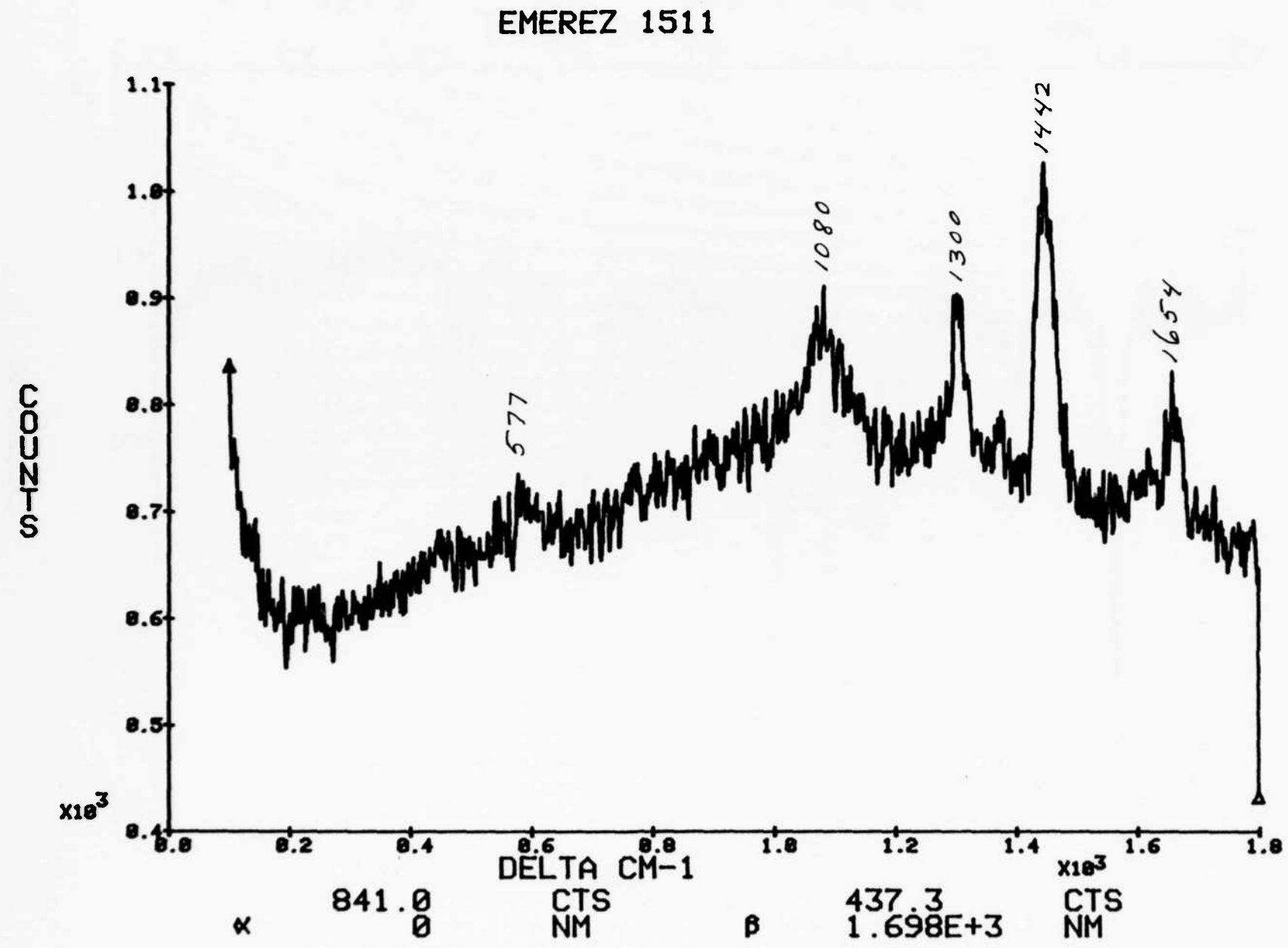

Figure 2. Raman spectrum of Emerez 1511.

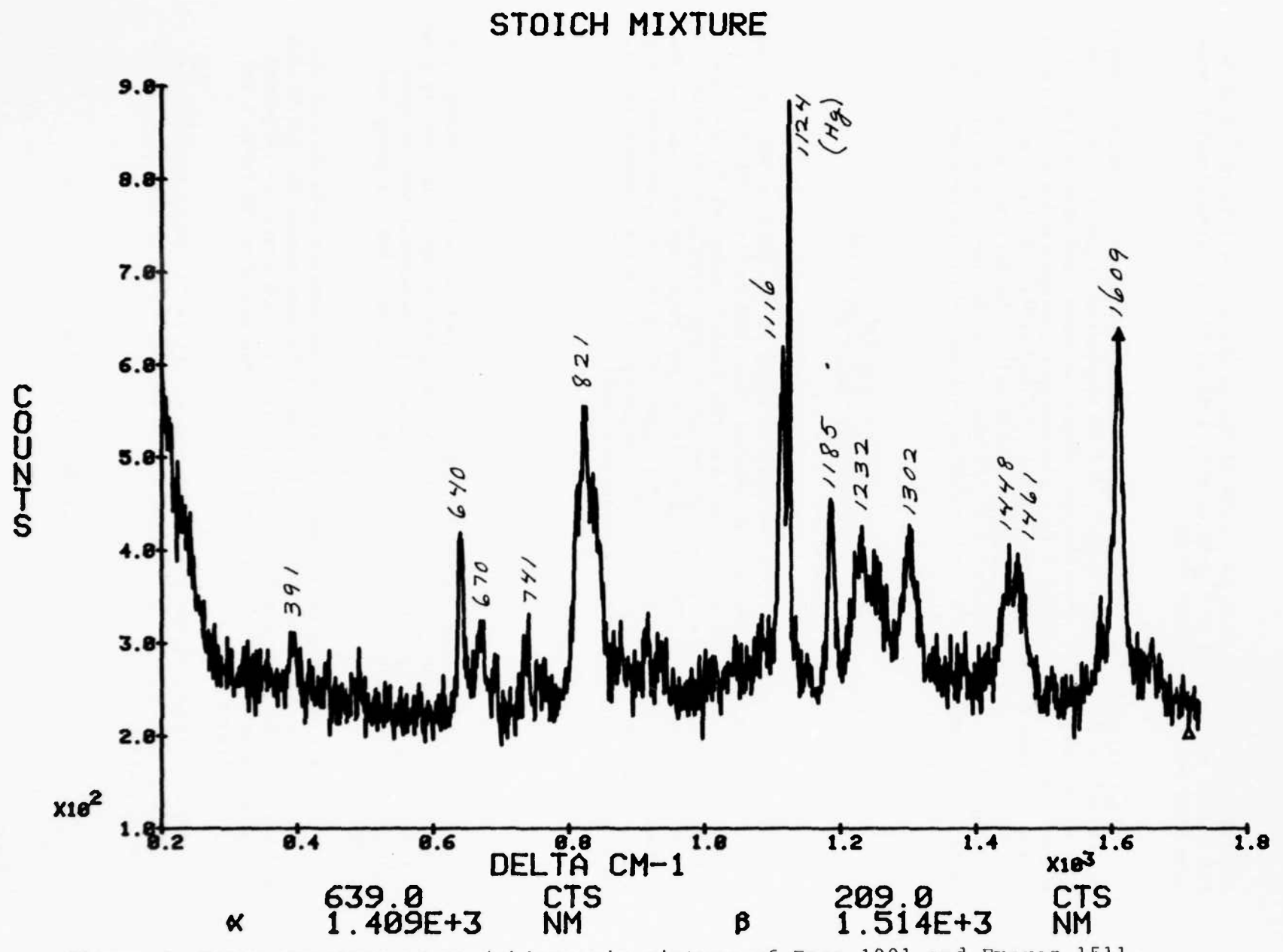

Figure 3. Raman spectrum of stoichiometric mixture of Epon 1001 and Emerez 1511.

interesting, however, that the ratio of the height of the 1461 cm^{-1} peak to the height of the 1609 cm^{-1} peak is much greater for the stoichiometric mixture than for the Epon 1001 alone.

Peak Ratio Method. We investigated the ratio between the height (above base line) of the 1461 cm^{-1} peak to the corresponding height of the 1609 cm^{-1} peak as an indicator of the relative amounts of Emerez and Epon originally present before cure. Figure 4 is a diagrammatic representation of the two peaks. We took photon counts at points A (1400 cm^{-1}), B (1460 cm^{-1}), C (1500 cm^{-1}), D (1609 cm^{-1}), and E (1650 cm^{-1}). We defined the peak ratio as $\overline{BF}/\overline{DG}$, to be calculated as follows, where the lower case letters represent photon counts at the frequencies designated by the corresponding capital letters:

$$\text{Peak ratio},\% = \frac{\underline{b} - [(40\underline{a} + 60\underline{c})/100]}{\underline{d} - [(41\underline{c} + 109\underline{e})/150]} \times 100 \quad .$$

For these determinations, we set the slits of the MOLE at 500 μ and the power at the source at 500 mw. We scanned from 1399 cm^{-1} to 1401 cm^{-1} at a rate of 10 cm^{-1}/min, and programmed the instrument to count at 40 stations per cm^{-1}; the mean square photon count over all the counting stations was taken as the reading a. We did similarly at the other four frequencies. The microcomputer associated with the instrument calculated the mean square photon count at each of the five analytical frequencies, and was programmed to calculate the peak ratio by the equation given above.

RESULTS

We prepared samples having various stoichiometric ratios of Emerez 1511 to Epon 1001. We examined each sample at a minimum of three and usually four points on the surface, and made several peak ratio determinations at each point without disturbing the sample or the microscope. Table I shows the results.

Separate analyses of variance on each of the samples show that at the 95% level there are no significant differences between points for any of the samples. We therefore pooled all the results for each sample to calculate an overall mean and 95% confidence limits. These are given in Table I and plotted in Figure 5.

The variances of the individual samples are sufficiently homogeneous to allow of pooling all the results into a regression line. The equation of this line is:

$$\text{P.R.} = 21.38 + 21.58\ \text{M.R.} \quad ,$$

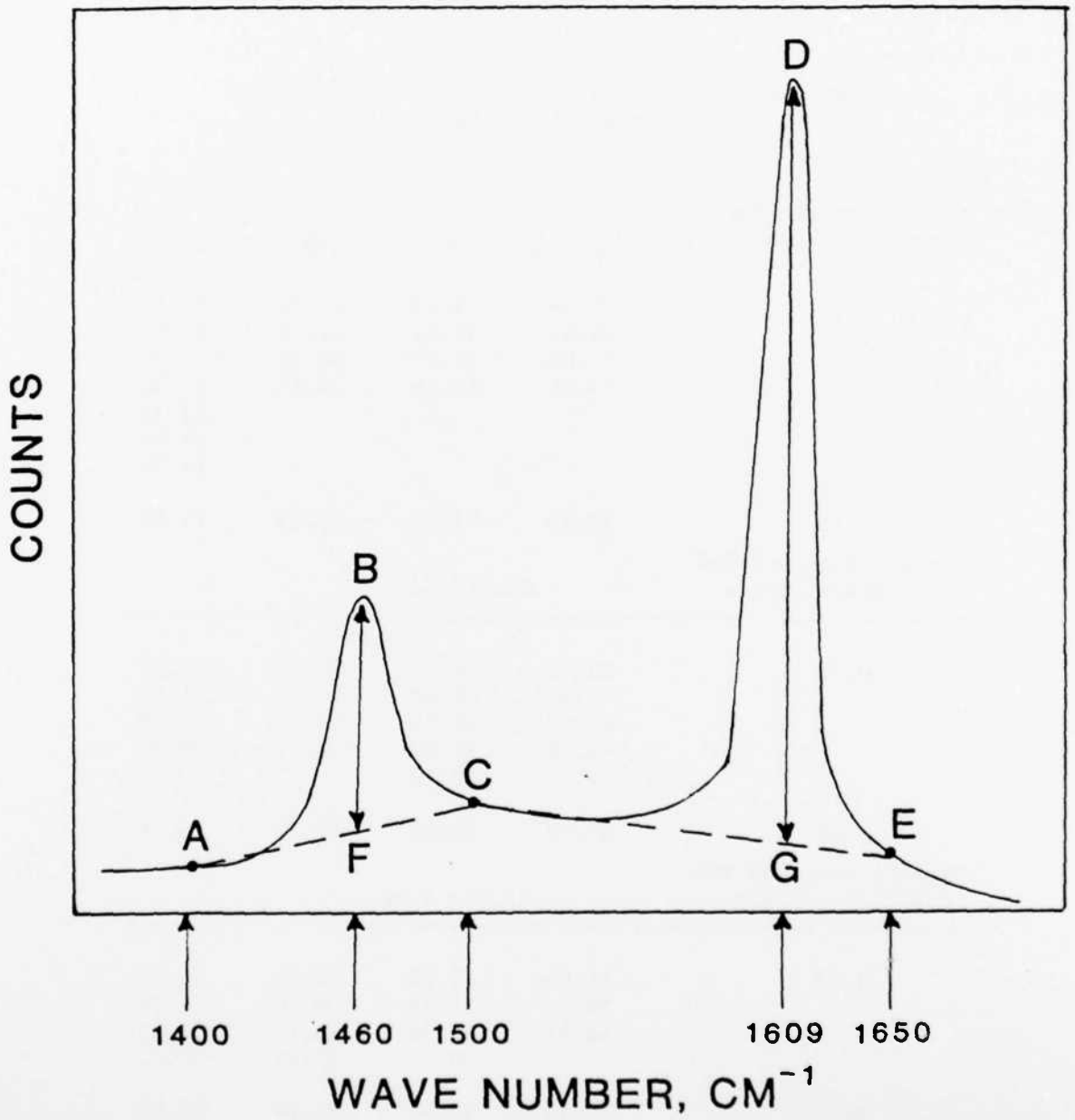

Figure 4. Schematic diagram of peak ratio method.

Table I

Peak Ratio as a Function of Stoichiometric Ratio of Emerez 1511 to Epon 1001

Stoichiometric Ratio, Emerez 1511/Epon 1001	Point 1	Point 2	Point 3	Point 4
0.25	26.34	15.47	28.83	23.82
	24.31	29.94	21.20	22.09
	31.07	21.77	34.46	35.93
	19.14	26.16	38.83	37.04
				35.33
				23.60
				14.71
Mean	25.22	23.34	30.83	27.50
Overall Mean and 95% Confidence Limits		26.84 ± 3.47		
0.50	33.22	49.70	37.71	30.55
	20.83	26.67	27.01	32.39
	47.12	21.64	23.77	26.63
	45.96	25.44	28.79	29.26
		37.70		
Mean	36.78	32.23	29.32	29.71
Overall Mean and 95% Confidence Limits		32.02 ± 4.54		
0.75	41.46	40.50	26.86	34.27
	39.12	35.74	39.70	24.74
	48.87	31.96	26.11	38.32
		50.43	35.95	29.92
Mean	43.15	39.66	32.16	31.81
Overall Mean and 95% Confidence Limits		36.26 ± 4.23		

Table I (Cont'd.)

Stoichiometric Ratio, Emerez 1511/Epon 1001	Point 1	Point 2	Point 3	Point 4
1.00	30.97	34.92	40.53	60.52
	37.92	30.55	55.00	65.26
	50.97	32.51	49.18	37.61
	42.20		63.03	44.65
Mean	40.52	32.66	51.94	52.01
Overall Mean and 95% Confidence Limits		45.05 ± 6.50		
1.50	49.04	47.55	54.38	
	56.78	52.84	58.57	
	51.50	56.18	62.51	
	44.31	47.19		
Mean	50.41	50.94	58.49	
Overall Mean and 95% Confidence Limits		52.80 ± 3.70		

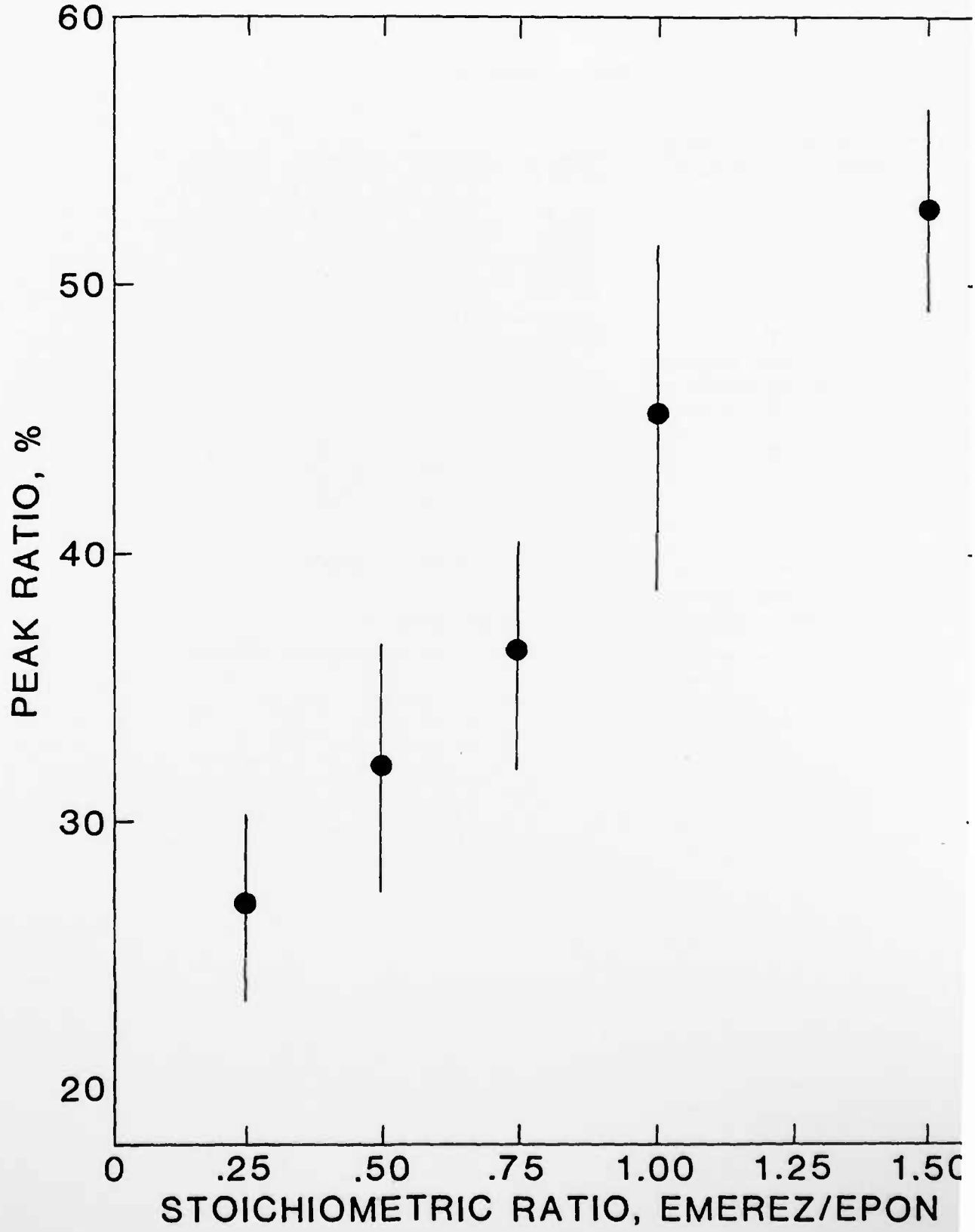

Figure 5. Means and 95% confidence limits for peak ratio determinations.

where P.R. is the peak ratio and M.R. the mole ratio.

Using equations found in statistical texts [1,2], we can calculate the confidence limits of a determination of mole ratio from a given set of readings of peak ratio. If four replicate determinations on a given spot are made, the 95% mole ratio confidence limits are about ±0.4; if the number of replicates is increased to nine, the confidence limits are about ±0.3. This precision is sufficient to detect pronounced inhomogeneities in the film.

ACKNOWLEDGEMENT

We wish to thank Ata-Uhr Rahman for the preparation of the samples.

REFERENCES

[1] P. D. Lark, B. R. Craven, R.C.L. Bosworth, "The Handling of Chemical Data," Pergamon: Oxford, 1968; Chapter IV.

[2] F. S. Acton, "Analysis of Straight Line Data," Wiley: New York, 1959.

Program #14

Effect of Acid-Base Interaction on Permeability and Mechanical Behavior of Model Protective Coatings

INTRODUCTION

The goal of this research is to determine the effects of pigment (filler)-binder interaction on the permeability and other properties of model coatings for corrosion resistance. In previous reports [1], it was shown that, as expected [2], the formation of a tight interface in zinc or glass-bead-filled epoxy films decreased the permeability to water vapor. The preliminary findings were consistent with the concepts of acid-base (or electron donor-acceptor) interaction [3]. That is, combinations of electron-accepting fillers with electron-donating binders (or vice versa) are predicted to exhibit stronger adsorption and interfacial adhesion than combinations of donors with donors or acceptors with acceptors. It was also shown that residual solvent tends to be retained even after rigorous drying— a phenomenon that may also reflect strong interaction between the casting solvent and the binder.

During this report period, research was continued with a glass-bead/phenoxy resin system as a model. The permeability to water vapor, dynamic mechanical response, and solvent-retention behavior were examined as a function of concentration and donor/acceptor character of the filler. Major emphasis was given to the adaptation of inverse gas chromatography (IGC) techniques to elucidate the donor/acceptor character. Results are described and discussed below.

Characterization of Acid-Base Character by Inverse Gas Chromatography

Traditional gas-liquid chromatography is used to determine a property of an unknown sample in a phase moving through a column containing a known stationary phase. However, a complementary or inverse analysis is possible. Thus a property of an unknown stationary phase can be determined with the aid of a known vaporizable solute in the moving phase; in effect, the vaporizable molecules serve as molecular probes [4]. This inverse-gas-chromatography (IGC) technique has proved to be quite useful in the determination of polymer-solvent and polymer-polymer interactions, many of which involve acid-base effects; the theory and applications have been recently reviewed [5]. More recently, IGC has been used successfully to evaluate polymer-filler interactions (with high-surface-area fillers) in terms of acid-base interactions [6]. Similar information can be obtained using adsorption techniques or Lehigh's microcalorimeter. However, the former is difficult to apply to small-surface-area beads, while the latter is not yet available for extensive general use. Thus, we thought it worthwhile to investigate

the applicability of IGC to our system.

The key parameter is the specific retention volume $V_g^o = t_r FJ/W_L$, where t_r is the retention time, F the carrier gas flow rate, J a compressibility correction factor, and W_L the weight of the material of interest. To minimize effects of adventitious experimental variations, a normalized interaction parameter, Ω, is useful [6a,6c]:

$$\Omega = V_g^o(\text{acidic probe})/V_g^o(\text{basic probe}) \qquad (1)$$

If the column and conditions are constant, then $\Omega = t_r(\text{acid})/t_r(\text{base})$. Thus Ω is a measure of the relative acid-base character; $\Omega = 1$, < 1, and > 1 for overall neutral, acidic, and basic surfaces, respectively.

Permeability in Pigment/Binder Systems

In the limiting case of a spherical, impermeable, and well-bonded (perfectly adherent) pigment or filler, the relative permeability, P_r, is given by (2):

$$P_r = P_c/P_p = V_p/(1+0.5\,V_f) \qquad (2)$$

where P and V are the permeability and volume fraction, respectively, and the subscripts p and f refer to polymer and filler, respectively. However, Eqn. (2) is invalid if the filler is not well bonded or wetted by the matrix or if the filler or interfacial region adsorbs the penetrant. To deal with such cases, Nielsen [7] proposed a more general model:

$$\frac{P_{cl}}{P_{pl}} = \frac{P_i}{P_{pl}V_f^n + P_i(1 - V_f^n)}\left(\frac{V_{li}}{\tau^*}\right) + \left(\frac{V_p + V_{lp}}{\tau}\right) \qquad (3)$$

where τ and τ^* are the tortuosities of the overall composite and the interface, respectively, and the subscripts l and i refer to the permeant and interface, respectively. For this discussion, τ^* is taken as equal to τ ($= 1 + 0.5\,V_f$); the value of n lies between zero (if channeling occurs) and 0.33 (for ideal spheres). Although use of Eqn. (3) requires curve-fitting, it does reflect realistic parameters, and successfully models trends in behavior of many systems [7].

The Model System

Glass beads were selected to model the pigment in the coating system because the geometry is simple and the surface can be readily modified to vary the nature of sites active in adsorption; such beads have been used successfully before [8].

EXPERIMENTAL

Inverse Gas Chromatography

A Perkin-Elmer Sigma 3 gas chromatograph equipped with a flame ionization detector was used at 50 (±0.5) and 75 (±0.5)°C; the temperature of the injection block and the detector cell was 150°C. Copper tubes (6.4 mm O.D. x 1.2 m) were used for the columns which, after cleaning and drying, were carefully packed with approximately 30 g of glass beads, coiled to fit the oven, and conditioned at T > 100°C for several hours. The probe molecules used, t-butanol (acidic, electron acceptor) and n-butylamine (basic, electron donor), have been used successfully before [6a,6c].

Sample Preparation

Films were cast in Al pans from 20-wt-% phenoxy resin in cellosolve acetate; glass beads (both untreated and treated with an aminosilane) were incorporated in amounts to yield the following volume fractions in the dried films: 0, 0.1, 0.2, and 0.4. Other films were cast using polystyrene, epoxy, and poly(vinyl chloride), and other solvents [9]. Drying was effected for 1 day at ambient temperature, followed by vacuum-treatment to reach constant weight at 40°C. Extruded samples of phenoxy (both dried and containing 0.7% H_2O) with and without the aminosilane treating agent at 0.1-V_f filler were compression-molded at 150°C and 3.5 MPa for 10 min.

Test Procedures

Permeability to water vapor at 50°C was determined as described previously [1b]. Solvent retention was measured gravimetrically during drying. Values of the glass transition temperature, T_g, were determined using a Perkin Elmer differential scanning calorimeter (DSC), model DSC-1B, and from the temperature of maximum loss modulus (E") observed in dynamic mechanical spectra (DMS) obtained using an Autovibron elastoviscosimeter model DDV-IIIC. Fracture surfaces of broken films were coated with a layer of Au/Pd and examined by scanning electron microscopy (SEM). The surfaces of the glass beads were analyzed by X-ray photoelectron spectroscopy (XPS).

RESULTS AND DISCUSSION

Filler Surface Characterization

Both SEM and XPS techniques revealed differences between the surfaces of the untreated and treated glass beads. Figure 1 shows the treated beads to have a roughened surface, presumably due to the coupling agent; the ESCA tests revealed the presence of elemental nitrogen on the surface of the treated, but not the untreated, beads. Thus the treated beads may be expected to present amino groups to the binder, although the uniformity of

(a)

(b)

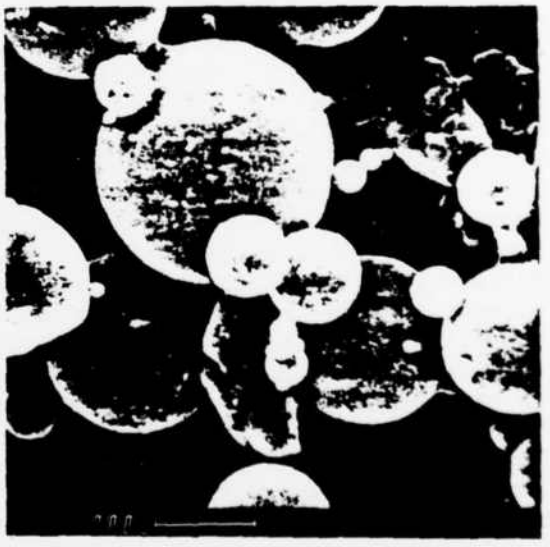

Figure 1. Scanning electron micrographs of glass spheres: (a) untreated; (b) treated with an aminosilane.

the treatment is not known.

Values of Ω, the normalized acid-base parameter, obtained in the IGC studies given in Table I indicate a major difference between the untreated and treated beads. While the former are acidic (electron acceptors, $\Omega < 1$), the latter are basic (electron donors, $\Omega > 1$). It has been shown [6c] that values of Ω (whether > or < 1) tend to approach unity as the temperature is increased. This effect is seen in the case of the treated glass, and is expected to be seen when tests are completed with the untreated.

Table I

Interaction Parameters Ω for the Glass Bead/Phenoxy System at Two Temperatures

	Ω	
T(°C)	Untreated	Treated
50	0.47	1.34
75	--	1.03

Differences in the ability to bond to the binder were also observed. SEM studies revealed that the untreated beads bonded with neither acid polymers [epoxy, chlorinated PVC, and phenoxy] nor basic ones [polystyrene and poly(methyl methacrylate)] [1b,9,10]. In contrast, the treated beads bonded well with both solvent-cast and compression-molded phenoxy (Fig. 2) and the epoxy binder, but not with polystyrene or poly(methyl methacrylate) (Fig. 3, top). Thus, as expected, the treated beads exhibit a predominantly basic surface that can interact with an acidic binder; the cellosolve acetate solvent is apparently not sufficiently basic to overcome the attraction of the filler for phenoxy molecules. However, strongly competitive effects of solvent were noted when films were cast using chlorinated poly(vinyl chloride) as binder and dioxane, tetrahydrofuran, and chloroform as solvents (Fig. 3, bottom). Evidently the two former solvents were sufficiently basic, and the latter sufficiently acidic, to inhibit adsorption. Similar solvent effects have been observed before [3a,3b]. The failure of the basic polymers to bond to the untreated glass may be due to a similar phenomenon.

Thus the validity of the acid-base concept as applied to filler-matrix interactions is amply confirmed in these systems.

Viscoelastic Behavior

The viscoelastic behavior is of interest because it reflects the state of a polymer composite as affected by the presence of the filler (Fig. 4) and, in this case, residual solvent (Fig. 5). As expected [2], the storage modulus

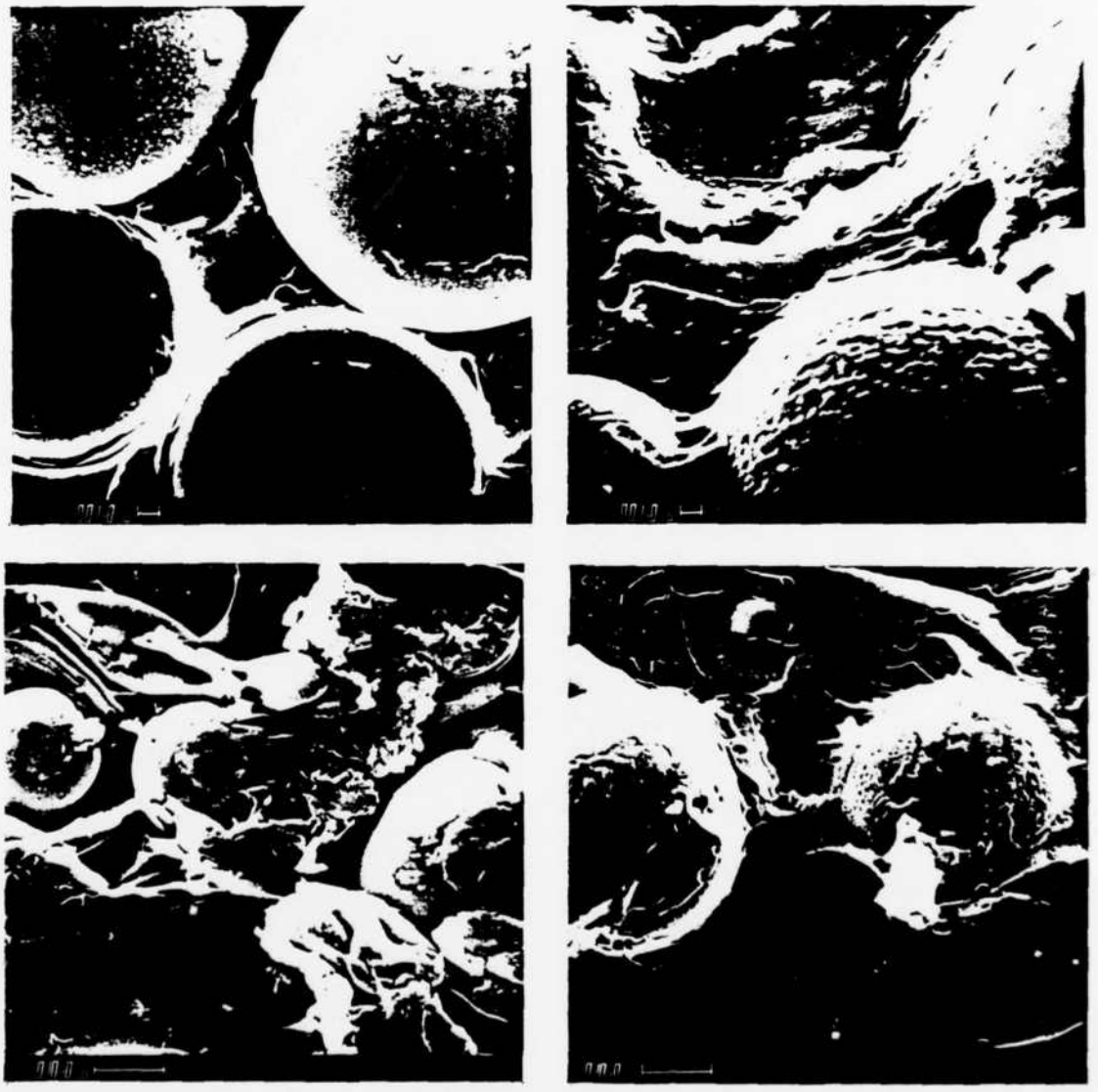

Figure 2. Fracture surfaces of glass-sphere-filled phenoxy films. Top, solvent-cast films: left, untreated; right, treated. Bottom, compression-molded: left, untreated; right, treated.

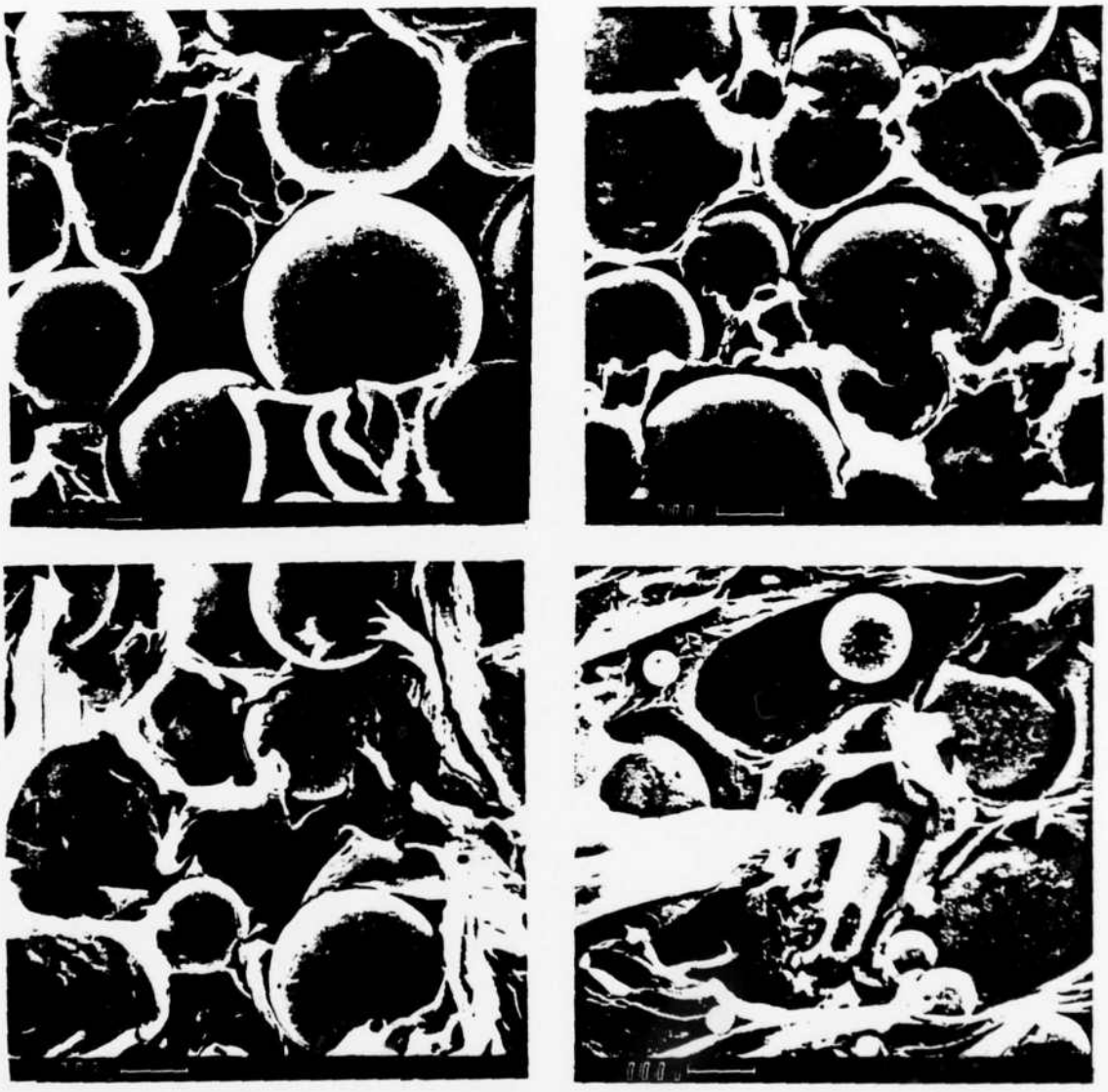

Figure 3. Fracture surfaces of glass-sphere-filled films. Top, polystyrene cast in xylene: left, untreated; right, treated. Bottom, chlorinated-poly(vinyl chloride) cast in THF: left, untreated; right, treated.

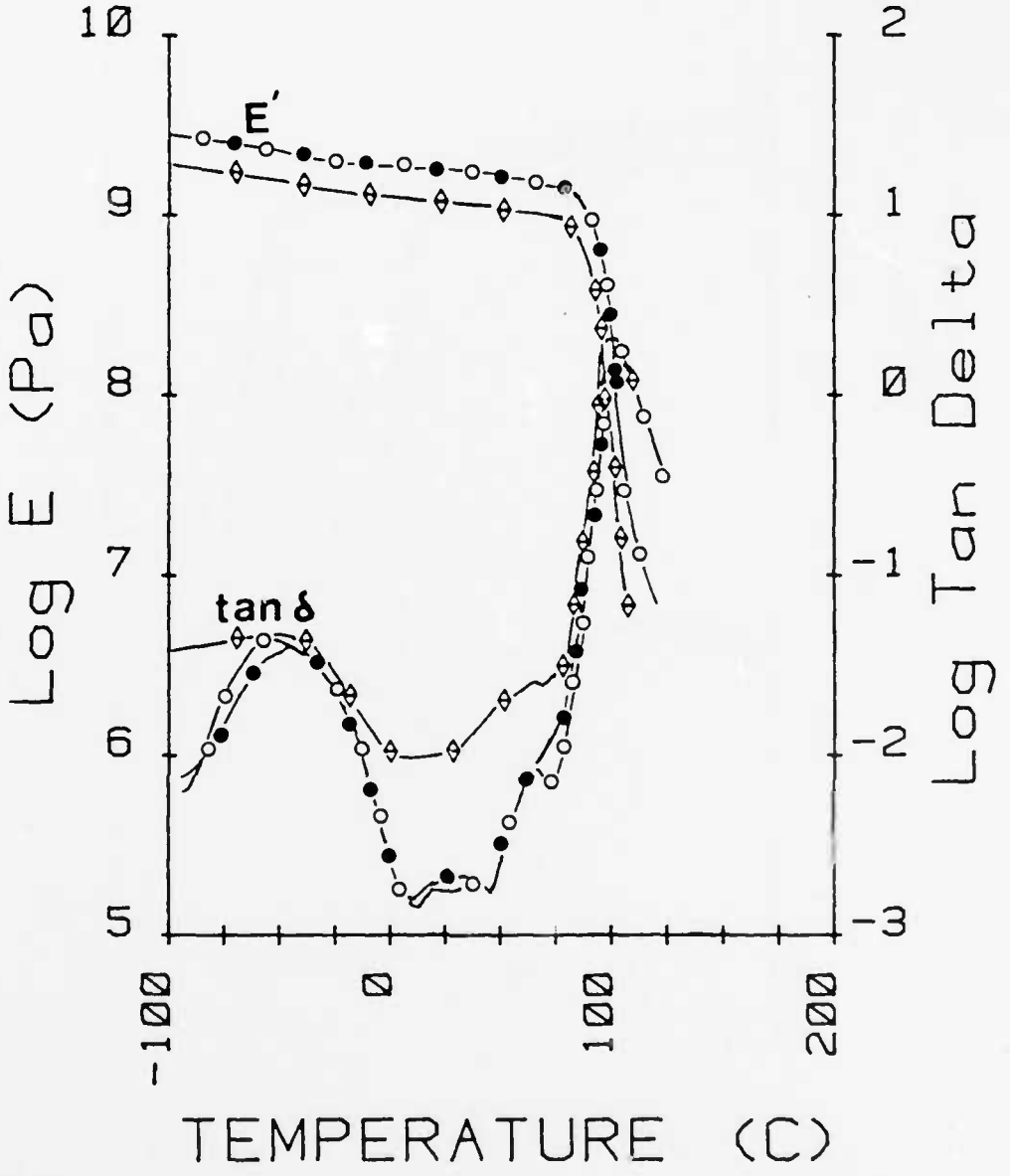

Figure 4. Dynamic mechanical spectra of compression-molded phenoxy specimens: ◊, dry resin; o, 0.1 volume fraction untreated glass spheres; ●, 0.1 volume fraction treated glass spheres.

AD-A139 086 CORROSION CONTROL THROUGH A BETTER UNDERSTANDING OF THE METALLIC SUBSTRAT..(U) LEHIGH UNIV BETHLEHEM PA CENTER FOR SURFACE AND COATINGS RESE.. H LEIDHEISER ET AL. 3/3

UNCLASSIFIED 01 JAN 84 N00014-79-C-0731 F/G 11/6 NL

END

DATE FILMED

4-84

DTIC

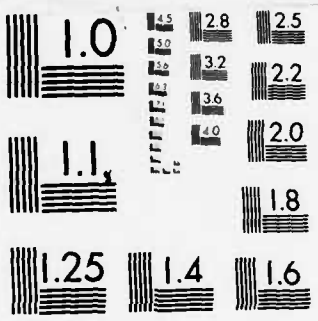

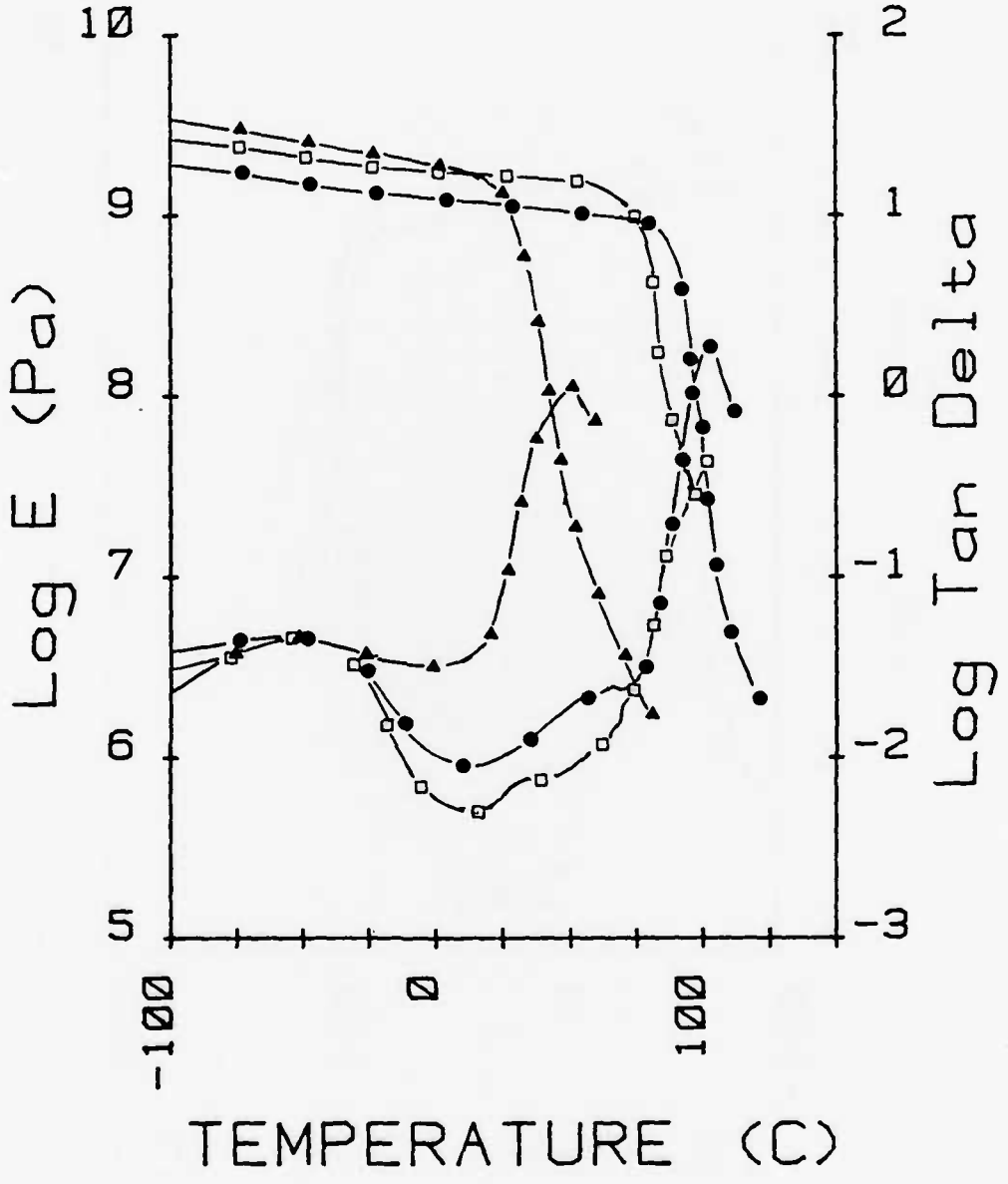

Figure 5. Dynamic mechanical spectra of glass-bead-filled phenoxy films ($V_F = 0.1$): ▲, solvent cast; ●, compression-molded, dry resin; □, compression-molded, resin containing 0.7 wt % H_2O.

in the glassy state, E', was increased by the treated and untreated fillers (in compression-molded films) by 22%, in good agreement with prediction (25%) [2]. Damping (as measured by tan δ) was decreased by the fillers, though more than expected between -10 and 75°C. As noted for a glass-bead-epoxy system [11], the T_g was not significantly increased (Table II), though increases have been noted in other systems [2].

Table II

Effect of Residual Water and Solvent on the T_g[a] of Phenoxy Binder Resin

Resin	Vol. Fraction Filler	Autovibron		DSC	
		T_g,°C	% wt loss[a]	T_g,°C	% wt loss[a]
Solvent-cast	--	33	1	26	1
Containing 0.7 wt % water	--	85	0.4	74	0.6
Dry resin	--	93	--	83	--
Dry resin (treated beads)	0.1	90-95	--	83	--
Dry resin (untreated beads)	0.1	90-95	--	81	--

[a]From the maximum in E". Note that Figures 4 and 5 show values of tan δ vs T (tan δ = E"/E').

[b]During testing.

(This is probably due to experimental error and the small value of V_f; increases in T_g were noted in solvent-cast films, as discussed below.) However, major effects on the dynamic spectra and DSC scans due to retained solvent or residual water were observed (Fig. 5 and Table II). Thus the T_g was decreased significantly by the presence of water, and much more by the presence of retained solvent. Similar effects were noted in the glass-sphere-filled films (see below). Each liquid acts as a plasticizer in this respect, but also as an antiplasticizer at temperatures $< T_g$, in which range values of E' are increased (a common effect with polar molecules). Retention of a basic solvent such as cellosolve acetate is consistent with acid-base concepts, in view of the acidity of the phenoxy binder.

In view of the significant effects of retained solvent (effects not always considered in the behavior of protective coatings), gravimetric studies

of weight loss during drying were made (Fig. 6 and Table III).

Table III

Retained Solvent in Glass Bead/Phenoxy Films as a Function of Filler Content

Volume Fraction Glass Beads	Retained Solvent at Equilibrium		
	Untreated	Treated	Theoretical
0		42.1	--
0.1	41.0	30.0	37.9
0.2	13.0	23.3	33.7
0.4	31.1	21.0	25.3

The drying curves exhibit the two stages proposed by Hansen [12]: an initial stage of rapid weight loss due to surface evaporation, followed by a stage of slower weight loss due to bulk diffusion. (The discontinuities reflect the change from air to vacuum drying.) Major effects of the amount and type of filler on the steady-stage amount of solvent are evident in Table III. After similar drying procedures, the amount of solvent retained (in the polymer phase) decreased with increasing filler concentration. However, the untreated beads tended to retain more solvent, and the treated beads less, than predicted based on the volume fraction of polymer.

We propose that with the untreated glass, solvent must be bonded to the polymer strongly enough to overcome the presumably easier diffusion not due to the weak interface. On the other hand, with the treated glass, the amount of solvent retained must be limited by the lower entropy of the polymer fraction involved in the tight and strong interface [2]. Measurements of solvent absorption in the compression-molded specimens should test this hypothesis. In any case, this behavior is consistent with the observations of Figure 2, though the tight interface is not reflected in a higher T_g for the films containing treated vs. untreated beads.

Figures 7a-7d show the effect of drying and filler content on T_g. Here a clear effect of filler content is seen; T_g increases with filler content in the constant-weight specimens, especially with those containing treated glass (from 33°C to 48°C, in the case of the latter). The differences between the films with treated and untreated glass appear to be entirely due to differences in the amount of retained solvent; values of T_g correlate well with solvent content regardless of surface treatment.

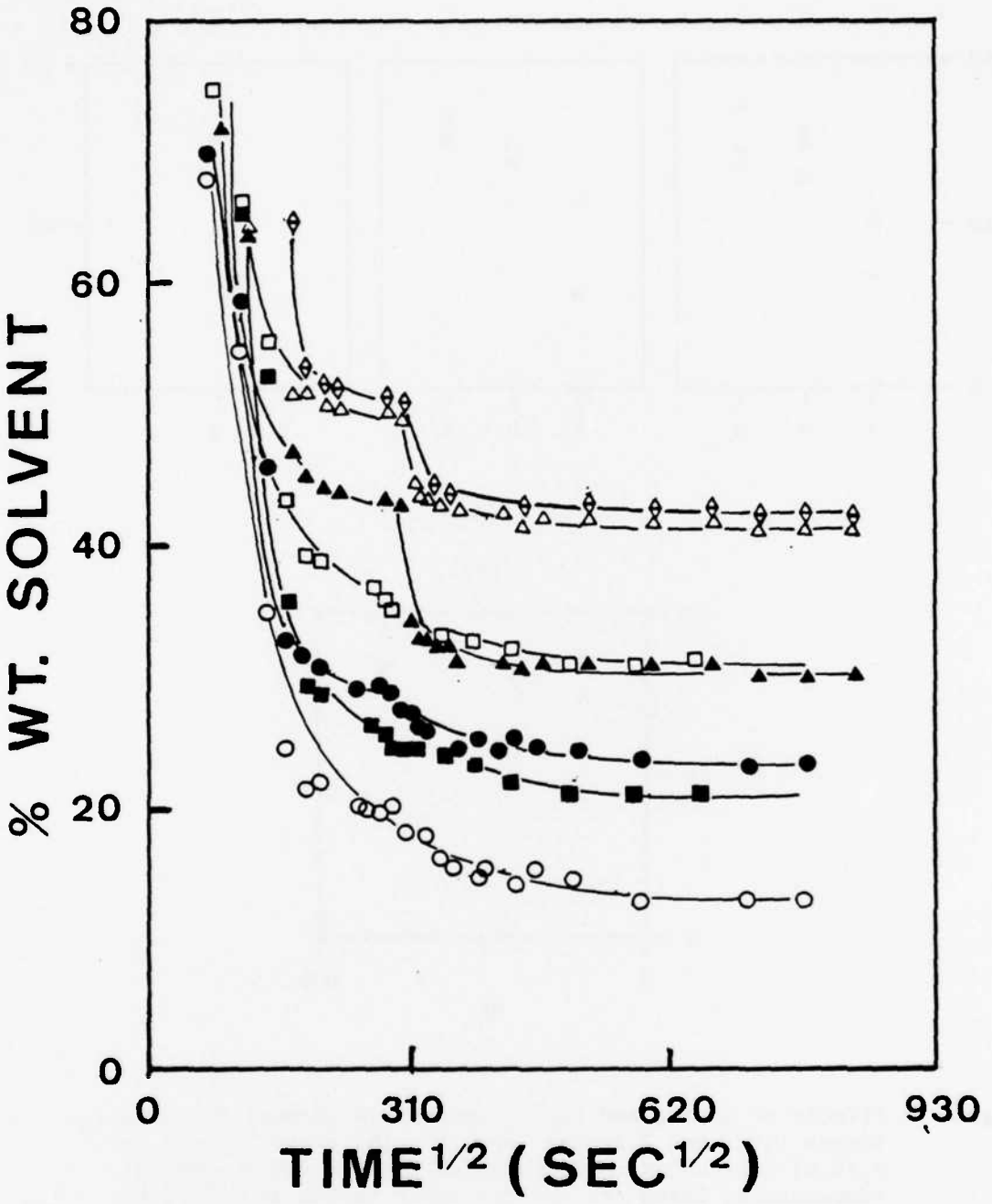

Figure 6. Solvent loss in glass-bead-filled phenoxy films as a function of [drying time]$^{1/2}$: ◊, unfilled control; △, ▲, V_F=0.1; ○, ●, V_f=0.2; □, ■, V_f=0.4. Open and closed symbols for filled systems refer to untreated and treated beads, respectively. The discontinuities reflect the change from air to vacuum-drying.

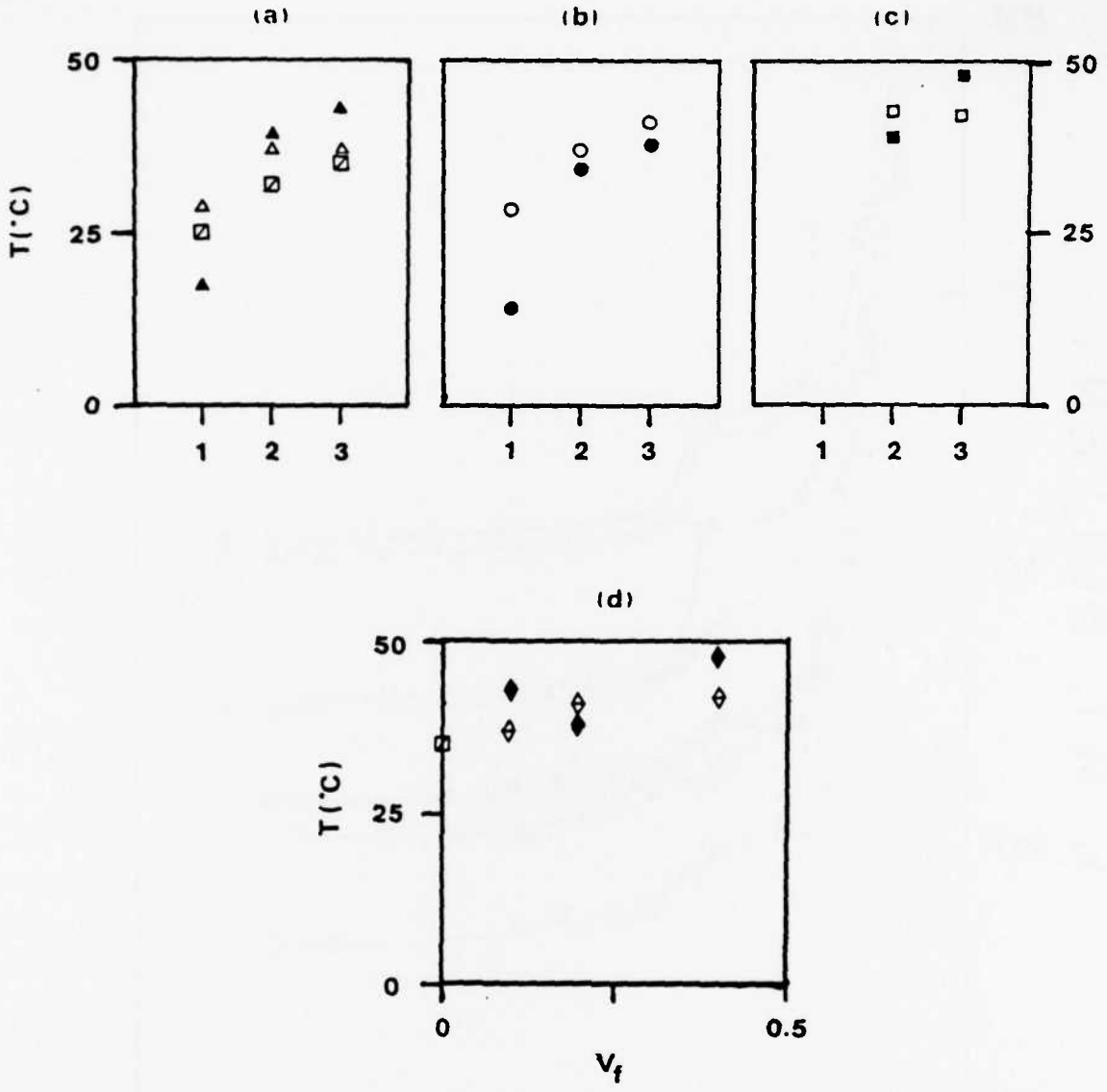

Figure 7. Effects of drying and filler content in phenoxy films on T_g. Stages 1, 2, and 3 in (a) [V_f=0.1], (b) [V_f=0.2], and (c) V_f=0.4] correspond to films dried for one day at ambient temperature, dried for one day under vacuum at 40°C (the second continuous day of drying), and dried to constant weight, respectively. Open and closed symbols refer to untreated and treated glass, respectively.

Permeability

As reported earlier [1b], values of P decreased rapidly with time, reaching a steady state at about 200 hr. Table IV and Figure 8 present steady-state values of the relative permeability, P_r, as a function of filler content. Although both treated and untreated fillers resulted in higher values of P than predicted by the limiting Eqn. (2) for the case of good adhesion with an impermeable filler, the films with untreated filler are much more permeable than those with treated filler at equal V_f. Although modeling with the Nielsen equation is complex, due to the presence of terms whose values are not experimentally available, preliminary calculations were made with various assumed values of the Nielsen parameters.

Table IV

Steady State Permeability Constants of Phenoxy Films

Vol. Fraction Filler	Permeability Constants, $P_c(P_r)$		
	Untreated Glass	Treated Glass	Theoretical
0[a]	-- (1.0)	-- (1.0)	(1.0)
0.05	6.1 (1.5)	5.9 (1.5)	(0.93)
0.20	12.0 (3.0)	6.5 (1.6)	(0.73)
0.40	15.4 (3.9)	5.3 (1.3)	(0.50)

[a] P(polymer) = 4.0.

Regardless of the permeability and liquid solubility, it was found that Nielsen's equation for spheres (n=1/3) could not hold for either the treated or untreated filler. However, the behavior of the films with untreated filler can be modeled if it is assumed that permeation involves channeling, e.g. through continuous porosity (n=0). Indeed a reasonable fit can be obtained if one assumes the following: P_i/P_{pl}=10, V_{li}=V_f, and V_{lp}=volume fraction retained solvent. (Note that Eqn. (3) becomes invalid at very low values of V_f.) Even with the treated filler, the assumption of channeling gives fair agreement, provided that P_i/P_{pl} is reduced to 2, keeping the other parameters the same. It may well be that the very high amounts of solvent retained may in effect provide a continuous capillary network in the polymer phase. Note also that the value of P_{pl} should be higher in the case of the bead systems than in the control, for the T_g of the former is greater than the test temperature. Since many protective coatings involve solvent-casting, these findings appear to merit further study. Indeed we are not aware of such studies of the role of retained solvent per se. Several experiments would be of interest, e.g. characterization of water take-up and distribution in the films as a function of solvent content and time. Other important questions

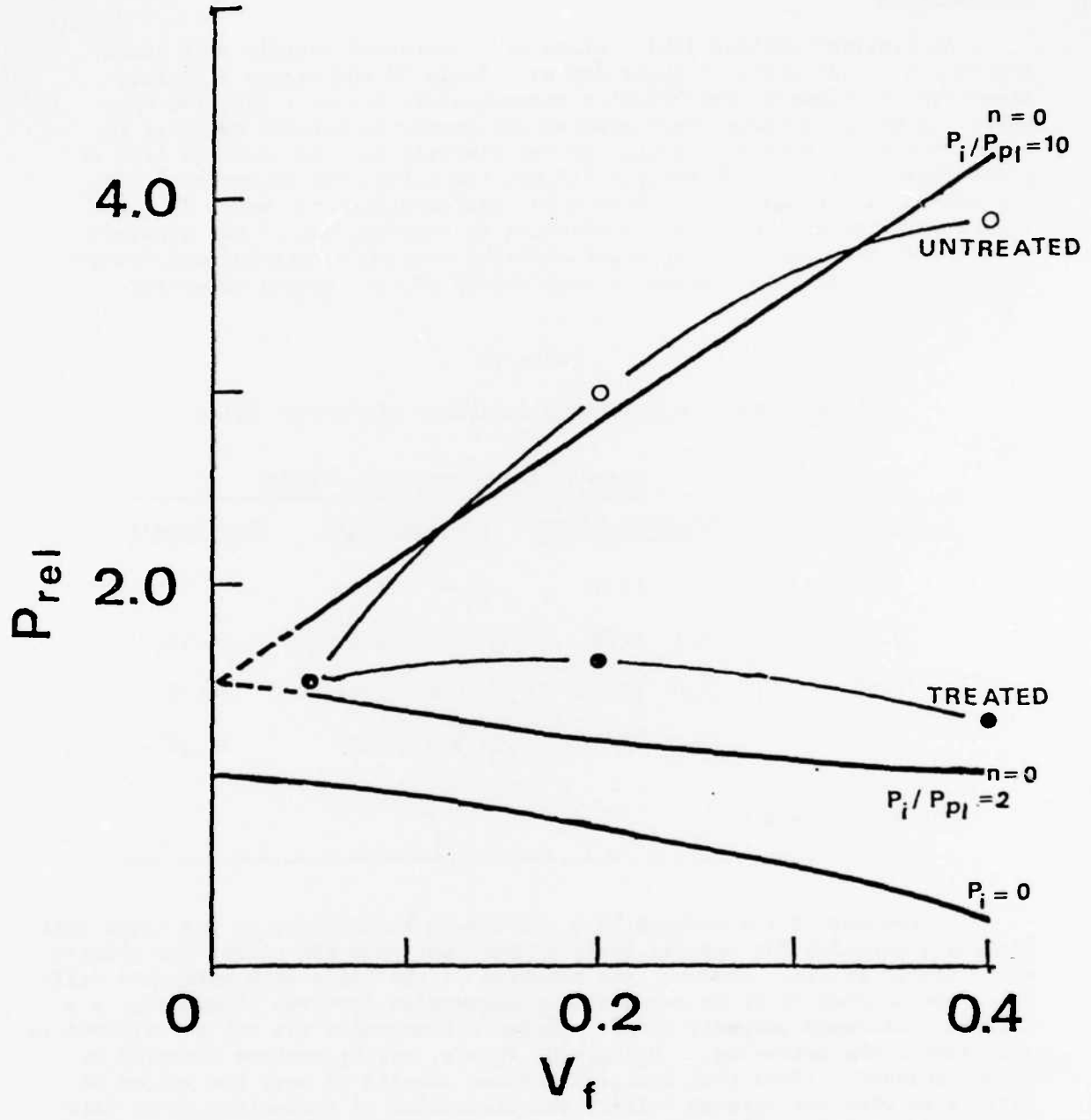

Figure 8. Relative permeability (at 50°C) of glass-sphere-filled phenoxy films as a function of filler content: ○; and ●, untreated and treated filler, respectively. Straight lines correspond to theoretical predictions: $P_i = 0$, Eqn. (2); $n = 0$, with $P_i/P_{pl} = 2$ and $P_i/P_{pl} = 10$, Eqn. (3).

also arise. The degree of adhesion after permeation may also be important in long-term behavior in service, and the effect on O_2 permeation remains to be examined. In any case, the greater the acid-base interaction, the greater the interfacial adhesion, and the lower the permeability to water vapor.

CONCLUSIONS

1. Inverse gas chromatography can be adapted to characterize the acid-base (donor-acceptor) character of low-surface-area fillers (in this case, glass beads).

2. Treatment of glass spheres with an aminosilane changes the surface character from acidic to basic.

3. In oil-dried glass bead/phenoxy films, the residual solvent content is high enough to greatly lower the T_g and change the dynamic mechanical response. The higher the interfacial adhesion and the higher the filler content, the lower the solvent retention. At the same time, the dynamic response, including T_g, is not affected by the interfacial adhesion.

4. The higher the interfacial adhesion, the lower the permeability to water vapor, though in these solvent-cast films the interface is not as tight as expected for perfect adhesion and complete wetting.

5. The acid-base concept is useful in interpreting the solvent retention, the interfacial wetting and adhesion and the permeability behavior.

REFERENCES

[1] a. Annual Report, this project, 1981.
b. Annual Report, this project, 1982.
c. J. A. Manson, J. S. Lin and A. Tiburcio, Org. Coat. Plast. Chem. 46, 121 (1982).

[2] J. A. Manson and L. H. Sperling, "Polymer Blends and Composites," Plenum Press, New York, Ch. 12 (1976).

[3] a. F. M. Fowkes and M. Mostafa, I&EC Prod. Res. Dev. 17, 3 (1978).
b. M. J. Marmo et al., I&EC Prod. Res. Dev. 15, 206 (1976).
c. J. Williams and J. A. Manson, Org. Coatings Plast. Chem. 42, 175 (1980).

[4] J. E. Guillet, in "Progress in Gas Chromatography," J. H. Purnell, Ed., John Wiley and Sons, New York, 1973, p.187.

[5] O. Olabisi, L. M. Robeson, and M. T. Shaw, "Polymer-Polymer Miscibility," Academic Press, New York, 1979.

[6] a. H. P. Schreiber, M. R. Wertheimer, and M. Lambla, J. Appl. Polym. Sci. 27, 2269 (1982).
b. C. S. Flour and E. Papirer, J. Coll. Interface Sci. 91(1), 69 (1983).
c. H. P. Schrieber, Org. Coat. Appl. Polym. Sci. 45, 22 (1982).

[7] L. E. Nielsen, J. Macromol. Sci. (Chem.), A1(5), 929 (1967).

[8] J. A. Manson and E. H. Chiu, J. Polym. Sci. Symp., 41, 95 (1973).

[9] A. C. Tiburcio, M.S. Report, Lehigh University (1983).

[10] G. Lin, Unpublished research, Lehigh University (1983).

[11] T. B. Lewis and L. E. Nielsen, J. Appl. Polym. Sci. 14, 1449 (1970).

[12] a. C. M. Hansen, J. Oil. Col. Chem. Assoc. 51, 27 (1968).
b. C. M. Hansen, Off. Dig. 37, 57 (1965).

Program #15

Diffusion of Ions and Water into Protective Organic Coatings and the Cathodic Delamination Process

INTRODUCTION

One of the major questions facing those who study cathodic delamination of protective organic coatings is the mechanism by which environmental species reach the delamination front. Free film studies have shown that all coatings are permeable to some environmental species, though the degree of permeability varies considerably. When a coating is present on a substrate, diffusion is restricted. In these cases the wet adhesive properties play a key role in determining the equilibrium concentrations of the diffusing species. When a defect is present in the coating, an additional diffusion pathway is introduced. The defect becomes an anodic site, and the area surrounding the defect acts as a condensed cathodic region. The conditions for cathodic disbonding have been established. To what extent does the introduction of a defect affect the ion uptake by a coating? What effect does cathodically polarizing a coated metal have on ionic permeability? Can a correlation be made between ionic uptake and the degree of cathodic disbonding? These questions form the foundation of this work.

EXPERIMENTAL

The use of radioisotopes as a tool to determine the uptake of ionic species by organic coatings has been previously discussed [1]. In this study ^{22}Na, ^{36}Cl and ^{137}Cs were used as tracer probes. Cold-rolled steel plates were spin coated with polybutadiene, alkyd topcoat (Rust-O-Leum #7791), and alkyd topcoat with a primer coat (Rust-O-Leum #7773). For each of these coating systems, ion uptake was monitored as a function of applied potential (open circuit or -0.800 VDC) for coatings with and without an imposed defect. Exposure cells consisted of cylinders cut from capped vials (1.4 cm diameter, 1.5 cm deep) secured to the test specimen (Fig. 1). For those samples undergoing cathodic polarization a three-electrode system consisting of the sample (working electrode) and the previously described impedance probe (counter electrode/reference electrode combination) [1] was used. Defects were introduced by scribing a 3 mm diameter circular hole through the coating.

Delamination studies were also carried out at the chosen potentials for all coating systems using 0.5M CsCl. The delamination front for polybutadiene is readily visible allowing direct measurement of the delaminated area without destroying the samples and the simultaneous measurement of ion uptake and delamination. For the alkyd coating systems it was necessary to use the

standard tape-pull delamination test after allowing several hours, usually overnight, for the coating to regain adhesion. Duplicate samples of those used for ion uptake were required to study the disbonding behavior of the alkyd systems.

Lateral diffusion studies were carried out on polybutadiene coated plates using ^{137}Cs as the tracer probe. A special two-compartment cell was used for these experiments (Fig. 2). The inner compartment consisted of a 10 mm diameter cylinder surrounding an 8 mm diameter defect cut into the coating. The outer compartment consisted of a second cylinder (~21 mm diameter) secured to the plate concentric to the first. The inner cell was filled with 0.5M CsCl doped with ^{137}Cs, the outer with undoped 0.5M CsCl. The degree of lateral diffusion was determined by monitoring both the plate and the outer cell solution for residual ^{137}Cs. Blanks were run to eliminate diffusion through the inner cell walls as a possible source of ^{137}Cs in the outer cell solution.

RESULTS AND DISCUSSION

As of this writing, almost all of the studies involving ^{137}Cs had been completed. These studies will be the focus of this discussion. The results from the ^{22}Na ^{36}Cl studies will be summarized in tabular form (Table II), paralleling the ^{137}Cs results quite closely (Table I).

Before proceeding with the experimental results, some comments about the coatings pertinent to interpretation of the results should be made. Alkyd paints are known to have poor wet adhesion properties, and the poor adhesion of the topcoat used here has previously been observed. It would be expected that the uptake profile for this coating, relative to coating deadhesion or delamination, would be markedly different than a well behaved coating such as polybutadiene. The primer acts as an inhibitor to diffusion through the coating by introducing aromatic groups at the coating-metal interface, but in the presence of a defect adhesion loss is expected since the primer alone has poor wet adhesive properties. Regardless of the system a spread in the observed permeabilities is to be expected. The use of radiotracers alone will give a range of permeabilities (Ref. [1], Table II). Since the overall trend is of more interest than the absolute permeability, graphic means will be used to report all uptake data.

Figures 3-6 show the mean Cs uptake curves for alkyd topcoat on cold-rolled steel without and with an imposed 3 mm defect. Polarizing plates coated with an intact film (Fig. 4) results in an approximate tenfold increase in the rate of Cs uptake over the non-polarized samples (Fig. 3). The introduction of a defect into an alkyd coating results in a similar tenfold increase (Fig. 5). Polarizing a defect sample to -0.800 V showed no apparent difference in the overall Cs uptake rate (Fig. 6). This lack of change in Cs uptake can be accounted for when the delamination behavior of the paint is taken into account.

Figure 7 shows the delamination of the alkyd paint at both open circuit and -0.800 VDC over a 12-hour period. In both cases non-linear behavior is

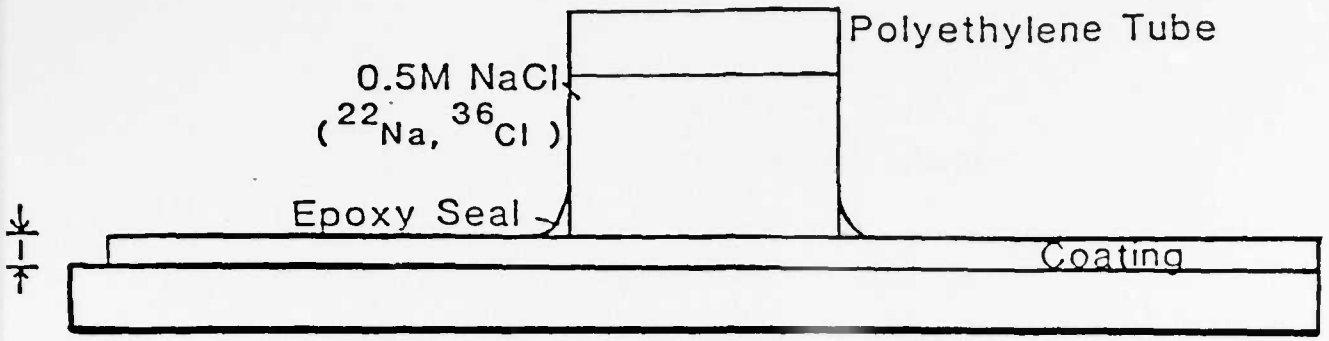

Figure 1. Radiotracer Uptake Cell

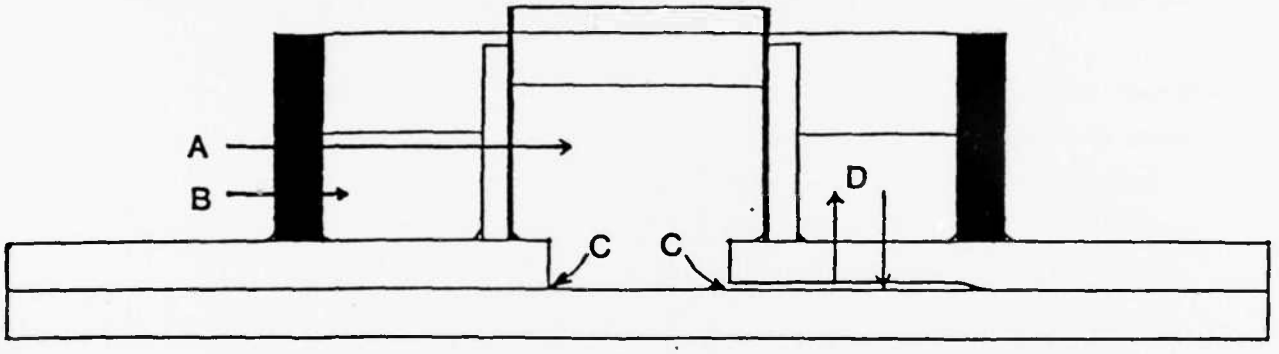

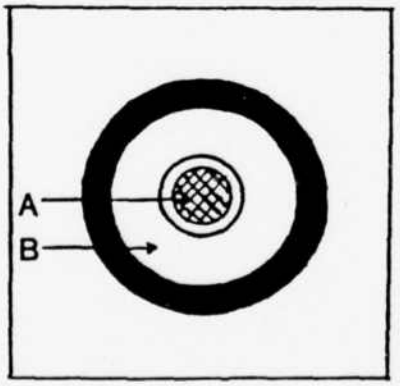

Figure 2. Lateral Diffusion Cell:
(A) Inner (defect) cell (78.5 mm , 0.5M ^{137}CsCl);
(B) Outer cell (Net area -352.8 mm ,0.5M CsCl);
(C) Lateral diffusion pathway (Cs^+, Cl^-, H_2O);
(D) Diffusion through coating ($Cs^+/^{137}Cs^+$ Exchange, H_2O).

Table I

Cs Uptake Summary: Cs Diffusion Coefficients
(cm^2/hr)

	Polybutadiene	Alkyd Topcoat	Alkyd Topcoat/Primer
Intact Film			
Open Circuit	$1.1 \pm (0.5) \times 10^{-9}$	$1.1 \pm 0.7 \times 10^{-7}$	$5.5 \pm (2.8) \times 10^{-10}$
-0.800 VDC	$1.3 \pm (0.7) \times 10^{-8}$	$9.3 \pm 3.4 \times 10^{-7}$	$8.3 \pm 0.5 \times 10^{-8}$
3 mm Defect			
Open Circuit	$3.2 \pm (1.6) \times 10^{-9}$	$1.1 \pm 0.5 \times 10^{-6}$	$2.2 \pm 1.3 \times 10^{-7}$
-0.800 VDC	$2.3 \pm (1.1) \times 10^{-8}$	$6.8 \pm (3.4) \times 10^{-7}$	$1.6 \pm (0.8) \times 10^{-6}$
Lateral Diffusion			
Open Circuit:			
Sample	$1.4 \pm (0.7) \times 10^{-8}$	--	--
Solution	$2.5 \pm (1.2) \times 10^{-8}$	--	--
-0.800 VDC	Under investigation		

Table II

NaCl Uptake Summary: NaCl Diffusion Coefficients (cm^2/hr)

Coating	Sodium		Chloride	
	Open Circuit	-0.800 VDC	Open Circuit	-0.800 VDC
Polybutadiene				
No Defect	$6.3 \pm 4.2 \times 10^{-9}$	$9.1 \pm (4.5) \times 10^{-9}$	$1.8 \pm 3.3 \times 10^{-9}$	$2.3 \pm (1.2) \times 10^{-9}$
3 mm Defect	$8.3 \pm (4.2) \times 10^{-9}$	$6.1 \pm (3.0) \times 10^{-9}$	Negligible	Negligible
Alkyd Topcoat				
No Defect	$7.0 \pm 4.6 \times 10^{-8}$	$5.6 \pm 1.1 \times 10^{-7}$	$2.3 \pm 1.2 \times 10^{-8}$	$7.0 \pm 1.5 \times 10^{-8}$
3 mm Defect	$5.4 \pm (2.7) \times 10^{-7}$	$5.5 \pm (2.7) \times 10^{-7}$	$1.3 \pm (2.7) \times 10^{-7}$	Negligible
Alkyd Topcoat & Primer				
No Defect	$8.5 \pm 2.4 \times 10^{-8}$	$1.2 \pm 0.6 \times 10^{-7}$	$1.9 \pm 3.7 \times 10^{-9}$	$4.5 \pm 2.4 \times 10^{-8}$
3 mm Defect	$2.3 \pm 0.8 \times 10^{-7}$	$2.7 \pm (1.3) \times 10^{-7}$	$7.6 \pm (3.8) \times 10^{-8}$	Negligible

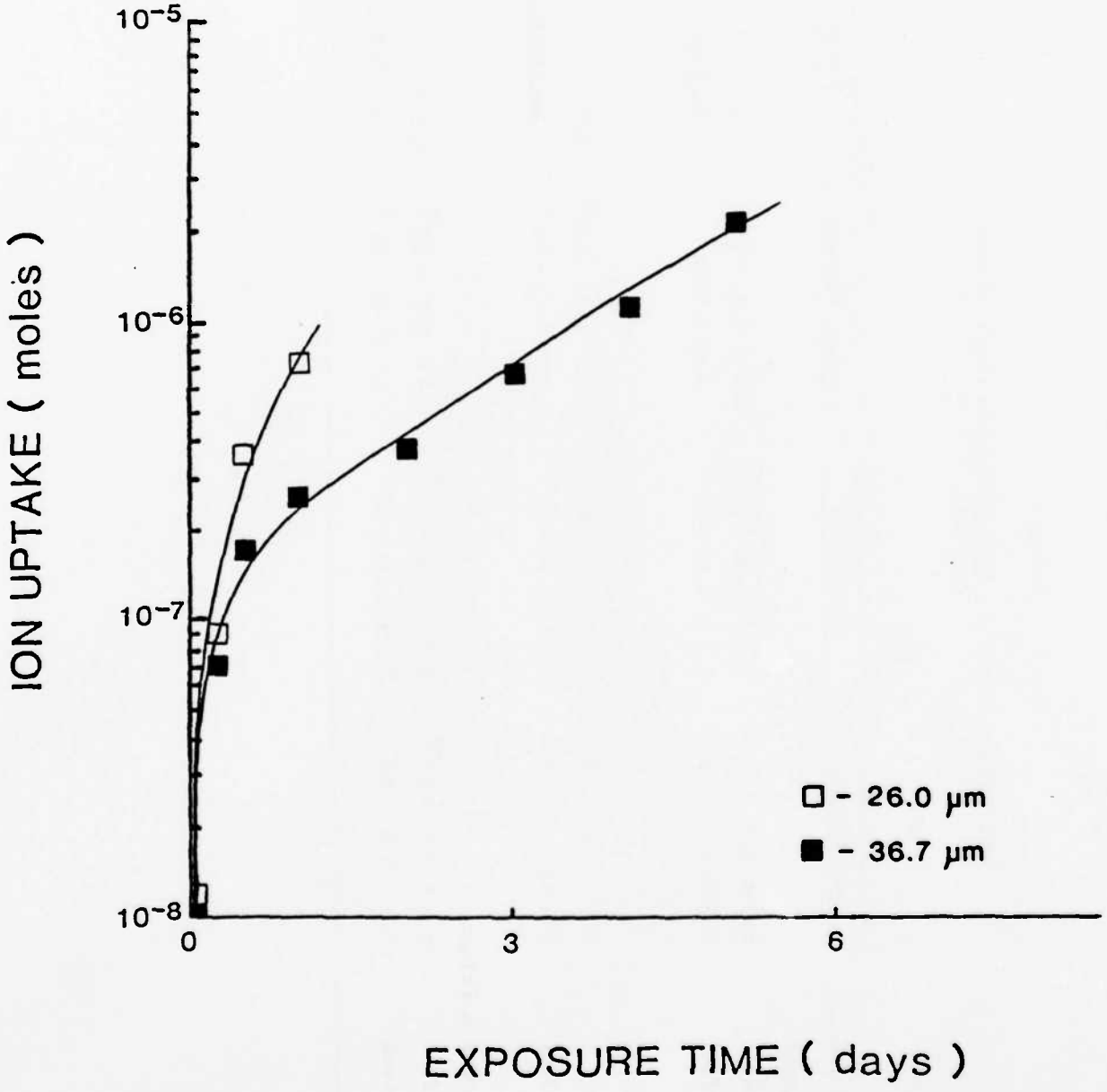

Figure 3. Cs uptake by alkyd topcoat on CRS.

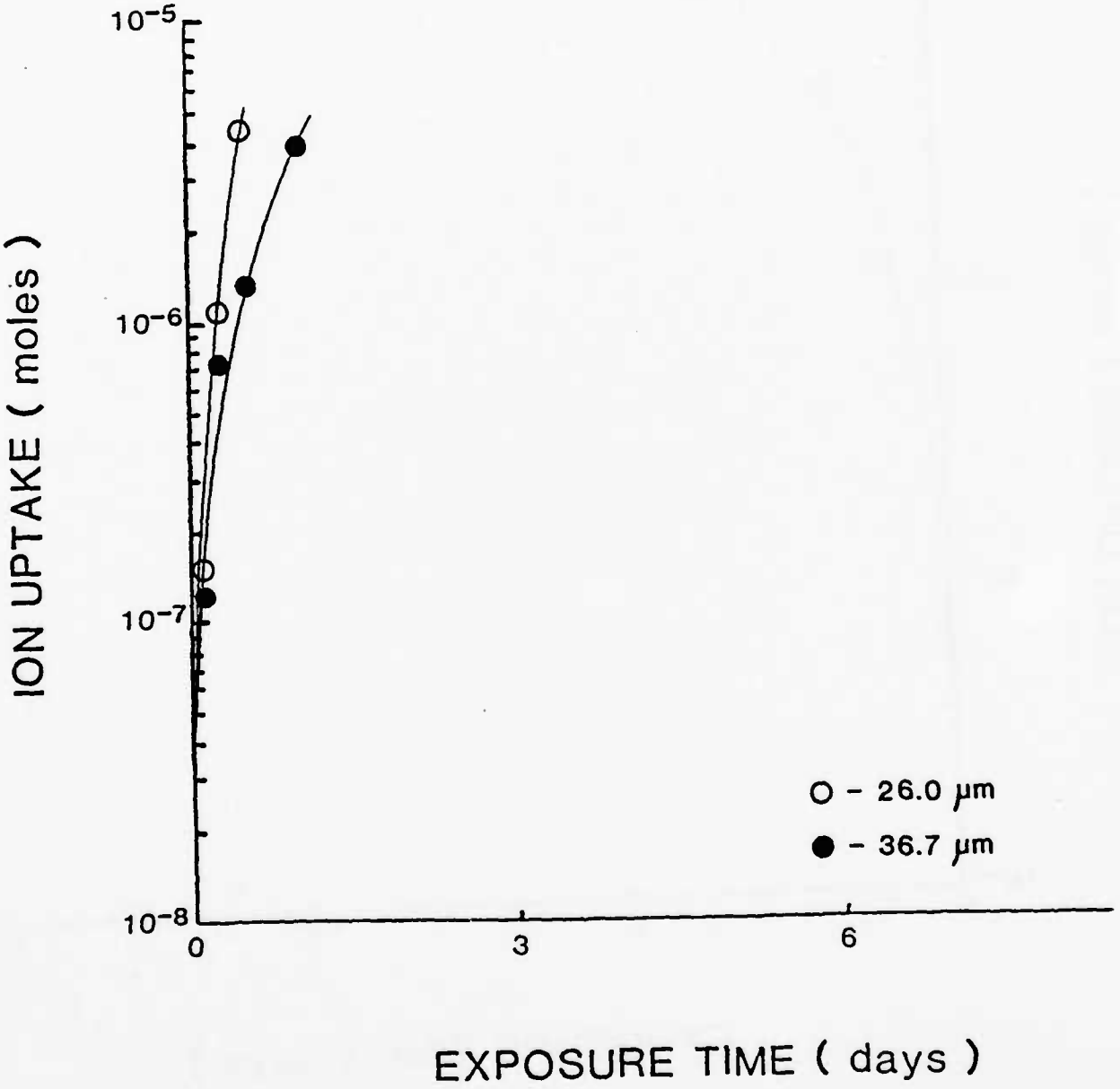

Figure 4. Cs uptake by alkyd topcoat on CRS.

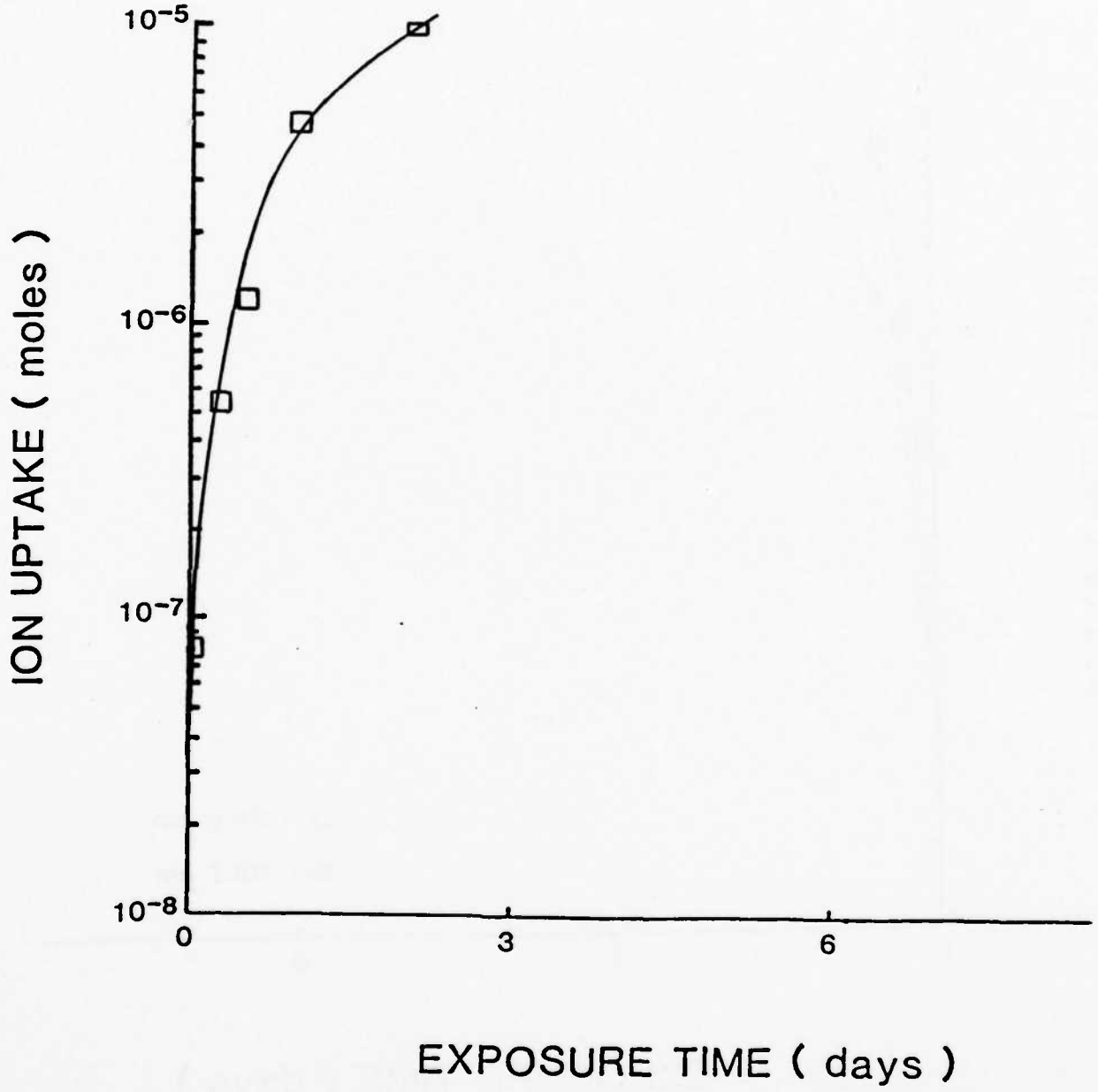

Figure 5. Cs uptake by alkyd topcoat: 3 mm defect.

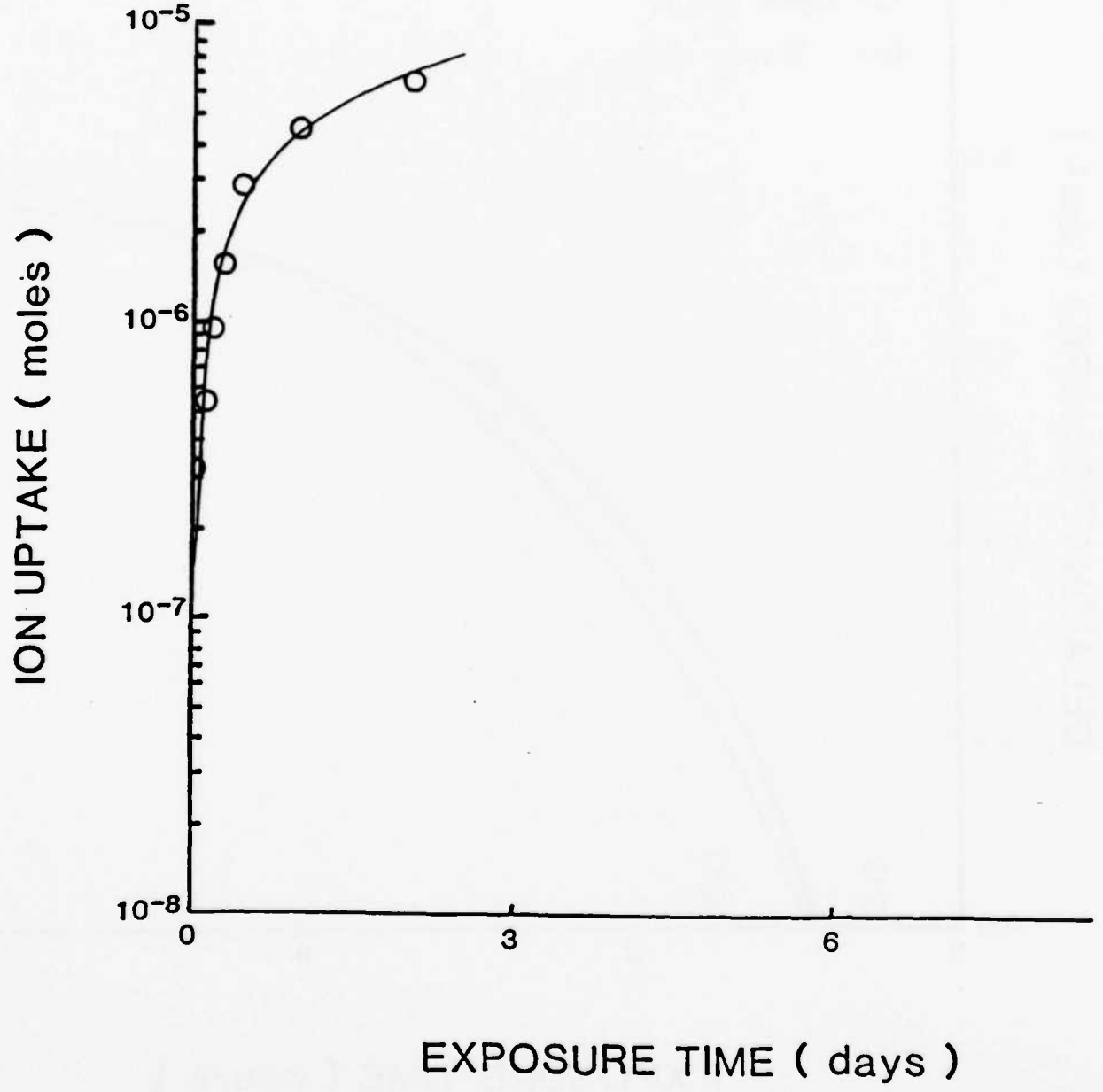

Figure 6. Cs uptake by alkyd topcoat: 3 mm defect.

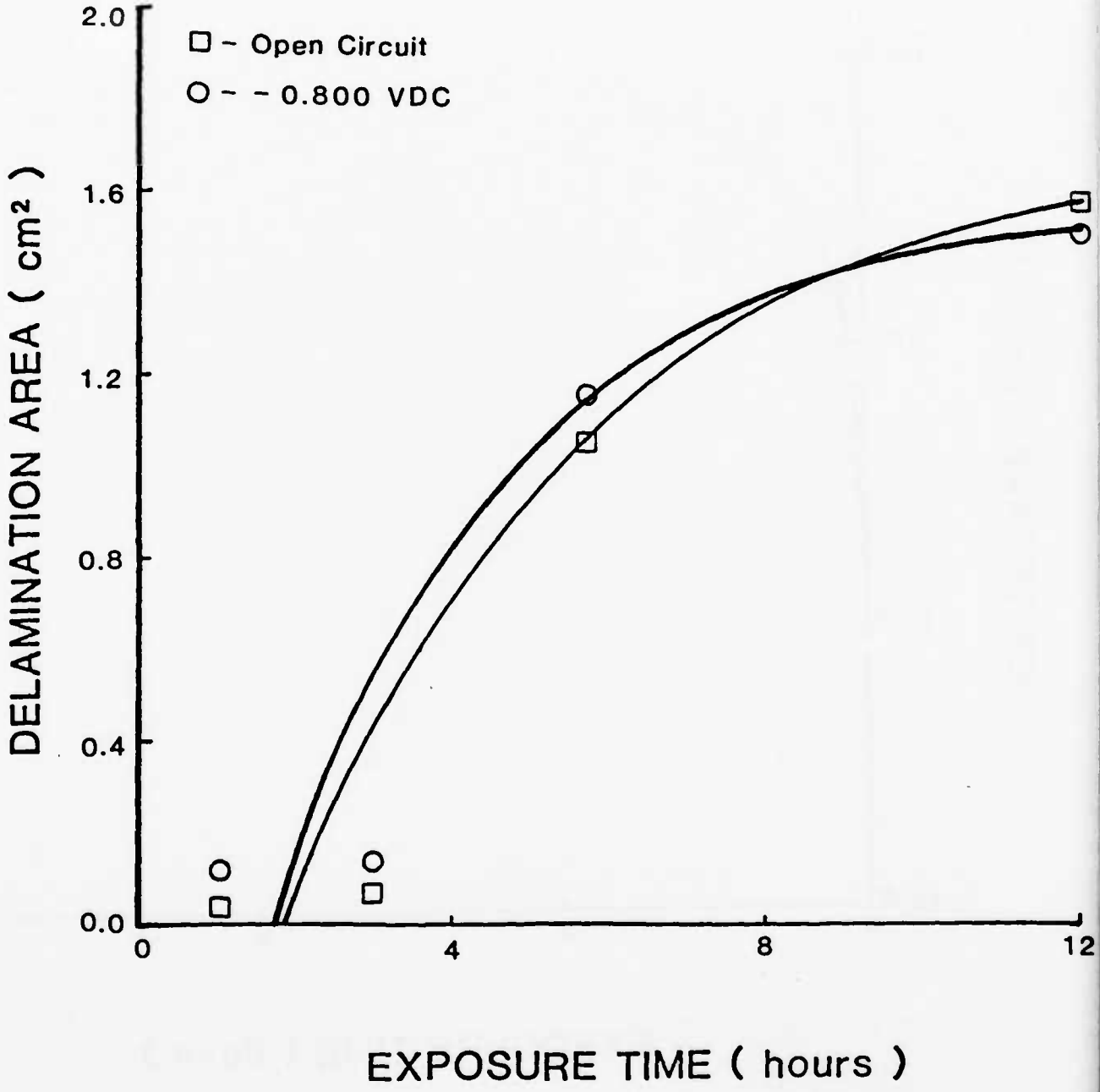

Figure 7. Delamination of alkyd topcoat.

observed, indicating that cathodic disbonding is not the primary mechanism for adhesion loss. This is consistent with the fact that the paint has poor wet adhesion properties. This would also account for the similarities in the ion uptake curves. The corrosion potential of the substrate is only 50 mV more positive than the applied cathodic potential. With wet adhesion loss there is direct access to the substrate from the defect, and the primary diffusion pathway would be through the solution. With a small difference in potential and direct access, similar uptake behavior would be expected. Figure 8 shows the relationship between uptake and delamination as a function of potential.

The uptake of Cs by the alkyd topcoat-primer sytem is summarized in Figures 9-12. Two major differences resulting from the addition of a primer layer are observed. First the primer appears to act as a barrier to ionic diffusion, with ion uptake by intact films being reduced at least an order of magnitude (Figs. 9,10). There is also a marked reduction in the uptake of Cs when a defect is introduced into the coating at open circuit (Fig. 11). Under polarization (Fig. 12) uptake by defect samples was nearly identical to that observed for topcoat-only samples.

Delamination behavior for this system is summarized in Figure 13. Note the linearity of the curves. This is characteristic of samples undergoing cathodic disbonding [2-4]. Cs uptake as a function of delaminated area is given in Figure 14. Again we observe a linear relationship between uptake and delamination at both potentials. The curves are nearly parallel suggesting that, once delamination occurs, potential affects only the rate of delamination and ion uptake, and not the relative amounts.

Similar results are observed for polybutadiene. Figure 15 shows the average Cs uptake by polybutadiene coated plates as a function of applied potential. The curves represent a nearly tenfold increase in uptake rate under cathodic polarization. Introduction of a defect into the coating results in only a twofold increase in uptake rate over the corresponding defect-free samples (Fig. 16). This can be accounted for by the good wet-adhesive properties of the coating and suggests that lateral diffusion would be of the same magnitude as diffusion through the coating. This will be discussed later when the lateral diffusion experiment is reviewed.

The delamination curves for polybutadiene are given in Figures 17 and 18. Unlike the alkyd studies, there is a marked difference (fivefold) in both the delay time (i.e., time prior to observed delamination) and the delamination rate. The rate differences are independent of the relative uptakes of Cs with delaminated area, which, as in the previous cases, are nearly identical (Fig. 19). Only the number of moles Cs taken up prior to delamination varies.

What effect does lateral diffusion have on delamination and overall ion uptake? It has already been suggested that lateral diffusion for the polybutadiene system is of the same magnitude as diffusion through the coating. Using the cell shown in Figure 2, the amount of Cs retained by polybutadiene as a result of lateral diffusion and the amount exchanged with the non-doped outer solution was determined at open circuit. From Figure 20 we see that after about a day's delay, Cs is exchanged with the outer solution at about the same rate as it is being retained by the coated steel. Within a few days the coating system appears to be approaching equilibrium and the uptake rate

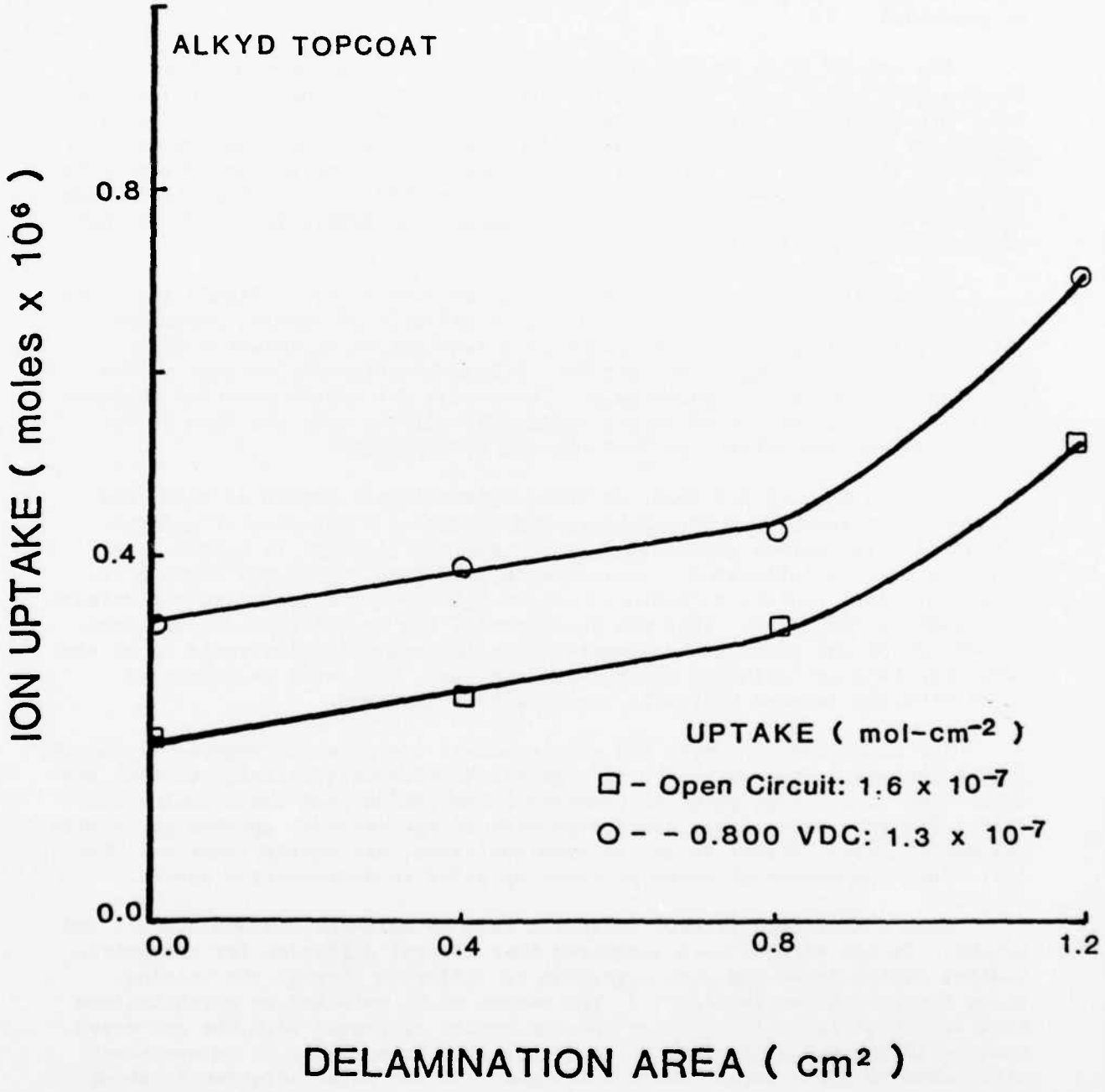

Figure 8. Cs uptake as a function of delamination area.

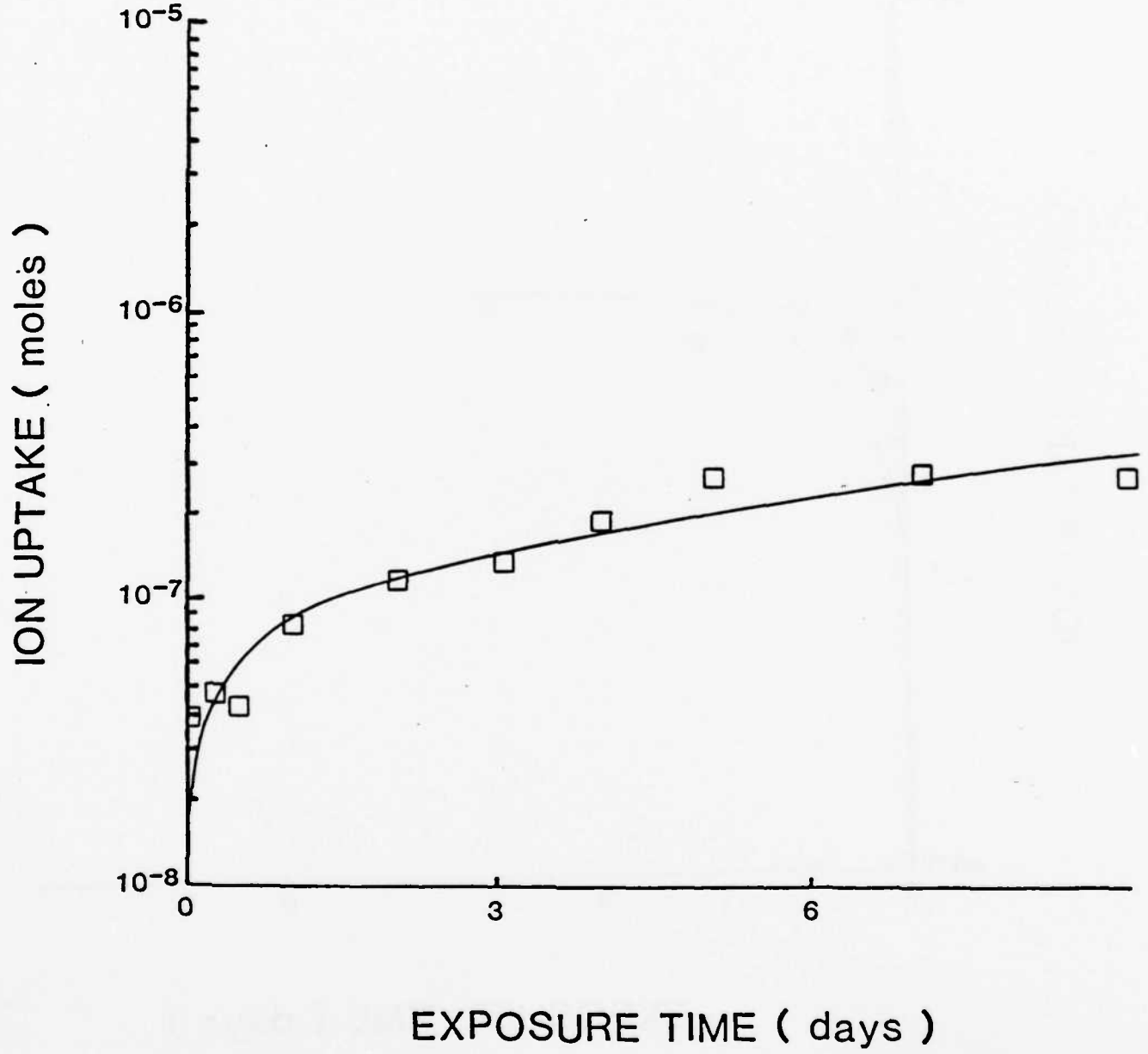

Figure 9. Cs uptake by alkyd system on CRS.

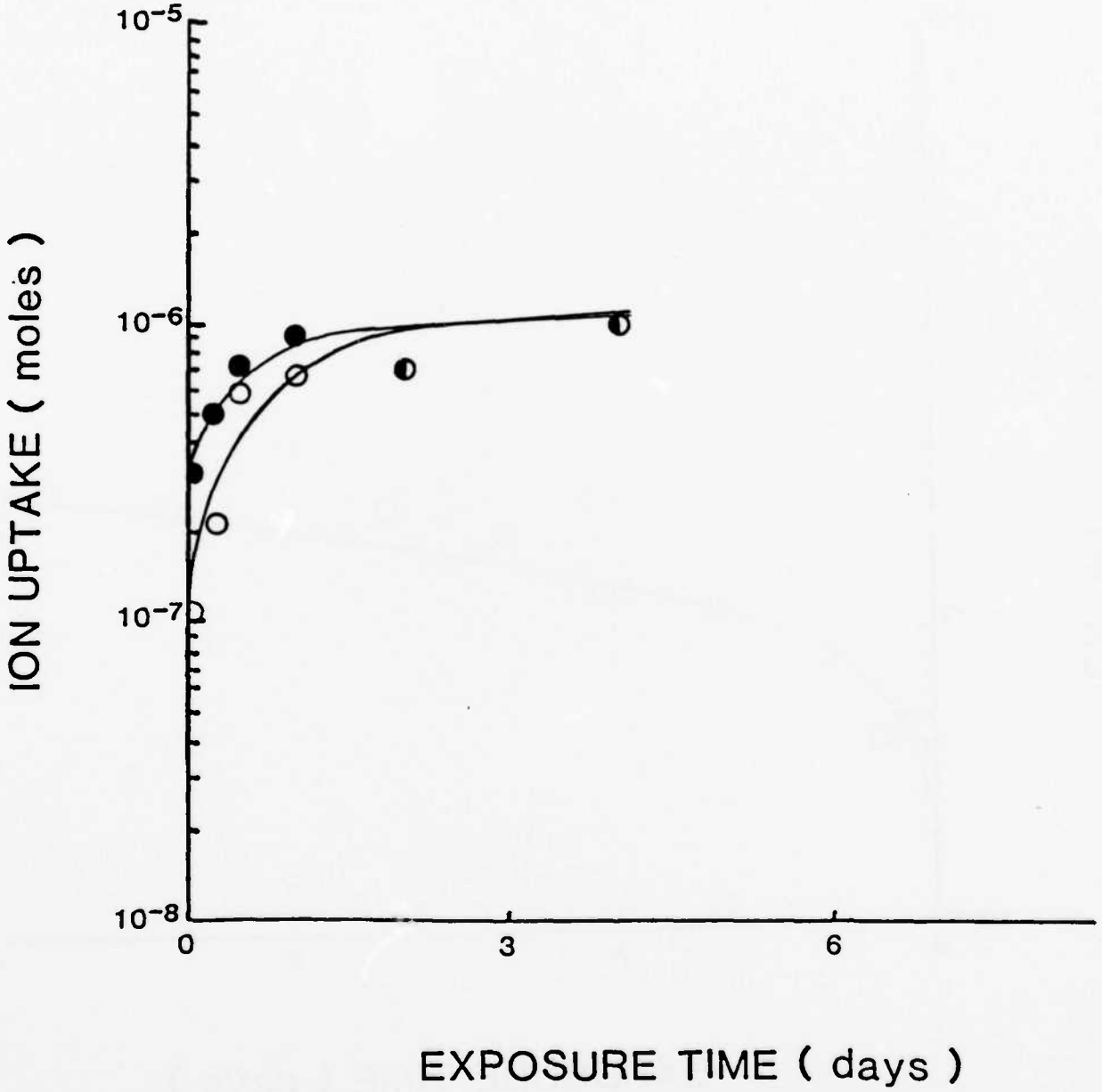

Figure 10. Cs uptake by alkyd system on CRS.

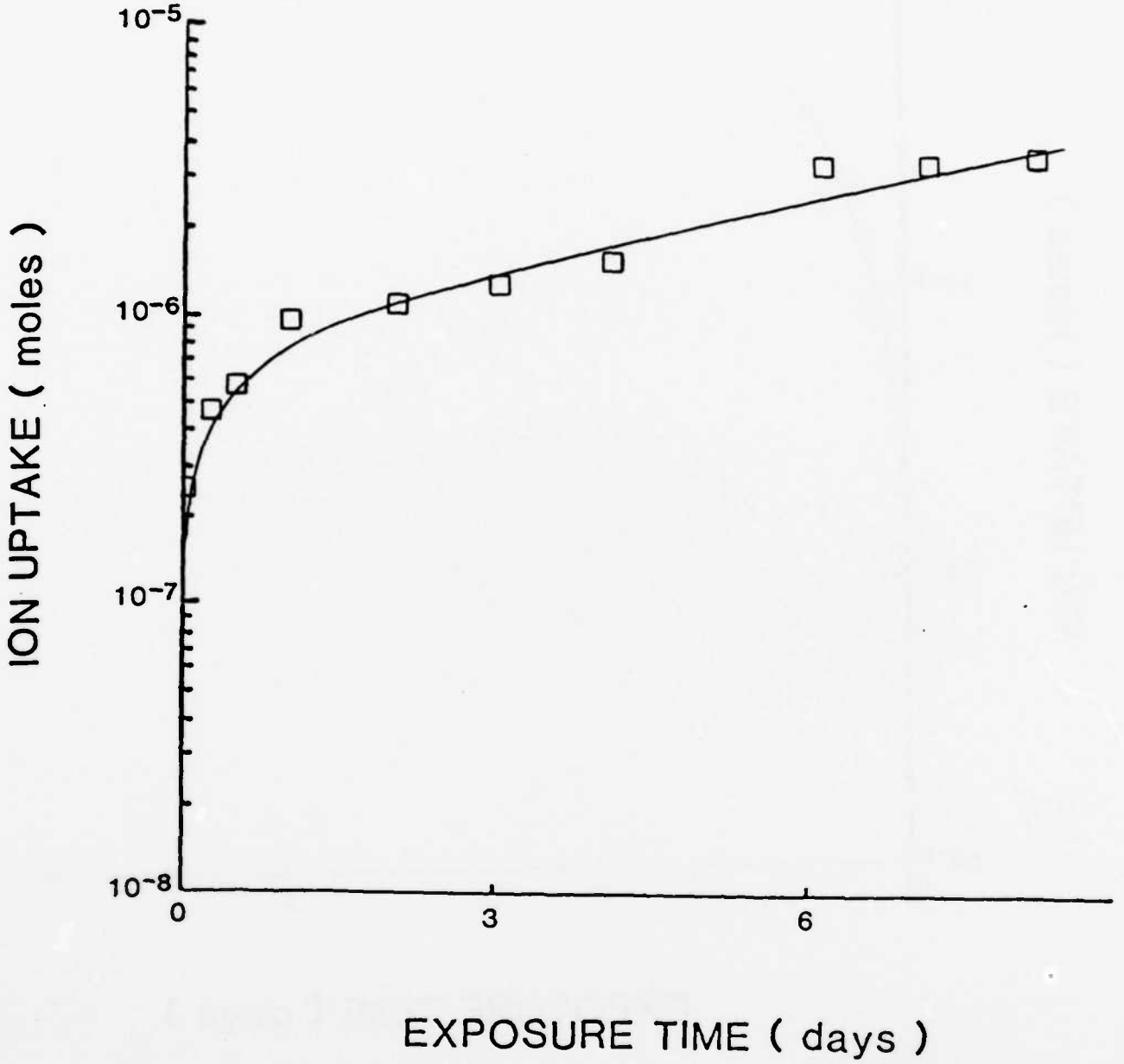

Figure 11. Cs uptake by alkyd system: 3 mm defect.

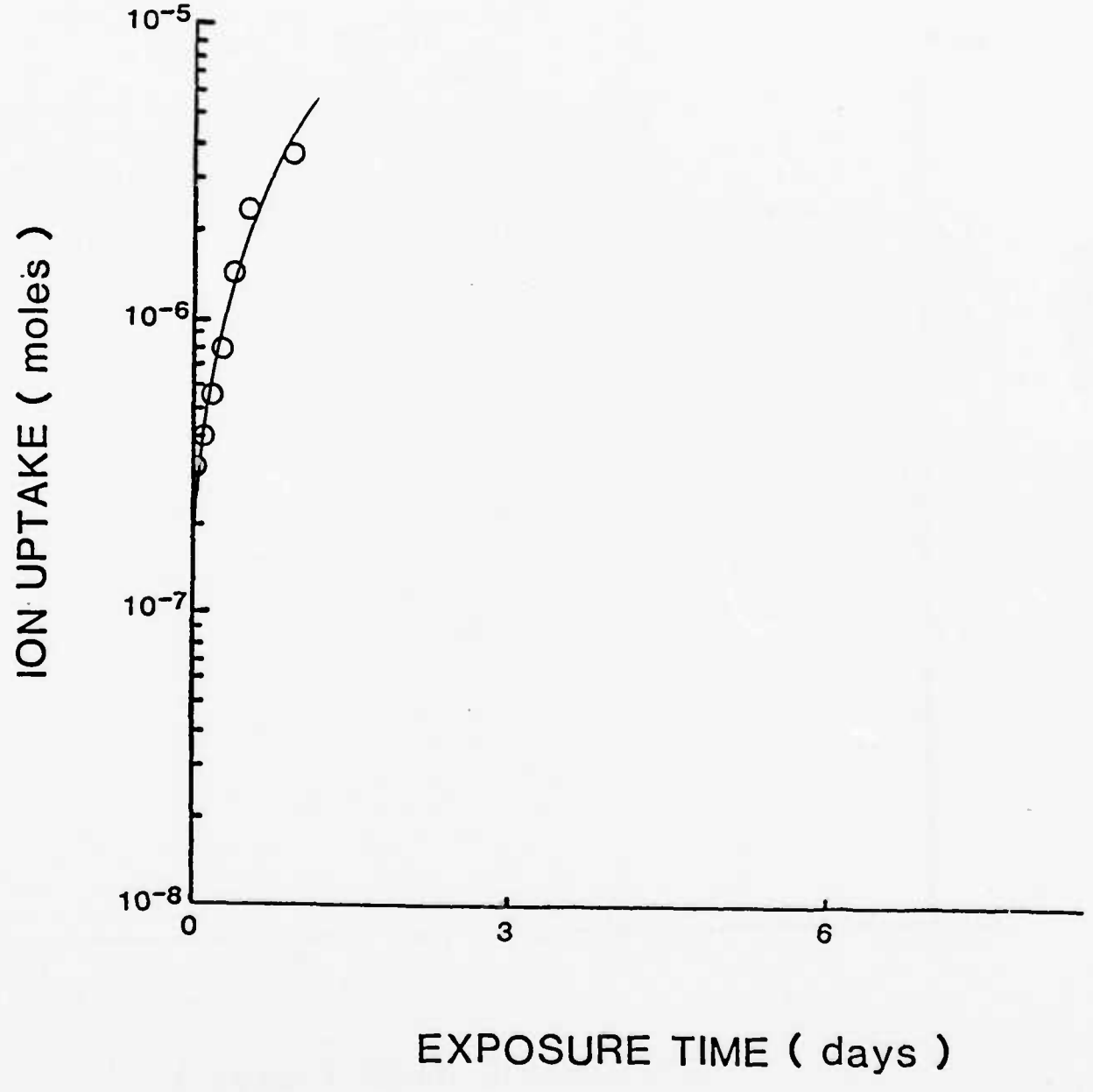

Figure 12. Cs uptake by alkyd system: 3 mm defect.

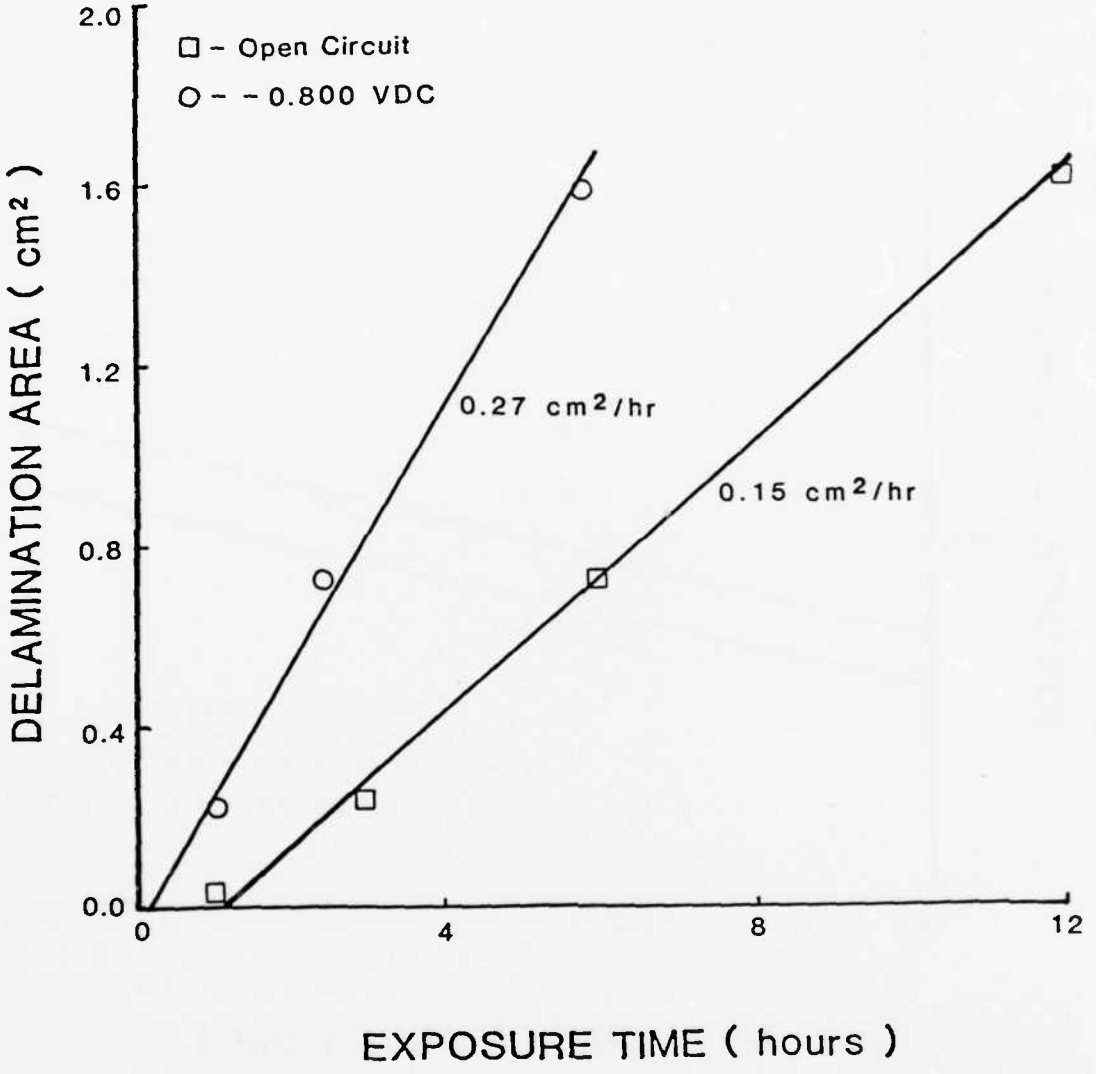

Figure 13. Delamination of alkyd system.

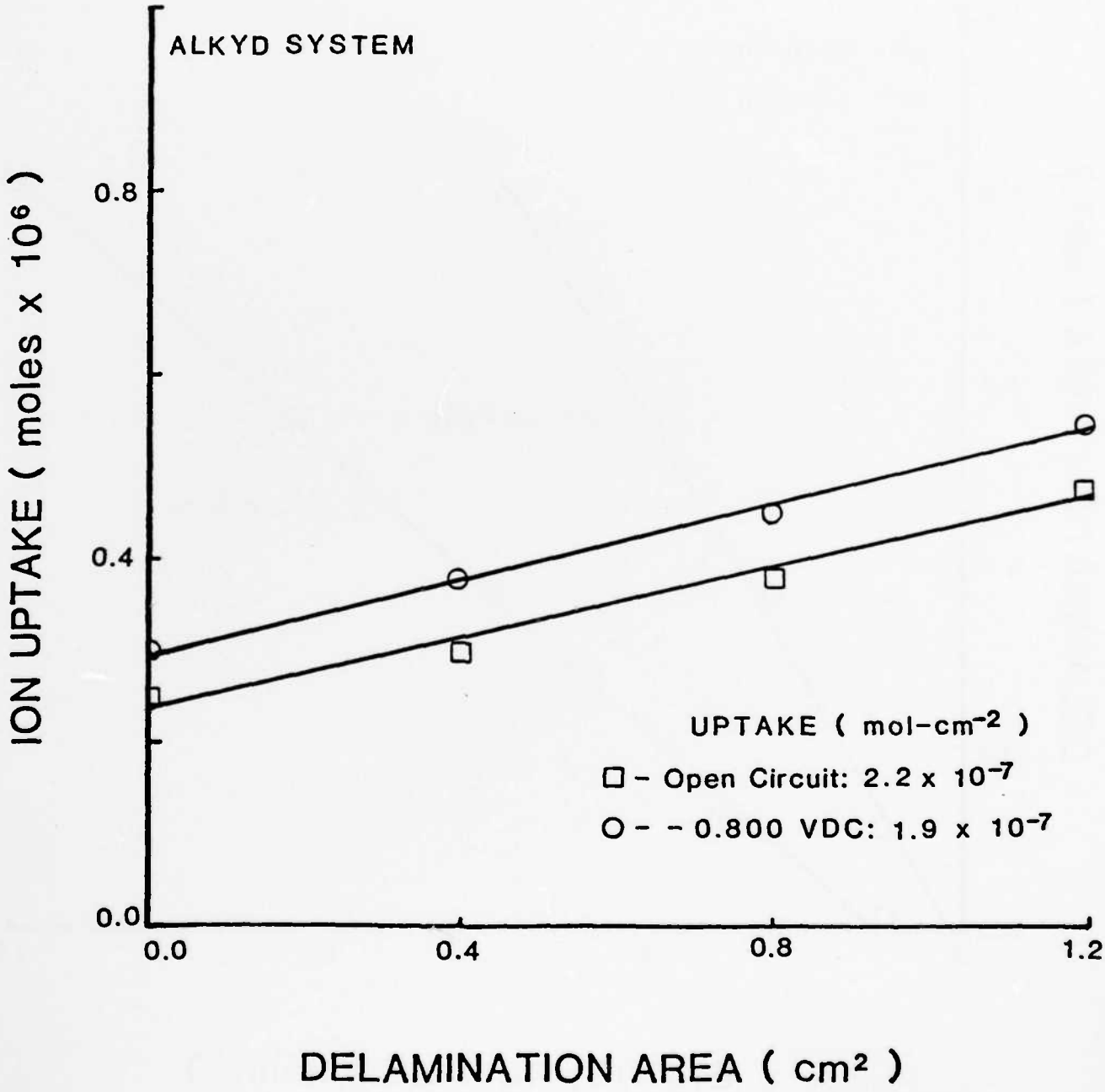

Figure 14. Cs uptake as a function of delamination area.

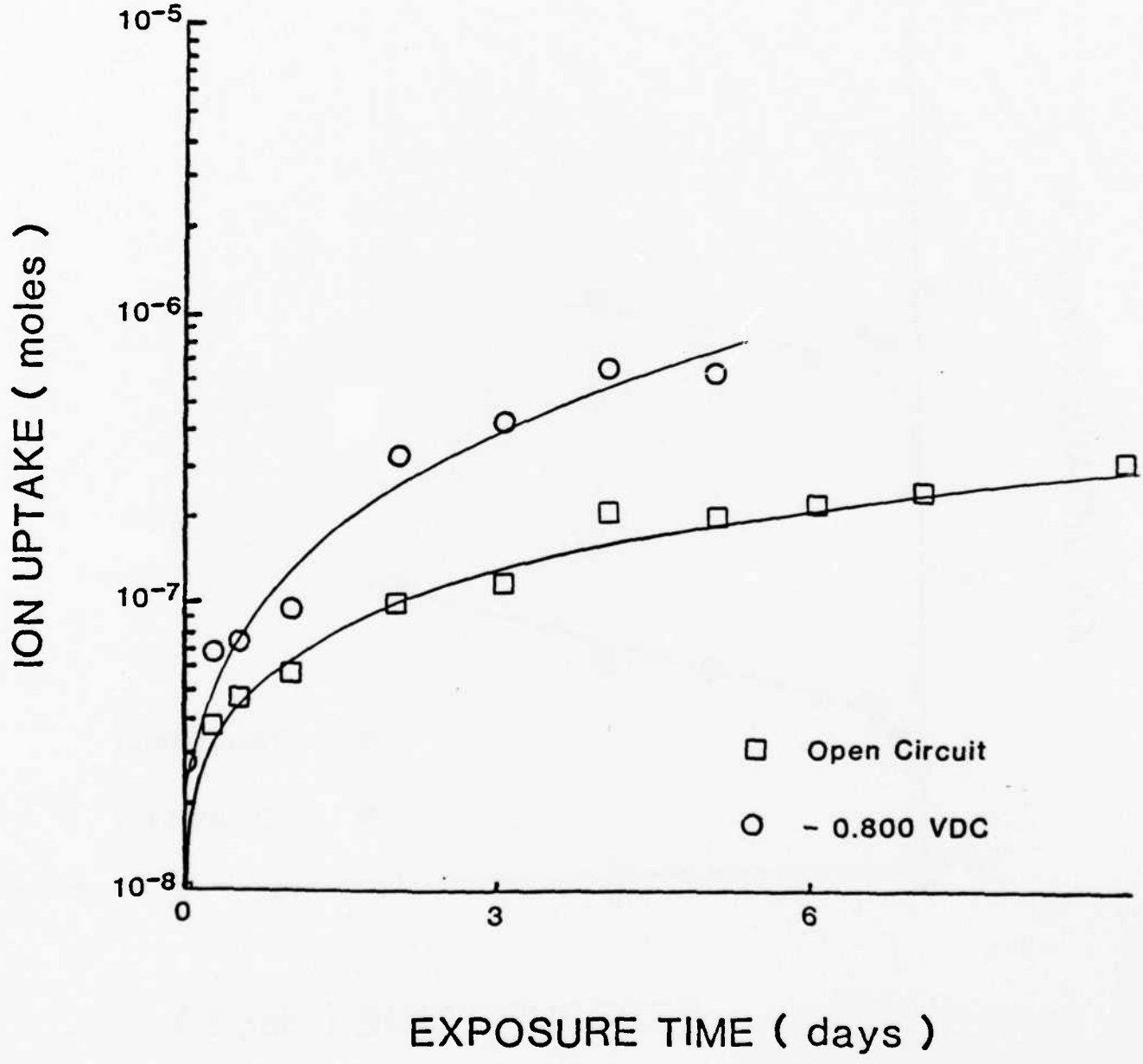

Figure 15. Cs uptake by polybutadiene on CRS.

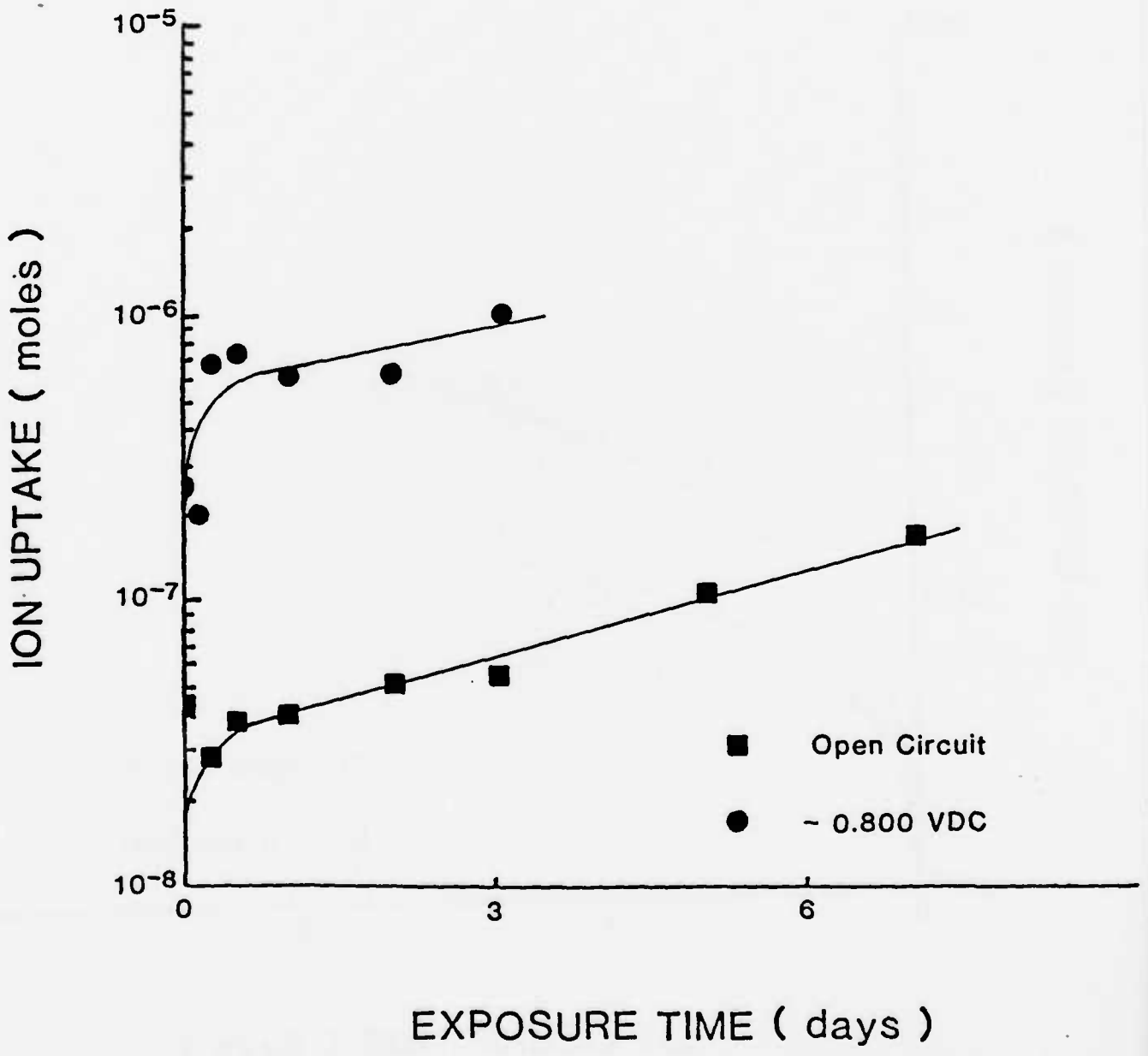

Figure 16. Cs uptake by polybutadiene on CRS: 3 mm defect

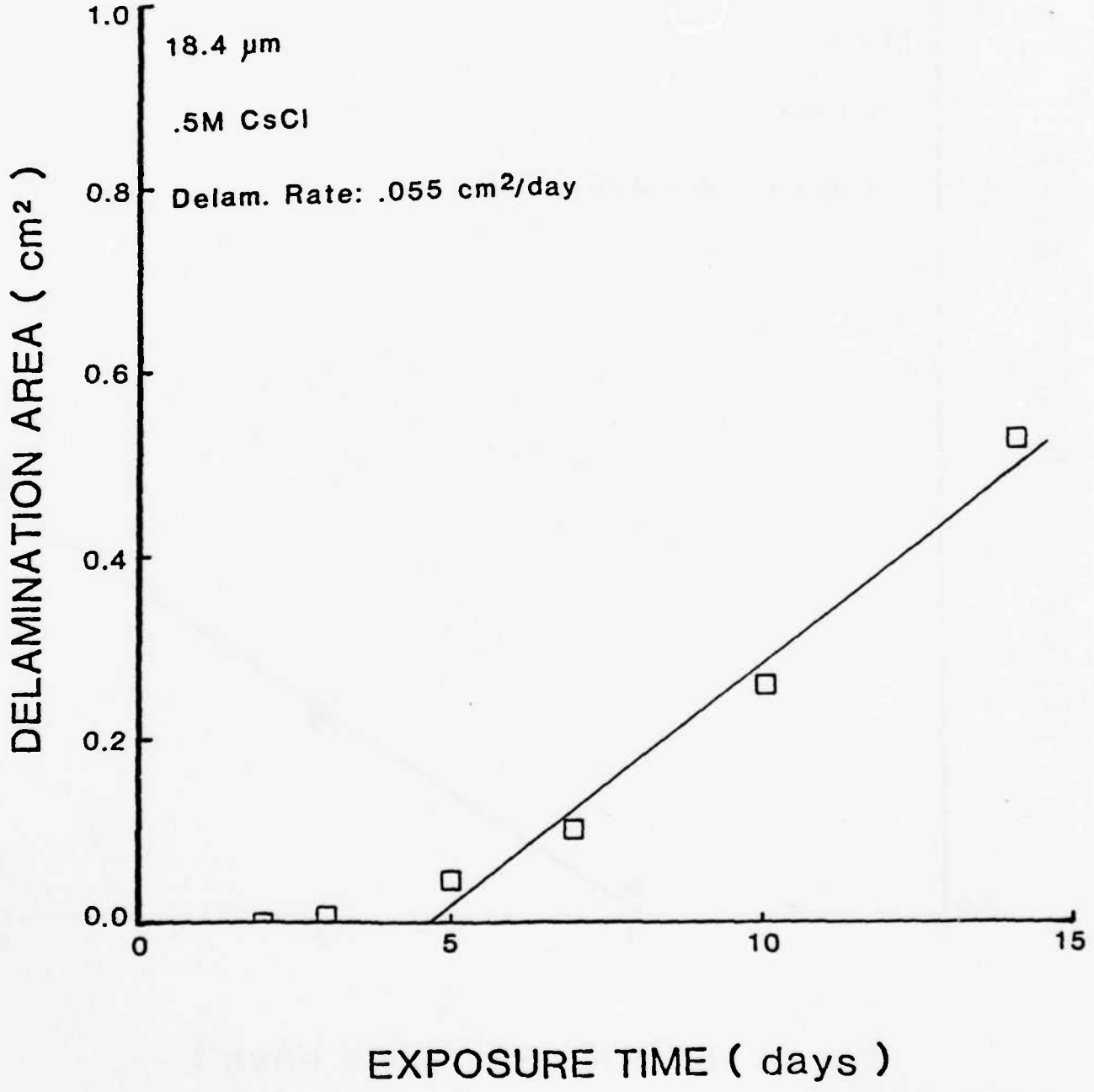

Figure 17. Delamination of polybutadiene at open circuit.

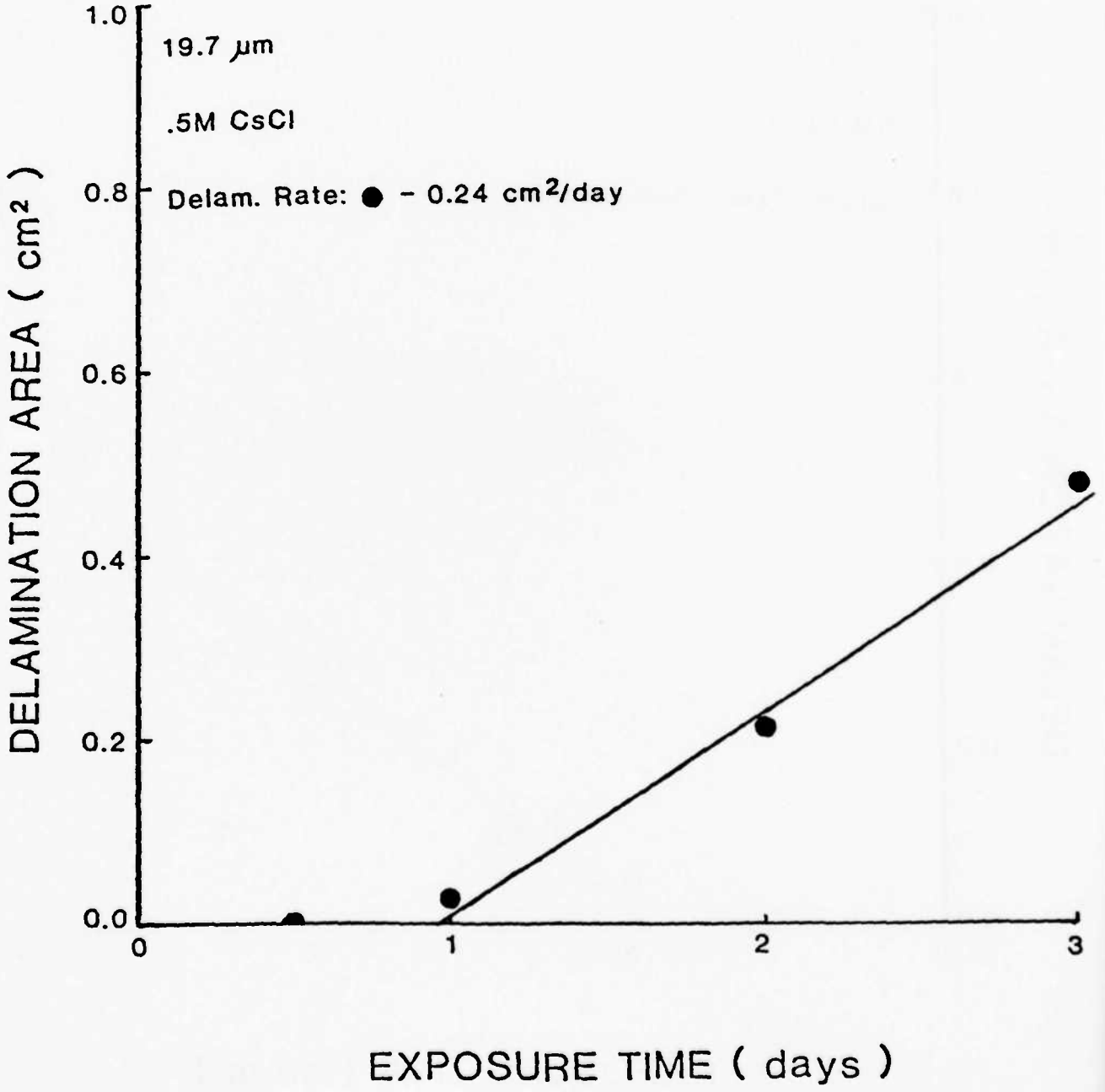

Figure 18. Delamination of polybutadiene at -0.800 VDC.

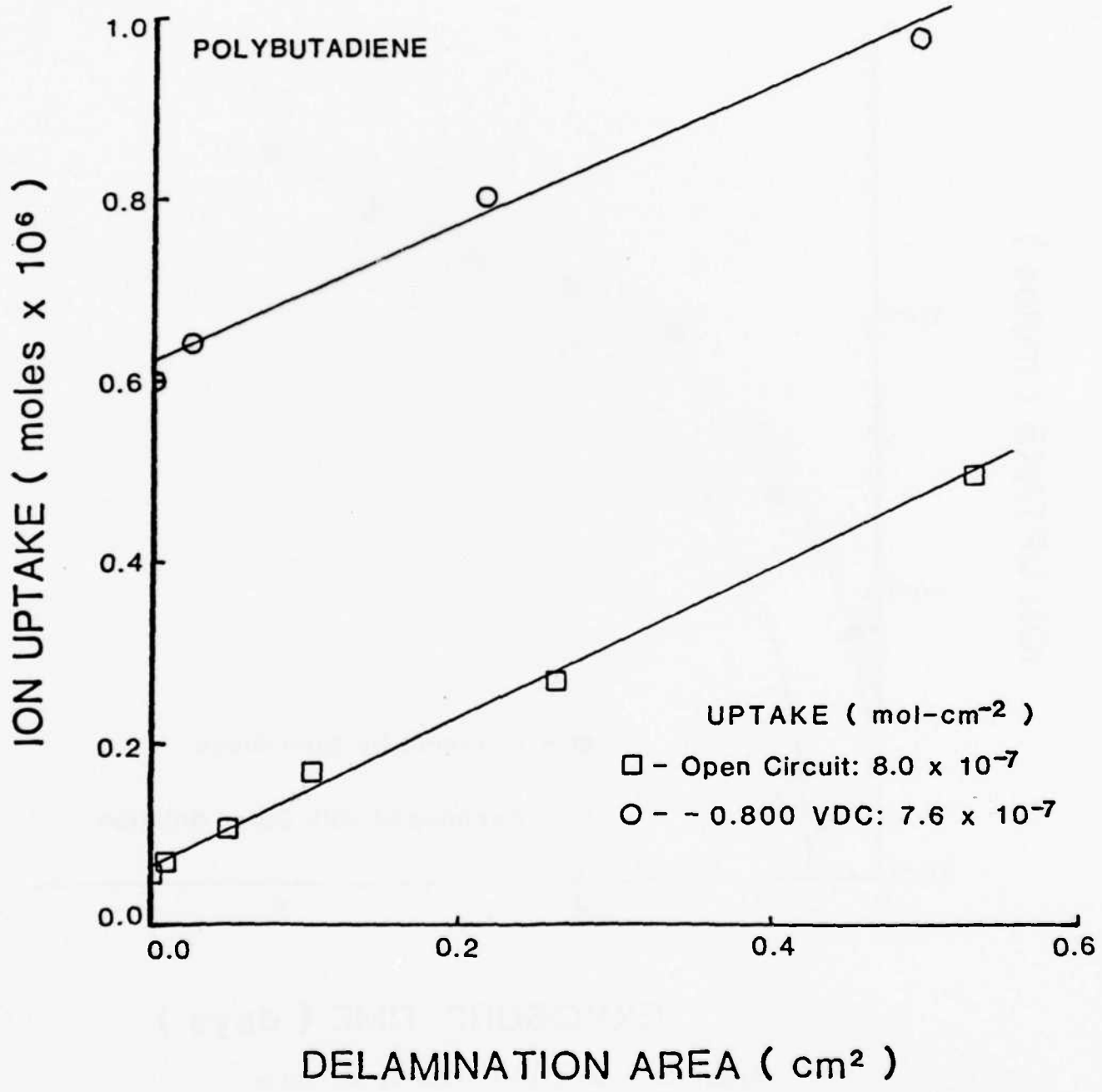

Figure 19. Cs uptake as a function of delamination area.

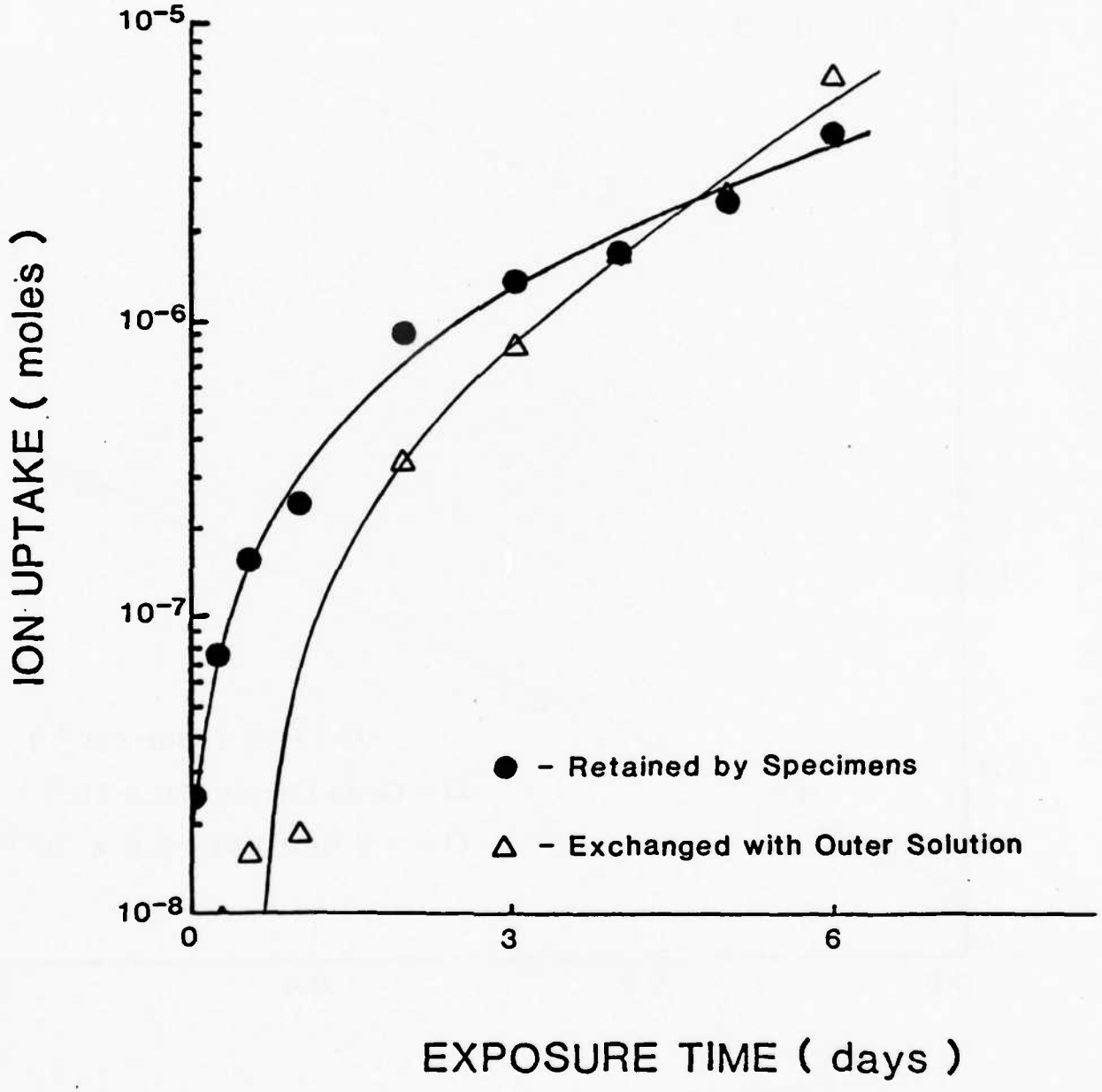

Figure 20. Open circuit lateral diffusion.

falls off. Lateral diffusion under cathodic polarization is presently under investigation.

CONCLUSIONS

Radiotracers have been used to study the relationship between ionic transport and the disbonding of protective coatings as a function of potential. The results of these studies are summarized in Tables I and II. It has been shown that the wet-adhesion character of a coating plays an important role in determining the ion uptake profile for that coating. Coatings with poor adhesion show small changes in uptake profile when polarized to -0.800 VDC, while coatings with good adhesion show increases of nearly an order of magnitude. Once delamination is initiated, ion uptake increases linearly with delaminated area. The magnitude of this uptake is independent of applied potential. Lateral diffusion studies of polybutadiene at open circuit show the rate of lateral diffusion to be of the same magnitude as diffusion through the coating.

REFERENCES

[1] Third Annual Report, "Corrosion Control through a Better Understanding of the Metallic Substrate/Organic Coating/Interface," December 1, 1982, p.111.

[2] H. Leidheiser, Jr., and W. Wang, "Corrosion Control by Organic Coatings," H. Leidheiser, Jr., Editor, Natl. Assoc. Corrosion Engrs., Houston, Texas, p.70 (1981).

[3] H. Leidheiser, Jr., and W. Wang, J. Coatings Technol. 53(672), 77 (1981).

[4] H. Leidheiser, Jr., W. Wang, and L. Igetoft, Prog. Organic Coat. 11(1), 19 (1983).

Program #16

An Understanding of the Principles Related to the Application of Paints to Rusted Steel Surfaces with Little or No Surface Preparation

INTRODUCTION

Fundamental information on the adhesion of polymer coatings to iron corrosion products can help to understand phenomena related to the painting of rusted steel surfaces after removal of only the loose surface rust. In order to obtain large surface areas for a polymer-iron oxide surface interaction study, iron corrosion products must be prepared in the form of colloidal sols. New processes were developed to prepare all the eight iron corrosion products, i.e., Fe_3O_4, α-Fe_2O_3, γ-Fe_2O_3, α-FeOOH, β-FeOOH, γ-FeOOH, δ-FeOOH and $FeCO_3$, in the form of colloidal sols in large quantities. These sols have large surface areas in the range of 3.4 to 206 m^2/g and have high solids contents in the range of 2.74 to 9.60 g/100 ml of aqueous phase. The uniformity of the particle size and the large specific surface areas of these particles make it possible to obtain polymer adsorption isotherms and determine acidic and basic sites on the surfaces of these particles.

The sols were cleaned by serum replacement or centrifugation-decantation. The compositions of these particles were confirmed by X-ray diffraction and Mössbauer spectroscopy. The specific surface areas were determined by argon gas adsorption. The particle morphology was determined by electron microscopy. The acid-base character of these surfaces was determined by adsorption isotherms with standard basic and acidic polymers. The preparation technique, the confirmation and characterization results, the polymer adsorption results and the conductometric titration data will be discussed and summarized.

Particle Growth Technique

All of the eight iron corrosion products were prepared using the processes adapted from industrial methods which were tailored to laboratory size. A 4-liter Pyrex glass beaker equipped with a mechanical stirrer was used as a reactor. For the particle growth techniques, a Plexiglas rack was constructed to hold the folded sheet iron in the reactor. A looped Tygon tubing with holes drilled in it was positioned in the bottom of the beaker to serve as an oxygen sparger.

The seed growing processes applied to α-Fe_2O_3, α-FeOOH, and γ-FeOOH particles could be demonstrated clearly by monitoring the stepwise growth process of α-Fe_2O_3 particles to 30 hr. This is a good demonstration of the effectiveness of the process in increasing the particle size and the solids

content simultaneously. The solid content of the sols, the particle sizes based on transmission electron micrographs, the particle sizes based on specific surface areas, and the specific surface areas for each growth stage are summarized in Table I

Table I

The Growing Process of α-Fe_2O_3 Particles

Growing Time	Solid Content	Particle Size Based on TEM	Particle Size Based on S.S.A.	Specific Surface Area
0 hr.	1.65%	0.010 μm	0.007 μm	171.4 m^2/g
6	5.70	0.015	0.013	85.6
12	8.73	0.025	0.026	44.7
18	11.63	0.033	0.036	31.5
24	14.77	0.040	0.047	24.4
30	21.00	0.050	0.061	18.7

Mössbauer Studies of Superparamagnetic δ-FeOOH

As mentioned in the last report (3rd Annual Report), all of the Mössbauer spectra were recorded at room temperature and the Mössbauer parameters were compared with the literature values to confirm the compositions of the prepared iron corrosion products. Earlier publications regarding the Mössbauer spectra of δ-FeOOH are in disagreement. Dezsi et al. [1] recorded the Mössbauer spectra of δ-FeOOH at different temperatures and found it to be ferrimagnetic below ~400°K; the octahedral and tetrahedral ratio of iron occupation was estimated to be 60 and 40 percent, resepctively. Loseva et al. [2] and Moskvin et al. [3] found δ-FeOOH to be paramagnetic at room temperature. Povitskii et al. [4] found δ-FeOOH to be superparamagnetic at room temperature if the particle size was less than 5 nm.

The Mössbauer spectra of δ-FeOOH were recorded using a constant acceleration spectrometer. The spectra were evaluated by fitting a sum of Lorentzian lines. All isomer shifts are given relative to α-Fe. The Mössbauer spectra are shown in Figures 1 and 2. The δ-FeOOH sample showed paramagnetic behavior above 120°K as indicated by the quadrupole splitting in the spectra in Figures 1 and 2, and ferrimagnetic characteristics below 70°K as indicated by the magnetic splitting in the spectra in Figure 2. The Mössbauer parameters of the δ-FeOOH samples are given in Table II. The population of the octahedral sites was about 70%, as estimated on the basis of Mössbauer line areas. This

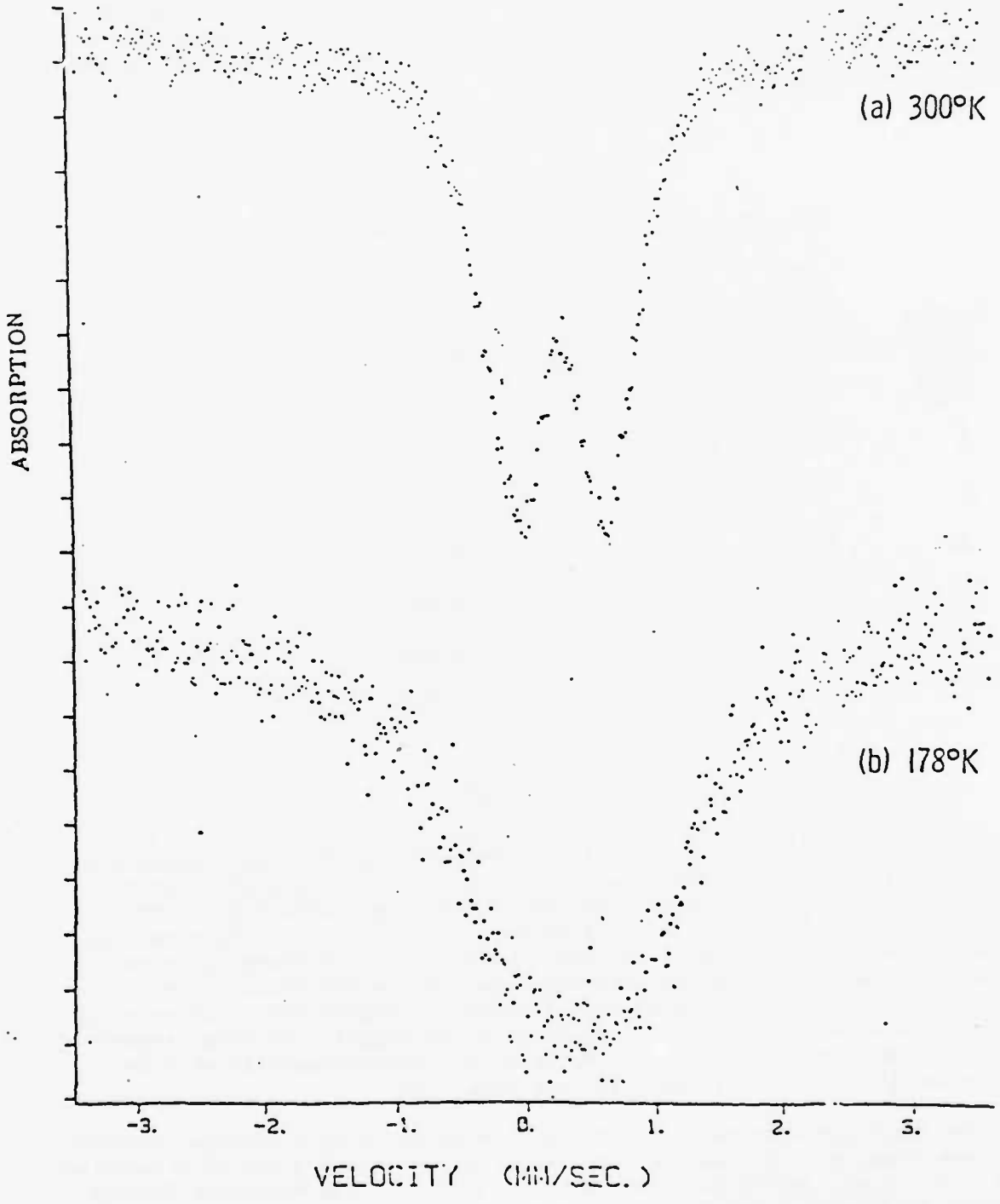

Figure 1. Mössbauer spectra of δ-FeOOH sample at different temperatures, (a) 300°K and (b) 178°K.

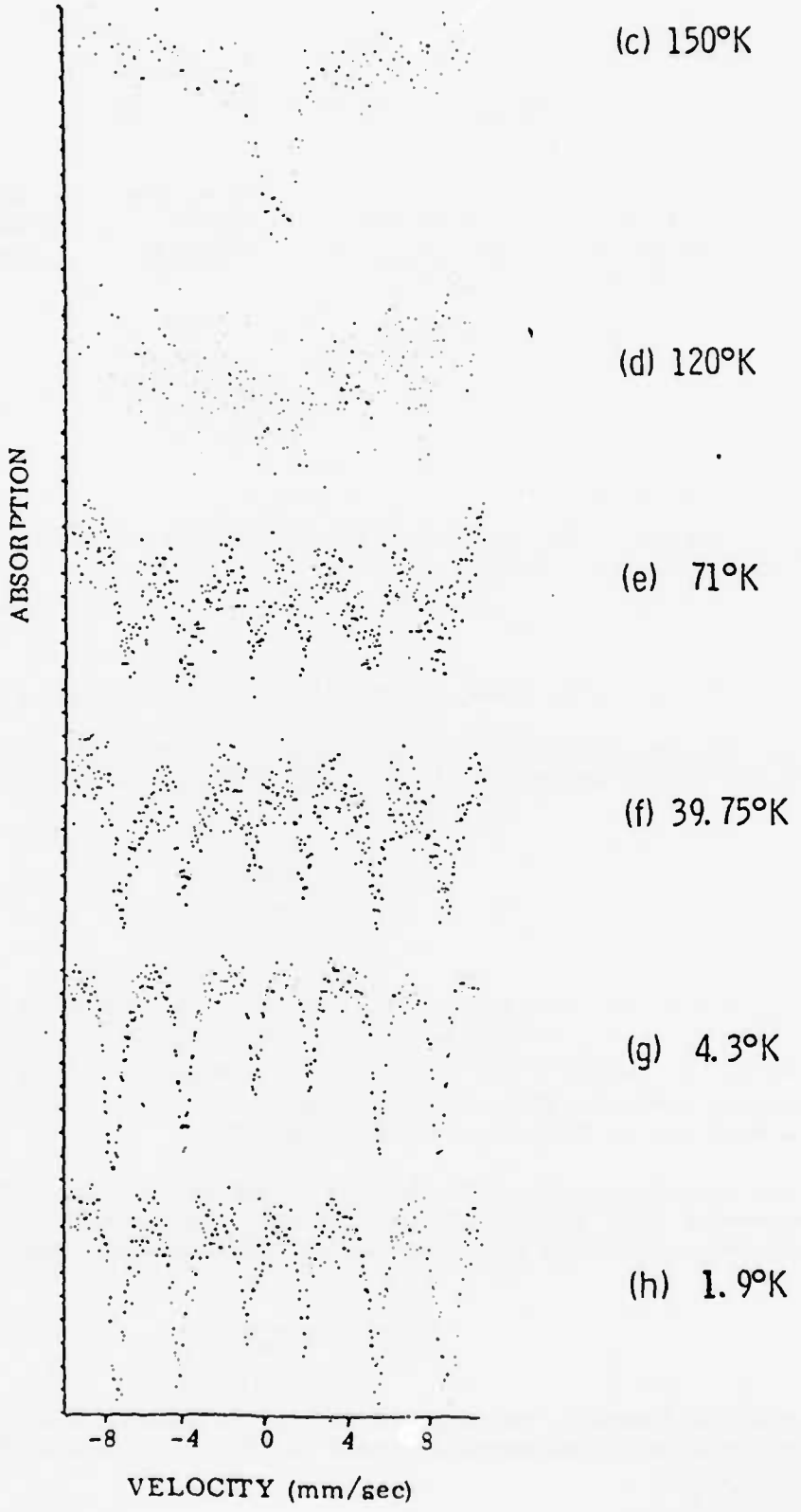

Figure 2. Mössbauer spectra of δ-FeOOH sample at different temperatures, (c) 150°K, (d) 120°K, (e) 71°K, (f) 39.75°K, (g) 4.3°K, and (h) 1.9°K.

Table II

Mössbauer Parameters of δ-FeOOH

T K	Isomer Shift (δ)* mm/s	Quadrupole Splitting (ΔE) mm/s	Effective Magnetic Field(H) T	Area of Ferrimagnetic Component %
300	0.33	0.63	0	0
1.9	0.63	--	(O) 51.2 (T) 49.2	100

*Relative to α-iron.

O and T represent the octahedral and tetrahedral sites in the ferrimagnetic component, respectively.

value is somewhat higher than that measured by Dezsi et al. [1].

The relaxation time of the magnetization vector (τ) of the superparamagnetic particles depends on their volume (V) and the absolute temperature (T):

$$\tau = \frac{1}{\tau_o} e^{KV/kT} \qquad (1)$$

where τ_o, K and k are the frequency, anisotropy and Boltzmann factors, respectively. If $\tau >> \tau_L$ (where τ_L is the Larmor precision time), the δ-FeOOH particle is ferrimagnetic; if $\tau << \tau_L$ it is paramagnetic. If $\tau \approx \tau_L$, there is a transition where the Mössbauer spectrum has broadened lines (see Mössbauer spectra measured at 70°K < T < 120°K in Figure 2).

The Larmor precision time depends on the nuclear spin (I), magnetic quantum number (m_I), gyromagnetic factor (g), nuclear magneton (μ_m), and effective magnetic field (H) according to the following equation:

$$\frac{h}{\tau L} = \frac{m_I}{I} g \mu_m H \qquad (2)$$

where h is the Planck's constant. Using the parameters of the ^{57}Fe nucleus and the actual effective magnetic field (H ≈ 50 T), Equation (2) gives $\tau_L = 2.5 \times 10^{-8}$ s.

The effective magnetic field is affected slightly by the particle volume, and this correlation is given by:

$$H = H(\text{bulk})\left[1 - \frac{kT}{2KV}\right] \qquad (3)$$

Taking into account the fact that the magnetic field measured at the same temperature by Dezsi et al. [1] for bulk δ-FeOOH was ~5% higher than that for our δ-FeOOH sample, the anisotropy constant of δ-FeOOH was calculated using Equation (3). For this calculation, the average particle volume of δ-FeOOH sample was estimated to be 120 nm^3, which gave a value for the anisotropy constant $k \simeq 10^5\ J/m^3$.

Assuming that, at the transition temperature (~100°K for δ-FeOOH sample), the relaxation time for the magnetization vector is equal to the Larmor precision ($\tau=\tau_L$), from Equation (1) and the anisotropy constant above we can get the value of the frequency factor $\tau_o \simeq 10^{12}\ s^{-1}$. This value is higher by two orders than that published by Morup and Topsoe [5]. This discrepancy may be caused by the fact that the particles of our δ-FeOOH are not spherical but have needle shapes.

The Polymer Adsorption Results and Discussion

The same method to prepare Fe_3O_4 particles for adsorption isotherm determination was used again to obtain the isotherms of γ-Fe_2O_3, δ-FeOOH and β-FeOOH. The isotherms are shown in Figures 3-5 for γ-Fe_2O_3, δ-FeOOH and β-FeOOH, respectively. The critical polymer solution concentrations to reach the plateau regions were around 1.0 g/100 ml, 1.0 g/100 ml and 2.0 g/100 ml for γ-Fe_2O_3, δ-FeOOH and β-FeOOH, respectively. The saturated polymer segments adsorbed per 100 $Å^2$ of γ-Fe_2O_3 were 18.9 for polymethyl methacrylate (3.1 mg/m^2), 0.96 for post-chlorinated polyvinyl chloride (0.13 mg/m^2), 7.0 for Epon 1001F (5.8 mg/m^2) and 0.65 for Emerez 1511 (0.3 mg/m^2). For δ-FeOOH they were 4.8 for polymethyl methacrylate (0.8 mg/m^2), 1.5 for post-chlorinated polyvinyl chloride (0.2 mg/m^2), 0.6 for Epon 1001F (0.5 mg/m^2) and 2.0 for Emerez 1511 (0.8 mg/m^2). For β-FeOOH, they were 168.6 for polymethyl methacrylate (28.0 mg/m^2), 623 for post-chlorinated polyvinyl chloride (83.5 mg/m^2), 20.4 for Epon 1001F (16.9 mg/m^2) and 104.9 for Emerez 1511 (41.4 mg/m^2).

All of the above data showed that γ-Fe_2O_3, δ-FeOOH and β-FeOOH surfaces are amphoteric. From the polymer adsorption isotherms of standard basic polymer, polymethyl methacrylate, and standard acidic polymer, post-chlorinated polyvinyl chloride, along with the oligomer adsorption isotherms of basic Emerez 1511 curing agent and acidic Epon 1001F epoxy resin, the surfaces of these three particles have higher amounts of acidic sites than basic sites. In some cases, such as Epon 1001F on γ-Fe_2O_3 and post-chlorinated polyvinyl chloride on β-FeOOH, the adsorption amounts increase with increasing polymer equilibrium concentration. This type of adsorption isotherm having a slope higher than zero or multiple plateau regions was found in the literature also. These shapes result because of the adsorption of aggregates in such high

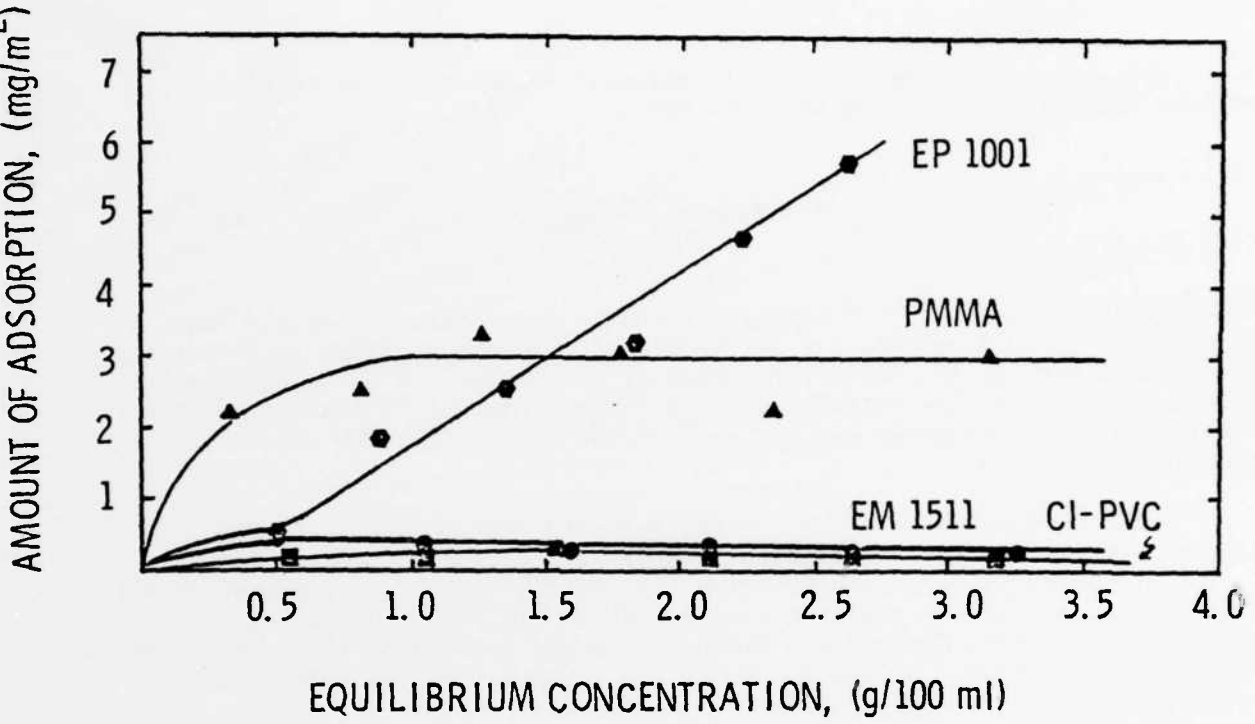

Figure 3. Adsorption isotherms of different polymers on γ-Fe_2O_3.

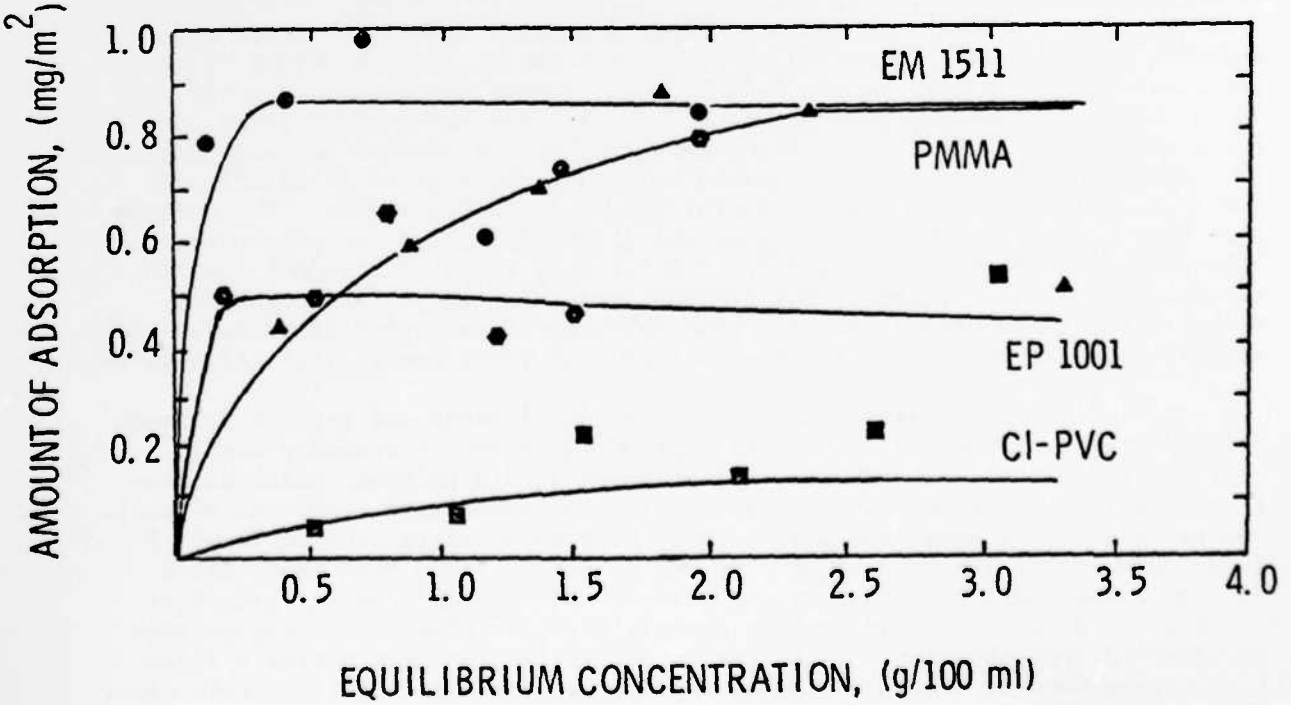

Figure 4. Adsorption isotherms of different polymers on δ-FeOOH.

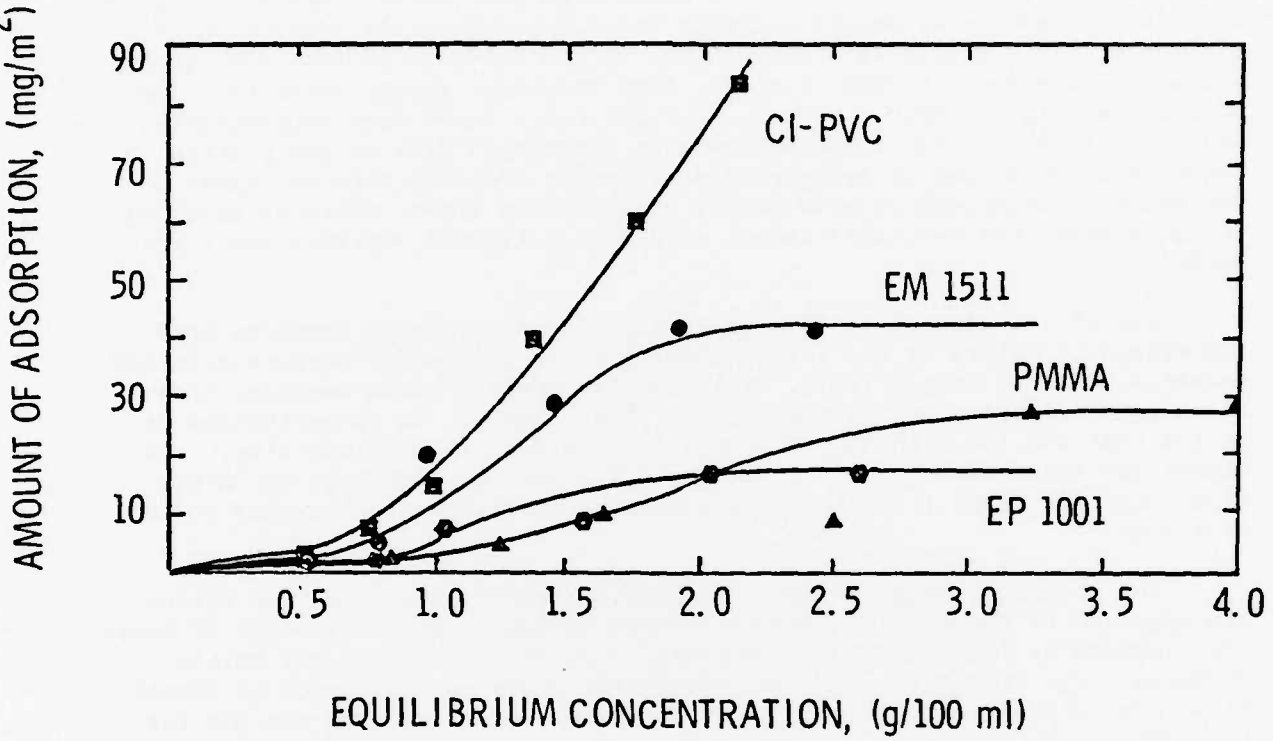

Figure 5. Adsorption isotherms of different polymers on β-FeOOH.

concentration polymer solution. The adsorption data showed that the adsorption of high molecular weight polymers was greater than the adsorption of oligomers. This result is a consequence of the tendency to form more compact surface layers for oligomers than for high molecular weight polymers. The adsorption data for Fe_3O_4, γ-Fe_2O_3, δ-FeOOH and β-FeOOH were reproducible. Table III shows the two different sets of adsorption data in the plateau region and the amount of polymers and oligomers adsorbed were all close to one another. Although in some cases, as mentioned above, there is adsorption of aggregates, the saturated amount of polymer/oligomer adsorbed was reproducible.

All of the adsorption data of prepared iron corrosion products are summarized in Tables IV and V in the units of mg polymer/m^2 surface area and segments/100 $Å^2$, respectively. The specific surface areas measured from argon gas adsorption are also listed in these tables. It is worthwhile to notice that the lower the surface area (the larger the particle size), the higher the amount of polymer adsorption. The smaller curvature on larger size particles makes it easier to adsorb more multiple-site-attached polymer molecules.

The polymer adsorption data of these laboratory-prepared iron oxides are compared to the data of commercial iron oxides in Table VI. All of these four commercial iron oxides were obtained from Pfizer Pigment and Metals Division. The iron oxide sols for adsorption study were prepared by dispersion. The differences in the iron oxide surface area, washing process for iron oxide particles, the polymer concentration used, and the procedure of the adsorption study make it impossible to compare these two sets of data quantitatively, but it is still possible to make qualitative comparisons. The results listed in Table VI showed that all four of these commercial iron oxides, i.e., Fe_3O_4, α-Fe_2O_3, γ-Fe_2O_3 and α-FeOOH, are also amphoteric and the acidic sites are also more numerous than the basic sites. Method A in Table VI showed the same trend of particle size effect as the laboratory-prepared particles. Generally speaking, the laboratory-prepared and commercial iron oxides have the same order of magnitude of adsorbed polymer.

Table III

Reproducibility of Polymer Adsorption Data

(mg polymer/m^2 surface area)

	#1				#2			
Iron Oxide	PMMA	Cl-PVC	Epon 1001F	Emerez 1511	PMMA	Cl-PVC	Epon 1001F	Emerez 1511
Fe_3O_4	12.0	6.4	5.7	8.9	11.6	7.2	5.2	8.3
γ-Fe_2O_3	3.1	0.13	5.8	0.3	2.7	0.11	4.7	0.35
δ-FeOOH	0.8	0.2	0.5	0.8	0.75	0.32	0.47	0.82
β-FeOOH	28.0	83.5	16.9	41.4	27.6	85.3	17.2	38.5

Table IV

Polymer Adsorption on Prepared Iron Oxides

Iron Oxide	Specific Surface Area (m^2/g)	Polymer Adsorption, mg polymer/m^2 surface area			
		PMMA	Cl-PVC	Epon 1001F	Emerez 1511
α-Fe_2O_3	3.4	83.0	103	180	393
α-FeOOH	56.3	8.36	2.53	15.1	9.48
γ-FeOOH	18.3	11.6	10.8	47.5	33.9
Fe_3O_4	82.5	12.0	6.4	5.7	8.9
γ-Fe_2O_3	68.9	3.1	0.13	5.8	0.3
δ-FeOOH	206.0	0.8	0.2	0.5	0.8
β-FeOOH	16.5	28.0	83.5	16.9	41.4

Table V

Polymer Adsorption on Prepared Iron Oxides

Iron Oxide	Specific Surface Area (m^2/g)	Polymer Adsorption, segments/100 $\mathring{A}^2$			
		PMMA	Cl-PVC	Epon 1001F	Emerez 1511
α-Fe_2O_3	3.4	499.	774.	216.	1003.
α-FeOOH	56.3	50.2	19.0	18.2	24.2
γ-FeOOH	18.3	70.0	80.8	57.0	86.8
Fe_3O_4	82.5	72.3	47.8	6.9	22.5
γ-Fe_2O_3	68.9	18.9	0.96	7.0	0.65
δ-FeOOH	206.0	4.8	1.5	0.6	2.0
β-FeOOH	16.5	168.6	623.	20.4	104.9

Table VI

Polymer Adsorption on Oxide Dispersions Prepared by Dispersion

Iron Oxide	Specific Surface Area (m^2/g)	Method	Polymer Adsorption, Segments/100 $Å^2$			
			PMMA	Cl-PVC	Epon 1001F	Emerez 1511
Fe_3O_4	5.72	A	57.8	174.	8.95	12.5
		B	843.	111.	2.35	27.6
α-Fe_2O_3	9.90	A	66.2	90.0	13.0	15.3
		B	541.	165.	24.7	43.4
α-FeOOH	10.66	A	57.8	90.1	4.34	7.41
		B	3550.	33.8	22.9	29.4
γ-Fe_2O_3	19.80	A	18.1	52.6	5.96	2.50
		B	1900.	12.0	10.6	33.2

The Conductive Titration

The acidic sites of these laboratory-prepared iron oxides can be determined quantitatively from conductometric titration with a strong base such as NaOH.

Approximately 0.016 g iron oxide particles dispersed in 200 ml distilled-deionized water was cleaned to constant conductivity (approximately 2.95×10^{-6} $ohm^{-1} cm^{-1}$ in average) and then titrated with 0.0200N NaOH solution. These results are shown in Figures 6-12. All these particles showed the typical strong acidic group titration curves. These titration data are listed in Table VII along with the adsorption data of PMMA standard basic polymer. It is believed that these data support the concept that the seven laboratory-prepared iron corrosion product particles have acidic FeOH functional groups on the surfaces which dominate over the basic groups.

Table VII

Polymer Adsorption and Conductometric Titration Data on Iron Oxides

Iron Oxide	PMMA Adsorption Segments/100 Å^2	Acidic Sites from Titration, Sites/100 Å^2	PMMA Adsorption Segments/Site
α-Fe_2O_3	499	30.1	16.6
α-FeOOH	50.2	1.81	27.8
γ-FeOOH	70.0	2.59	27.0
Fe_3O_4	72.3	0.397	182
γ-Fe_2O_3	18.9	0.482	39.2
δ-FeOOH	4.8	0.379	12.7
β-FeOOH	168.6	13.2	12.8

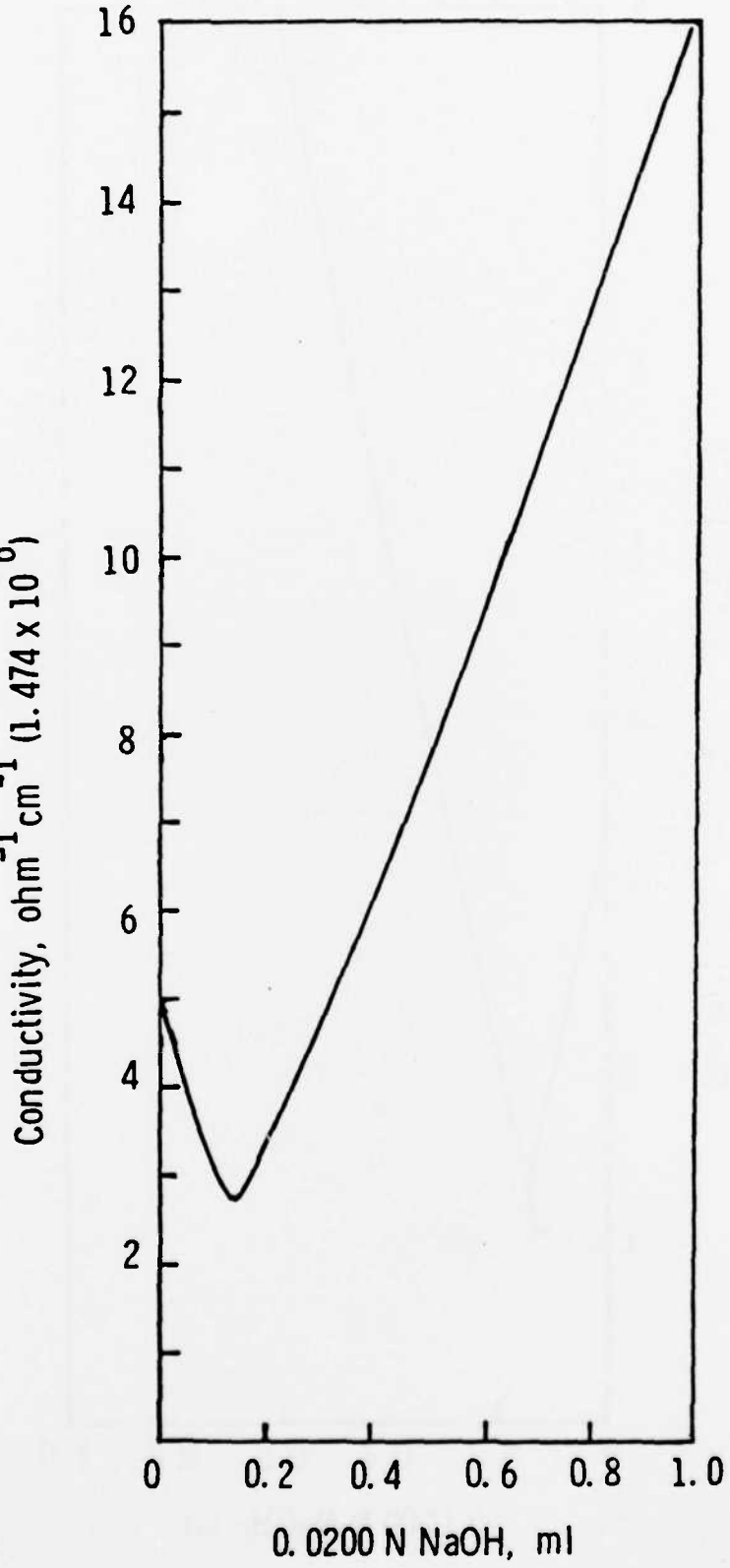

Figure 6. Conductometric titration of α-Fe_2O_3 (0.0158 g in 200 ml dispersion).

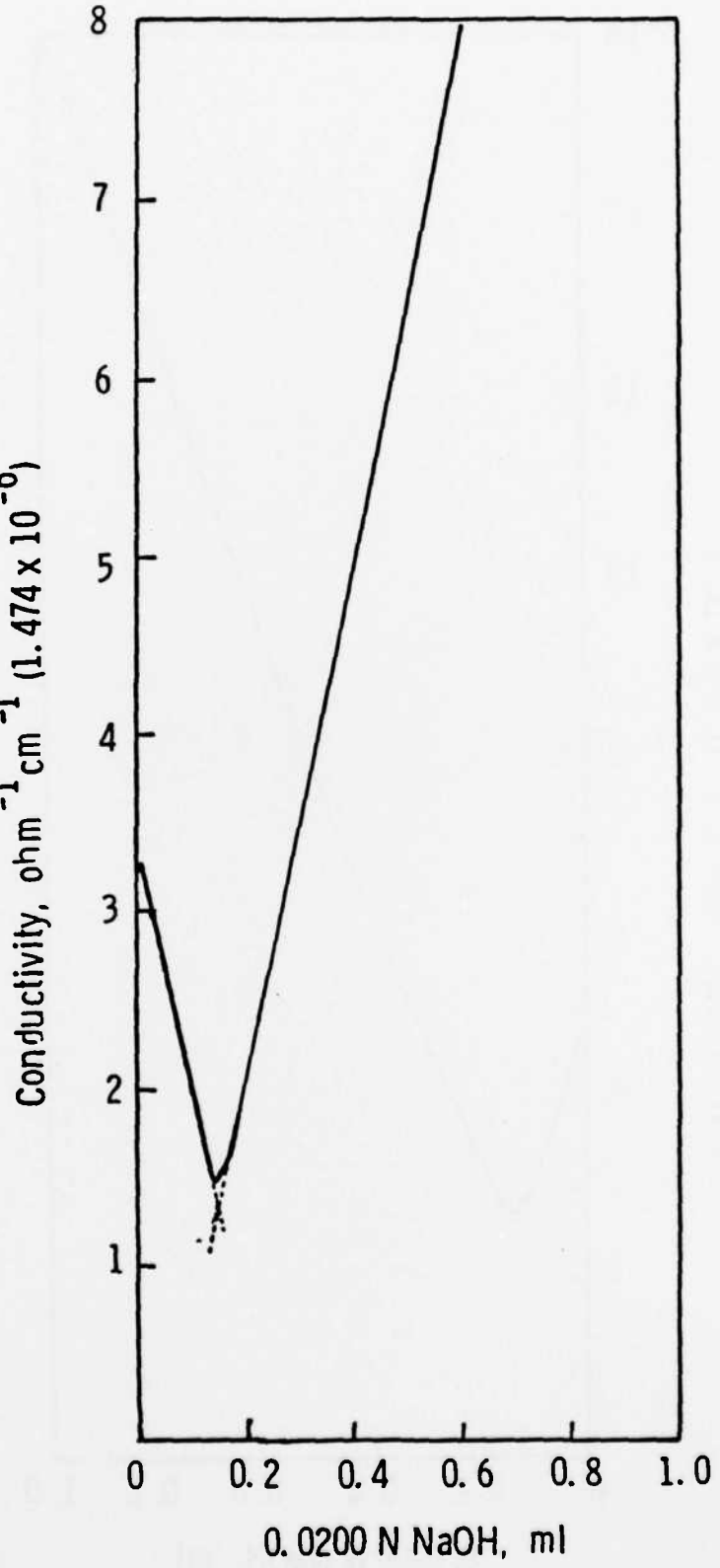

Figure 7. Conductometric titration of α-FeOOH (0.0171 g in 200 ml dispersion).

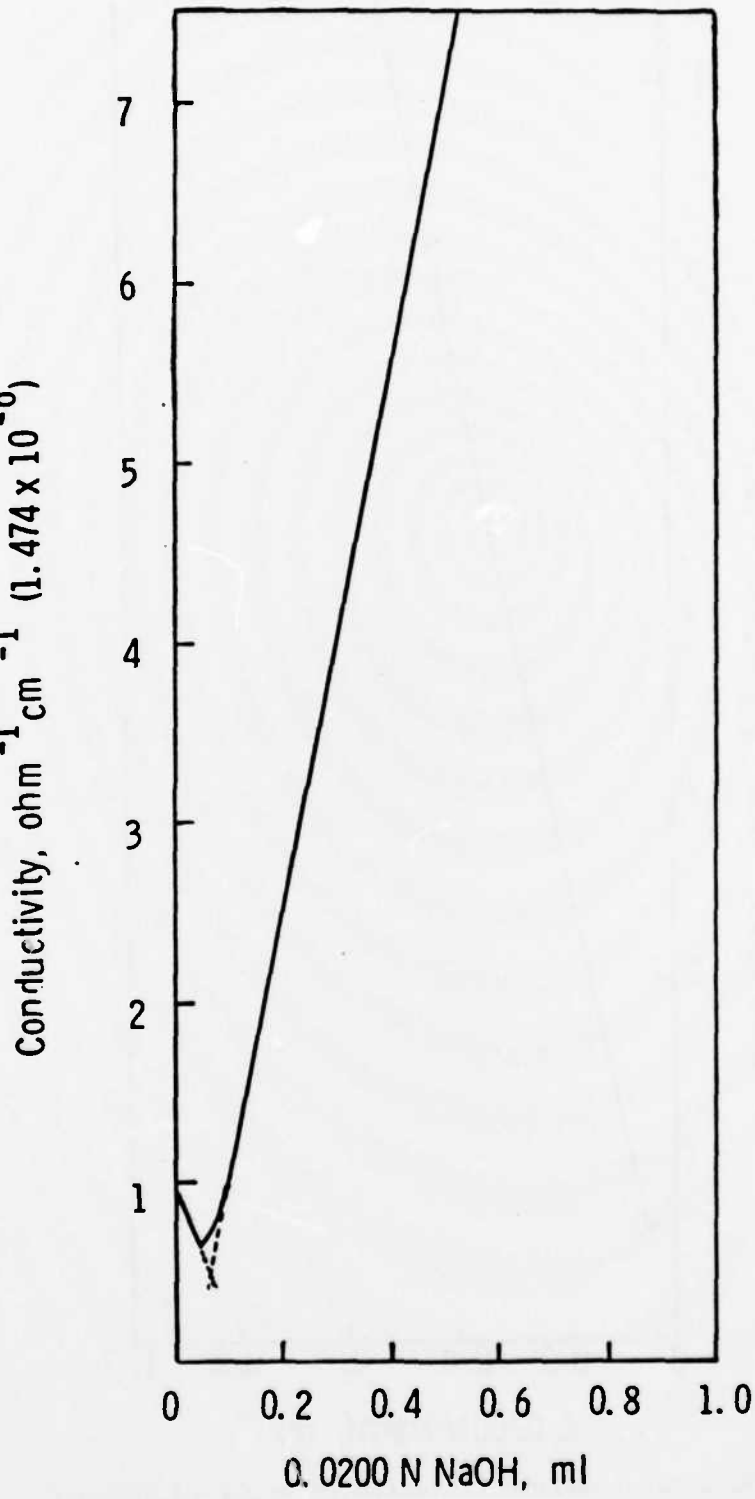

Figure 8. Conductometric titration of γ-FeOOH (0.0150 g in 200 ml dispersion).

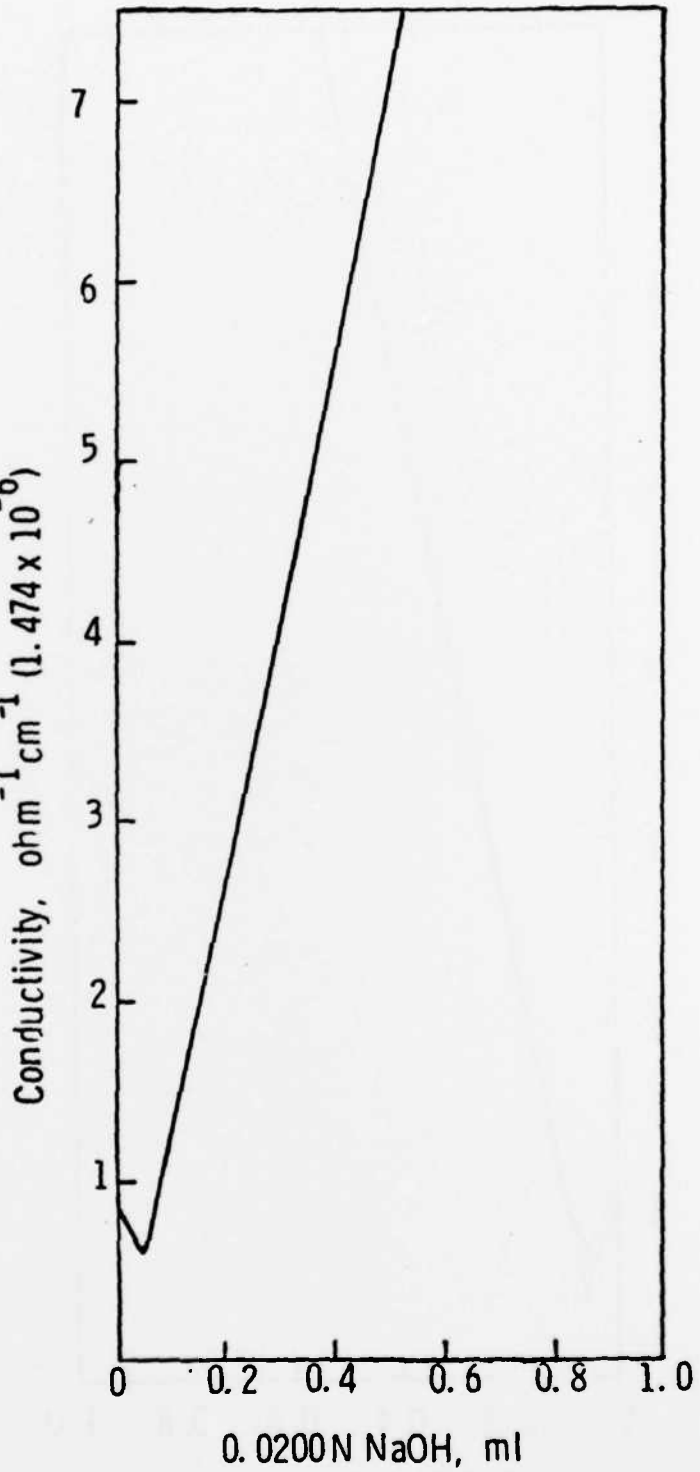

Figure 9. Conductometric titration of Fe_3O_4 (0.0163 g in 200 ml dispersion).

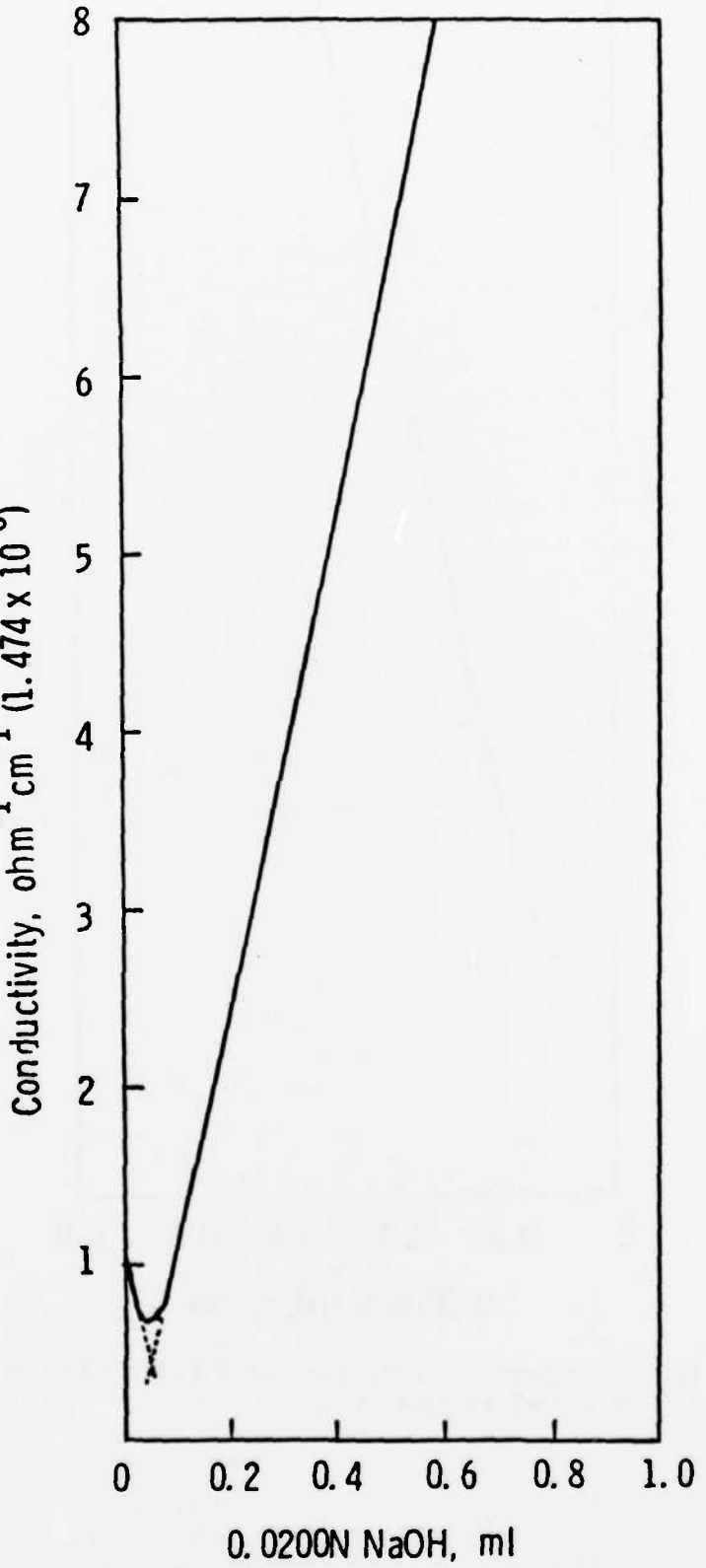

Figure 10. Conductometric titration of γ-Fe_2O_3 (0.0171 g in 200 ml dispersion).

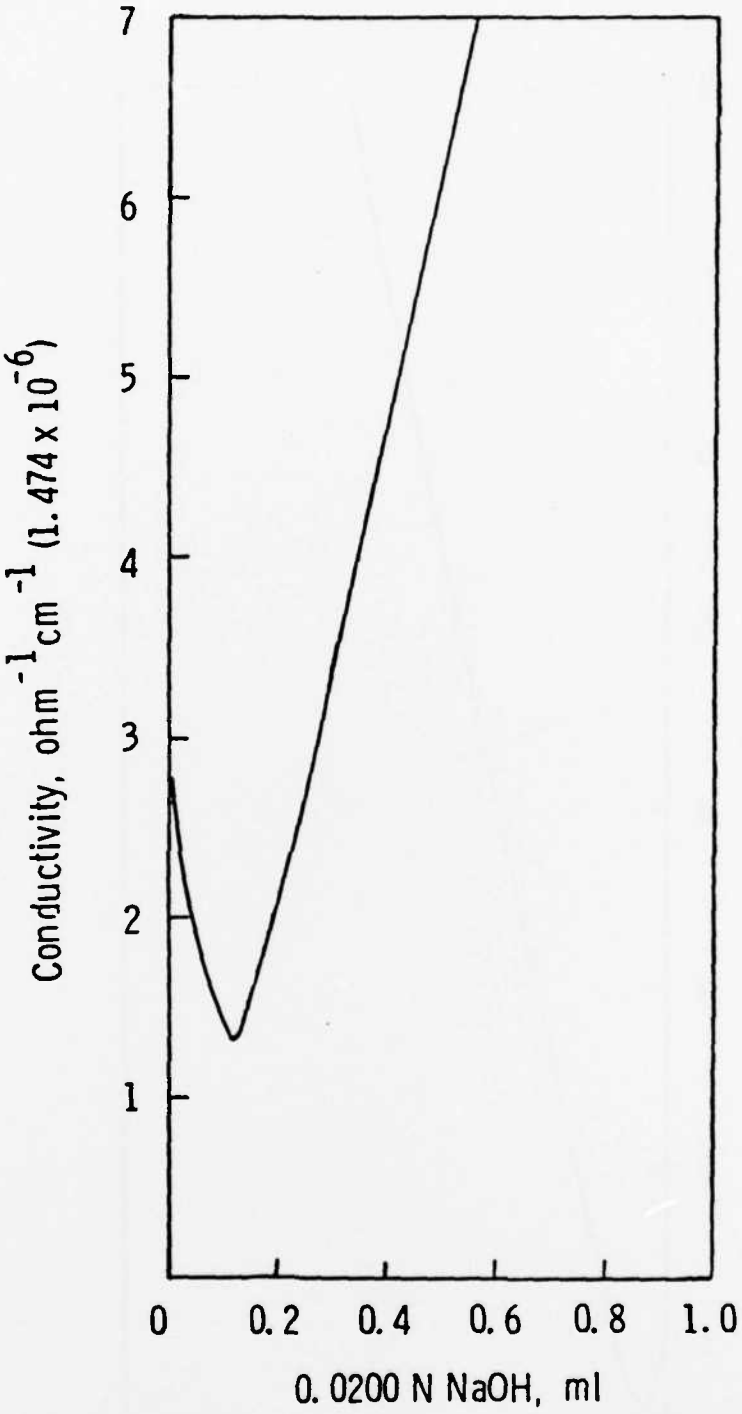

Figure 11. Conductometric titration of δ-FeOOH (0.0174 g in 200 ml dispersion).

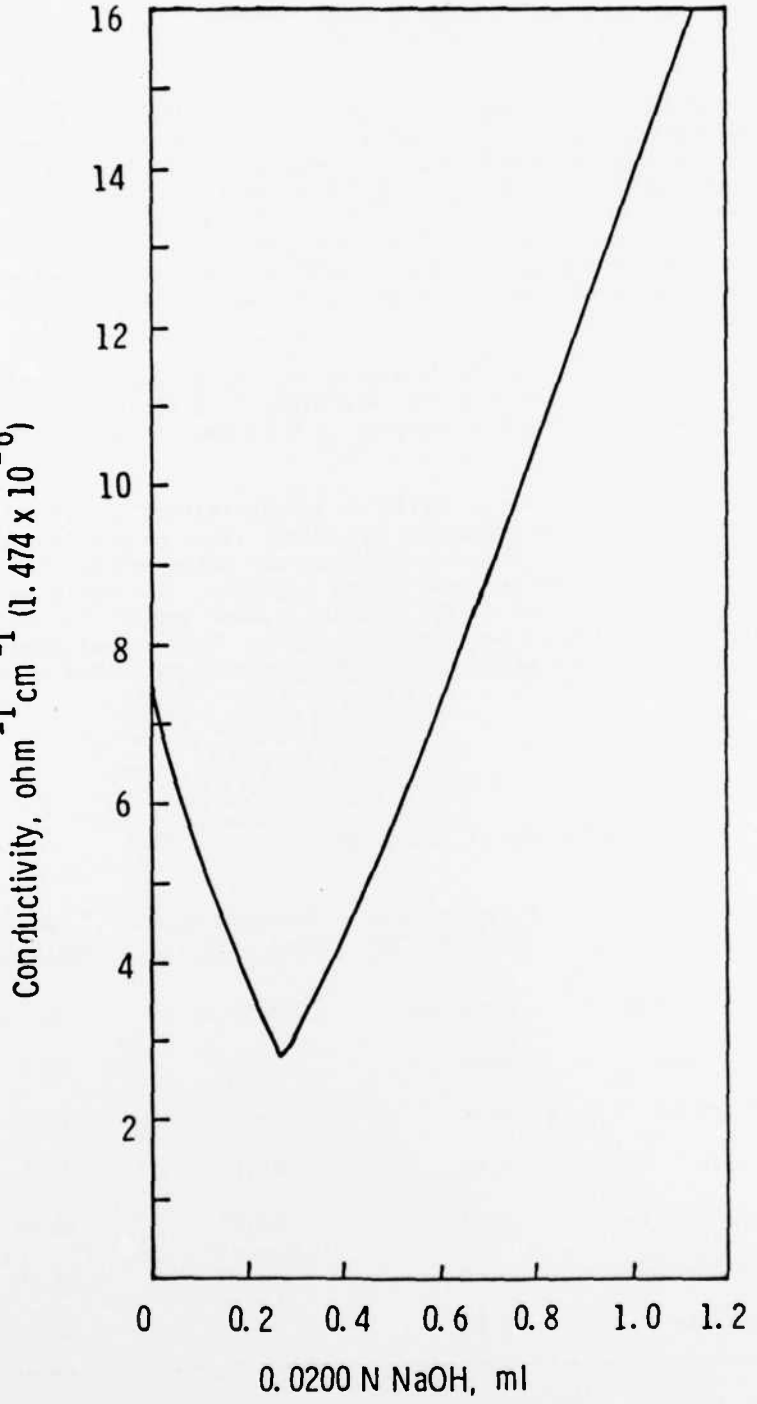

Figure 12. Conductometric titration of β-FeOOH (0.0146 g in 200 ml dispersion).

CONCLUSIONS

From the particle morphology obtained from transmission electron microscopy and argon gas adsorption (Table VIII) along with the adsorption data (Tables V and VII) for these laboratory-prepared corrosion product particles, it was concluded that the larger the particle, the greater the amount of polymer adsorption. This conclusion is consistent with the conductometric titration results. From the titration results in Table VII, the larger particles have a higher density of acidic sites. This density effect together with the surface curvature effect makes the larger particles adsorb a greater amount of polymer.

From Table VII it is possible to deduce that every acidic site of the iron oxide particle surface is attached to a segment of the PMMA molecule and loops of approximately 30 PMMA segments long project into the polymer solution.

The PMMA molecule used has a degree of polymerization of 3,000. This PMMA molecule will occupy approximately 100 acidic sites on the iron oxide surfaces. The conformation of the adsorbed polymer molecules is multiple-site attachment with loops between the anchor segments. The end-to-end distance of the PMMA coil is about 340 Å which is much larger than the adsorption thickness calculated from Table VII, 45 Å. This calculation showed that the conformation of the adsorbed polymer molecules described above is realistic.

Table VIII

The Morphology of the Prepared Iron Oxides

Particle	Particle Shape	Particle Size Based on TEM	Particle Size Based on S.S.A.	Specific Surface Area
α-Fe_2O_3	Spheroidal	0.10 μm	0.30 μm	3.4 m^2/g
α-FeOOH	Acicular	0.30	--	56.3
γ-FeOOH	Acicular	0.70	--	18.3
Fe_3O_4	Cubic	0.01	0.01	82.5
γ-Fe_2O_3	Cubic	0.01	0.02	68.9
δ-FeOOH	Needlelike	0.03	--	206.0
β-FeOOH	Spindle	0.60	--	16.5

REFERENCES

[1] T. Dezsi, L. Keszthelyi, D. Kulgowczuk, B. Molnar, V. A. Eissa, Phys. Stat. Sol. 22, 617 (1967).

[2] G. V. Loseva, N. V. Murashko, Izv. Akad. Nauk SSSR, Neorg. Mater. 7, 1467 (1971).

[3] L. V. Moskvin, A. A. Efimov, L. A. Varosin, G. A. Usacheva, S. B. Tamilov, A. C. Petrov, At. Energy 46, 27 (1979).

[4] A. Povitskii, E. F. Makarov, N. V. Murashko, A. N. Salugin, Phys. Stat. Sol. 33A, 783 (1976).

[5] S. Morup, H. Topsoe, Appl. Phys. 11, 63 (1976).


DAT
FILM

γ-Fe_2O_3	Cubic			
δ-FeOOH	Needlelike	0.03	--	206.0
β-FeOOH	Spindle	0.60	--	16.5